IMPROVING THE UNDERSTANDING AND SIMULATION OF PRECIPITATION FORMING PROCESSES THROUGH COMBINED ANALYSIS OF MICROPHYSICAL MODELS AND MULTI-FREQUENCY DOPPLER RADAR OBSERVATIONS

INAUGURAL-DISSERTATION

ZUR

ERLANGUNG DES DOKTORGRADES

DER MATHEMATISCH-NATURWISSENSCHAFTLICHEN FAKULTÄT

DER UNIVERSITÄT ZU KÖLN

VORGELEGT VON

MARKUS KARRER

AUS BIETIGHEIM-BISSINGEN

KÖLN, OKTOBER 2021

BERICHTERSTATTER:
DR. STEFAN KNEIFEL
PROF. DR. ROEL NEGGERS

TAG DER MÜNDLICHEN PRÜFUNG:
2. DEZEMBER 2021

ABSTRACT

The society is strongly influenced by precipitation, which forms by cloud microphysical processes, e.g., sedimentation and aggregation. These processes determine where and how clouds precipitate relevant for the global water cycle, freshwater availability, and flooding.

However, the precipitation forming processes are poorly understood and pose a significant challenge to earth system modeling. Challenges arise from the difficulties of deriving parameterizations from laboratory experiments or observations. Even if accurate process parameterizations could be derived, implementing them into numerical models poses additional challenges due to computational cost and unresolved scales. In the last decades, rapid progress has been made in modeling and observing microphysical processes, which enables or even necessitates further studies that exploit the synergy between both fields.

In this thesis, microphysical models are employed that either resolve the microphysical processes up to the single particle level (3D snowflake model and Lagrangian particle model) or are computationally efficient (bulk scheme). The explicit models are used to derive parameterizations and provide detailed insights into the processes that can be used in the less explicit models. Improving the less explicit but computationally efficient bulk schemes is particularly important, as they are indispensable for weather and climate prediction. Output from all models is compared to observations that provide information either on individual particle properties (in situ particle observations) or average properties of large particle ensembles (multi-frequency Doppler radar observations). These model-observation combinations are used to improve the knowledge about the microphysical processes and their representation in the microphysical models.

3D snowflake models simulate the complex shape of ice particles, the representation of which presents a major difficulty for microphysical schemes. In Study I, such a 3D snowflake model is used to derive parameterizations of particle properties, such as mass as a function of size, monomer number and shape. Hydrodynamic models are used to additionally derive the particle velocity. The most detailed parameterizations are used to assess the effect of aggregate composition on the particle properties, which is challenging to do with observations alone. It is found that aggregate properties change smoothly with increasing monomer number but differ substantially depending on the monomer shapes that constitute the aggregates. Other, less detailed parameterizations can be readily applied in bulk microphysical schemes to improve the physical consistency of these schemes. In simulations

with a Lagrangian particle model, it can be shown that these less detailed parameterisations are very accurate even if they only distinguish between the two classes of monomers and aggregates. Comparing the parameterization with in situ observations ensures that they are physically realistic in size ranges where observations are available. In addition, the physical principles of the 3D snowflake and hydrodynamic models help to ensure that the parameterizations are realistic even in size ranges for which it is difficult to obtain observations.

In Study II, parameters that are important for the microphysical description of sedimentation and aggregation in a two-moment scheme bulk microphysics scheme are constrained by observations. Traditionally, microphysical parameterizations are tuned to improve the prediction of few variables of interest, such as the precipitation rate. This procedure likely introduces compensating errors, since adjusting one parameter may improve the prediction of these variables even if that change leads away from the most physically meaningful value of the parameters. Therefore, a different approach is used in this study that uses several variables from multi-frequency Doppler radars simultaneously and focuses on single or few processes to avoid this issue of underdetermined parameters. First, the observed statistics are used to evaluate microphysical parameters in an idealized 1D model, which allows efficient testing of all key parameters. These simulations reveal that the simulation of aggregation is most sensitive to the aggregate particle properties, the aggregation kernel formulation and the size distribution width and less sensitive to the monomer habit and the sticking efficiency. A statistical comparison between 3D large-eddy simulations with the default and the new scheme setup and the observations show that previously existing large biases of too fast and too large particles in the scheme could be substantially reduced. This bias reduction can be attributed to the improved simulation of sedimentation and aggregation.

Since a large portion of precipitation reaches the ground as rain but forms in the ice phase, processes in the melting layer are an essential part of precipitation modeling. In Study III, an approach is used to infer the dominance of growth or shrinkage processes through the relationship of reflectivity flux at the melting layer boundaries. In addition, radar Doppler spectra and multi-frequency observations are used to evaluate assumptions of the approach and to classify profiles according to the degree of riming. For unrimed profiles, growth processes increase the mean mass only slightly. For rimed profiles, shrinking processes lead to a substantial decrease the mean mass probably caused by particle breakup. Simulations using a Lagrangian particle model reveal that breakup processes for which parameterizations are available can not reproduce the observed decrease of the mean mass for rimed profiles and suggest that further laboratory studies of collisional breakup of melting particles are needed.

ZUSAMMENFASSUNG

Die Gesellschaft wird stark vom Niederschlag beeinflusst, der sich durch mikrophysikalische Prozesse, z.B. Sedimentation und Aggregation, bildet. Diese Prozesse bestimmen, wo und wie Niederschlag ensteht, was für den globalen Wasserkreislauf, die Verfügbarkeit von Süßwasser und Überflutungen von Bedeutung ist.

Die Prozesse, die zu Niederschlag führen, sind jedoch nur unzureichend bekannt und stellen eine große Herausforderung für die Modellierung des Erdsystems dar. Herausfordernd ist sowohl die Ableitung von Parametern aus Laborexperimenten oder Beobachtungen, als auch die Implementierung dieser Parameter in numerische Modelle. Für letzteres sind besonders die begrenzter Rechenzeit und unaufgelösten Skalen kritisch. In den letzten Jahrzehnten wurden rasche Fortschritte bei der Modellierung und Beobachtung mikrophysikalischer Prozesse erzielt, welche weiterführende Studien die die Synergie zwischen beiden Bereichen nutzt, ermöglicht und dringend notwendig macht. In dieser Arbeit werden mikrophysikalische Modelle verwendet, die entweder die mikrophysikalischen Prozesse bis auf die Ebene einzelner Partikel auflösen (3D-Schneeflockenmodell und Lagrangesches Partikelmodell) oder rechnerisch effizient sind (Bulk-Schema). Die expliziten Modelle werden zur Ableitung von Parametrisierungen verwendet und liefern detaillierte Einblicke in die Prozesse, die in den weniger expliziten Modellen verwendet werden können. Die Verbesserung der weniger expliziten, aber rechnerisch effizienten Bulk-Schemata ist besonders wichtig, da sie für die Wetter- und Klimavorhersage unverzichtbar sind. Die Ergebnisse aller Modelle werden mit Beobachtungen verglichen, die entweder Informationen über einzelne Partikeleigenschaften (in situ-Partikelbeobachtungen) oder über die durchschnittlichen Eigenschaften großer Partikelensembles (Mehrfrequenz-Dopplerradarbeobachtungen) liefern. Diese Modell-Beobachtungs-Kombinationen werden verwendet, um das Wissen über die mikrophysikalischen Prozesse und deren Abbildung in Mikrophysik Schemata zu verbessern.

3D-Schneeflockenmodelle simulieren die komplexe Form von Eispartikeln, die eine große Schwierigkeit für mikrophysikalische Modelle darstellt. In Studie I wird solch ein 3D-Schneeflockenmodell verwendet, um Parametrisierungen von Partikeleigenschaften abzuleiten, wie z.B. die Masse als Funktion der Größe, Monomerzahl und -form. Hydrodynamische Modelle werden verwendet, um zusätzlich die Fallgeschwindigkeit abzuleiten. Die detailliertesten Parametrisierungen werden benutzt, um die Bedeutung der Aggregatzusammensetzung zu beurteilen, was anhand von Beobachtungen allein nur schwer möglich ist. Es zeigt sich, dass sich die Aggregateigenschaften mit

zunehmender Monomerzahl gleichmäßig verändern, sich aber je nach Monomertyp, aus denen die Aggregate bestehen, erheblich unterscheiden. Andere, weniger detaillierte Parametrisierungen können ohne weiteres in Bulk-Schemata angewendet werden, um die physikalische Konsistenz dieser Schemata zu verbessern. In Simulationen mit einem Lagrangen Partikelmodel kann gezeigt werden, dass diese weniger detaillierten Parameterisierungen auch dann sehr akkurat sind, wenn sie nur zwischen den beiden Klassen der Monomere und der Aggregate unterscheiden. Der Vergleich der Parametrisierung mit in situ-Beobachtungen stellt sicher, dass sie in Größenbereichen, für die Beobachtungen vorliegen, physikalisch realistisch sind. Darüber hinaus tragen die physikalischen Prinzipien der 3D-Schneeflocken- und hydrodynamischen Modelle dazu bei, dass die Parametrisierungen auch in Größenbereichen realistisch sind, für die es schwierig ist, Beobachtungen zu erhalten.

In Studie II werden wichtige mikrophysikalische Parametrisierungen der Sedimentation und Aggregation, die in einem Bulk-Schema verwendet werden, durch Vergleich mit Beobachtungen verbessert. Traditionell werden mikrophysikalische Parametrisierungen optimiert, indem einige wenige Variablen von Interesse, z.B. die Niederschlagsrate, optimiert werden. Dieses Vorgehensweiße führt wahrscheinlich zu Kompensationsfehlern, da die Anpassung eines Parameters die Vorhersage der Variablen von Interesse auch dann verbessern kann, wenn die neuen Parameter dadurch stärker von physikalisch sinnvollsten Wert abweichen. Im Gegensatz dazu wird durch den gleichzeitigen Vergleich mehrerer Variablen von Mehrfrequenz-Doppler Radaren und die Fokussierung auf einzelne oder wenige Prozesse das Problem der unterbestimmten Parameter vermieden. Zunächst werden die Radarstatistiken verwendet, um mikrophysikalische Parameter in einem idealisierten 1D-Modell (das ein effizientes Testen aller wesentlicher Parameter erlaubt) zu evaluieren. Diese Simulationen zeigen die stärkste Sensitivität für die Partikeleigenschaften der Aggregate, die Formulierung des Aggregationskernels und die Breite der Größenverteilung und eine geringere Sensitivität für die Monomerpartikeleigenschaften und die Hafteffizienz. Der statistische Vergleich zwischen den 3D-Simulationen mit dem default und dem neuen Schema und den Beobachtung zeigt, dass zuvor bestehende großen Abweichungen von zu schnellen und zu großen Partikel im Schema reduziert werden konnten. Diese Verringerung der Abweichungen kann auf die verbesserte Simulation von Sedimentation und Aggregation zurückgeführt werden.

Da ein großer Teil des Niederschlags den Boden als Regen erreicht, sich aber in der Eisphase bildet, sind Prozesse in der Schmelzschicht ein wesentlicher Bestandteil der Niederschlagsmodellierung. In Studie III wird ein Ansatz angewendet, der die Dominanz von Wachstums- oder Schrumpfungsprozessen durch die Beziehung des Reflektivitätsflusses an den Rändern der Schmelzschicht ableitet. Zudem werden Radar-Doppler-Spektren und Multifrequenzbeobachtungen benutzt um Annahmen des Ansatzes zu evaluieren und Profile nach dem Verreifungsgrad zu klassifizieren. Bei unverreiften Profilen erhöhen Wachstumsprozesse die mittlere Masse geringfügig. Bei verreiften Profilen führen Schrumpfungsprozesse zu einer deutlichen Abnahme der mittlere Masse, was wahrscheinlich durch das Auseinanderbrechen von Partikeln verursacht wird. Simulationen mit einem Lagrangeschen Partikelmodell zeigen, dass Aufbruchsprozesse, für die Parametrisierungen verfügbar sind, die beobachtete Abnahme des Reflektivitätsflusses nicht reproduzieren können, und deuten darauf hin, dass weitere Laborstudien zu dem Auseinanderbrechen von schmelzenden Partikel nach Kollision erforderlich sind.

CONTENTS

1 INTRODUCTION

1.1 MOTIVATION

Clouds cover about 70% of the earth's surface (King et al., 2013; Stubenrauch et al., 2013). However, only one in ten clouds form precipitation that reaches the ground (Lohmann et al., 2016, Chapter 7). For precipitation to occur, the particles must be large enough for the terminal velocity of the particles to overcome the updrafts that lead to the cloud formation in the first place. Furthermore, only particles large enough to reach the ground despite sublimation or evaporation can lead to precipitation if there is an undersaturated layer below the cloud base (Lohmann et al., 2016, Chapter 7).

Knowing if, where, and how clouds precipitate is fundamental to simulate their radiative effects, the global water cycle, freshwater availability, natural hazards, and local weather conditions. Precipitation decreases the lifetime of clouds, which, in turn, decreases their impact on radiation (Boucher et al., 2013). The net cloud radiative effect (which is overall cooling) can be estimated increasingly better (Raschke et al., 2016; Loeb et al., 2018), but limited knowledge about cloud properties, which are strongly affected by cloud microphysics, hamper further improvements (Boucher et al., 2013). Thus, besides changes in global circulation, cloud microphysics determine how cloud properties respond to climate change and how the cloud radiative effect will change. Furthermore, precipitation constitutes an important source of freshwater. The quantification and monitoring of freshwater supplies is critical for the society, especially in a changing climate. For example, the changing location, intensity, and thermodynamic phase of the precipitation, due to climate change will require adaption strategies to maintain water supplies (Barnett et al., 2005). Also, precipitation can pose a major life-threatening and economic-loss risk. For example, high precipitation rates can lead to flooding (Ward et al., 2020). Finally, precipitation (timing, probability, location, and type) is considered the most relevant aspect of weather forecast by the public (Lazo et al., 2009).

Despite their importance to the climate system and human activities, many components of cloud and precipitation processes remain poorly understood and represent a large uncertainty for climate modeling and numerical weather prediction (Boucher et al., 2013; Bauer et al., 2015). One of the biggest sources of uncertainty for these models stem from the simulation of cloud microphysical processes, which are processes that take place at the level of the individual particles. These uncertainties result from both, the knowledge gaps about the processes and the difficulty to represent the processes efficiently in numerical models (Morrison et al., 2020). For example, it is not well known how the shape of ice particles influence their ability to aggregate. Furthermore, in computationally efficient numerical models, the shape of ice particles can only be roughly approximated or simulated. Thus, even if the knowledge about the effect of particle shape on aggregation could be improved, further investigations are necessary that investigate how the models can benefit from this improved knowledge. The simulation of cloud microphysics is especially challenging, when the cloud dynamics (also referred to as cloud macrophysics) have to be partially parameterized, too. In this case, both parameterization have to be well coupled. For example, additional assumptions about the depositional growth of a particle population are required if small scale variations of vertical air motions are diagnosed, e.g. by a turbulence scheme, but are not explicitly predicted, e.g. in a direct numerical simulation.

About 70% of the global precipitation forms via cold rain (Mülmenstädt et al., 2015; Heymsfield et al., 2020). The term cold rain refers to precipitation formation where particles grow first via ice growth mechanisms (depositional growth, aggregation, and riming), melt at temperatures above 0°C and reach the ground as raindrops. The cold rain precipitation pathway is predominant because it can involve several efficient growth processes (ice growth mechanisms, condensation and collision-coalescence). Additionally, cold rain often forms in clouds with a large vertical extent, which allows the particles to grow over a long time. Ice microphysical processes are especially complicated to simulate with microphysics schemes because ice particles have complex shapes, which influence all microphysical processes, and all three thermodynamic phases of water must be considered (Morrison et al., 2020). Three processes relevant to precipitating clouds are investigated in this dissertation and discussed in the following: sedimentation, aggregation, and melting.

A precondition for precipitation is that the particles' fall speed overcomes the upwind typically present in clouds. Just after nucleation, cloud ice particles are small and have a negligible fall speed with respect to the air. However, if the air is supersaturated, depositional growth increases the particles' mass, and thus velocity, so that a fall speed of 0.1m/s can be reached within minutes (Lohmann et al., 2016, Section 8.3). Other ice growth processes, such as riming and aggregation, further increases the particles' velocity, and, thus, precipitation can also occur in clouds with higher upwind and subsaturated air below the cloud base. How fast ice particles fall exactly depends on their size and shape (Locatelli and Hobbs, 1974; Heymsfield and Kajikawa, 1987; Mitchell et al., 1990b), which is a result of the above-mentioned processes.

Aggregation, like depositional growth and riming, is a process that increases the size and velocity of ice particles, thus, contributing to precipitation formation. Unfortunately, many parameters needed to describe and simulate aggregation are poorly constrained and challenging to represent in microphysical models. Before particles can aggregate, they must collide. If the particles are larger than a few μm, the collisions happen primarily due to differential sedimentation because the fall speed are larger than Brownian or turbulent motions (Jacobson, 2005, Section 15.6). The rate of these collisions is determined by the particle properties (geometry and velocity). Parameterizations of particle geometry and velocity obtained from in situ observations (Kajikawa, 1972; Locatelli and Hobbs, 1974; Mitchell et al., 1990a) are often based on small samples and limited size range due to the limitations of the observational methods. Therefore, those parameterizations are subject to considerable uncertainties especially at very small and large sizes. Moreover, even when robust parameterizations for different habits (characteristic monomer shapes) and particle types (e.g., aggregates, graupel) are found, it is still challenging to represent the vast variability of particle shapes in microphysics schemes. For example, most bulk schemes allow just a single mass-size relationship for all monomers (cloud ice), although the diversity of observed particle shapes is vast. Since not all collisions lead to aggregation, the sticking efficiency that describes what portion of the particles stick after the collisions must also be considered. The sticking efficiency is known to be large at temperatures about -15°C (dendritic growth zone) and close to the 0°C (Phillips et al., 2007; Connolly et al., 2012; Barrett et al., 2019). However, also, the values of the sticking efficiency are subject to great uncertainty, mainly due to limitations and scarcity of laboratory studies.

Processes in the melting layer determine how the ice and the rain particle population, e.g., their mean sizes, are connected, which is especially relevant for cold rain formation. The melting process of individual particles has been studied in the laboratory (Knight, 1979; Rasmussen and Heymsfield, 1987; Oraltay and Hallett, 1989; Mitra et al., 1990; Oraltay and Hallett, 2005). These studies explained the observed melting rate by thermodynamic considerations and observed breakup under certain conditions (e.g., large rimed particle and strongly subsaturated air). Also, microphysical processes present in ice clouds, e.g., aggregation, were observed in the melting layer by in situ (Stewart et al., 1984; Yokoyama et al., 1985; Barthazy et al., 1998; Heymsfield et al., 2015) and remote sensing (Klaassen, 1988; Fabry and Zawadzki, 1995) observations. Again, microphysics schemes must simplify the representation of the processes and can only be as accurate as process understanding allows. Challenging is especially the representation of the particle properties of partially melted particles (Szyrmer and Zawadzki, 1999; Phillips et al., 2007; Thériault and Stewart, 2010; Frick et al., 2013; Cholette et al., 2019). Furthermore, better knowledge and quantification of collision and breakup processes of these particles is required for accurate modeling of the melting layer.

To improve simulation and understanding of microphysical processes, various modeling and observational techniques have been developed. In the following, these techniques are discussed, focusing on the techniques used in this dissertation.

Microphysics schemes simulate various processes and are usually applied in the framework of dynamical models, such as large-eddy simulations. How explicitly microphysics schemes simulate the processes varies from scheme to scheme, and so does their computational cost (Khain et al., 2015). The trade-off between accuracy and computational cost allows the most explicit schemes (e.g., Lagrangian particle models) to be used only for research purposes and relatively small simulation domains. Lagrangian particle models simulate the evolution of individual particles and their interactions with other particles using statistical methods, e.g., Monte-Carlo simulations (Grabowski et al., 2019). Numerical weather prediction and climate models need to apply the computational cheaper bulk schemes. Bulk schemes are computationally efficient because they only simulate microphysical process rates of a small number of particle distribution moments (typically one to three) for few hydrometeor categories (typically three to six). This bulk approach makes a number of simplifications about hydrometeor microphysical properties necessary.

Remote sensing observations of clouds, e.g., by radars, are vital to evaluate numerical models, along with laboratory studies and in situ observations. Laboratory studies have provided invaluable insights (e.g. Bailey and Hallett, 2004; Connolly et al., 2012) on specific processes at the single-particle level and are therefore indispensable for developing microphysics schemes (Morrison et al., 2020). In situ observations can provide detailed information about particle size distribution and particle properties (Locatelli and Hobbs, 1974; Mitchell et al., 1990a; Heymsfield, 2003; Heymsfield et al., 2015). However, both areas, laboratory experiments and in situ observations, have limitations. Laboratory experiments are limited to the investigation of single or few processes acting simultaneously and can not take the variety of processes and conditions present in natural clouds into account. In situ methods indeed observe natural clouds but still have a relatively low spatial and temporal coverage. Therefore, the large coverage of remote sensing observations is indispensable for studying microphysical processes and their interaction in complex systems that clouds represent. However, the information about hydrometeors and microphysical processes gained by remote sensing observation is indirect and has to be interpreted carefully. For example, radars do not observe quantities of the particle population directly modeled by microphysical schemes, such as number or mass concentration, but variables such as reflectivity that depend in a complex way on these bulk hydrometeor as well as scattering properties.

Radars provide increasingly detailed information about cloud and precipitation processes and are especially valuable for studying microphysical properties (Fabry and Zawadzki, 1995; Illingworth et al., 2007; Kollias et al., 2020). The most basic quantity derived from radars, the reflectivity was used to infer precipitation strength already since the 1950s. In the last decades, radars have also been deployed in space, enabling the derivation of climatologies of precipitation (Kummerow et al., 1998; Huffman et al., 2010) and even clouds (Stephens et al., 2008; Stubenrauch et al., 2013). Radars are especially suitable for studying clouds because of their ranging capabilities (unlike passive instruments, the signal received by radars can directly be assigned to the location of the hydrometeors) and the ability to penetrate even through optically thick clouds (in contrast to lidars). Since reflectivity provides only limited average information about the particle population more advanced techniques have been developed to infer different particle population characteristics, e.g., velocity, size and shape especially relevant to improve the understanding of ice microphysical processes. Doppler capabilities add information about the particles' velocity. Combining radars of different frequencies (Battaglia et al., 2020b) and exploiting radar polarimetry (Ryzhkov and Zrnic, 2019) allows to estimate characteristic particle sizes and shapes.

1.2 OBJECTIVES

This dissertation was carried out in the framework of the Emmy Noether project "Optimal combination of Polarimetric and Triple frequency radar techniques for Improving Microphysical process understanding of cold clouds" (EN OPTIMice) and therefore shares several objectives with this project. EN OPTIMice aims at exploiting synergistic remote sensing observations to improve model parameterization and understanding of ice and mixed-phase microphysical processes. Improving model parameterization and process understanding can best be done iteratively, as better models help to understand processes better, and better process knowledge facilitates model development. This dissertation draws extensively on earlier work from the EN OPTIMIce project, which provided observational datasets and forward modeling frameworks and thus paved the way to detailed model-observational comparisons.

In this dissertation, observations are used to improve the understanding of microphysical processes focusing on sedimentation, aggregation, and processes in the melting layer. Furthermore, this improved understanding is incorporated into various microphysical models The models used range from a 3D snowflake model that generates three-dimensional particle shapes (Leinonen and Szyrmer, 2015), to a Lagrangian particle model (Brdar and Seifert, 2018), a 1D idealized model applying the two-moment bulk microphysics scheme from Seifert and Beheng, 2006 (SB scheme), and 3D large-eddy simulations (Heinze et al., 2017) also using the SB scheme. Insights and parameterizations gained by the more detailed models are used consecutively in the less detailed models. Also the observations used span a wide range, from in situ single particle to remote sensing observations applying Doppler radars with multiple frequencies (Neto et al., 2019; Neto, 2021); thus, the different observations allow to exploit the respective advantages (e.g., explicitness, numerical efficiency) of the different models. With this approach, models and observations can be used synergistically to infer more about microphysical processes and improve microphysics schemes.

1.3 OVERVIEW OF THE STUDIES

Figure 1.1 illustrates how the various models and observations are combined in the studies comprising this dissertation (Study I-III) and in the publications closely related to this dissertation (Ori et al., 2020, 2021; Mróz et al., 2021). Study I and Ori et al., 2021 generate three-dimensional ice particle shapes using the 3D snowflake model from Leinonen and Szyrmer, 2015 to characterize particle and scattering properties. Study I provides detailed parameterizations of particle properties, such as velocity-size relationships, that are evaluated against in situ single particle observations. These parameterizations are used in the SB scheme and the Lagrangian particle model McSnow (Brdar and Seifert, 2018). The microphysical and scattering properties from Ori et al., 2021 are tailored and used for realistic forward simulations, such as in the model-observation applications of Ori et al., 2020 and Study II. Building on the evaluation of ice particle growth processes in Ori et al., 2020 that finds a large overestimation of particle size and velocity, Study II implements the particle properties derived in Study I alongside other modifications. In this way, an improved sedimentation and aggregation parameterization in the SB scheme could be achieved. Both studies use the multi-frequency Doppler radar observations of Neto et al., 2019. In an analysis additional to Study II (Section 4.1), the simulations of the size distribution of the SB scheme are evaluated against simulations of McSnow. Other applications of the multi-frequency Doppler radar observations are the melting layer studies of Mróz et al., 2021 and Study III. Mróz et al., 2021 retrieve the ice particle size distribution using assumptions about the processes in the melting layer and applying the microphysical and scattering properties of Ori et al., 2021 to a case study. Based on a multi-month dataset presented in Neto, 2021, Study III investigates the difference in microphysical processes within the melting layer between profiles in which unrimed and rimed particles are present above the melting

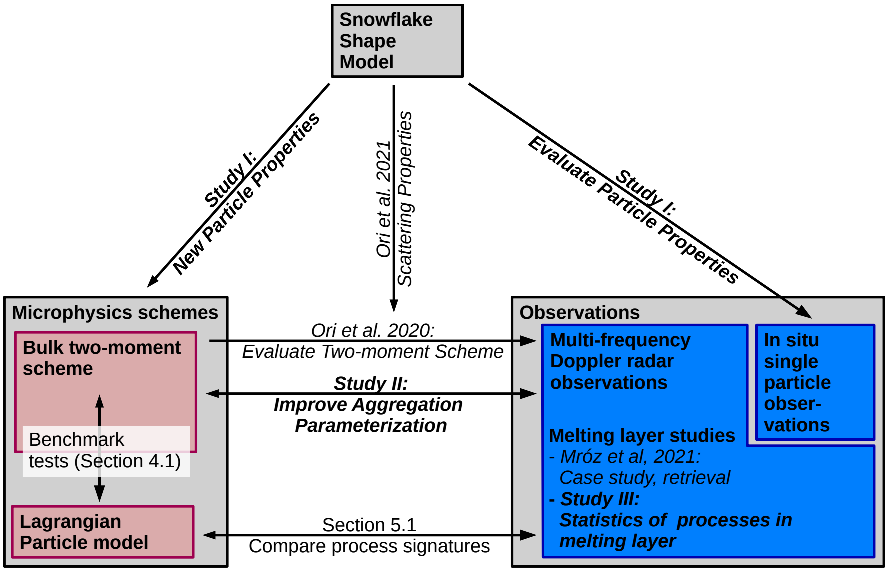

Figure 1.1: Overview of the models and observations, and their usage in the studies that comprise this dissertation or are strongly connected with this dissertation.

layer. Finally, in a supplementary study to Study III (Section 5.1), simulations of the melting layer performed with McSnow are compared with the observed melting layer statistics.

1.3.1 *Study I: Ice Particle Properties Inferred From Aggregation Modelling*

In Study I parameterizations of ice monomers' and aggregates' particle properties have been derived with the 3D snowflake model of Leinonen and Szyrmer, 2015. The use of a 3D snowflake model allows addressing research questions concerning particle properties that are difficult to answer with the commonly used approach: the in situ observation of ice particle properties. A shortcoming of in situ observations is that they can not observe the full range of sizes and level of detail relevant for microphysical modeling. Particle property parameterizations used in microphysics schemes have often been derived from manual observations, which collected and classified individual particles in effort-taking work (e.g., Locatelli and Hobbs, 1974) and thus could sample only some tenths of particles. In contrast, with snowflake models, a vast number of particles can be created conveniently, and the composition of the particles can be controlled in great detail. An aggregate database is generated containing about 105'000 individual aggregates with a huge range of monomer numbers (from one to 1000) and particle sizes (from a few 100 µm to about 5 cm). The properties of the generated snowflake shapes are evaluated against in situ observations. This database allows investigating how important the monomer number and type (e.g., plates, needles) information is for parameterizing aggregate properties. Combining the parameterization derived from the snowflake shapes with hydrodynamic theory allows assesing how well different functional relations can parameterize the particles' velocity.

Main outcomes: Particle properties change smoothly with increasing monomer number but differ substantially for different monomer types.

The Atlas-type velocity-size approximations work well when considered separately for monomers and aggregates.

The main results of Study I concern the dependency of aggregate properties on the monomer composition and the representation of terminal velocity in microphysics schemes. It is found that the particle properties (mass, area, and particle velocity) change smoothly with increasing monomer numbers for all monomer types. However, particle properties of aggregates composed of different monomer types differ substantially. Although the separation between monomers (cloud ice) and aggregates (snow), as implemented, e.g., in the SB scheme, can not represent the smooth transition of aggregate properties with increasing monomer number, this simplification does not considerably impact the simulation of aggregation (as shown with sensitivity studies performed by McSnow simulations). Concerning the terminal velocity, the effect of different approximations has been investigated. Most microphysics schemes approximate the velocity-size relationship by power-law relations. In contrast to the power-law relations, Atlas-type relations can account for the asymptotic approach of a limiting value at approximately 1 m/s. It is found that aggregation rates are overestimated when assuming power-law relations once centimeter-sized particles are present, but can be accurately simulated when assuming Atlas-type relations.

1.3.2 *Study II: Constrain Bulk Scheme Parameterizations*

The combination of a simple model setup and cloud radar observation can strongly constrain ice microphysical parameters.

Study II presents a novel approach to improve our general understanding of microphysical processes using aggregation as an example, by linking aggregation theory applied in model parameterizations of a two-moment scheme with radar statistics. First, the study explores how sensitive the simulated multi-frequency Doppler observations are to various parameters relevant to the simulation of aggregation. To this end, the particle properties of Study II are used in the microphysics scheme. To enable the use of these particle properties, new formulations for the bulk aggregation rates had to be derived as new functional relationships (e.g., the Atlas-type velocity-size relations) are applied. Second, comparing the idealized single-column simulation with multi-month statistics of observations could constrain several aggregation parameters by minimizing the difference between simulated and observed profiles. Since major simplifications are necessary in the idealized single-column simulations, the scheme's performance is also tested in more realistic 3D large-eddy simulations.

Aggregation is most sensitive to particle properties and aggregation kernel formulation.

Study II shows, that the simulated mean mass increase due to aggregation is susceptible to the selection of the particle properties and the aggregation kernel formulation. In contrast, the simulated mean mass is weakly sensitive to the size distribution width. This low sensitivity could indicate that the simulation of the size distribution shape is of secondary importance. However, an additional analysis (Section 4.1) showed that aggregation rates might be slightly lower when the size distribution is calculated explicitly with a Lagrangian particle model. Unlike the simulated mean mass, the simulated dual-wavelength ratios (which are indicators of the particle sizes derived from the multi-frequency observations) are sensitive to the size distribution width because the dual-wavelength ratios are disproportionately sensitive to large particles, which are more frequent in broad distributions. Thus, the size distribution width appears as a critical component in linking modeled mean mass to indicators related to mean mass from multi-frequency observations. Interestingly, the additional analysis in Section 4.1 also suggests that the number concentrations of large particles are well simulated by the new version of the SB scheme. Thus, the good agreement between simulated mean size and the dual-wavelength ratio when using the improved microphysical parameters would probably also hold if the size distribution would be considered more explicitly in the SB scheme.

The size distribution width is a crucial parameter for linking the model to multi-frequency observations.

Overall, the simulation of sedimentation and aggregation by the two-moment scheme could be improved. The bias of too fast and too large particles observed by Ori et al., 2020 could be strongly reduced, as shown by a statistical comparison of multi-month observations and 3D large-eddy simulations with the old and improved scheme setup. The velocity-size relations derived in Study I contribute largely to the reduction of these biases. These relations affect the particle velocity directly and the particle size indirectly through its influence on the aggregation rates. This reduction of the biases also improved the prediction of surface precipitation in a case study where a strong sublimation layer was present.

Biases in particle velocity and size of two-moment scheme could be reduced.

1.3.3 *Study III: Melting Layer Processes*

Study III revisits the approach of Drummond et al., 1996, which compares the reflectivity flux at the melting layer top and bottom (reflectivity flux ratio approach). This comparison can be used to estimate how the microphysical processes occurring within the melting layer change the mean mass of the particle population. An increase of the reflectivity flux stronger/weaker than expected by the change in scattering properties is attributed to an increase/decrease in mean mass. However, this connection between the reflectivity flux ratio and the change in mean mass is only valid if certain assumptions are met. The study evaluates some of the assumptions, such as neglecting the influence of vertical wind. To this end, characteristics of the Doppler spectra (e.g., the velocity of particles with negligible terminal velocity) are exploited. The multi-frequency Doppler radar observations are also used to separate profiles by their predominant particle type. Thereby it can be investigated which processes in the melting layer might be more and which might be less important for profiles with predominantly unrimed or rimed particles at the top of the melting layer.

Mean mass increase slightly and decreases substantially for unrimed and rimed profiles within the melting layer.

Study III elaborates on the statistics of the reflectivity flux ratio for different particle classes and reports indications for the reasons for the differences. Profiles of radar observables within the melting layer and model simulations are analyzed to learn which processes might cause the differences between the particle classes. The mean mass of the profiles with unrimed particles at the melting layer top (unrimed profiles) increases slightly when viewed over the entire melting layer. In contrast, the mean mass of the rimed profiles decreases substantially. Since other shrinking processes could be excluded, it is concluded that the decrease of the mean mass for rimed profiles is most likely caused by collisional breakup of melting particles. This breakup process might also occur for unrimed profiles, even at a similar rate, but could be compensated by higher aggregation rates for these profiles. An additional analysis in Section 5.1 shows that the breakup mechanisms currently implemented in McSnow (shedding, hydrodynamic and collisional breakup of liquid droplets), which explicitly predicts particle evolution of melting particles, can not explain the observed reflectivity flux ratio for rimed profiles. This finding supports the hypothesis of Karrer et al., 2021b that collisional breakup of melting particles might be necessary to consider. Implementing this process in models is possible only after further investigations, including quantification of process rates in laboratory studies.

The consideration of collisional breakup of melting particles might be necessary to explain the observations in the melting layer.

2 THEORY

This chapter provides an overview of cloud ice microphysical processes (Section 2.1) and techniques to simulate and observe these processes utilizing microphysical models (Section 2.2) and radar remote sensing techniques (Section 2.3). Emphasis is placed on the ice microphysical processes most relevant to this dissertation and the modeling and observational techniques employed, which are valuable for inferring these processes.

2.1 ICE MICROPHYSICAL PROCESSES

Ice microphysical processes determine the properties of many different cloud types that contain ice-phased particles. Each of these cloud types is affecting society: Non-precipitating clouds (e.g. cirrus clouds) have significant radiative effects; precipitating clouds produce a large amount of precipitation over a short (e.g., deep convective clouds) or longer time period (e.g., nimbostratus clouds). However, investigations of growth processes with multi-frequency Doppler radars are most insightful when observing stratiform clouds with a large vertical extent. In these clouds, many different processes take place, and characterization of these processes is more feasible compared to the highly variable convective clouds. Therefore, the overview of microphysical processes is shown exemplarily for these clouds in Figure 2.1 and discussed in the following.

Cloud ice particles originate from heterogeneous or homogeneous nucleation. The particles first increase in size by depositional growth from the vapor (Section 2.1.1), gaining enough velocity to both sediment towards the ground (Section 2.1.2) and collide with other ice particles, possibly forming aggregates (Section 2.1.3). In the presence of cloud droplets, the particles also grow by riming, which is a particularly efficient process in converting condensed water mass from the supercooled liquid state to the precipitating ice phase (Section 2.1.4). If the particles reach wetbulb temperatures above 0°C they inevitably start to melt (Section 2.1.5). Once below the melting layer and thus completely melted, the particles undergo pure liquid microphysics processes like diffusional growth, evaporation, collision-coalescence, or liquid breakup (Lohmann et al., 2016, Chapter 7).

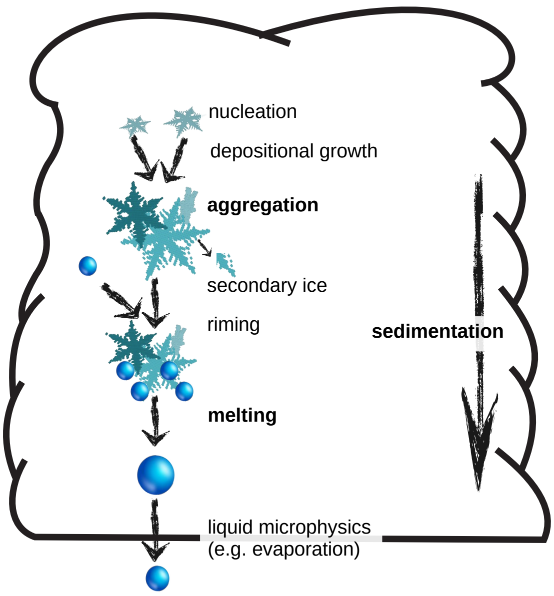

Figure 2.1: Overview of microphysical processes in stratiform clouds with the focus on ice growth processes (modified version of Figure 12.3 in Lohmann et al., 2016).

2.1.1 *Depositional Growth*

Ice particles gain mass by depositional growth in supersaturated conditions (relative humidity with respect to ice RH_i >100%). As a result, the particles get a considerable terminal velocity v (Section 2.1.2) to sediment to lower parts of the cloud and grow there through other microphysical processes. Therefore, depositional growth can also be seen as a starting mechanism for precipitation formation. In contrast, at subsaturated conditions (RH_i <100%), the particles lose mass due to sublimation, which occurs mainly below the cloud base. The resulting phase transition from vapor to ice releases latent heat. As a result, the diffusional flux and the heat transfer between particle and ambient air must be considered (Lamb and Verlinde, 2011, Section 8.3) to derive the rate by which the mass m of an individual ice particle changes:

$$\frac{dm}{dt} = 4\pi C(D_{max})\rho_i G_i f_v \left(RH_i/100\% - 1\right) \tag{2.1}$$

C is the particles capacitance (which depends on the particles' size D_{max} and shape), ρ_i the bulk ice particle density, f_v the ventilation coefficient, and G_i is a factor depending on atmospheric state variables (Equation 8.41 in Lamb and Verlinde, 2011). Depositional growth increases the mass concentration and mean mass of particle populations, while it does not affect the number concentration.

Ice crystals can grow by depositional growth into various shapes depending on the temperature and humidity (Bailey and Hallett, 2004; Bailey and Hallett, 2009) (Figure 2.2). The common feature between all the shapes is the underlying hexagonal structure created by the ice Ih lattice structure, which is dominant at the typical atmospheric conditions (Lohmann et al., 2016, Section 8.3). Based on this hexagonal structure, the particle shapes can be broadly classified as planar and columnar prisms (inset box in Figure 2.2) depending on the temperature and humidity. The shapes of particles growing in highly supersaturated air deviates from solid hexagonal prims because in these conditions the growth does not occur in thermodynamic equilibrium (Lohmann et al., 2016, Section 8.2), but is kinetically limited. Other complex particle shapes such as polycrystals also occur, especially at lower temperatures, and non-symmetrical particles are generally the rule rather than the exception (Bailey and Hallett, 2009).

A model of the ice crystal growth that can fully explain the different growth mechanisms leading to the various habits does not exist yet, but several mechanisms are described or postulated (Libbrecht, 2017). Whether the growth happens preferentially at the basal or prism faces resulting in columnar or planar particles (inset box in Figure 2.2) can be explained, at least partially, by the different attachment coefficients. These coefficients can be interpreted as the probability that a water vapor molecule is incorporated into the ice crystal lattice after contact with the ice surface (Libbrecht, 2019, Section 3.1). In highly supersaturated air, growth is rapid, and diffusion can not supply vapor molecules fast enough to maintain a homogeneous field of water vapor concentration around the particle, resulting in shapes that can be very different from solid hexagonal prisms. For example, dendritic shapes form because the water vapor concentration has local maxima at the corners of the basal hexagonal faces, which leads to the branching events on each of the six corners of the hexagons (Libbrecht, 2019, Chapter 4). As a result of this first branching event, the water vapor concentration field shows further local minima, leading to new branching events and finally to the complex fractal shape of dendrites.

In mixed-phase clouds, depositional growth occurs at or near the water saturation due to the presence of liquid droplets. At water saturation, the depositional growth is the strongest at about -15°C because at this temperature, the absolute supersaturation over ice is the largest. If the humidity is lower than the water saturation but higher than the ice saturation, the Wegener-Bergeron-Findeisen process leads to an efficient ice particle growth at the expense of the liquid particles (Korolev, 2007).

2.1.2 *Sedimentation*

Clouds can stay at about the same height over many hours only because small particles sediment very slowly, and even small upwinds keep the particles in levitation. Larger particles, however, have con-

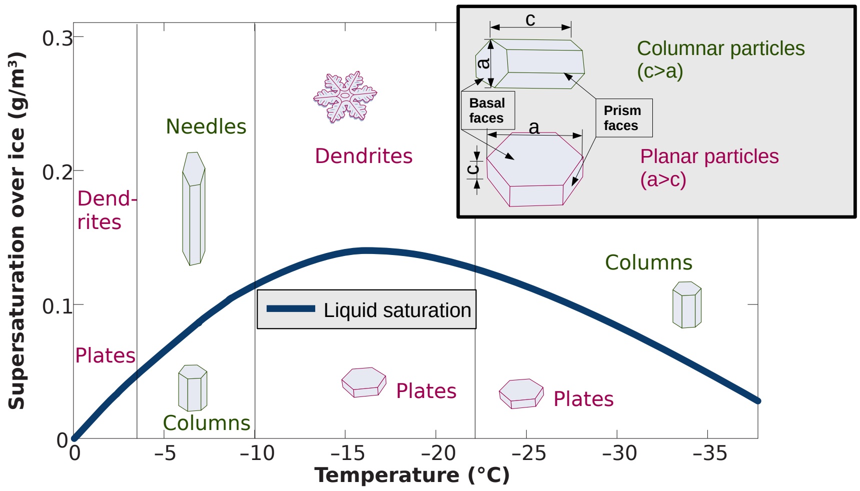

Figure 2.2: Habit diagram depicting ice particle shapes at typical for a given temperature and humidity range. The blue line depicts the ice supersaturation at liquid saturation. The inset plot shows the terminology of the geometry of columnar and planar particles (modified from Libbrecht, 2017, Figure 1)

siderable velocity and can therefore sediment beneath the cloud and occasionally precipitate to the ground.

In general, hydrometeors fall at speed close to their terminal velocity v because the particle growth or shrinking is continuous, and thus equilibrium of the acting forces is almost always given. Exceptions are particle breakup and turbulent flows, where the particles' inertia should be considered (Khain and Pinsky, 2018, Section 5.5).

Forces acting on the particles with mass m are the gravitational force:

$$F_{grav} = m \cdot g, \tag{2.2}$$

with the gravitational acceleration g, and the drag force F_{drag}

$$F_{drag} = \frac{1}{2} \cdot \rho_{air} \cdot A \cdot v^2 \cdot C_D, \tag{2.3}$$

which is a product of the air density ρ_{air}, the area projected to the horizontal A, v, and the drag coefficient C_D.

Hydrodynamic models calculate v based on this equilibrium consideration by introducing a Best number, which depends only on particle and air properties (Abraham, 1970; Bohm, 1989; Pruppacher and Klett, 2010; Khvorostyanov and Curry, 2002, 2005; Heymsfield and Westbrook, 2010). Together with theoretical and empirical relations between the Best and the Reynolds number Re, v can be derived from the definition of Re:

$$\mathrm{Re} = \frac{\rho v D}{\eta}, \tag{2.4}$$

where ρ is the air density, D the particle size and η the air viscosity. The formulations of v and its derivation are shown for different hydrodynamic models in Study I. Here, only the general characteristics of v are explained based on Equations 2.2 and 2.3.

Since ice particles have extremely diverse shapes, a single v size relation cannot approximate the v of all particles. However, one can intuitively analyze the evolution of v with size by looking at its asymptotic behavior for small and large sizes. At small sizes D, v is close to 0m/s and increases for all hydrometeors because F_{drag} increases weaker than F_{grav} due to a rapid decrease of C_D. For large snowflakes, v is about constant because C_D is constant and m and A scale both approximately with D^2. Similar accounts, by the way, for large raindrops.

The v predicted by hydrodynamic models fits well with empirical relationships and can complement them where measurements are difficult (Mitchell et al., 1990a). Empirical relations have been reported for many different ice particle shapes (ice habits, aggregates, rimed particles) (Langleben, 1954; Locatelli and Hobbs, 1974; Heymsfield and Kajikawa, 1987; Mitchell et al., 1990a; Barthazy and Schefold, 2006; Weitzel et al., 2020; Vázquez-Martín et al., 2021), but the sample numbers and observed size range remains limited.

2.1.3 *Aggregation*

Besides riming, aggregation is a collision process, which efficiently increases the ice particle sizes and therefore contributes to precipitation formation. Unlike deposition growth, aggregation does not directly change the mass concentration but increases the mean mass. This increase in mean mass results from the decrease in the number concentration. The aggregation process removes two smaller particles from the particle population and creates an aggregate with greater mass and size than the original aggregation partners (illustrated in Figure 2.3). First, the general problem of calculating the evolution of the size distribution due to collision processes is described. Then, the specifics of the aggregation processes are highlighted.

The effect of aggregation can be quantified by describing the change of the number concentration at a given size or mass (Figure 2.3). Since the mass of the aggregate is simply the sum of the masses of the aggregating particles, the formulation of the size distribution as a function of mass $f(m_i)$ has advantages over the formulation as a function of the maximum dimension $f(D_{max,i})$. The change of the

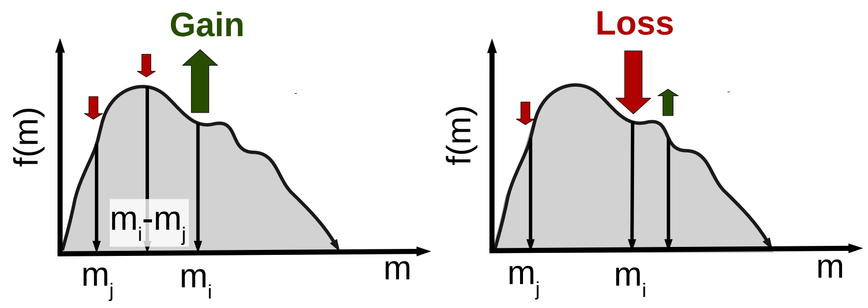

Figure 2.3: Illustration of the stochastic collection equation (SCE) (modified from Figure 1 of Karrer et al., 2021a). Left: A collision of particles with mass m_j and $m_i - m_j$ that increases the number concentration f at mass m_i. Right: A collision of particles with mass m_j and m_i that decreases f at m_i. Red (green) arrows indicate a decrease (increase) of the number concentration at the given mass due to the collision process.

concentration $f_m(m_i)$ at mass m_i is given by the stochastic collection equation (SCE) (Pruppacher et al., 1998; Khain et al., 2015):

$$\frac{\partial f(m_i)}{\partial t} = \int_0^{m_i/2} f(m_j) f(m_i - m_j) K(m_i - m_j, m_j) dm_j - \int_0^{\infty} f(m_i) f(m_j) K(m_i, m_j) dm_j, \quad (2.5)$$

where K is the, so called, aggregation kernel. The first term considers the gain of particles of mass m_i when particles with masses m_j and $m_i - m_j$ collide (left part of Figure 2.3). The second term incorporates the loss of particles of mass m_i by collisions with particles of mass m_j (right part of Figure 2.3).

Ice particles are usually large enough to allow neglecting turbulence effects for the calculation of collision rates (Jacobson, 2005, Section 15.6). Thus, the collision kernel K_{coll} can be formulated by considering the volume swept out by both colliding particles moving at relative velocity $|v_i(m_i) - v_j(m_j)|$ in a given time (illustrated by Figure 2.4):

$$K_{coll}(m_i, m_j) = A_{coll}(m_i, m_j) E_{coll}(m_i, m_j) |v_i(m_i) - v_j(m_j)| \quad (2.6)$$

More intuitively, this kernel can be viewed as the probability that two particles i and j collide within 1s (Gillespie, 1975). The collision cross-section A_{coll} is given by the sum of the circles circumscribing the horizontal projection of the two colliding particles in the simple case of spherical particles (or horizontally aligned oblate spheroid). For complex-shaped particles, considering the true projected areas (black circles in Figure 2.4), excluding voids in the circumscribing circles (gray circles in Figure 2.4) might be more accurate (Connolly et al., 2012; Kienast-Sjögren et al., 2013; Morrison and Milbrandt, 2015; Dunnavan, 2021). The aggregate at the bottom of Figure 2.4, resulting from the aggregation process shown, illustrates why considering the true projected areas instead of the circumscribing circle might be more precise. In this case, the connection point of the colliding particles (marked by a red circle) is not at the edge of the circumscribing circle of the smaller particle but inside of it.

The collision efficiency E_{coll} has to be introduced because A_{coll} overestimates the true collision cross-section even when the non-spherical shape is taken into account. Smaller particles tend to follow the streamlines, deflect along the larger particles' edges, and thus move around them without contact.

Furthermore, the velocity difference $|v_i(m_i) - v_j(m_j)|$ between the colliding particles influences the collision rates (arrows in Figure 2.4). The larger this velocity difference is, the less time the faster particle needs to catch up with the slower particle.

After a collision occurs, the particles might adhere to each other, rebound, or break into several particles (Pruppacher et al., 1998, Chapter 14).

In the case of aggregation, the sticking efficiency E_{stick} describes the likelihood that two particles stick after a collision, and K_{coll} has to be complemented by E_{stick} to calculate the aggregation kernel K_{agg}:

$$K_{agg} = K_{coll} E_{stick} \tag{2.7}$$

E_{stick} is usually parameterized as a function of temperature only (Mitchell, 1988; Connolly et al., 2012), but the influence of additional parameters like the collision kinetic energy has also been investigated (Phillips et al., 2015). In general, E_{stick} is increasing with increasing temperature due to the increasing thickness of the quasi-liquid layer at the surface of the particles (Slater and Michaelides, 2019). However, the general increase of

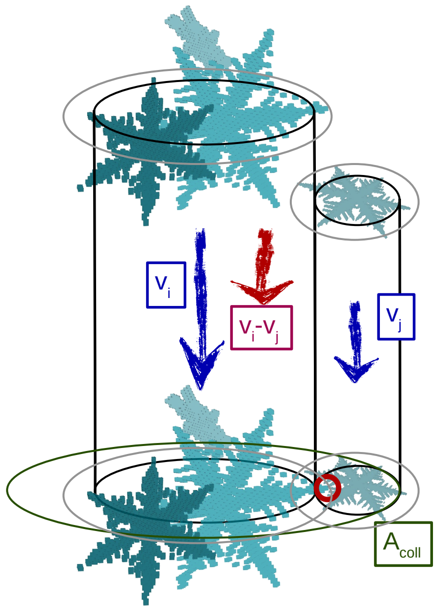

Figure 2.4: Illustration of the collision cross-section and differential sedimentation. Black circles illustrate the true projected areas. Gray (green) circles illustrate the circumscribing circles of the horizontal projection of the two colliding particles (the resulting aggregate). Arrows indicate the absolute and relative v of the particles. The red circle highlights the point of contact.

stickiness of the ice surface is superimposed by the interlocking mechanism. At temperatures of about -15°C the particles are likely to exhibit a dendritic shape (Section 2.1.1) which augments the chances of ice crystals to interlock with each other mechanically, and thus form a stable connection. Also electrical charge of particles has been reported to enhance E_{stick}, especially at low temperatures (Stith et al., 2002, 2004; Connolly et al., 2005; Gallagher et al., 2012).

The combination of the sintering and interlocking mechanisms causes E_{stick} to have pronounced peaks around -15 and 0°C. This temperature dependency of E_{stick} has been suggested to be responsible for the occurrence of large aggregates at these temperatures (Hobbs et al., 1974; Lamb and Verlinde, 2011). This conjecture is supported by the frequent observation of dendrite and needle monomers within large aggregates (Lawson et al., 1998), which are preferentially formed at these temperatures.

2.1.4 *Riming*

The collection of a supercooled liquid droplet by an ice-phased particle is called riming. Being a collision process, riming can also be described by the SCE (Equation 2.5) and the collision kernel (Equation 2.6) in the same way as aggregation. Still, characteristic differences arise from the typical size of the liquid droplets and the thermodynamic phase.

In contrast to aggregation, one collision partner, the cloud droplet, typically has a substantially lower v and m, and thus E_{coll} can be small. In the case of tiny droplets (smaller than about 10μm), the inertia of the droplets is so small that E_{coll} approaches zero, and riming can not take place (Böhm, 1992, e.g.,). Another difference between riming and aggregation is that the liquid droplets always adhere to the ice particle, as they freeze immediately after contact (Lamb and Verlinde, 2011, Section 9.4). Thus E_{stick} can be assumed to be one.

Riming increases v because it increases the particles' mass considerably, while the area changes little (Lamb and Verlinde, 2011, Section 9.2). This increase in v allows distinguishing rimed particles from unrimed particles, e.g., by Doppler radars (Section 2.3.3). Multi-frequency observations provide additional indications of the riming degree (Kneifel et al., 2015; Mason et al., 2018; Li et al., 2020) (Section 2.3.2). In stratiform clouds, riming generates graupel particles, which fall with v up to 3 m/s (Locatelli and Hobbs, 1974; Mitchell et al., 1990a). In convective clouds, the high vertical wind speed produces high liquid water concentration in which large hailstones can form with v exceeding 10m/s (Lamb and Verlinde, 2011, Section 9.2). Due to these large v, rimed particles can remain frozen over a large distance at temperatures above 0°C before melting (Section 2.1.5), and hailstones can reach the ground even in summer convective storms.

Since riming requires the presence of liquid droplets and their amount increases with temperature (Korolev et al., 2003; Pinsky et al., 2015), the frequency of riming increases strongly with temperature and is very infrequent at temperatures below -10°C in stratiform clouds (Kneifel and Moisseev, 2020).

2.1.5 *Melting*

Melting of ice-phased particles occurs if the particle temperature exceeds 0°C. At which ambient air temperature the melting starts and how fast it proceeds is a complex thermodynamic problem because all three phases of water play a role (Pruppacher et al., 1998, Section 16.3). At water saturation and for particles with low v, melting starts at 0°C, and requires only a few hundred meters. However, subsaturated conditions and large v can lead to delayed (Heymsfield et al., 2015, 2021) and prolonged melting (Lamb and Verlinde, 2011, Section 12.4), respectively.

The time required to melt and the evolution of the ice particle properties have been studied in the laboratory (Knight, 1979; Rasmussen and Heymsfield, 1987; Oraltay and Hallett, 1989; Mitra et al., 1990; Oraltay and Hallett, 2005). According to these studies, melting starts at the edges of the particles. Then, the meltwater flows towards the center because of aerodynamic forces and capillary action. Finally, the occasionally complex structure of the ice particles collapses into a spherical or oblate droplet. During this process, the particles v increases due to the increasing compactness.

Laboratory studies also observed shedding of liquid droplets for graupel and hail larger than 9 mm (Rasmussen and Heymsfield, 1987; Pruppacher et al., 1998) and breakup of ice fragments in subsaturated conditions (Knight, 1979; Oraltay and Hallett, 1989; Mitra et al., 1990; Oraltay and Hallett, 2005). These processes are illustrated in Figure 2.5.

Melting is vital to consider, both from an observational and modeling viewpoint. The melting layer is a prominent feature detectable by remote sensing observations (Fabry and Zawadzki, 1995, Section 4.4) but also challenges the retrieval of precipitation rates (Smyth and Illingworth, 1998; Battaglia et al., 2003; Mason et al., 2017). Szyrmer and Zawadzki, 1999 described how the latent heat released by melting induces convective cells in their dynamic, thermodynamic, and microphysics coupled simulations. Furthermore, the changes in the thermodynamic phase (melting and refreezing) at or near the surface are essential for modeling hazardous situations, e.g., affecting road traffic (Stewart et al., 2015).

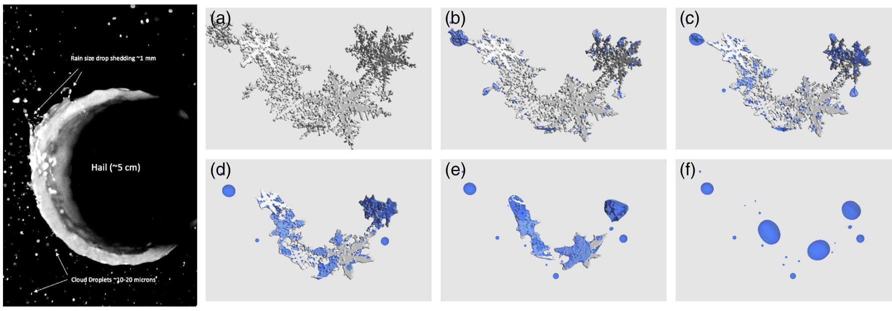

Figure 2.5: Image and visualization of the shedding (left) and melting fragmentation (right) process. Left: Image of a wet hailstone which sheds liquid drops (taken from Sills and Joe, 2019) ©2019 Taylor & Francis Group. Used with permission. Right: Six melting stages of a slightly rimed aggregate which melts into several fragments (taken from Leinonen and Lerber, 2018). ©2018 American Geophysical Union. Used with permission.

2.1.6 *Other Ice Microphysical Processes*

Ice formation can occur via freezing of pure water droplets below about -38°C (homogeneous nucleation) or with the aid of aerosols already at higher temperatures (heterogeneous nucleation) (Lohmann et al., 2016). Possible heterogeneous nucleation mechanisms, the conditions (temperature, humidity) under which different aerosol types can initiate nucleation, and typical concentrations of ice nucleating particles are summarized, e.g., by Hoose and Möhler, 2012 and Kanji et al., 2017.

In principle, the number of ice nuclei should be similar to the number of ice particles if homogeneous nucleation (nucleation of pure liquid droplets) is not excessive. However, the number concentration of ice particles sometimes exceeds the number concentration of ice nuclei by one order of magnitude, and only the presence of secondary ice formation can explain this difference (Lohmann et al., 2016, Section 8.1). Several secondary ice formation processes have been summarized by Korolev and Leisner, 2020.

2.2 MICROPHYSICAL MODELS

Microphysical models simulate the shape of individual particles, the change in particle properties (e.g., mass, monomer number) of individual particles, and the evolution of the entire size distribution (Figure 2.6). Suitable for different applications, these models represent the particles either very explicitly or use simpler assumptions that make the model more computationally efficient. 3D snowflake models provide the most explicit representation of particle properties (Figure 2.6a)). These models simulate the three-dimensional shape of the particles and their changes with different microphysical processes (e.g., aggregation, riming). In less detailed models (microphysics schemes), particle properties or even size distributions follow predefined relationships.

Due to their computational efficiency, microphysics schemes can be applied within complex numerical models (global circulation models (GCM), numerical weather prediction (NWP) models, large-eddy models (LES)) that simulate the interaction of many atmospheric processes like dynamics, radiation, etc., on a huge range of scales (Morrison et al., 2020). The most detailed application of microphysics schemes within complex model employs Lagrangian particle models (LPM) (Section 2.2.2) in direct numerical simulations, which explicitly resolve dynamics, including turbulence at the mm scale. LPMs predict the motion and evolution of individual particles (Figure 2.6b)). For applications that require a more computational efficient process description (e.g., NWP), bulk schemes (Section 2.2.4) are used in simulations with coarse grid resolutions, in which also the dynamics have to be parameterized to some degree. Bulk schemes assume the hydrometeors to be distributed according to a predefined functional form and predict the evolution of one or several moments of this distribution (Figure 2.6d). Hydrometeors can be categorized into one or several classes and evolve in an Eulerian coordinate system. Another Eulerian approach is the bin scheme approach, which also has been applied in complex numerical models (Figure 2.6c)(Section 2.2.3).

This dissertation makes use of a 3D particle model (aggregation model, Leinonen, 2013), a LPM (McSnow, Brdar and Seifert, 2018), and a bulk scheme (Seifert-Beheng two-moment scheme (SB scheme), Seifert and Beheng, 2006) (Figure 2.6a)). Although 3D particle models (Section 2.2.1) are not considered a classical element of microphysical models and are not applied in complex numerical models (e.g, LES), using such a model to support the microphysics schemes fits perfectly with the objectives of this dissertation (Section 1.2).

2.2.1 *3D Snowflake Models*

Snowflake models generate shapes of snowflakes by simulating the evolution of ice particle shapes due to various ice processes (e.g., aggregation, riming and melting). Snowflake models can be separated into empirical and physical approaches (Tyynelä and Lerber, 2019; Kneifel et al., 2020). Empirical models generate aggregates that follow an a priori defined fractal dimension or mass-diameter relationship. These models are particularly useful when one wants to match desired particle properties, e.g., those used by a microphysics scheme, and needs to find consistent scattering properties.

Physical aggregation models mimic the aggregation process by simulating its physical mechanisms with stochastic algorithms (Westbrook, 2004; Maruyama and Fujiyoshi, 2005). More specifically, these models

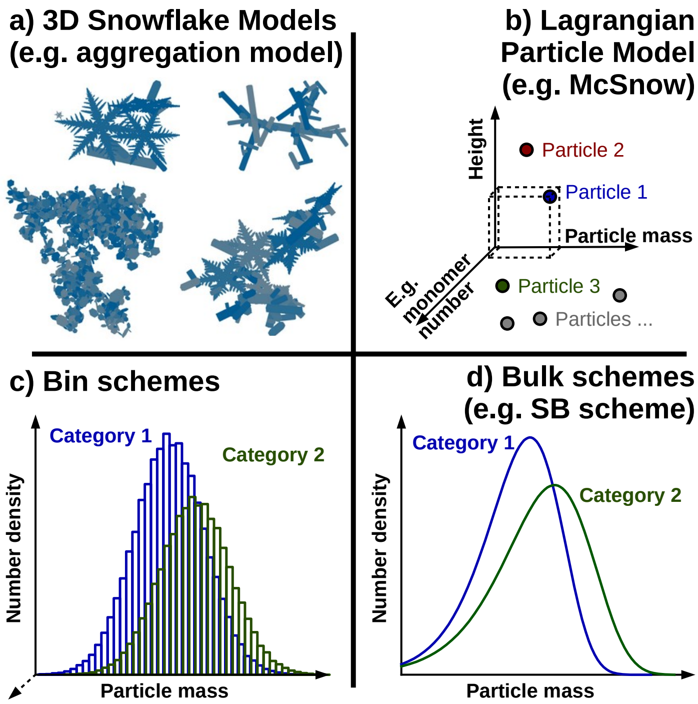

Figure 2.6: Schematic of microphysics models and their representation of particle properties and size distributions. a) 3D Snowflake models simulate shapes of aggregates with realistic monomer shapes explicitly. b) Lagrangian particle models (LPM) simulate the evolution of particle population by simulating several attributes (e.g., monomer number) of individual particles. c) Bin schemes simulate the size distribution of one or more categories. The dashed arrow in c) indicates that either single- or multidimensional distributions can be predicted. d) Bulk schemes predict one or more moments of the size distribution using several categories with fixed particle properties.

attach 3D ice crystal shapes and select collision pairs from a particle ensemble considering an aggregation kernel (Section 2.1.3). In addition to deriving the scattering properties of realistically shaped snowflakes, this approach allows inferring microphysical characteristics of the particles. For example, Westbrook et al., 2004a explained the observed scaling relation of aggregates - mass scales with size to the power of two - using a physical aggregation model. The aggregation model used in this dissertation (Leinonen, 2013) is based on the concept of Westbrook, 2004 and has been extended to, additionally, mimic the riming (Leinonen and Szyrmer, 2015) and melting (Leinonen and Lerber, 2018) process and consider various realistic monomer shapes.

2.2.2 *Lagrangian Particle Model*

Lagrangian particle models (LPMs) predict the motion and evolution of the mass and other attributes of individual particles, and therefore have several advantages over Eulerian models. For example, processes rates can be calculated by simply applying an ordinary differential equation, e.g., Equation 2.1 for depositional growth. Furthermore, in contrast to Eulerian schemes, LPMs can represent collision processes, e.g., aggregation, in their true statistic nature (Grabowski et al., 2019). The Lagrangian framework allows considering the probability of collision between individual particles using, e.g., Monte Carlo algorithms (Shima et al., 2009; Brdar and Seifert, 2018).

The biggest challenge in applying Lagrangian particle models is the computational cost. Morrison et al., 2020 estimated that simulating each particle individually in a direct numerical simulation allows simulating only 1 m^3 of a particle population with a number concentration of $10^8 m^{-3}$ with current computers. In superparticle models, such as McSnow, computational costs are reduced by simulating only a subset of particles representing the entire particle population (Shima et al., 2009). The multiplicity of a superparticle determines how many real particles it represents. Since the superparticles can only account for average properties of all particles, a probability density function must be assumed to consider the variability within all real particles represented by a superparticle (Shima et al., 2009). The width of this probability density function depends on the multiplicity. This variable width allows the model to converge to a multiplicity of one against the simulation of all real particles. In contrast, a high multiplicity leads to a smooth representation of the particle population, which cannot represent its details.

The superparticle method remains computationally cheaper than bin schemes when the number of predicted dimensions increases. This computational efficiency allows using LPMs in LES even when considering multidimensional microphysical problems as cloud droplet activation (Hoffmann, 2017) and mixed-phase microphysics (Brdar and Seifert, 2018; Shima et al., 2020). Simulating mixed-phase clouds with multidimensional LPMs allows prescribing particle properties with a great degree of detail and consider, e.g., the dependency of particle geometry on the degree of riming and rime density (Seifert et al., 2019).

2.2.3 *Bin Schemes*

Bin schemes represent the size distribution explicitly using typically several tens of size bins (Figure 2.6c)). Therefore, they can predict the complex evolution of the size distribution, e.g., under the influence of aggregation. Bin schemes with multidimensional distributions or several categories can consider the variance in particle properties (Khain et al., 2015) but quickly become numerically infeasible with an increasing number of dimensions (Grabowski et al., 2019). Besides numerical diffusion and difficulties in simulating the stochastic nature of collision processes, the high numerical costs for multidimensional applications such as ice microphysics are the main disadvantages of bin schemes (Grabowski et al., 2019; Morrison et al., 2020).

2.2.4 *Bulk Schemes*

Bulk schemes predict one or more moments M:

$$M(k) = \int_0^\infty x^k \, f(x) \, dx \tag{2.8}$$

of the particle distribution $f(x)$ for several particle categories. x can be either the particle mass or size. All bulk schemes predict the mass concentration ($M(1)$ if x is the particle mass) because mass continuity is crucial for any model (Cotton et al., 2011, Section 2.4). Two-moment schemes additionally predict the number concentration ($M(0)$) (Ziegler, 1985; Meyers et al., 1997; Morrison et al., 2005; Seifert and Beheng, 2006; Thompson et al., 2008, e.g.,). The number concentration prediction is beneficial since microphysical processes like nucleation or breakup affect this quantity directly, and the mean mass (mass divided by number concentration) is important to consider in the process rates. Three-moment schemes predict a third moment, in addition to mass and number concentration, mostly $M(2)$ (if x is the particle mass) which is assumed to be proportional to the reflectivity factor (Milbrandt and Yau, 2005; Szyrmer et al., 2005; Naumann and Seifert, 2016; Milbrandt et al., 2021). Considering this third moment allows to simulate the width of the distribution explicitly, is useful when comparing with radar observations, and controls excessive size sorting, which is an artifact present in two-moment schemes (Wacker and Seifert, 2000; Milbrandt and Yau, 2005).

In contrast to LPMs and bin schemes, bulk schemes need to assume a functional relationship of the particle size distribution. Mostly the modified gamma distribution

$$N(x) = N_0 x^{\mu} \exp\left(-\lambda x^{\gamma}\right), \tag{2.9}$$

or simplifications of this equation (setting γ=1 or even μ=0) are chosen. $N(x)$ is the normalized number concentration at the size x and N_0, μ, λ and γ are parameters of the distribution. The more moments predicted, the more parameters in Equation 2.9 can be modeled. Additional parameters must be set to a fixed value or assumed to follow a predefined relation to other prognostic quantities.

Bulk schemes require the formulation of microphysical process rates for only a few moments of the size distribution and a few hydrometeor categories. This requirement poses a challenge for the accurate simulation of the processes. For example, the evolution of a particle population under the action of collision is a stochastic process, which allows the occasion of the rapid growth of individual particles through collision-coalescence or aggregation. A particle can grow faster than the average because it initially experiences first collisions with a low probability. Then it continues to grow preferentially due to its larger size and substantially enhances the growth of the total particle population (Grabowski et al., 2019). While this phenomenon can be simulated by LPMs, where it can manifest itself, e.g., in a peak in the size distribution, the smooth size distribution assumed by the bulk scheme is unable to capture the phenomenon.

The formulation of bulk process rates, e.g., collision rates, is also mathematically rather complex. Integration over the entire distribution often does not provide an analytical solution without major simplifications (Khain et al., 2015). Any change in particle parametrizations, such as v, requires a lengthy revision of process rates which might also increase the computational cost of the microphysical scheme. In contrast, LPMs do not require an analytical solution for bulk process rates because they solve for the evolution of individual particles and particle interaction directly at the particle level. For example, Seifert et al., 2014 thoroughly investigates the derivation of collision rates required to introduce non-spherical particle shapes. They found that modifying the functional form of the v-size relations can significantly improve the accuracy of the collision rates with only a slight increase in computational cost.

Despite the challenges regarding the representation of particle populations and processes in bulk schemes, particle properties are represented in these schemes in an increasingly sophisticated way. While early cloud schemes predicted only one moment for two categories (namely cloud droplets and rain) and no ice-phased categories (Kessler, 1969), the addition of several ice phase categories (e.g., cloud ice, snow, graupel, and hail) (Cotton et al., 1982; Lin et al., 1983) allowed considering the variety of ice particle properties partly. Introducing additional prognostic variables which are not moments of the size distribution allowed considering continuous changing particle properties due to riming (Morrison and Milbrandt, 2015), melting (Cholette et al., 2019), and habit evolution (Jensen et al., 2017; Tsai and Chen, 2020).

2.3 RADAR REMOTE SENSING

Besides in situ observations, remote sensing is the primary technique to observe clouds. Passive remote sensors detect the intensity of the radiation that is emitted from various sources and partially absorbed or scattered on its way to the sensor (Ulaby et al., 2014). Information about hydrometeors can be inferred from passive remote sensors either because the hydrometeors emit radiation themselves or interact with it. However, the signals detected by passive remote sensors can not be directly assigned to hydrometeors at a specific location. In contrast, active sensors, namely radars and lidars, emit radiation themselves and detect the intensity of backscattered radiation. The ability to emit radiation with a short pulse allows assigning the backscattering hydrometeors to a specific range of distance from the instrument (Parker, 2010, Section 18.5). Radars have been proven beneficial to observe precipitation and clouds since the 1950s (Fabry and Zawadzki, 1995) and continue to be a primary type of sensor employed at different platforms (Illingworth et al., 2007; Kollias et al., 2020; Battaglia et al., 2020a).

Reflectivity, the most basic quantity derived from radar observations, quantifies the backscattered power received by the radar, which depends on the observed hydrometeors, but also the radar design, e.g., operating wavelength (Fabry, 2015, Section 3.1). To compare observations from different radars, the equivalent radar reflectivity factor:

$$Z_e = \frac{\lambda^4 \eta}{|K_w|^2 \pi^5} \tag{2.10}$$

has been introduced. Here, λ is the radar wavelength, $|K_w|^2$ the dielectric factor of liquid water and η the volume-averaged backscattering cross-section (also called reflectivity):

$$\eta = \int_0^\infty N(D)\sigma_b(D)dD, \tag{2.11}$$

where σ_b is the single-particle backscattering cross-section and $N(D)$ is the size distribution. In the case of liquid spherical particles much smaller than λ, σ_b can be well approximated by the Rayleigh approximation:

$$\sigma_{b,\mathrm{droplet}} = \frac{\pi^5 |K_w|^2 D^6}{\lambda^4} \tag{2.12}$$

In this case, Z_e is proportional to the sixth moment of $N(D)$:

$$Z_{e,\mathrm{droplets}} = \int_0^\infty N(D) D^6 dD, \tag{2.13}$$

which motivated the definition of Z_e in the first place. For particles with sizes near or larger than λ and particles containing ice in general, σ_b differs from Equation 2.12 (Section 2.3.1). The different dependency of σ_b on the particle size and shape for different wavelengths is used by the multi-frequency approach (Section 2.3.2).

Besides Z_e, the Doppler velocity (Section 2.3.3) and polarimetric signature (Section 2.3.4) of the backscattered signal provide details of the hydrometeor properties, such as fall velocity and particle shape.

2.3.1 *Backscattering of Ice and Snow Particles*

Hydrometeors scatter the radiation emitted by the radar (Liou, 2002, Section 1.1), which determines Z_e received by the radar. Scattering occurs basically in all directions, but since radars detect only the backscattered energy and multiple scattering is negligible for the commonly used frequencies (Battaglia et al., 2020a), only backscattering is considered here.

For ice-phased particles much smaller than λ, the Rayleigh approximation is valid, and $\sigma_b \lambda^4/|K|$ is independent of λ (Figure 2.7). In this case, Equation 2.12 can also be used for snow if $|K_w|^2$ is replaced by the dielectric factor of the air-ice mixture (Bohren and Battan, 1980). For larger sizes, where the maximum dimension D_{max} is in the order of or larger than λ, radiation scattered at different parts of the particles interfers destructively and leads to σ_b smaller than predicted by the Rayleigh approximation (differential scattering). With increasing D_{max}, this reduction appears first for the shortest wavelength (W-Band, $\lambda{\approx}3.2$ mm), then for Ka-Band ($\lambda{\approx}8.6$ mm), and finally for the X-Band ($\lambda{\approx}31.9$ mm). How strong the deviations from the Rayleigh approximation are, depends on the particle shape and wavelength (compare σ_b of unrimed and rimed aggregates in Figure 2.7a) and b)).

Owing to the complexity of ice-shaped particles, the calculation of their scattering properties is complicated, and many approaches applying different assumptions have been proposed (Kneifel et al., 2018, 2020). One such approach is the self-similar Rayleigh-Gans approximation (Hogan and Westbrook, 2014), which takes advantage of the self-similar structures of aggregates (Westbrook, 2004) and is used to compute σ_b from 3D snowflake models in Figure 2.7. Such scattering calculations are at the heart of forward operators like the Passive and Active Microwave TRAnsfer model (Mech et al., 2020), e.g., used in Study II.

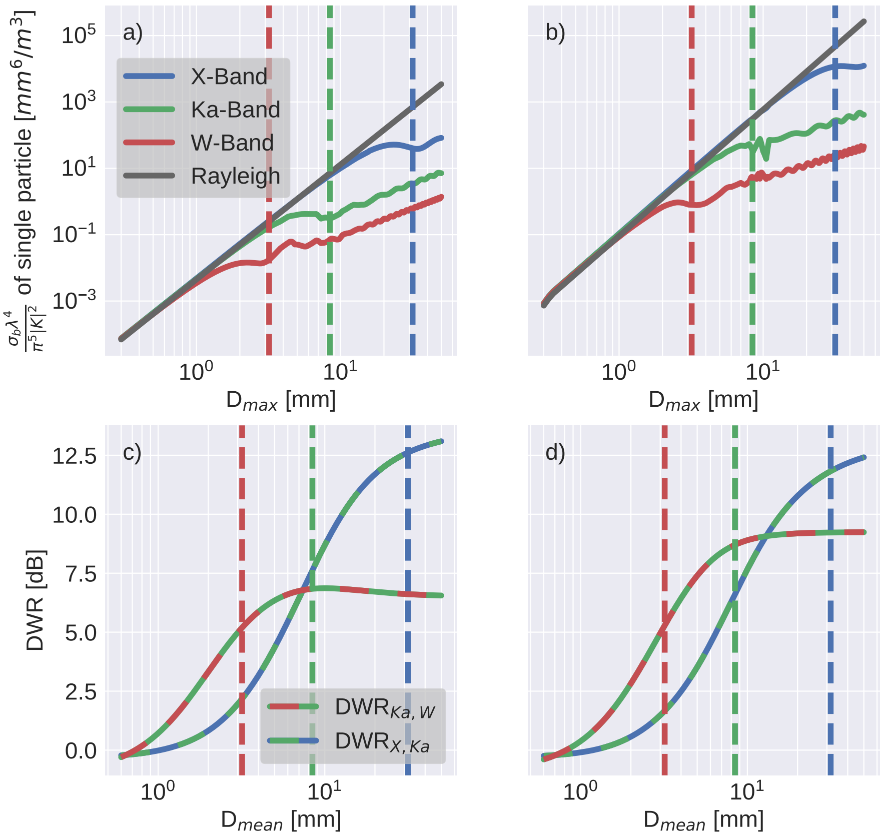

Figure 2.7: Scattering properties at different wavelengths and for different particle types. Normalized single-particle backscattering cross-section σ_b (a) and b)) and dual-wavelength ratios (DWR) (c) and d)) for unrimed particles (left; a) and c)) and rimed particles with equivalent liquid water path of 0.5 kg/m^2 (right; b) and d)). a) and b) uses the maximum dimension, c) and d) the mean mass diameter as a size indicator. Both unrimed and rimed particles are the "CaE mix" aggregates presented by Ori et al., 2021. The "CaE mix" aggregates are a computer-generated model of mixed aggregates composed of column and dendrite monomers created with the aggregation model from Leinonen and Moisseev, 2015. Radar wavelengths are indicated with vertical dashed lines: W-Band: $\lambda \approx 3.2$ mm; Ka-Band: $\lambda \approx 8.6$ mm; X-Band $\lambda \approx 31.9$ mm. In a) and b) also the Rayleigh-approximation is shown in grey. Exponential size distribution is assumed to derive the DWR. Adapted from the Figures 2.13 and 2.16 of Neto, 2021.

2.3.2 *Multi-frequency Approach*

Since reflectivity Z_e of a single frequency provides only one value for a whole particle population, different properties, e.g., its number concentration and mean mass, can not be estimated unambiguously. In other words, particle populations with different properties can cause the same value of Z_e. For example, a population with a relatively high mean mass and lower number concentration can have the same Z_e as a population with a relatively low mean mass but higher number concentration. To reduce ambiguity in the interpretation of the radar return, analyzing Z_e of several radars with different frequencies is beneficial.

The advantages of the multi-frequency approach can be easily explained by the previously discussed dependence of the backscattering cross-section on particle size, shape, and radar wavelength. If radars of different frequencies observe the same particle, the backscattered energy differs depending on characteristic particle properties. However, radars do not observe single particles but an ensemble of particles in a volume, which size is determined by the radar beamwidth and range resolution. Considering only the first moment of the radar Doppler spetrum (Section 2.3.3) (Z_e), the dual-wavelength ratio:

$$DWR = \frac{Z_{e,\lambda_1}}{Z_{e,\lambda_1}}, \tag{2.14}$$

with the Z_e at different wavelengths λ in linear units (mm^6/m^3), is the only directly observable quantity that leverages on differential scattering. In the first order, the DWRs depend mainly on the mean size of the PSD. In contrast to Z_e, DWRs do not depend on the number concentration. However, the DWRs of two particle populations with the same mean size can differ from each other due to different particles' shapes and PSD widths (Battaglia et al., 2020b). On the one hand, these additional influences make it difficult to assign the mean size to the DWRs directly; on the other hand, these dependencies allow characterization of the particle shapes and PSD width (Kneifel et al., 2011; Kneifel et al., 2015; Mason et al., 2019). Combining multi-frequency observations with Doppler velocities gives additional constraints. For example, this combination allows deriving the degree of riming and the mean particle density (Mason et al., 2018). The lower panels of Figure 2.7 shows that the combination of X-, Ka-, and W-Band radars allow estimating the mean size of PSD in the range of about 1 mm to 30 mm, because in this range either $DWR_{Ka,W}$ or $DWR_{X,Ka}$ is increasing. At sizes below 1 mm, the non-Rayleigh scattering effects are too small to be detected with the given frequency combinations, and $DWR_{Ka,W}$ approaches zero. At large sizes, $DWR_{X,Ka}$ approaches a constant, though non-zero, value.

Challenges of the multi-frequency approach are the volume matching and the calibration of the radars, which are carefully executed and discussed by Neto et al., 2019 and Neto, 2021. Volume matching is crucial because only when the same particles or particles with similar properties are observed, the DWRs can be attributed to differential scattering. Similar accounts for the calibration, since offsets in Z_e bias the DWRs directly.

2.3.3 *Doppler Velocity Spectra and Radar Moments*

The Doppler effect induces a frequency shift of the backscattered radiation relative to the reference signal (Section 19.1, Parker, 2010), which contains information about the particles' motion with respect to the radar. As these frequency shifts are very small, most radars do not observe this shift directly, but rather the phase shift between consecutive pulses. How large the range of observed velocities and how finely resolved the velocity bins are, depends on the pulse repetition frequency (number of radiation pulses emitted per time) and the number of spectral bins (Section 5.5, Fabry and Zawadzki, 1995).

If the radar is pointing vertically, the Doppler velocity is the sum of the particles' terminal velocity v and the vertical air motion w. In stratiform clouds v is typically larger than w (Lamb and Verlinde, 2011, Section 12.4) and might even be neglected in some cases.

Since v depends on particle size and shape, the presence of distinct particle populations (small ice, aggregates, rimed) and processes (nucleation, secondary ice production) can be inferred from the Doppler spectrum at a given height and change with height (spectrogram) (e.g, Zawadzki et al., 2001). The addition of spectrally resolved polarimetric observations (Section 2.3.4) supports this characterization and process identification (Moisseev et al., 2015; Pfitzenmaier et al., 2018). Retrievals of the rain (Moisseev and Chandrasekar, 2007; Tridon and Battaglia, 2015) and snow (Barrett et al., 2019; Mróz et al., 2020) size distribution from Doppler spectra have been proposed but, especially in the case of snow, require strongly simplified assumptions about the particle properties, vertical wind, and turbulence.

The evolution of full Doppler spectra with time and height is a multidimensional problem that has been mostly studied only for smaller time series (e.g., Zawadzki et al., 2001; Verlinde et al., 2013). The moments of the Doppler spectrum can be more easily used for statistical analysis because there is only one value per time and height to consider. In addition to Z_e, the first (mean Doppler velocity MDV) and second (spectral width) Doppler moments are the most commonly used for ice microphysical processes investigations. In the case of w=0, MDV is the reflectivity-weighted v, and its profile reveals information about particle shape and size, and thus ice growth processes (Section 2.1) (Matrosov et al., 2002; Avramov et al., 2011; Szyrmer et al., 2012). In the absence of vertical wind and turbulence, the spectral width depends on the standard deviation of the Doppler velocity. This standard deviation is connected to the variance in the particle shapes and the width of the PSD (Mace et al., 2002; Deng and Mace, 2006; Ding and Liu, 2020).

The main challenge for analyzing Doppler spectra and their moments is the separation of the superposing effects of v and w. For microphysical studies, v is of primary interest, but also w must be considered. Vertical air motions manifests themselves in shifts of the Doppler spectra (larger scale) and broadening (shear wind, turbulence) (Fabry and Zawadzki, 1995, Section 5.2), and is therefore strongly affecting MDV and the spectral width. These vertical wind effects typically influence the spectra and moments from radars operating at shorter wavelengths less than radars operating at longer wavelengths because they can ensure a smaller bandwidth and thus smaller observation volume.

2.3.4 *Radar Polarimetry*

Similar to the multi-frequency approach, most polarimetric radar quantities provide additional information about the particle population because they represent ratios between two quantities that are affected by number concentration in the same way and thus do not depend on the number concentration (Meneghini and Liao, 2007). An exception is the Specific Differential Phase (K_{DP}), which is interesting precisely because it depends mainly on the number concentration.

Dual-polarization radars can detect Z_e and phase of the backscattered signal in two polarizations planes emitted previously in one or both planes to infer information about the size, shape, orientation, and phase composition (ice and liquid) of hydrometeors (Kumjian, 2013; Ryzhkov and Zrnic, 2019). Radar polarimetry leverages primarily on the nonspherical shape of the particles in the projection orthogonal to the wave propagation direction. Since the particles are mostly horizontally oriented, the polarimetric signals that are due to particle oblateness are strongest for radar instruments operating at low elevation angles. Therefore, observations from radars whose scanning patterns include low elevation angles are operationally applied for melting layer detection and rain rate estimation (Bringi and Chandrasekar, 2001, Section 7.3 and Chapter 8), as well as investigation of ice particle shapes and processes (Ryzhkov and Zrnic, 2019). However, vertically aligned radars also show fingerprints of certain particle shapes, e.g., needles (Oue et al., 2015) and melting particles (Baldini and Gorgucci, 2006), since they can also backscatter the incident radiation in a depolarized manner.

3 ICE PARTICLE PROPERTIES INFERRED FROM AGGREGATION MODELLING

Karrer, M., Seifert, A., Siewert, C., Ori, D., von Lerber, A., & Kneifel, S. (2020). **Ice particle properties inferred from aggregation modelling**. *Journal of Advances in Modeling Earth Systems*, 12(8), e2020MS002066, https://doi.org/10.1029/2020MS002066

JAMES Journal of Advances in Modeling Earth Systems

RESEARCH ARTICLE
10.1029/2020MS002066

Key Points:
- We simulated aggregates to study the impact of monomer number and type onice particle properties
- Ice particle properties show a smooth transition from monomers to aggregates
- The saturation of terminal velocity needs to be taken into account when simulating snow aggregation

Supporting Information:
- Supporting Information S1

Correspondence to:
M. Karrer,
markus.karrer@uni-koeln.de

Citation:
Karrer, M., Seifert, A., Siewert, C., Ori, D., von Lerber, A., & Kneifel, S. (2020). Ice particle properties inferred from aggregation modelling. *Journal of Advances in Modeling Earth Systems*, *12*, e2020MS002066. https://doi.org/10.1029/2020MS002066

Received 30 JAN 2020
Accepted 14 MAY 2020
Accepted article online 11 JUN 2020

Ice Particle Properties Inferred From Aggregation Modelling

M. Karrer[1], A. Seifert[2], C. Siewert[2], D. Ori[1], A. von Lerber[1,3], and S. Kneifel[1]

[1]Institute for Geophysics and Meteorology, University of Cologne, Cologne, Germany, [2]Deutscher Wetterdienst, Offenbach, Germany, [3]Finnish Meteorological Institute, Helsinki, Finland

Abstract We generated a large number 105,000 of aggregates composed of various monomer types and sizes using an aggregation model. Combined with hydrodynamic theory, we derived ice particle properties such as mass, projected area, and terminal velocity as a function of monomer number and size. This particle ensemble allows us to study the relation of particle properties with a high level of detail which is often not provided by in situ measurements. The ice particle properties change rather smoothly with monomer number. We find very little differences in all particle properties between monomers and aggregates at sizes below 1 mm which is in contrast to many microphysics schemes. The impact of the monomer type on the particle properties decreases with increasing monomer number. Whether, for example, the terminal velocity of an aggregate is larger or smaller than an equal-size monomer depends mostly on the monomer type. We fitted commonly used power laws as well as Atlas-type relations, which represent the saturation of the terminal velocity at large sizes (terminal velocity asymptotically approaching a limiting value) to the data set and tested the impact of incorporating different levels of complexity with idealized simulations using a 1D Lagrangian super particle model. These simulations indicate that it is sufficient to represent the monomer number dependency of ice particle properties with only two categories (monomers and aggregates). The incorporation of the saturation velocity at larger sizes is found to be important to avoid an overestimation of self-aggregation of larger snowflakes.

Plain Language Summary We have simulated and analyzed the properties, such as mass, area, and terminal fall velocity of snowflakes using a computer model. The snowflakes in the atmosphere form by collisions of ice crystals present in many different shapes. In the computer model, ice crystal shapes typically found in the atmosphere are stuck together to create three-dimensional snowflakes. The properties of the snowflakes depend on the shape and the number of ice crystals that are stuck together. While in weather and climate models, the properties of ice crystals and snowflakes are often assumed to be very different even if they are of the same size, we find very little differences in their properties. Many weather and climate models assume that snowflakes have a higher fall velocity the larger they are, although field observations have shown that particles larger than a few millimeters all fall with similar velocity. We fitted new parameterizations of the particle velocities which can remove this deficiency in the models. Finally, we used another model and showed that it might be sufficient to divide the properties of the ice particles in only two categories. However, it is important to consider the almost constant velocity of the large snowflakes.

1. Introduction

The terminal velocity v_{term} of ice monomers and aggregated ice particles and its relation to size has manifold impacts on precipitation and radiative effects of ice containing clouds. For example, Morales et al. (2019) show that parameters describing v_{term} of aggregates have the largest impact on the precipitation of simulated orographic clouds. Experiments with global climate simulations revealed that also radiative fluxes are very sensitive to changes in v_{term} (Jakob, 2002). Sanderson et al. (2008) found that v_{term} of ice is the second most influential parameter for the climate sensitivity in their multimember perturbed physics General circulation model ensemble. Constraining v_{term} of cloud ice and aggregated ice particles can reduce the degrees of freedom in model tuning (e.g., to improve top of atmosphere radiative fluxes Schmidt et al., 2017) and improve the physical consistency in atmospheric models.

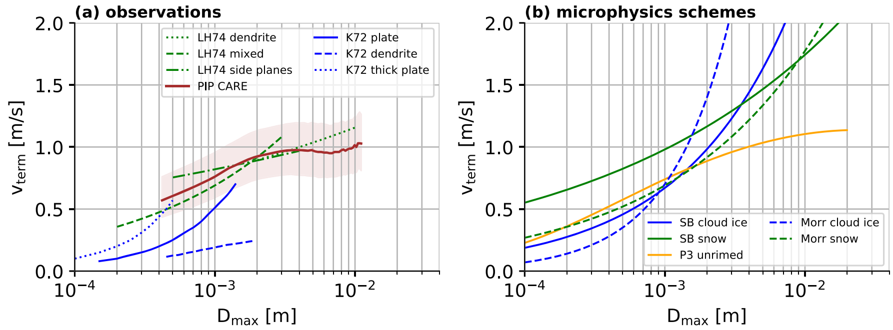

Figure 1. (a) In situ measurements of v_{term} of monomers (separated by monomer type; blue Kajikawa, 1972) and aggregates composed of different monomers (green: LH74 Locatelli & Hobbs, 1974) and particle ensembles from the PIP-CARE data set (see section A0.1). (b) v_{term} of unrimed ice particles in two-moment microphysics schemes. The blue line represents the implementation of cloud ice (monomers), the green line the implementation for the snow (aggregates) category in (solid lines, SB Seifert & Beheng, 2006) and (dashed lines, Morr Morrison et al., 2005). The Predicted Particle Property (P3) scheme (Morrison & Milbrandt, 2015) assumes identical properties for all unrimed particles (yellow line).

The importance of v_{term} of ice particle has been early recognized and has motivated first observational studies in the first third of the 20th century. Using initially manual observations and microphotography, pioneering studies such as (Brown, 1970; Kajikawa, 1972; Langleben, 1954; Locatelli & Hobbs, 1974; Nakaya & Terada, 1935; Zikmunda & Vali, 1972) investigated the relation of v_{term} to the particle's size for various ice particle habits and aggregates. In addition to the direct measurements of velocity, several studies started to investigate the principle relation between particle properties such as mass, size, and projected area to v_{term} which allows deriving v_{term} from these quantities (Cornford, 1965; Heymsfield, 1972). Due to the large efforts in performing these often manual measurements, the sample size of the derived relations is rather small. For example, some of the relations of the widely used relations by Locatelli and Hobbs (1974) are only based on 10–50 particles. One can assume that particles with ideal monomer types might have been subjectively chosen in order to easier associate the derived relationships to certain well-defined shapes. Nevertheless, the relations of size, mass, area, and v_{term} derived in these early studies are still used in microphysics parameterizations (e.g., the v_{term}-size relation of the snow category in Morrison and Milbrandt (2015) is taken from Locatelli and Hobbs (1974) mixed aggregates; see Figure 1). In Figure 1a, a selection of the aforementioned v_{term} relations is shown for their defined size range. The spread of velocities for different ice particle monomers is relatively high (e.g., Kajiwa, 1972) reported v_{term} to be about 0.2 m s^{-1} for a dendrite but about 0.5 m s^{-1} for a plate monomer. In contrast, v_{term} of aggregates of different monomer types appears to be relatively similar and always close to 1 m s^{-1} in the reported size range.

Evolving computer technology allowed the realization of automated particle measurement systems such as the 2D Video Disdrometer (2DVD Kruger & Krajewski, 2002), the Snow Video Imager (SVI Newman et al., 2009), its successor the Particle Imaging Package (PIP Tiira et al., 2016), the Hydrometeor Velocity and Shape Detector (HVSD Barthazy et al., 2004), or the Multi-Angle Snowflake Camera (MASC Garrett et al., 2012). These systems are based on optical methods to capture particle size and terminal velocity. Unlike in the early studies, particle property relations (Barthazy & Schefold, 2006; Brandes et al., 2008; Garrett & Yuter, 2014; Zawadzki et al., 2010) are now based on a very large number of particles which are classified by automated algorithms rather than visual selection (Bernauer et al., 2016; von Lerber et al., 2017). All optical disdrometers have a smallest detectable size limit (e.g., 0.1–0.2 mm for 2DVD), which implies that measurements close to this limit should be interpreted with care. A general behavior, which is revealed by all instruments, is a "saturation" of aggregate terminal velocities (i.e., terminal velocities asymptotically approaching a limiting value) at approximately 1 m s^{-1} for unrimed particles and sizes larger than a few millimeters (Figure 1a).

Most ice microphysics schemes use two categories for unrimed ice particles, which are commonly denoted as cloud ice and snow/aggregates. Relations between particle properties, such as size (e.g., the maximum dimension D_{max}), mass m, projected area A, or v_{term}, are defined for each category. Examples of the v_{term}

dependence on size which are implemented in widely used two-moment schemes are shown in Figure 1b. When comparing these relations with observations (Figure 1a), we miss the saturation behavior of v_{term} for larger sizes in most relations. This discrepancy is expected as most schemes use power laws, which are unable to represent a saturation behavior. Alternative "Atlas-type" three-parameter fits have been suggested (Seifert et al., 2014), but so far, they have not been tested thoroughly. The recent Predicted Particle Properties (P3) scheme (Morrison & Milbrandt, 2015) uses only one ice category and a look-up table approach for v_{term}, which better matches the saturation at large sizes. At the smaller size range, the snow category is found for all schemes to fall significantly faster than the ice category with the same size. Considering that v_{term} depends strongly on m and A of the particle, it might sound plausible, that for example, an aggregate of a few plates should fall faster than a single plate of the same size. Unfortunately, most observations do not provide sufficiently detailed information about monomer number and type which would be needed to answer the question of whether there exists a "jump" in v_{term} for the number of monomers exceeding a certain threshold. Fairly direct observations of the particles' m and A are only available from manual, particle-based observations (e.g., Locatelli & Hobbs, 1974).

An interesting new tool to better understand the underlying principles of aggregation and its effects on particle properties are aggregation models (Hashino & Tripoli, 2011; Leinonen & Moisseev, 2015; Ori et al., 2014; Przybylo et al., 2019; Westbrook et al., 2004a). Those models use idealized monomer shapes (e.g., dendrites, needles, plates, and columns) with particle properties matched to in situ observations. Aggregates simulated with the model by Westbrook et al. (2004a) helped to better understand theoretical scaling relations associated to aggregation such as the increase of aggregate mass with size by a power of two (Westbrook et al., 2004b), which was known from several previous in situ observations. This model has been extended by Leinonen and Moisseev (2015) providing a large number of monomer shapes and also provides an option to rime the aggregate (Leinonen & Szyrmer, 2015). This allowed to better understand the evolution of size and mass of a large number of aggregates which were increasingly rimed (Seifert et al., 2019).

To infer v_{term} from modeled ice particles or aggregates, computational fluid dynamics is an accurate but also computational costly method. It has been recently applied to idealized ice particle shapes (Bürgesser et al., 2019; Hashino et al., 2016; Nettesheim & Wang, 2018), and more computations with more complex shapes can be expected shortly. Hydrodynamic theory is a computational cheaper alternative to calculate v_{term} based on a number of bulk particle characteristic, rather than the complex 3D shape (e.g., Böhm, 1992; Heymsfield & Westbrook, 2010; Khvorostyanov & Curry, 2005). The accuracy of hydrodynamic theories has recently been evaluated by ice particle analogs falling in an oil tank (Westbrook & Sephton, 2017). The experimental results show deviations smaller than 20% for the Heymsfield and Westbrook (2010) theory. A problematic aspect of these theories is still the formulation of the scaling toward higher Reynolds number (i.e., large particles) and the simulation of more complex particle shapes (Westbrook & Sephton, 2017).

Aggregation models in combination with hydrodynamic theory have recently been used to study v_{term} of aggregates (Hashino & Tripoli, 2011; Schmitt et al., 2019). Hashino and Tripoli (2011) identified a dependency of the aggregation rate and aggregate mass on the mean size and type of the monomers. Schmitt et al. (2019) analyzed v_{term} and its variability of simulated aggregates composed of hexagonal prisms taken from a monodisperse monomer size distribution. They found that the variability of v_{term} is caused by the variability of the number of monomers N_{mono} and the monomers' aspect ratio.

In this study, we aim to study the dependency of m, A, and v_{term} on size, monomer number, and type. For this, we create a large number of aggregates with various monomer types including also mixtures of different monomer types. The monomer size is sampled from a size distribution rather than a constant size to better represent real ensembles of aggregates. Central questions of this study are, how important is the monomer number and type information for parameterizing aggregate properties and how well can they be parameterized by different functional relations?

To answer these questions, we describe in section 2 the aggregation model and the created data set of unrimed aggregates as well as the hydrodynamic theory to calculate v_{term} based on m and A of these particles. The simulated particle properties are compared to in situ observations in section 3. Section

4presents several parameterizations of the particle properties. Finally, in section 5, we use a 1D Lagrangian particle model to test the impact of including different complexity of particle properties for aggregation

2. Methods

2.1. Aggregation Model

We use the aggregation model developed by Leinonen and Moisseev (2015) which includes a large number of realistic monomers (hexagonal plates, dendrites, columns, and needle). Originally, the aggregation model was designed to produce realistic snow particle structures which can then be used to calculate their scattering properties (Leinonen & Moisseev, 2015; Leinonen et al., 2018). The model has also been used to systematically investigate microphysical processes, such as riming (Seifert et al., 2019).

The shape characteristics (length, thickness, etc.) of the monomers are predefined by geometric relations based on in situ observations (Leinonen & Moisseev, 2015). The aggregation process starts with generating N_{mono} monomers with sizes following a predefined inverse exponential probability density function $p_d(D_{\max})$,

$$p_d(D_{\max}) = \lambda exp(-\lambda D_{\max}), \tag{1}$$

where λ^{-1} is the size parameter of the monomer distribution and $D_{\max}$ is the maximum size of the monomer. The higher λ^{-1}, the larger are the sizes of the monomers.

The monomers sizes are sampled from the monomer distribution and assembled until an aggregate consisting of N_{mono} monomers is build up. In each aggregation step, pairs of particles are selected according to a simplified gravitational collection kernel. The probability distribution of collision among each possible particle pair is calculated as being proportional to the particle geometric cross sections and differential fall speed (Westbrook et al., 2004a). The two colliding particles form an aggregate which then becomes one of the candidates for the next aggregation step. This process includes the collision between aggregates. The aggregation code is publicly available at https://github.com/jleinonen/aggregation, and more details on the implementation can be found in Leinonen and Moisseev (2015). During the aggregation process, the collecting particles are partially aligned with the principal axis in the *x-y* plane. Rotations around the principal axis are performed randomly with a standard deviation of 40°. The collected particles are randomly aligned, which mimics the complex flow in the vicinity of other particles (Leinonen & Moisseev, 2015).

The aggregation simulations performed in this study differ from previous studies in two main aspects. The first aspect is the resolution of the particle structure. The particle is internally represented by a three-dimensional lattice with a predefined distance of the volume elements of typically 40 μm. This distance was found to be sufficiently small for scattering computations, while being coarse enough in order to keep the numerical costs for the scattering computations in a reasonable range. However, we discovered that for small particle sizes, the theoretical relations for certain particle properties (see Fig. 1 in Leinonen and Moisseev (2015)) are not exactly matched by the discretized particle. This discrepancy can be easily explained when considering for example that plate monomers with $D_{\max} < 3.03$ mm consist of only one layer of volume elements if the default resolution of 40 μm is used. This does not necessarily affect the aggregate properties of those monomers as shown in Leinonen and Moisseev (2015); however, in our study, the focus is to investigate the transition from small to larger sizes particles. Hence, we need to refine the resolution especially for small particles.

As a compromise between computational feasibility and having fine enough resolved particles, aggregates with $N_{\mathrm{mono}} \leq 100$ are simulated with a resolution of 5 μm, while aggregates with $N_{\mathrm{mono}} \geq 100$ are simulated with 10-μm resolution. With a resolution of 5 μm (10 μm), a plate monomer with $D_{\max}$= 3 mm has a thickness of 4 (8) volume element layers. It should be noted that the sensitivity to resolution is smaller for monomer types with less extreme aspect ratios (e.g., columns).

The second major difference to previous aggregation studies using the model by Leinonen and Moisseev (2015) is that we extended the code in a way that we can also generate aggregates composed of monomers with different habits. The motivation for this new feature was based on observations that larger snowflakes often consist of a mixture of dendrites and needles (Lawson et al., 1998). The modified code extends

Table 1
Mass-Size ($m(D_{\max}, N_{\text{mono}}=1)=a_{m,1}D_{\max}^{b_{m,1}}$) and Projected Area-Size ($A(D_{\max}, N_{\text{mono}}=1)=a_{A,1}D_{\max}^{b_{A,1}}$) Relationships for Monomers (N_{mono}=1) used in the Aggregation Model

Monomer type	$a_{m,1}$ (kg m$^{-b_m}$)	$b_{m,1}$	$a_{A,1}$ (m^2 m$^{-b_A}$)	$b_{A,1}$
Plate	0.788	2.48	0.631	1.99
Needle	0.005	1.89	0.002	1.42
Dendrite	0.074	2.33	0.142	1.94
Column	0.046	2.07	0.008	1.54

Note. All monomers have a grid resolution of 5 μm. The shapes are predefined in the aggregation model and mostly based on Pruppacher and Klett (1998) (see Fig. 1 in Leinonen and Moisseev, 2015).

Equation 1 to be the joint distribution of multiple mono-dispersed distributions. Each monomer distribution is defined by its own settings (e.g., monomer type, mean size, and truncation). The joint distribution is defined by the relative weights of each mono-dispersed distribution. These modifications have been merged to the main aggregation code and are also publicly available.

In order to account for a large variability of naturally observed particle shapes (Bailey & Hallett, 2009), we simulated a large suite of aggregates consisting of plates, columns, dendrites, needles, and mixtures of dendrites and columns. The m–$D_{\max}$ and A–$D_{\max}$ relations for the monomers are given in Table 1. Two sets of aggregates with mixed monomer types were created. For the first mixture, the selection of the monomer type is random with the same probability density function for both monomer types ("Mix1"). This would represent a scenario, where dendrites and needles coexist with similar PSD and likelihood of aggregation. For the second mixture, the monomers with $D_{\max}$ < 1 mm are columns, while dendrites are taken for larger monomers ("Mix2"). This choice is motivated by the fact that at temperatures below −20°C, the particle shape is less distinct but mostly described by polycrystals, while at temperatures between −20°C and −10°C, one finds more planar and dendritic crystals (Bailey & Hallett, 2009). Considering a thick cloud, we could assume that the small polycrystal or columnar crystals forming in the upper part of the cloud begin to form the first aggregate and then further grow by collection of larger dendrites at lower layers. Of course, both scenarios are quite ad hoc, and more detailed studies are needed to better understand the real properties of mixed-monomer aggregates. Our mixtures are thus rather intended to qualitatively analyze the differences of mixed monomer aggregates compared to single-monomer type aggregates (as done in another recent study by Dunnavan et al., 2019).

The aggregation process strongly depends on the number concentration of particles and their relative terminal velocity differences. In conditions which are less favorable for aggregation (e.g., low number concentration), the particles can grow by depositional growth to relatively large sizes before aggregation becomes the dominant process. It is therefore possible that aggregation involves very different monomer sizes. In order to account for this variability, we vary λ^{-1} in a large range from 50 μm to 10 mm with 500 different values of λ^{-1}, spaced evenly in the logarithmic space. The monomer distribution is limited to sizes of 100 μm up to 3 mm following Leinonen and Moisseev (2015) in order to be consistent with the typical size range of observed ice particles. Due to this truncation of the inverse exponential distribution, the mean monomer size differs from λ^{-1} and ranges from 150 μm to 1.48 mm.

The spacing of the monomer number (Table 2) is finer at low N_{mono} and becomes more coarse at larger numbers. In this way, we can investigate the changes at small monomer numbers with greater detail. In fact, we expect the largest changes in snow properties at the transition from single monomers to aggregates composed of few pristine crystals as shown in earlier studies (Dunnavan et al., 2019; Schmitt & Heymsfield, 2010). The coarser spacing of N_{mono} also limits computational costs. With our settings, we obtain maximum aggregates sizes ranging from 3 to 5 cm which means that we include also the typically observed large snowflakes during intense snowfall on the ground (Lawson et al., 1998).

In Figure 2, several examples of similar sized aggregates simulated with different combinations of λ^{-1}, N_{mono}, and monomer types are shown. In total, 105,000 particles were simulated. Apart from the visual differences of shapes and structure, also the particle properties such as mass, area, or terminal velocity show a wide range of values although all aggregates have maximum sizes ranging between 3 and 5 mm.

2.2. Hydrodynamic Models

Hydrodynamic models are needed in order to derive the terminal velocity v_{term} from the particle's mass m, projected area A, and maximum size $D_{\max}$. The most commonly used hydrodynamic models are Böhm (1992, hereafter B92), Khvorostyanov and Curry (2005, hereafter KC05), and Heymsfield and Westbrook (2010, hereafter HW10). All models are based on particle boundary layer theory and rely on the Best number (X) approach (Abraham, 1970). v_{term} is calculated via,

10.1029/2020MS002066

Table 2
Grid Resolution, Size Parameter λ^{-1} of the Monomer Distribution, and Number of Monomers N_{mono} used to Create the Aggregate Data Set

Resolution	λ^{-1}	N_{mono}	D_{max} of the aggregate
5 μm	50 μm–10 mm	1, 2, 3, ..., 10, 20, 30, ..., 100	≈1–2 cm
10 μm	50 μm–10 mm	200, 300, ..., 1,000	≈3–5 cm

Note. D_{max} denotes the maximum size range of the generated aggregates in the data set.

$$v_{\mathrm{term}} = \eta \; Re\;(X)/(\rho_a D_{\mathrm{max}}), \tag{2}$$

where η is the dynamic viscosity, Re the Reynolds number (parameterized as a function of X), and ρ_a is the air density. X is defined as

$$X = C_d Re^2, \tag{3}$$

where C_d is the drag coefficient. The proportionality of X to the particle properties is given by

$$X \sim m D_{\mathrm{max}}^{0.5} A^{-0.25}, \tag{4}$$

for B92.

For this study, we decided to use B92 because it best represents the saturation of v_{term} for our simulated particles at larger aggregate sizes (Figure A2) in accordance with observations (Figure 1). B92 includes an

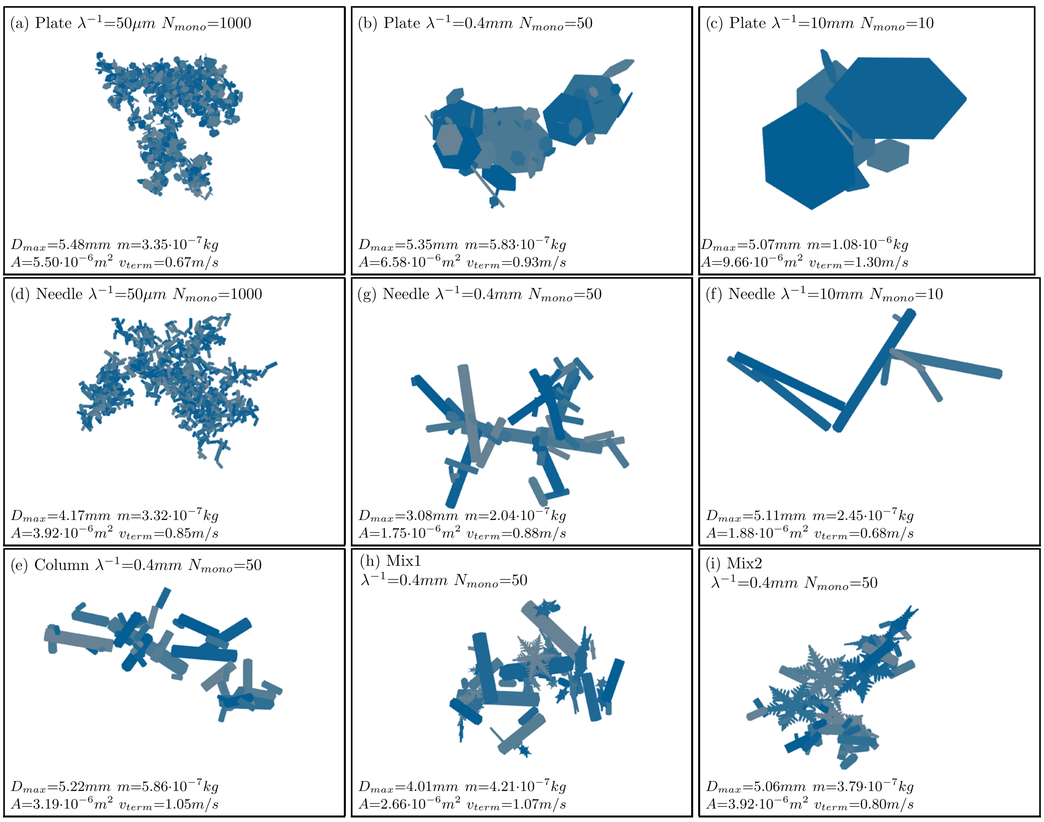

Figure 2. Examples of simulated aggregates with various size parameters (λ^{-1}), number of monomers N_{mono}, and monomer types. All aggregates have a comparable maximum size (in the range between 3 and 5 mm). The terminal velocity v_{term} is calculated using the hydrodynamic model by Böhm (1992; see section 2.2).

empirical correction of X due to wake turbulence which increases the drag of large particles. X depends on the aspect ratio α, which is larger than one for prolate and smaller than one for oblate particles. For this study, we set α to 1.0, because aggregates with small values of N_{mono} are not easily classifiable as either prolate or oblate and show in general a large variability of α (Jiang et al., 2019).

To be able to interpret the dependency of v_{term} on N_{mono} in section 4.3, we sketch here how v_{term} scales with D_{max} in the simplified case of $Re \ll 1$ (Stokes drag) and $Re \gg 1$ (Newtonian drag). For $Re \ll 1$, C_D is approximately proportional to $1/Re$. Inserting this approximation and Equations 3 and 4 into Equation 2 yields

$$v_{term} \sim m D_{max}^{-0.5} A^{-0.25}. \tag{5}$$

If we approximate m and A by the power laws $m = a_m D_{max}^{b_m}$ and $A = a_A D_{max}^{b_A}$, we can express v_{term} solely as a function of D_{max}:

$$v_{term} \sim D_{max}^{b_m - 0.5 - 0.25 b_A}. \tag{6}$$

For $Re \gg 1$, C_D is approximately constant. In this case, Equation 3 gives us $Re \sim X^{0.5}$, and by using again the Equations 2 and 4, we get

$$v_{term} \sim \left(m D_{max}^{-1.5} A^{-0.25}\right)^{0.5} \sim \left(D_{max}^{b_m - 1.5 - 0.25 b_A}\right)^{0.5}. \tag{7}$$

In both extreme cases of Re, v_{term} increases the faster with size the higher $b_m - 0.25 b_A$ is, and we expect this also to be in between these cases where Re transitions from $Re \sim X$ to $Re \sim X^{0.5}$. This has certain implications for the dependency of v_{term} on N_{mono} (section 4.3).

The differences between the three hydrodynamic models as well as an analysis of the potential impact of changing to different hydrodynamic models is discussed in the Appendix A2.

3. Comparison of the Simulated Particle Properties to In Situ Observations

3.1. Mass- and Area-Size Relations

Particle properties, such as m, A, and D_{max}, are used in hydrodynamic models to calculate v_{term} (section 2.2). We compare our relations of these particle properties and v_{term} with frequently used relations that are based on in situ measurements from Locatelli 306 and Hobbs (1974, LH74) and Mitchell (1996, M96). LH74 defined an equivalent diameter that is equal to "the diameter of the smallest circle into which the aggregate as photographed will fit without changing its density." M96 collected observations as a function of D_{max} without specifying the exact definition. The definitions of particle size used in these studies are limited by the observation equipment used, and the conversion from one to the other is not trivial. In our simulation study, we can access the full 3D structure of the particles and use the true maximum size (i.e., the maximum distance between any two points of the particle) as size definition.

Except for the aggregates of dendrites, which have a considerably lower density than LH74 aggregates of dendrites, the absolute value of m of the simulated aggregates is similar to the observations, where the same monomer type is available (Figure 3). The slope of the $m - D_{max}$ relation from this study is comparable to the slope from M96, while LH74 report lower slopes for the aggregates of dendrites. The $m - D_{max}$ relation of the mixed aggregates ("aggregates of unrimed radiating assemblages of plates, side planes, bullets, and columns," LH74 mix), however, has a similar slope to the simulated Mix2 aggregates. The mixS3 and sideplane aggregates from M96 are similar to many simulated aggregates (composed of different monomers).

M96 derived $A - D_{max}$ relations for "assemblages of planar polycrystals in cirrus clouds" (M96 polycrystal in Figure 3) based on observations in a relatively small size range and applied them to other aggregate types. This $A - D_{max}$ relation is also used in several microphysics schemes (Brdar & Seifert, 2018; Morrison & Milbrandt, 2015). The absolute value of A given in M96 is slightly higher than A of the simulated particles from this study (except for the aggregates of plates). The slope of the $A - D_{max}$ relations is slightly higher ($b_A = 1.88$) in M96 observations compared to the relations from this study ($1.79 < b_A < 1.88$). Observations of aggregates composed of the same monomer types than the one used in these studies are not available.

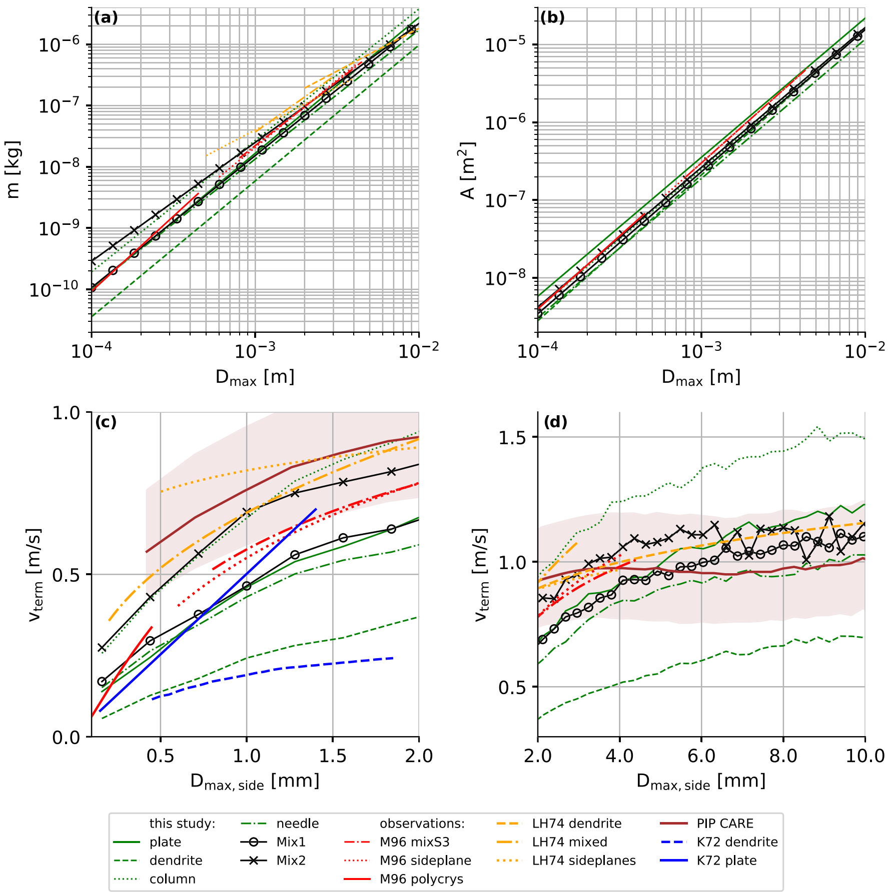

Figure 3. Particle properties of simulated aggregates from this study (green and black), from previous studies (Kajikawa, 1972; Locatelli & Hobbs, 1974; Mitchell, 1996) (M96, LH74, and K72) and measurements of ice particle observed by PIP at the CARE site (brown, see text). (a) m versus D_{max}; (b) A versus D_{max}; (c) median (and 25th and 75th percentile for PIP CARE) of v_{term} versus side projected maximum dimension $D_{max,side}$ for data from this study and versus the size definition of the respective study (v_{term} is directly observed in K72 and LH74 and calculated with B92 from the m–D_{max} and A–D_{max} relations of M96) (d) same as (c) but for larger sizes. Note that K72 observations are for single monomers.

3.2. Terminal Velocity-Size Relations

Observations of v_{term} versus size have been reported using several different definitions of the diameter (Szyrmer & Zawadzki, 2010). To facilitate a consistent comparison between the observations from the PIP instrument (which are described in Section A0.1) and v_{term} of the simulated aggregates, we use the same bin sizes as the PIP instrument to derive the median v_{term}. Moreover, we derive the maximum dimension from a side projection of the modeled particle in the same way as in the observations from the PIP instrument described by (von Lerber et al., 2017) ($D_{max,side}$; Figures 3c and 3d). Displayed are the median and the 25th and 75th percentiles of v_{term} of the detected particles. Bins with fewer than 1,000 particles are excluded from the statistics. Although LH74, M96, and Kajikawa (1972, K72) did not use the same definition as the PIP-CARE data set, fits from this study are also shown in Figures 3c and 3d because they can ease the comparison with other studies.

At small sizes (D_{max}< 1 mm), v_{term} of the simulated aggregates of dendrites is close to v_{term} of the monomers from Kajikawa (1972, K72, Figure 3c). The plate monomers in K72 are reported with a similar v_{term} as the aggregates of plates, needles, and Mix1 (which all have similar values). Note that v_{term} of plates and dendrites from K72 and v_{term} of all aggregates simulated in this study (except for the aggregates of columns and "Mix2") are considerably smaller than v_{term} of the aggregates from the PIP-CARE data set and LH74. The

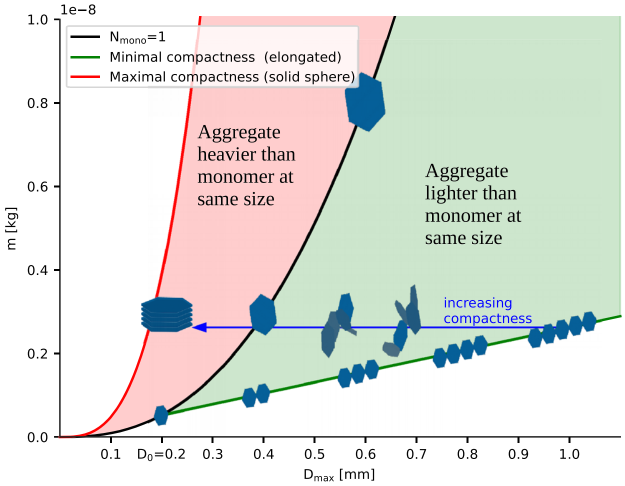

Figure 4. Schematic illustration of how compactness of aggregates can cause them to be heavier or lighter compared to a monomer of the same size. For simplicity a monodisperse monomer size distribution with monomer sizes of D_{max} = 0.2 mm is used. The red line indicates the maximum theoretical compactness of mass of an ice sphere. The black lines shows the m–D_{max} relation of the monomer (plate). The green line represents the m–D_{max} relation of the least compact configuration of the plate monomers in an aggregate by aligning the plates along their maximum dimension. Particles have lower mass ($f_m < 1$) in the green shaded area and larger mass ($f_m > 1$) in the red shaded region compared to an equal-size plate.

observations from LH74 are within the 25th and 75th percentile of the PIP-CARE data set. The median of v_{term} of the simulated aggregates of this study increases faster with size compared to the in situ observations at sizes of several millimeters (Figure 3d). Only v_{term} of the mixture of small columns and large dendrites ("Mix2") has a comparably low slope. Potential reasons for this mismatch are limitations of the observations at these sizes (Brandes et al., 2008), turbulence affecting the observations (Garrett & Yuter, 2014), missing processes in the aggregation model (e.g., depositional growth on aggregates), imperfect parameterizations in the hydrodynamic model, or the dominance of monomer type mixtures in the aggregates.

Figures 3c and 3d also show v_{term} calculated with B92 and the m–D_{max} and A–D_{max} relations from M96 (which did not measure v_{term} directly). The simulated slope of v_{term} from M96 observed aggregates is similar to the one simulated in this study, while the absolute value is slightly higher.

At sizes larger than about 5 mm, the simulated and the observed v_{term} reach a saturation value close to 1 m s^{-1}. The median of v_{term} of most simulated aggregates lies within the 25th and 75th percentile in the sub-centimeter range, except the aggregates with the most extreme density (aggregate of dendrites and aggregates of columns). Thus, based on this comparison, these aggregates can be considered most representative for many aggregates found in the atmosphere.

4. Parameterization of Particle Properties

The relationships between hydrometeor properties such as mass, size, projected area, and velocity are key components in any ice microphysics scheme, and they strongly influence various microphysical processes (e.g., sedimentation, depositional growth, aggregation, or riming). Different microphysics schemes require a more or less simplified parameterization of particle properties. To address these different needs, we derive in this section fits for m and A as a function of D_{max} and N_{mono} that can be used in microphysics schemes, which can predict m and N_{mono} given a certain D_{max} (section 4.2). Of course, most bulk schemes require less detailed fits, and hence, we also derive fits of m, A, and v_{term} as a function of D_{max} or the mass-equivalent diameter D_{eq}. This also allows us to assess the potential error of the less detailed fits (section 4.5), while their impact on modeled processes is studied later in section 5.

4.1. Fitting Approach for Monomer Number-Dependent Particle Properties

The particle properties of the monomers are defined a priori in the aggregation model and based on well-established observations. In contrast, the aggregate properties are determined by the aggregation process and change with increasing N_{mono}. As we are particularly interested in quantifying how key particle properties of aggregates differ from the properties of the same-sized monomers, we normalize the aggregate properties by the property of a monomer with the same D_{max}

$$f_p(D_{max}, N_{mono}) = \frac{p(D_{max}, N_{mono})}{p(D_{max}, N_{mono} = 1)}. \tag{8}$$

p represents the particle properties (mass or area), $p(D_{max}, N_{mono}{=}1)$ is the property of single monomers (given in Table 1), and f_p is the normalizing function. A normalizing function which is larger (smaller) than 1 indicates that the aggregate properties are larger (smaller) than its composing monomer with the same size (Figure 4).

To fit f_p to various monomer types, we parameterize f_p by a power law and express the coefficients by rational functions to fit the dependency on N_{mono} similar to the approach presented in Frick et al. (2013).

Table 3
Coefficients in the Normalizing Functions f_m and f_A (Notation as in Equation 9) for Different Monomer Types

Monomer type	$a_{f,m}$	$a'_{f,m}$	$b_{f,m}$	$b'_{f,m}$	$a_{f,A}$	$a'_{f,A}$	$b_{f,A}$	$b'_{f,m}$
Plate	−0.673	0.364	−0.092	0.091	−0.473	0.322	−0.021	−0.166
Needle	0.162	−0.008	0.018	0.102	0.349	0.005	0.060	0.013
Dendrite	−0.288	0.215	−0.042	−0.056	−0.100	0.131	−0.019	−0.059
Column	0.079	−0.006	0.033	0.086	0.273	0.025	0.058	0.034

$$\begin{aligned} f_p(D_{\max}, N_{\text{mono}}) &= a(N_{\text{mono}})\, D_{\max}^{b(N_{\text{mono}})} \\ &= 10^{\frac{a_{f,p}\log_{10}(N_{\text{mono}})}{1+a'_{f,p}\log_{10}(N_{\text{mono}})}} D_{\max}^{\frac{b_{f,p}\log_{10}(N_{mono})}{1+b'_{f,p}\log_{10}(N_{\text{mono}})}}. \end{aligned} \tag{9}$$

The coefficients of f_p for all monomer types can be found in Table 3. Note that we excluded the mixture of monomer types from the monomer-dependent analysis because our normalization approach cannot be applied to monomer mixtures.

4.2. Dependence of Aggregate Mass and Area on Monomer Number

Motivated by the common classification of unrimed ice hydrometeors in cloud ice and snow in many bulk schemes, we will investigate in this section how mass and area change when building up an aggregate with an increasing number of monomers. In particular, we want to explore whether the properties change smoothly with monomer number or whether they show any sharp transition at certain monomer numbers.

When we compare the mass of an aggregate with the mass of its monomer of the same size, we find in some conditions the aggregate to be heavier or lighter than the monomer. The relevant mechanisms which explain this behavior are illustrated in Figure 4 for aggregates of plates. Note that we assume for simplicity a monodisperse monomer distribution in Figure 4. When we consider pure depositional growth, we obtain a specific m–$D_{\max}$ relation for each monomer type (Table 1; black line in Figure 4). One extreme aggregation scenario, which leads to the maximal size of an aggregate with a given number of monomers (which in this simplified case of a monodisperse distribution also determines its mass), would be if we assume that all monomers align along their maximum dimension. Clearly, the resulting aggregate would have a smaller m than a monomer of the same size. Of course, this maximal elongated assemblage of monomers is rather unlikely, and thus, the aggregate will have a more compact structure. If we imagine rearranging the monomers inside the aggregate in a progressively more packed configuration (indicated by the horizontal arrow in Figure 4), we might be able to reach the point where the size of the aggregate equals the one of the equal-mass monomer. At this point, it might be even possible to pack the monomers in a way that their size is smaller than an equal-mass monomer. A simple example of such an extreme packing would be to stack a number of plates on top of each other, that is, along their smallest axis. Whether an aggregate can be smaller than an equal-mass monomer is of course also dependent on how close the monomer m–$D_{\max}$ relation is to the theoretical maximum packing of an equal-mass sphere.

The dependency of A on N_{mono} can be understood analogously. Also, for A, the maximal elongated assemblage of the monomers leads to a lower A of the aggregate compared to the monomer of the same size, but in reality, the monomers will assemble in a more compact way. In addition, we have to consider that A is not simply additive as it is the case for m. Overlap (in the horizontally projected plane) and nonhorizontal alignment of the constituting monomers lead to a smaller A than the sum of A of the constituting monomers. Based on these simplified considerations, it becomes clear that the dependency of m and A on N_{mono} is determined by the exponent of the monomer power laws and the overall “compactness” of the aggregates.

When considering the monomer dependence of all simulated aggregates, we find the most different behavior for plate and needle aggregates. For plate aggregates, m and A steadily decrease for a given $D_{\max}$ with an increasing number of monomers (Figures 5b and 5d). From the principal considerations discussed in Figure 4, this behavior can be well understood. The plate monomers have the largest exponent ($b_{m,1} = 2.48$) of all monomers (Table 1), while the monomers itself show relatively loose connections within the aggregate (Figures 2a–2c). Interestingly, the aggregate mass for very small N_{mono} can be slightly larger than the

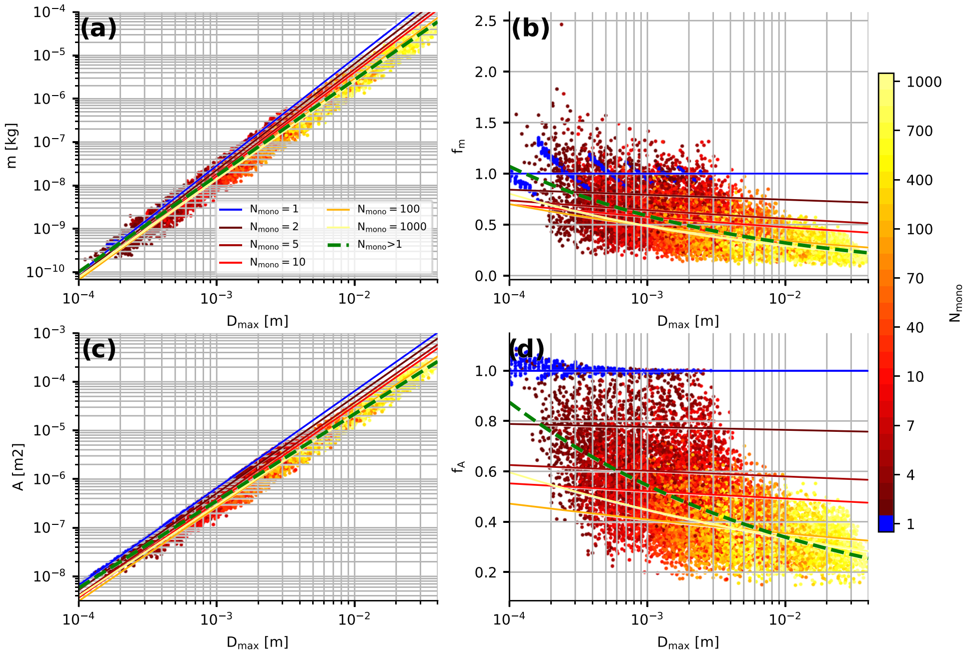

Figure 5. (a and c) m and A of the simulated plate aggregates as a function of D_{max}. (b and d) The normalizing functions f_m and f_A (defined in Equation 8) quantify the deviation of the aggregates' m or A from a monomer with same D_{max}. The dots indicate the properties of individual particles with the color showing N_{mono}. Lines indicate m and A for constant N_{mono} as a result of the monomer number dependent fits and for all aggregates ($N_{mono} > 1$).

equal-size monomer, while A is immediately decreasing for $N_{mono} > 1$. This effect can be easily understood when considering, for example, two plates that connect in a 90° angle of their major axes.

An opposite behavior is found for needle aggregates (Figures 6b and 6d). With increasing N_{mono}, both m and A of the aggregates become larger than the equal-size monomers. In contrast to plates, the needle monomers have the lowest exponents for the m and A power laws (Table 1). The aggregates of the more one-dimensional needles also show a more compact packing.

The deviation of the particle properties of the individual simulated particles from the fit is characterized by the mean absolute error (Table A2), which is smallest for plates (0.1190 for f_m and 0.0816 for f_A) and largest for needles (0.3737 for f_m and 0.3926 for f_A). The mean absolute error also shows that the monomer number-dependent fit is superior to the more simple power law fit (section 4.4) when there is a substantial dependence of the particle property on N_{mono}.

Dendrite and column aggregates have been analyzed similarly (according figures can be found in Supporting Information S1). The dendrites are similar to plates, while the columns are similar to needles. However, for all aggregate types, we find on average a relatively smooth transition of m and A when changing from single monomers to aggregates. For these two particle properties, we are unable to identify a “jump” due to the onset of aggregation. The next sections will show whether this behavior will change when deriving terminal velocity from m and A.

4.3. Dependence of Terminal Velocity on Monomer Number

The terminal velocity for all aggregates was calculated with the hydrodynamic model of B92 (section 2.2). In Figure 7a, v_{term} is shown as a function of D_{max} for plate aggregates. Note that the fits have been derived by applying B92 to the m–D_{max} and A–D_{max} fits (Table 3) rather than fitting them directly to the cloud of individual v_{term}. In this way, we are consistent with the way how v_{term} relations are usually connected to m–D_{max} in bulk schemes. The terminal velocity of plate aggregates steadily decreases with increasing N_{mono}. This dependency is much less pronounced at small D_{max} as compared to the largest sizes. However, it should be noted that the fits for very small monomer numbers are probably unrealistic for large D_{max} as we do not

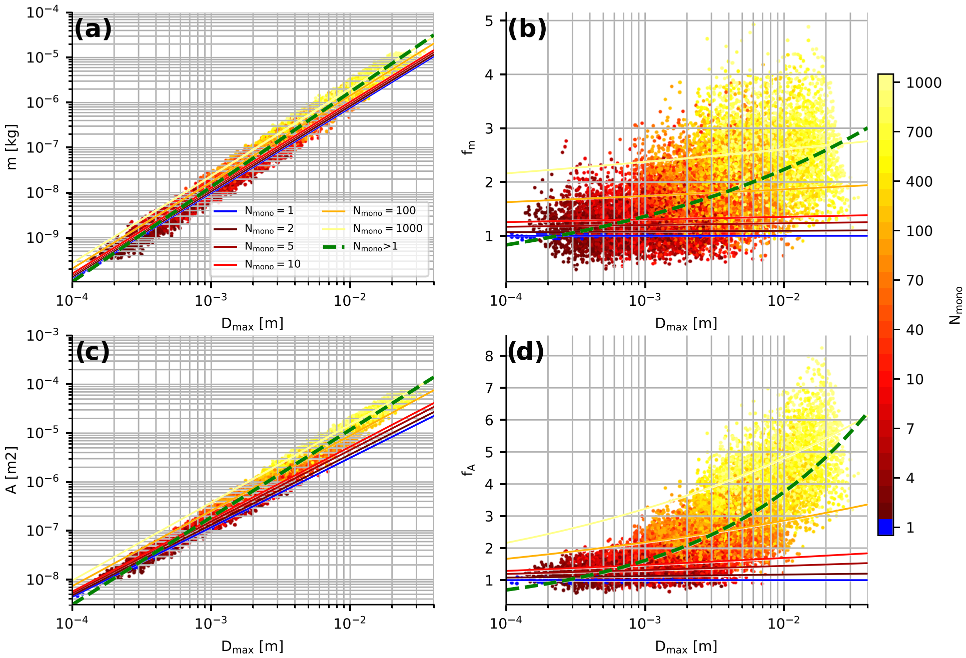

Figure 6. Same as Figure 5 but for aggregates of needles.

expect aggregates of centimeter sizes to be composed of only a few large plates. In fact, the here used geometrical relations for the plate monomers are only valid up to a size of 3 mm (Pruppacher & Klett, 1998).

We find a similar decreasing v_{term} with increasing N_{mono} for dendrites (see supporting information S1). As we might expect from the different change of m and A with N_{mono} seen in Figure 7a, also the behavior of v_{term} with increasing N_{mono} is different for needles (Figure 7). Needle aggregates seem to fall slightly faster when their monomer number increases. Interestingly, all aggregates reveal a very low dependence of v_{term} on monomer number at small sizes which is in contrast to assumptions in some microphysics schemes that distinguish between monomers and aggregates (e.g., Seifert & Beheng, 2006; Tsai & Chen, 2020). Besides, all aggregates reveal a saturation of v_{term} at large (centimeter) sizes which is in good agreement with

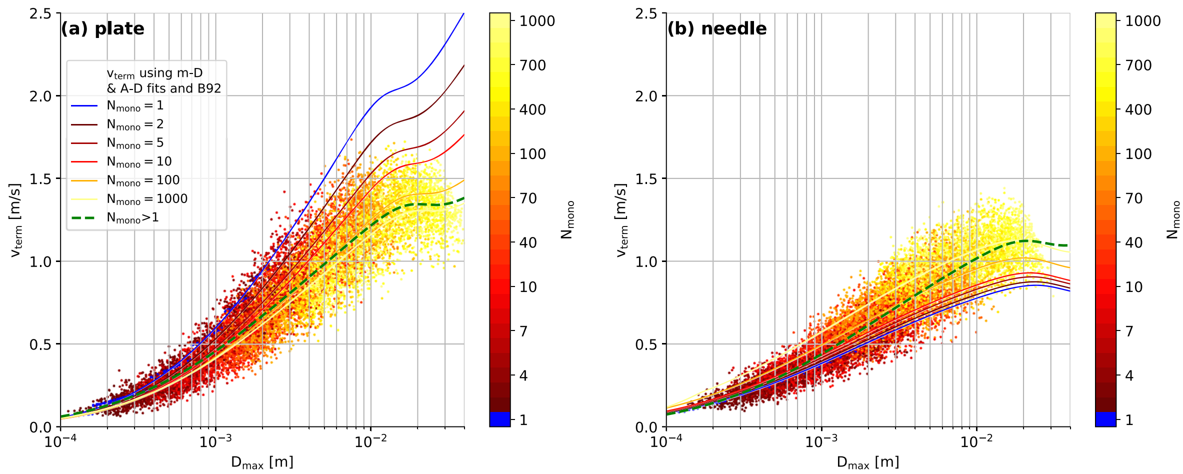

Figure 7. v_{term} versus D_{max} for the simulated aggregates of plates and needles. The dots indicate the properties of individual particles with the color showing N_{mono}. Lines indicate v_{term} for constant N_{mono} as a result of the monomer dependent fits and for all aggregates ($N_{mono} > 1$). Note that the fits have been derived by applying B92 to the $m–D_{max}$ and $A–D_{max}$ (Table 3) fits rather than fitting them directly to the cloud of individual v_{term}.

Table 4
Mass-Size ($m(D_{\max}) = a_{m,\mathrm{agg}} D_{\max}^{b_{m,\mathrm{agg}}}$) and Projected Area-Size ($A(D_{\max}) = a_{A,\mathrm{agg}} D_{\max}^{b_{A,\mathrm{agg}}}$) Relationships for Aggregates ($N_{mono} > 1$) in the Aggregate Model

Monomer type	$a_{m,\mathrm{agg}}$ (kg m$^{-b_m}$)	$b_{m,\mathrm{agg}}$	$a_{A,\mathrm{agg}}$ (m^2 m$^{-b_A}$)	$b_{A,\mathrm{agg}}$
Plate	0.076	2.22	0.083	1.79
Needle	0.028	2.11	0.045	1.79
Dendrite	0.027	2.22	0.090	1.88
Column	0.074	2.15	0.060	1.79
Mix1	0.045	2.16	0.070	1.83
Mix2	0.017	1.94	0.066	1.79

observations (Figure 1). However, the absolute value of the saturation v_{term} ranges from 0.8 to 1.6 m s^{-1} depending on the monomer type.

Because v_{term} of monomers and aggregates is converging toward the same value at small sizes (Figure 7), we can use the previously derived scaling relation (Equations 6 and 7) to relate the dependency of v_{term} on N_{mono} to the exponents b_m and b_A of the monomers ($b_{m,1}$ and $b_{A,1}$) and aggregates ($b_{m,\mathrm{agg}}$ and $b_{A,\mathrm{agg}}$) in the m–$D_{\max}$ relation. Starting from a similar value of v_{term} at small sizes, v_{term} of an average aggregate increases slower than v_{term} of a monomer if $s_{\mathrm{monodep}} = b_{m,\mathrm{agg}} - b_{m,1} - 0.25(b_{A,\mathrm{agg}} - b_{A,1}) < 0$ (cf. Equations 6 and 7). As a result, at larger sizes, v_{term} of the aggregate is lower than v_{term} of the monomer. In an analog way, v_{term} of an aggregate is larger than v_{term} of the monomer if $s_{\mathrm{monodep}} > 0$. As $b_{m,\mathrm{agg}}$ and $b_{A,\mathrm{agg}}$ are similar for all aggregates (Table 4), the sign of v_{term} with increasing N_{mono} depends mainly on $b_{m,1}$ and $b_{A,1}$. For plates and needles, s_{monodep} equals −0.21 and 0.12, respectively.

How the particle properties change with increasing N_{mono} as well as the absolute values of calculated v_{term} depends on the choice of the hydrodynamic model. Finding the optimal formulation of hydrodynamic models for ice and snow particles is still an active field of research (Nettesheim & Wang, 2018; Westbrook & Sephton, 2017) and outside the scope of this study. In Appendix A2, we tested the sensitivity of the results to the choice of the hydrodynamic model for plate aggregates. HW10 seems to yield overall similar results to

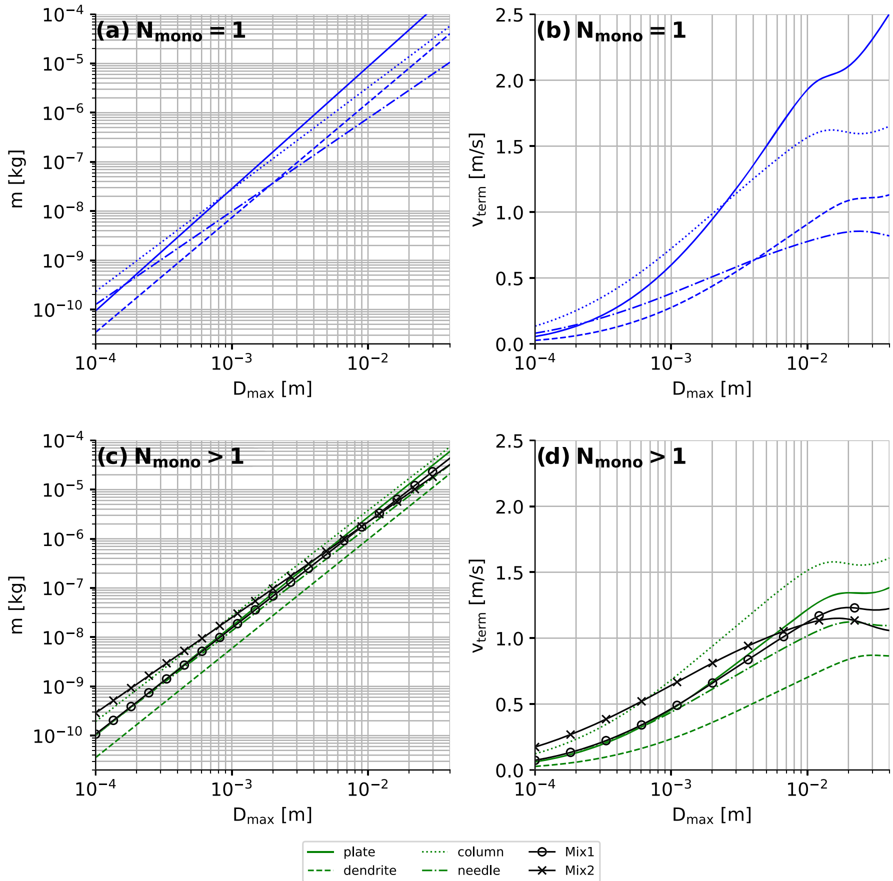

Figure 8. Particle (a and c) m and (b and d) v_{term} as a function of $D_{\max}$ calculated with B92 using the derived m/A–$D_{\max}$ relations (Tables 1 and 4). Particles are separated into (a and b) single monomers and (c and d) aggregates composed of various monomer types (see legend).

Table 5
Derived Coefficients of the Power-Law and Atlas-Type Fits (Equations 10 and 11) for Monomers and Aggregates of Different Monomer Types

Monomer type	$\alpha_{D_{eq}}$ (m s^{-1})	$\beta_{D_{eq}}$ (m s^{-1})	$\gamma_{D_{eq}}$ (m^{-1})	$a_{v,D_{max}}$ (m$^{1-b_{v,D_{max}}}$ s^{-1})	$b_{v,D_{max}}$
$N_{mono} = 1$					
Plate	2.265	2.275	771.138	90.386	0.755
Needle	0.848	0.871	2,276.977	9.229	0.481
Dendrite	1.133	1.153	1,177.000	41.870	0.755
Column	1.629	1.667	1,585.956	22.800	0.251
$N_{mono} > 1$					
Plate	1.366	1.391	1,285.591	30.966	0.635
Needle	1.118	1.133	1,659.461	17.583	0.557
Dendrite	0.880	0.895	1,392.959	24.348	0.698
Column	1.583	1.600	1,491.168	23.416	0.534
Mix1	1.233	1.250	1,509.549	21.739	0.580
Mix2	1.121	1.119	2,292.233	8.567	0.393

B92 except for the saturation at large diameters. Due to the absence of the turbulence correction in HW10, v_{term} increases also at large diameters. For KC05, the monomer dependence is much weaker. However, all hydrodynamic models show an overall small monomer dependence at small particle sizes.

It has also been observed (e.g., Garrett & Yuter, 2014) that tumbling of particles caused for example by turbulence might decrease the effective projected area and therefore increase v_{term}. We also tested the sensitivity of our results to different degrees of tumbling (section A0.2.2). As expected, the effect of tumbling is largest for single crystals (due to their more extreme aspect ratio) but strongly decreases for aggregates. Certainly, for aggregates, the choice of the hydrodynamic model has a larger effect of v_{term} than different assumptions on particle tumbling.

4.4. Mean Particle Properties of Monomers and Aggregates of Different Monomer Types

The relatively continuous change of particle properties with N_{mono} found in the last section justifies a simplified fit, which is also necessary for implementing the results into common bulk microphysics schemes. These schemes often only contain two classes for unrimed ice particles, usually denoted as cloud ice (monomers) and snow (aggregates).

Figures 8a and 8b show the derived m–D_{max} relations for single monomers (N_{mono}=1) and the derived v_{term} based on the m–D_{max} and A–D_{max} relations summarized in Table 1. Similar fits of m and v_{term} to aggregates of any monomer number larger than 1 are shown in Figures 8c and 8d; the fit coefficients can be found in Table 4.

The m–D_{max} relations for monomers show a larger spread especially for larger sizes as compared to the aggregates. This is expected considering that the exponents for monomers range between 1.89 and 2.48 (Table 1), while the exponents for aggregates are between 1.95 and 2.22 (Table 4). The values for aggregates agree well with theoretical aggregation studies (Westbrook et al., 2004b) as well as in situ observations (section 3.1). Despite the similar exponent, the effective density of the aggregates varies considerably (compare m at a given size in Figure 8c), which is in agreement with previous studies (Dunnavan et al., 2019; Hashino & Tripoli, 2011), even though their approaches to simulate aggregates are very different from the approach used in this study. Aggregates of columns exhibit the highest density, while aggregates of dendrites show the lowest density.

The differences in the m–D_{max} relation are linked to the resulting v_{term}–D_{max} relation (Figures 8c and 8d). At $D_{max} = 5$ mm, the v_{term} of different monomers spread nearly 1 m s^{-1}. The differences are in general smaller for aggregates. Interestingly, most aggregate types reveal very similar v_{term}. The main exceptions are dendrite aggregates with the slowest and column aggregates with the fastest v_{term}. v_{term} of the Mix2 aggregates increases slower with increasing D_{max} compared to the other aggregates.

Similar to the previous monomer number dependent fits, also the "two-category" fits show similar v_{term} at small sizes. The monomer type appears to have in general a much larger impact on v_{term} than the classification into certain N_{mono} regimes.

4.5. Power-Law and Atlas-Type Fits for Terminal Velocity

Power-law fits for m, A, and v_{term} are commonly used in bulk schemes. Especially for v_{term}, the power law introduces inconsistencies with observations because a saturation value for v_{term} as observed for raindrops or snowflakes cannot be represented. Instead of using standard power laws in the form,

$$v(D_{max}) = a_{vD_{max}} D^{b_{vD_{max}}}, \tag{10}$$

and the two fit parameters $a_{vD_{max}}$ and $b_{vD_{max}}$, Atlas et al. (1973) proposed a three-parameter ($\alpha_{D_{eq}}$, $\beta_{D_{eq}}$, and $\gamma_{D_{eq}}$) formulation

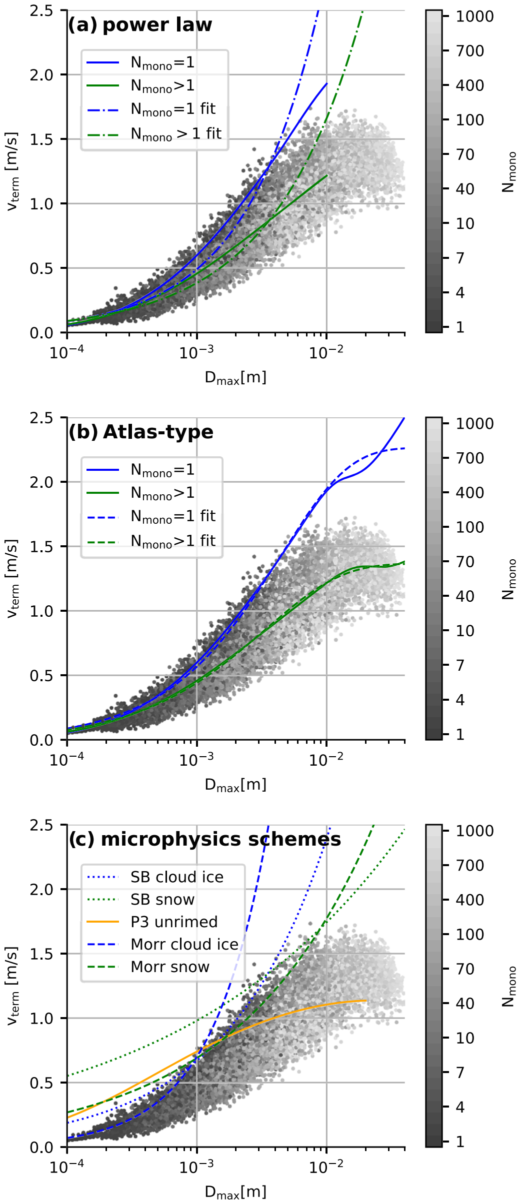

Figure 9. v_{term} of individual plate aggregates (gray scale, a–c) and v_{term} derived with B92 and the m/A–D_{max} of plate monomers (Table 1, solid blue line in a and b) and aggregates (Table 4, solid green line in a and b). Power-law (dashed-dotted, a) and Atlas-type fits (dashed-dotted, b) have been applied to the directly calculated v_{term} (solid lines) rather than the individual points. (c) v_{term} used in microphysics schemes (same as in Figure 1b).

$$v_{\mathrm{term}}(D_{\mathrm{eq}}) = \alpha_{D_{\mathrm{eq}}} - \beta_{D_{\mathrm{eq}}} \exp(-\gamma_{D_{\mathrm{eq}}} D_{\mathrm{eq}}). \tag{11}$$

Formulating this "Atlas-type" fit with the mass equivalent diameter D_{eq} instead of D_{max} has been found to provide optimal fit quality for snow aggregates (Seifert et al., 2014). For small (large) values of D_{eq}, v_{term} approaches $\alpha_{D_{\mathrm{eq}}} - \beta_{D_{\mathrm{eq}}}$ ($\alpha_{D_{\mathrm{eq}}}$). With increasing values of γ, the transition from small to larger values of v_{term} is shifted toward larger values of D_{eq}. Approximations for bulk collision rates based on Atlas-type fits can be found in Seifert et al. (2014) which makes them usable in bulk microphysics schemes without the necessity of look-up tables.

Power-law and Atlas-type relations have been applied to the various aggregates and the fit coefficients are summarized in Table 5. For the fitting, we did not use v_{term} of the individual particles but directly applied to fit to v_{term} derived with B92 and the existing m–D_{max} and A–D_{max} relations.

In Figure 9, the different fits are compared for plate monomers and their aggregates. Note that the saturation region ($D_{\mathrm{max}} > 1$ cm) has been excluded for the power-law fits. It can be seen in Figure 9b that the Atlas-type fit is very close to the theoretical line calculated with B92 and the m–D_{max} and A–D_{max} relations. The power-law fits (Figure 9a) provide only a close fit to the theoretical values at the smaller size range. Between 300 μm and 4 mm, they cause a slight underestimation, while at larger sizes, they increasingly overestimate v_{term}. Similar fits have been derived for all aggregate types (Table 5, figures for other monomer types similar to Figure 9 can be found in the supporting information S1).

When we compare the calculated v_{term} with some widely used microphysics schemes (Figure 9c), we find most schemes to overestimate v_{term} at small sizes (except of the cloud ice category in Morrison et al., 2005). The absolute values for v_{term} at small sizes are strongly dependent on monomer type, and hence, additional constraints should be provided by additional observations. However, the aggregation model shows independent on the monomer type that at submillimeter sizes, there should be no strong "jump" in v_{term} between ice particles and small aggregates. Also, in the centimeter-size range, models using a power-law formulation are strongly overestimating v_{term} for all aggregate types.

5. Application and Sensitivity Tests in the Lagrangian Particle Model McSnow

In this section, we will test the possible impact of implementing particle properties with different amount of complexity (monomer number dependence) or different fitting functions (power law vs. Atlas type) on the simulation of sedimentation, aggregation, and depositional growth. For this, we use a one-dimensional setup of the Lagrangian particle model McSnow (Brdar & Seifert, 2018), which provides the flexibility to implement the different particle property formulations.

For simplicity, only sedimentation, depositional growth, and aggregation are considered in our simulations. Aggregation is calculated with a Monte-Carlo algorithm following Shima et al. (2009), and the sticking efficiency of Connolly et al. (2012) is used. McSnow is based on the Lagrangian super particle approach (Shima et al., 2009), which allows deriving not only the particle mass and its multiplicity X_{mult} but also predicts the number of monomers the particle is composed of. This information is key to test the N_{mono} dependent particle relations. The thermodynamic profiles and the overall setup is similar to previous simulation studies

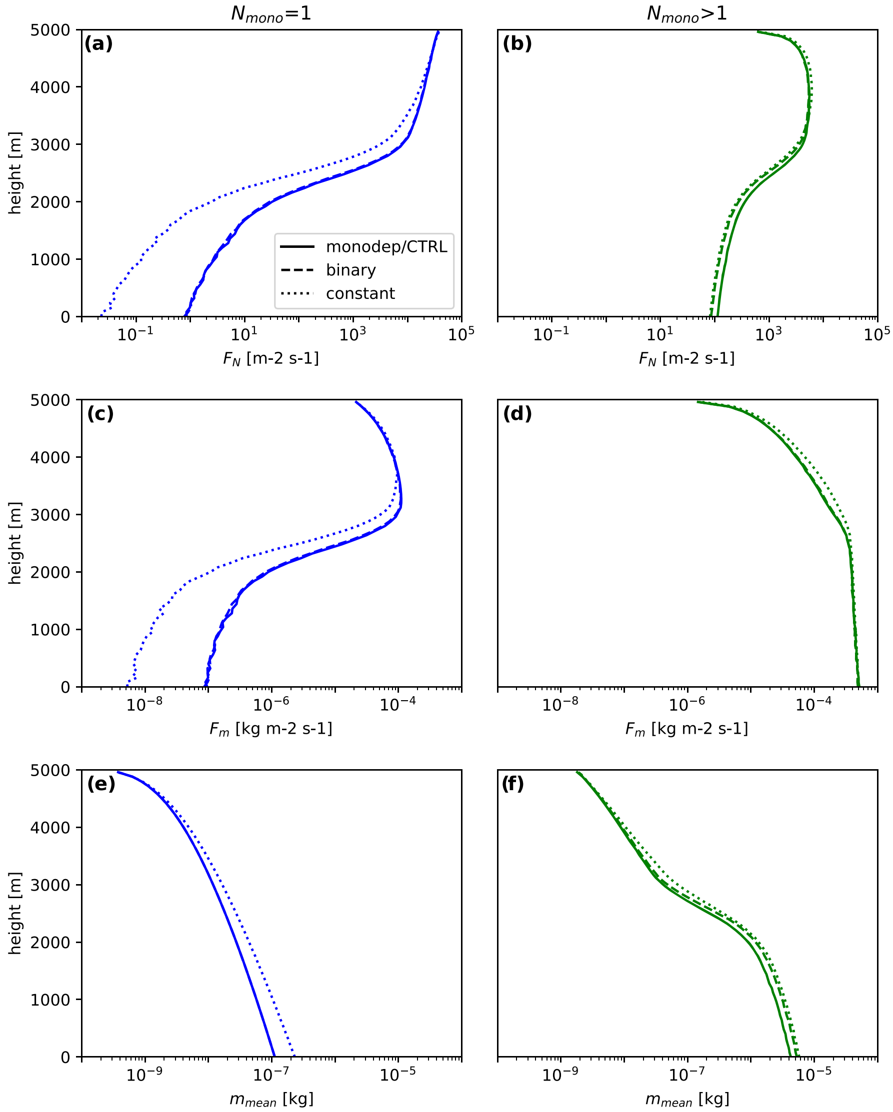

Figure 10. Idealized McSnow simulation using the N_{mono}-dependent fit for plates ("monodep"; Table 3), the separation between N_{mono}=1 and $N_{\mathrm{mono}} > 1$ ("binary"; Tables 1 and 4) and single relation (the one fitted to all aggregates) for all N_{mono} ("constant"; Table 4) for plates. For each individual super particle, B92 is used directly to calculate v_{term}. Shown are height profiles of (a and b) number flux F_N, (c and d) mass flux F_m, and (e and f) mean mass m_{mean}. The particles are categorized into $N_{\mathrm{mono}} = 1$ (left) and $N_{\mathrm{mono}} > 1$ (right).

with McSnow in Brdar and Seifert (2018) and Seifert et al. (2019). Particles are initialized at the upper boundary of the 5-km thick domain with a mass flux of F_m=2·10^{-5} kg s^{-1} and a mean mass of the particle size distribution of m_{mean}= 2·10^{-10} kg. The initial ice particles follow a generalized gamma distribution of particle mass with a shape parameter of 0 and a dispersion parameter of 1/3 (following Eq. 9 in Khain et al., 2015). The temperature decreases linearly from 273.1 K at z = 0 km to 242.2 K at z = 5 km. The supersaturation over ice is held constant at 5% with respect to ice in the whole column and is not consumed by the growth of the particle. The simulations are performed with 250 vertical levels, which result in a vertical resolution of 20 m. The model time step is set to 5 s, and the initial multiplicity is chosen to be 1,000. The simulations are run for 10 hr, from which the last 5 hr are averaged in 10-min intervals to reduce noise in the analyzed profiles.

Table 6
Settings of the McSnow Control (CTRL) and Sensitivity Runs

Simulation	Habit	m–$D_{\max}$/A–$D_{\max}$ relations	v_{term}–$D_{\max}$ relations	Precipitation rate (mm h^{-1}) (difference to CTRL)	$m_{\text{mean,sens}}$ (μg) ($m_{\text{mean,sens}}$/ $m_{\text{mean,CTRL}}$)
in Figure 10					
CTRL/monodep	Plate	$f_p(N_{\text{mono}},D_{\max})$	B92	1.844	4.214
Binary	Plate	$f_p(N_{\text{mono}}=1;N_{\text{mono}}>1,D_{\max})$	B92	1.763 (−4.4%)	5.241 (1.2)
Constant	Plate	$f_p(N_{\text{mono}}>1,D_{\max})$	B92	1.833 (−0.6%)	5.789 (1.4)
in Figure 12					
Atlas	Plate	$f_p(N_{\text{mono}}=1;N_{\text{mono}}>1,D_{\max})$	Atlas type	1.881 (+2.0%)	4.424 (×1.0)
Powerlaw	Plate	$f_p(N_{\text{mono}}=1;N_{\text{mono}}>1,D_{\max})$	Power law	1.761 (−4.5%)	21.013 (×5.0)
Powerlawlimit	Plate	$f_p(N_{\text{mono}}=1;N_{\text{mono}}>1,D_{\max})$	Power law (imposed limit: $v_{\text{term}} <= \alpha_{D_{eq}}$)	2.106 (+14.2%)	3.087 (×0.7)
in Figure 11					
Needle CTRL/monodep	Needle	$f_p(N_{\text{mono}},D_{\max})$	B92	1.988	13.173
Needle Binary	Needle	$f_p(N_{\text{mono}}=1;N_{\text{mono}}>1,D_{\max})$	B92	2.019 (+1.6%)	10.443 (0.8)
Needle Constant	Needle	$f_p=f(N_{\text{mono}}>1,D_{\max})$	B92	2.038 (+2.5%)	10.390 (0.8)

Note. The second column specifies the monomer type from which the m–$D_{\max}$ and A–$D_{\max}$ (and v_{term}–$D_{\max}$ for the Atlas and power law run) fit is taken. The third column denotes how the N_{mono} dependency is represented. $f_p(N_{\text{mono}},D_{\max})$ is the normalizing function with full N_{mono} dependence (section 4.1), $f_p(N_{\text{mono}}=1;N_{\text{mono}}>1,D_{\max})$ denotes only a binary seperation in $N_{\text{mono}}=1$ and $N_{\text{mono}}>1$, and $f_p=f(N_{\text{mono}}>1,D_{\max})$ indicates that the fit for all aggregates $N_{\text{mono}}>1$ is taken for all particles (section 4.4). The fourth column indicates whether v_{term} is calculated using B92 or with a parameterized relation of v_{term}–$D_{\max}$ (section 4.5). The fifth column shows the precipitation rate ($F_m(z = 0$ m)) and in brackets its deviation from the "CTRL" run. The last column lists the mean mass m_{mean} at the surface and the ratio of m_{mean} between the simulation and its "CTRL" run (in brackets).

In the following, we will focus the comparison on particle number flux (F_N), mass flux (F_M), and mean mass m_{mean} (which is the ratio between the integrated mass density q_m and the integrated number density q_N).

In the first simulation experiment shown in Figure 10, we include particle properties for which the full N_{mono} dependence is taken into account (Table 6). In this setup, we call hereafter the control simulation ("CTRL"). Profiles are separated into single monomers ($N_{\text{mono}} = 1$) and aggregates ($N_{\text{mono}} > 1$) to better distinguish the effects on what we might define as "cloud ice" and "snow" category in a bulk scheme. This separation might be important considering that there can be cases of weak aggregation. With weak aggregation, most of the particles will remain monomers, and thus, it is especially important to match profiles of these particles accurately.

In general, aggregation decreases the number flux (F_N), while the increase in the mass flux (F_m) is due to depositional growth. The mass flux of aggregates increases also due to conversion from monomers to aggregates by aggregation. The combination of both processes is causing m_{mean} to continuously increase toward the surface. Aggregation rates in McSnow are proportional to the gravitational collection kernel (Eq. 21 in Brdar & Seifert, 2018). Thus, the probability of collision for two particles is high if they have strongly different v_{term} and if the sum of their cross-sectional areas is large. F_N of the monomers ($N_{\text{mono}} = 1$) decreases monotonically with decreasing height because the monomers are converted into aggregates ($N_{\text{mono}} > 1$) by the aggregation process and there is no source of monomers like nucleation considered (Figure 10a). This decrease of F_N (and increase of m_{mean}) is especially strong at heights between 2 and 3 km. This region of enhanced aggregation is found at heights where the temperature is close to −15°C where the sticking efficiency has a local maximum. As a result of the conversion of monomers to aggregates, F_N of the aggregates increases at heights higher than about 3.5 km (Figure 10b). At lower heights, the number of aggregate-aggregate collisions outweighs the number of monomer-monomer collisions, and thus, F_N of the aggregates decreases.

The signature of the conversion from monomers to aggregates is also seen in F_m of the monomers (Figure 10c). Especially in the region of enhanced aggregation, this leads to a strong decrease of F_m. In the heights above this region, depositional growth outweighs the loss of mass of the monomers to the aggregates, and thus, there is an increase of F_m with decreasing height. F_m of the aggregates increases monotonously due to both depositional growth of the aggregates and conversion from monomers to

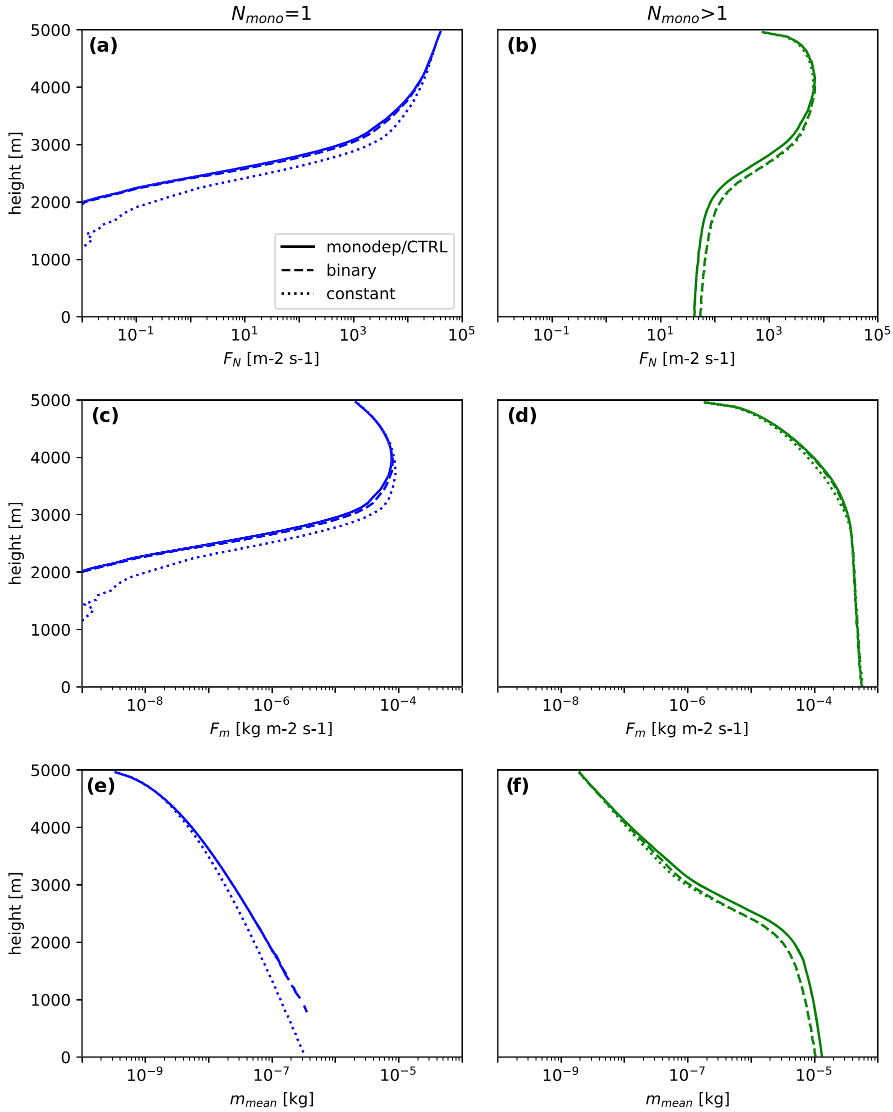

Figure 11. Same as Figure 10 but for needle monomers and aggregates.

aggregates (Figure 10d). In this setup, the change of F_m with height is governed by v_{term} and q_N at a given height. For example, a combination of low v_{term} and high q_N at upper layers leads to a large increase in F_m. Simply speaking, a large number of slow falling ice crystals can grow efficiently by deposition which increases F_m.

5.1. Sensitivity to Representation of Monomer Number Dependency

The "CTRL" simulation is now compared to simulations with a binary separation into single-monomer particles and aggregates of any monomer number larger than 1 (binary). An additional simulation is performed with no monomer number dependence (constant). Here, the particle properties that were fitted to the mean of all aggregates are used for all particles. All simulations are done for plate and needle monomers and aggregates because we found the monomer dependence to be most pronounced for these monomer types. For the other monomer types, the effect of N_{mono} can be expected to be smaller.

The most apparent difference between the simulations with different representations of the N_{mono} dependencies for plate monomers and aggregates of plates is the faster decrease of F_N and F_m and faster increase of m_{mean} of the monomers (N_{mono} = 1) in the "constant" simulation (Figure 10). A slightly

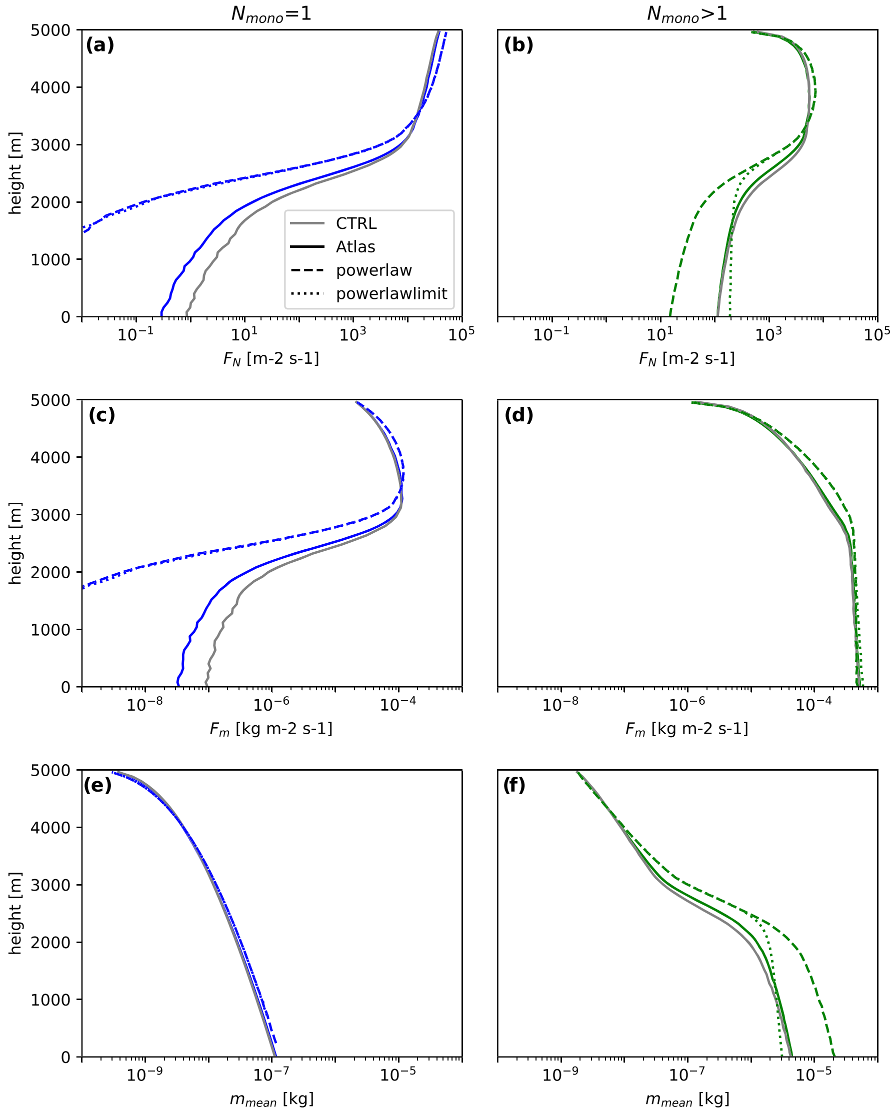

Figure 12. Idealized McSnow simulation using $m\text{–}D_{\max}$ and $A\text{–}D_{\max}$ for plate monomers and aggregates of plates (see Tables 1 and 4) and power law (without ("powerlaw") and with imposing an upper limit on v_{term} ("powerlawlimit"), which is consistent with the saturation value of the Atlas-type relation) and Atlas-type $v_{\text{term}}\text{–}D_{\max}$ relations for plate monomers and aggregates of plates (see Table 5). Overlayed is the CTRL/monodep simulation in gray (see also Figure 10). Shown are height profiles of (a and b) number flux F_N, (c and d) mass flux F_m, and (e and f) mean mass m_{mean}. The particles are categorized into $N_{\text{mono}} = 1$ (left) and $N_{\text{mono}} > 1$ (right).

faster decrease of F_N (faster increase of m_{mean}) for aggregates ($N_{\text{mono}} > 1$) with decreasing height can be seen for both the "binary" and the "CTRL" simulation. However, all of the simulations show very similar profiles.

Figure 11 shows the same experiment as Figure 10 but using the parameterizations for needles instead of plates. Also, for needles, the most remarkable difference between the simulations is the difference between the "constant" and the "CTRL" run (Figures 11a and 11e). Also, aggregate-aggregate collections are less effective in the "CTRL" run (Figures 11b and 11f). Note that all monomers have been depleted by aggregation at a height of about 1,000 m, and thereby, m_{mean} is not defined below.

Overall, the differences of m_{mean} at the ground of the total ice particle population are small (factor of 1.2 and 1.4 higher m_{mean} for the "binary" and "constant" simulation for plates and factor of 0.8 lower m_{mean} for the "binary" and "constant" simulation for needles, Table 6).

Also, the differences in the precipitation rates (F_m) are small (less than 5%; see Table 6). These small differences are due to the small difference of the absolute value of v_{term} at small sizes (Figure 7) and q_N at upper heights, which lead to a similar mass uptake (Figure 10). However, the precipitation rate between the "Plate CTRL" simulation and the "Needle CTRL" simulation is relatively large (Table 6), which might be due to the strongly different v_{term} of the monomers.

The N_{mono} dependency is even weaker for aggregates composed of other monomer types (sections 4.2 and 4.3). In summary, the simulation experiments with different monomer dependency indicate that a binary separation between single monomers and aggregates performs similarly well as relations which take into account a more detailed monomer dependency. Some but still small differences are found if no monomer dependency is taken into account, that is, a single ice class for all monomer numbers is assumed. In our simulation, particles with low N_{mono} are only prevalent at cold temperatures, where aggregation is less important due to the low sticking efficiency. Additional simulations (shown in the supporting information S1) with lower F_m and therefore weaker aggregation show that the "binary" simulations stay very close to the "CTRL" simulation, while the "monodep" simulations show considerably larger deviations. Hence, we find that the classical separation in cloud ice (monomers) and snow (aggregates) is sufficient for the aspects of monomer number-dependent particle properties.

5.2. Sensitivity to the Parameterization of Terminal Velocity

In this section, we test the sensitivity of the simulations to different implementations of the $v_{\mathrm{term}}-D_{\mathrm{max}}$ formulation. In Figure 12, v_{term} of plate monomers and aggregates is parameterized either as power-law or Atlas-type fit.

As we saw in Figure 9, the power-law and Atlas-type fits match very closely at small particle sizes. This explains the very close matching of the three simulations in the upper part of the simulated profiles (Figure 12) where the PSD is dominated by small particles. As soon as the aggregation becomes stronger (below ca. 3 km), F_N in the simulations using the power law (Figure 12b) is much lower than for Atlas-type. The decreasing number flux of aggregates with lower height (Figure 12b) also indicates that especially the self-collection of aggregates is stronger than for Atlas type. In the same height region, the mean mass of the aggregates (Figure 12f) is strongly increased for the power law (factor of 5). Instead of using an Atlas-type fit to consider the saturation of the terminal velocity, one can also think of imposing an upper limit on v_{term} in the power law relation. In the "Powerlawlimit" simulation, we chose the saturation value of the Atlas-type fit ($\alpha_{D_{\mathrm{eq}}}$) as an upper limit. This limit does not only affect the sedimentation but also all processes which depend on v_{term} (e.g., aggregation). In this way, the overestimation of m_{mean}, caused by an unlimited increase of v_{term}, can indeed be prevented, but the height profile of F_N and m_{mean} is not as well matched as with the Atlas-type approximation. As expected, the continuously increasing v_{term} in the unlimited power law leads to much stronger growth of aggregates as compared to relations which include the saturation velocity at large particle sizes. This is an interesting finding and could be one reason for the overestimation of radar reflectivities found at lower layers in ice clouds simulated with the Seifert-Beheng scheme (Heinze et al., 2017).

Although m_{mean} of the aggregates is much larger for the power law, the difference to the Atlas type in precipitation rates is very small (smaller than 5%; Figure 12d and Table 6). Note that in more realistic cases, as for example in presence of stronger sublimation layers, the difference in m_{mean} can induce larger differences in the precipitation rate because larger particles can fall through a thicker layer of subsaturated air before they sublimate completely.

6. Summary and Conclusions

In this study, we generated a large ensemble of ice aggregates (ca. 105,000 particles) using an aggregation model and hydrodynamic theory to study the change of particle properties such as mass m, projected area A, and terminal velocity v_{term} as a function of monomer number N_{mono} and size. The aggregates were composed of various monomers types (plates, dendrites, needles, and columns), monomer sizes, and monomer numbers. In order to test the impact of habit mixtures, we also included in our analysis two different mixtures of dendrites and columns. The choice of mixing specifically dendrites and columns was motivated by in situ observations of the composing monomers in large aggregates sampled on the ground (Lawson et al., 1998).

When comparing our aggregate properties with in situ observations, we find m and A to be very similar to the results presented in Mitchell (1996) but the slope of our $m{-}D_{\mathrm{max}}$ relations is larger than the slope given in Locatelli and Hobbs (1974). A better agreement with Locatelli and Hobbs (1974) and also with theoretical considerations in Westbrook et al. (2004b) is reached for mixtures of small columns and larger dendrites (Mix2). Interestingly, this monomer mixture also achieves the best agreement with observed $v_{\mathrm{term}}{-}D_{\mathrm{max}}$ relations. Considering the large spread in the observations (Figure 3), we can overall conclude that our aggregate ensemble matches the observed range of variability and does not show any substantial bias.

Our synthetic aggregate ensemble allowed us to investigate the transition of particle properties from single crystals to aggregates with increasing number of monomers in a level of detail which is currently unavailable from in situ observations. For m and A as a function of size, we find the relations to change rather smoothly with increasing N_{mono}. The differences introduced by the choice of the monomer type are found to be overall larger than due to the number of monomers. We find the exponents in the $A{-}D_{\mathrm{max}}$ and $m{-}D_{\mathrm{max}}$ relations of the monomers to be closely connected to the resulting change with N_{mono}.

The derived $A{-}D_{\mathrm{max}}$ and $m{-}D_{\mathrm{max}}$ relations including the monomer type and number dependence were then used to calculate $v_{\mathrm{term}}{-}D_{\mathrm{max}}$ relations. Again, we find a rather smooth transition from single crystals to aggregates rather than a “jump” as found in several microphysics schemes (Figure 1b). For small sizes below a few millimeters, our results suggests that the “ice” and “snow” category of microphysics schemes should have similar properties. At larger sizes, the aggregates v_{term} are found to deviate more from the monomers. Again, the monomer type is found to have a larger impact than the monomer number. Aggregates of plates tend to be faster, while aggregates of needles are slower than the equal-size monomer. In accordance to in situ observations, our simulations reveal for all aggregate types a saturation of v_{term} at centimeter sizes. However, the saturation value varies for the different aggregate types from 0.8 to 1.6 m s^{-1}.

In order to potentially implement our results in microphysics schemes, we derived two-parameter power-law fits and three-parameter Atlas-type fits for single monomers ($N_{\mathrm{mono}} = 1$) and aggregates ($N_{\mathrm{mono}} > 1$) representing the commonly used ice and snow classes in models. The new power-law fits match the small sizes well and avoid unrealistic “jumps” found in current schemes. However, the power laws are unable to represent the saturation of v_{term} at larger sizes. The Atlas-type fits are found to match the entire size range well and should thus be considered to be implemented in ice microphysics schemes as they do not substantially increase the computational costs while strongly improving the realism of the relations.

We finally tested the impact of implementing monomer dependence, habit type, and velocity fitting method on idealized aggregation simulations. For this, we used a new 1D Lagrangian Monte Carlo model which allowed us to implement the derived relations with different degree of complexity. The simulations experiments revealed that there is only a very small impact of using a relation of only two monomer categories (single particle and aggregate) as compared to a continuous monomer number dependence. A single category which does not take any monomer number into account shows slightly larger deviations, but the variability due to monomer type is in general larger than the impact of monomer number.

In a second simulation experiment, we investigated the impact of using a power law or an Atlas-type fit for v_{term}. The simulations show very small differences in the upper part of the cloud where the profiles are dominated by small particles which are fitted similarly well with the two relations. Once aggregation becomes more dominant and the spread of particles sizes shifts to larger sizes, the simulations using the power law lead to a much stronger aggregation and in particular stronger self-aggregation of particles as compared to the Atlas-type fit. The impact of the widely used power-law relations for v_{term} should thus be further studied for bulk schemes as it seems to be likely that they might cause an overestimation of aggregation and snow particle sizes.

We also shortly investigated the sensitivity of our derived relations to particle tumbling and the choice of the hydrodynamic theory. While tumbling can significantly affect the properties of single monomers, it has a surprisingly small effect on our results for the aggregates. The choice of the hydrodynamic theory is a larger source of uncertainty which should be further investigated in future studies. It seems to be important in the future to better constraint the composition of aggregates regarding the monomer type. This question could be approached by improved in situ techniques but also with detailed models that allow to predict the particle habit such as presented in (e.g., Jensen et al., 2017; Shima et al., 2019; Woods et al., 2007).

10.1029/2020MS002066

Table A1
Proportionality of the Best Number X on the Particle Properties (Mass m and Projected Area A), Scaling Relations of the v_{term}–D_{max} Relations and $s_{monodep}$ in Different Hydrodynamic Models (Böhm, 1992, B92; Heymsfield & Westbrook, 2010, HW10; Khvorostyanov & Curry, 2005, KC05)

	B92	HW10	KC05
$X\sim$	$mD_{\mathrm{max}}^{0.5}A^{-0.25}$	$mD_{\mathrm{max}}A^{-0.5}$	$mD_{\mathrm{max}}^{2}A$
$v_{\mathrm{term,Re}\ll1}\sim$	$D_{\mathrm{max}}^{b_m-0.25b_A-0.5}$	$D_{\mathrm{max}}^{b_m-0.5b_A}$	$D_{\mathrm{max}}^{b_m-b_A+1}$
$v_{\mathrm{term,Re}\gg1}\sim$	$\left(D_{\mathrm{max}}^{b_m-0.25b_A-1.5}\right)^{0.5}$	$\left(D_{\mathrm{max}}^{b_m-0.5b_A-1}\right)^{0.5}$	$\left(D_{\mathrm{max}}^{b_m-b_A}\right)^{0.5}$
$s_{\mathrm{monodep}}=$	$b_{m,\mathrm{agg}}-b_{m,1}$ $-0.25(b_{A,\mathrm{agg}}-b_{m,1})$	$b_{m,\mathrm{agg}}-b_{m,1}$ $-0.5(b_{A,\mathrm{agg}}-b_{A,1})$	$b_{m,\mathrm{agg}}-b_{m,1}$ $-(b_{A,\mathrm{agg}}-b_{A,1})$

Note. The derivation of the scaling relations is shown exemplary for B92 in section 2.2. s_{monodep}, which gives an estimate of the sign and strength of the dependency of v_{term} on N_{mono} is defined in section 4.3.

Appendix A

A.1. Video Disdrometer Data Set

The terminal velocity v_{term} of the simulated aggregates from this study is compared to recent observations of falling ice particle properties and frequently used literature in section 3.2. These surface observations are from the Centre for Atmospheric Research Experiments (CARE), Canada. It is a research facility of the Air Quality Research Branch of the Meteorological Service of Canada, located about 80 km north of Toronto, Ontario (lat = 44 13′58′′N, lon = 79 46′53′′W). The instrumentation includes a video disdrometer, PIP, precipitation weighing gauge, and meteorological measurements of, for example, wind velocity.

More detail about PIP can be found in von Lerber et al. (2017) and references therein. The particle sizes are recorded in the range of 0.2–26 mm (disk equivalent diameter) with a resolution of 0.2 mm, which is converted to the side projected D_{max}. In practice, the minimum reliable size with measurement of v_{term} is approximately 0.5 mm. Observations of the side projected maximum dimension $D_{\mathrm{max,side}}$ can be conducted from the grayscale video images. The velocity v_{term} is obtained from the observations of the consecutive frames. The observed v_{term} utilized in the Figures 1a, and 3c, and 3d are separated from the whole data set by limiting the exponent of the "5-min m−D relation" between 1.7 and 2.2 to exclude rimed particles (von Lerber et al., 2017). To apply this m−D threshold, the mass of the single particle and D_{max} has to be retrieved. The mass estimate of a single particle is calculated from the observed v_{term}, corrected D_{max}, and

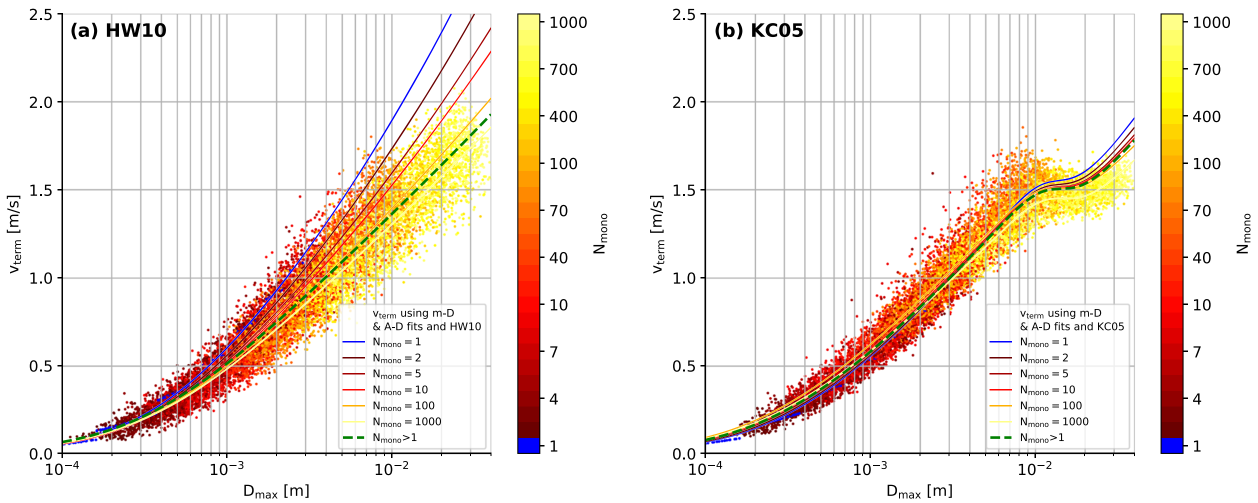

Figure A1. Same as Figure 7a (aggregates of plates) but using HW10 in (a) and KC05 in (b).

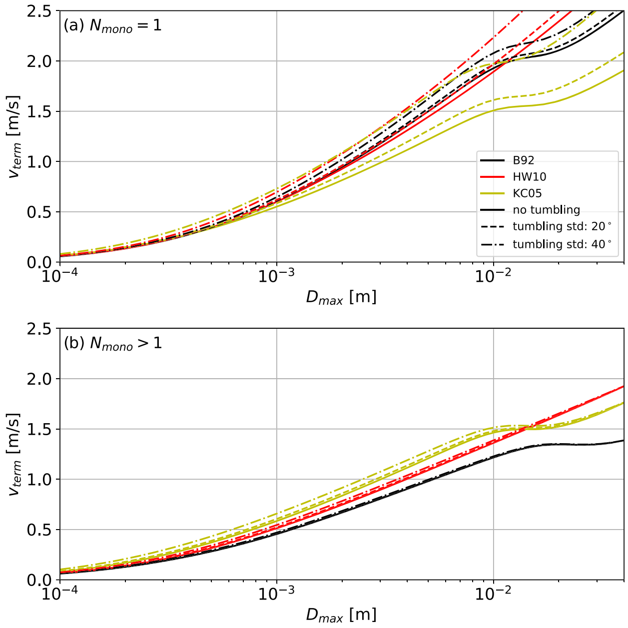

Figure A2. v_{term} based on m/A–D fits (Tables 1 and 4) and different hydrodynamic models. The particles are horizontally aligned ("no tumbling") rotated by 20° or 40° around the principal axis to mimic different strength of tumbling. (a) plate monomers; (b) aggregates of plates.

area ratio using different parametrizations of the hydrodynamic theory (Bohm, 1989; Heymsfield & Westbrook, 2010; Mitchell & Heymsfield, 2005). For each snowfall event, each of these parameterizations is calculated and the one which minimizes the error in the estimate of the liquid water equivalent precipitation with respect to the precipitation gauge is selected for that event. This procedure and the related uncertainties are described more in detail in von Lerber et al. (2017). Additionally, observations during 5-min intervals, where the mean horizontal wind speed exceeds 4 m s^{-1}, are excluded to reduce turbulence effects (similar to Brandes et al., 2008).

After applying these filters, the data set, which covers the winters from 2014 to 2017 with 48 snowfall events, contains about 4.3 million ice particles. It should be noted that PIP is providing a measurement of the ensemble of particles and no particle by particle-based classification is performed. Hence, the measurement volume includes mixtures of different habits.

A.2. Sensitivity of the Terminal Velocity to the Hydrodynamic Model and Tumbling

A.2.1. Hydrodynamic Models

As mentioned in section 2.2, the hydrodynamic models of B92, KC05, and HW10 differ in several aspects. The $Re(X)$ relation requires assumptions about particle surface roughness, which are differently implemented in the models. Also, the definition of X is different (Table A1). While in B92 X is proportional to $mD_{\mathrm{max}}^{0.5}A^{-0.25}$, X is proportional to $mD_{\mathrm{max}}A^{-0.5}$ in HW10 and $mD_{\mathrm{max}}^{2}A^{-1}$ in KC05. As a result in B92 and HW10, v_{term} increases slower with decreasing area ratio (A_r=$4A\pi^{-1}D^{-2}$) than in the formulation of KC05. The empirical correction of X due to wake turbulence is also applied in KC05 but not in HW10.

These differences affect the behavior of v_{term} at large sizes and the monomer number dependency (which we quantify by s_{monodep}). Without the empirical correction of X (which considers wake turbulence), v_{term} only saturates if $v_{\mathrm{term,Re}\gg 1}$~$D^0$. For example with HW10, the saturation would be reached for b_m−$0.5b_A$−1=0 (Table A1). This is, for example, not the case for aggregates of plates simulated in this study, and therefore, HW10 does not predict a saturation of v_{term} at larger sizes (Figure A1a).

Also, the sign and the strength of the increase/decrease of v_{term} with increasing N_{mono} depends on the formulation of X. In section 4.3, we introduced s_{monodep} as a measure for this monomer number dependency. Applying this measure to the aggregates of plates yields $s_{\mathrm{monodep}} = -0.21$ for HW10 and $s_{\mathrm{monodep}} = -0.06$ for KC05. Both HW10 and KC05 show the decrease of v_{term} with increasing N_{mono} which we saw when using B92, but this decrease is very weak for KC05.

A.2.2. Tumbling

To investigate the effect of the tumbling of the aggregates (as reported, e.g., by Garrett & Yuter, 2014) on the projected area A and v_{term}, the particles are tilted with a standard deviation of 0° , 20° , 40°, and 60° , around the principal axis (Figure A2). This is done only after the final aggregate is assembled and thereby does not influence the structure of the aggregates. This rotation reduces A, and in turn, v_{term} increases.

The monomers (top panel in Figure A2) are stronger effected by tumbling (especially at large D_{max}) due to their lower aspect ratio (not shown). The largest increase in v_{term} with increasing tumbling is found for KC05 due to the largest increase in the Best number with decreasing A (see section 2.2). B92 shows the least influence of tumbling, which increases v_{term} at maximum by about 0.1 m s^{-1} and has a negligible effect on v_{term} for the aggregates.

Table A2
Mean Absolute Error of the Normalizing Function f_m and f_A for the Monomer Number Dependent "monodep" Fits (Section 4.2) and the Power Law Fits (Section 4.4) for the Particle Mass m and Projected Area A

Monomer type	f_m monodep	f_m power law	f_A monodep	f_A power law
Plate	0.1190	0.1261	0.0816	0.0950
Needle	0.3737	0.4539	0.3926	0.5916
Dendrite	0.1698	0.1721	0.1575	0.1566
Column	0.2436	0.2456	0.2728	0.3343

A.3. Mean Absolute Error of the Mass and Area-Size Relations

In sections 4.2 and 4.4, we provided fit relations for mass and area with and without taking into account the monomer number dependency of the simulated aggregates. The mean absolute error of the fits shown in Tables 3 and 4 (normalized by the properties of the monomers; e.g., shown for plates with the green dotted lines in Figure 5) is shown in Table A2.

Acknowledgments

Contributions by M.K., S.K. and D.O. were funded by the German Research Foundation (DFG) under grant KN 1112/2-1 as part of the Emmy-Noether Group Optimal combination of Polarimetric and Triple Frequency radar techniques for Improving Microphysical process understanding of cold clouds (OPTIMIce). A.v.L. gratefully acknowledges the funding by the Deutsche Forschungsgemeinschaft (DFG, German Research Foundation) Project-ID 268020496 TRR 172, within the Transregional Collaborative Research Center "ArctiC Amplification: Climate Relevant Atmospheric and SurfaCe Processes, and Feedback Mechanisms (AC)^3". M. K. also acknowledges support by the Graduate School of Geosciences of the University of Cologne. The source code of McSnow used in this study is hosted at GitLab, and access can be granted by A. S. on request. We also thank Jussi Leinonen for fruitful discussions and for making his aggregation model freely available at GitHub (https://github.com/jleinonen/aggregation). We thank David Hudak and Peter Rodriguez from Environment Canada for providing the PIP measurement from the CARE site. The CARE site is part of the NASA GPM (Global Precipitation Measurement) Ground Validation (GV) program. Model output data of the aggregation model and McSnow are accessible at the ZENODO platform (https://doi.org/10.5281/zenodo.3606668). We also acknowledge the constructive comments of two anonymous reviewers, which helped to improve the manuscript.

References

Abraham, F. F. (1970). Functional dependence of drag coefficient of a sphere on Reynolds number. *Physics of Fluids*, *13*(8), 2194–2195. https://doi.org/10.1063/1.1693218

Atlas, D., Srivastava, R. C., & Sekhon, R. S. (1973). Doppler radar characteristics of precipitation at vertical incidence. *Reviews of Geophysics*, *11*(1), 1. https://doi.org/10.1029/RG011i001p00001

Bailey, M. P., & Hallett, J. (2009). A comprehensive habit diagram for atmospheric ice crystals: Confirmation from the laboratory, AIRS II, and other field studies. *Journal of the Atmospheric Sciences*, *66*(9), 2888–2899. https://doi.org/10.1175/2009JAS2883.1

Barthazy, E., Göke, S., Schefold, R., & Högl, D. (2004). An optical array instrument for shape and fall velocity measurements of hydrometeors. *Journal of Atmospheric and Oceanic Technology*, *21*(9), 1400–1416. https://doi.org/10.1175/1520-0426(2004)021 <1400:AOAIFS>2.0.CO;2

Barthazy, E., & Schefold, R. (2006). Fall velocity of snowflakes of different riming degree and crystal types. *Atmospheric Research*, *82*(1-2), 391–398. https://doi.org/10.1016/j.atmosres.2005.12.009

Bernauer, F., Hürkamp, K., Rühm, W., & Tschiersch, J. (2016). Snow event classification with a 2D video disdrometer—A decision tree approach. *Atmospheric Research*, *172-173*, 186–195. https://doi.org/10.1016/j.atmosres.2016.01.001

Bohm, H. P. (1989). A general equation for the terminal fall speed of solid hydrometeors. *Journal of the Atmospheric Sciences*, *46*, 2419–2427. https://doi.org/10.1175/1520-0469(1989)046<2419:AGEFTT>2.0.CO;2

Böhm, J. (1992). A general hydrodynamic theory for mixed-phase microphysics. Part I: Drag and fall speed of hydrometeors. *Atmospheric Research*, *27*(4), 253–274.

Brandes, E. A., Ikeda, K., Thompson, G., & Schönhuber, M. (2008). Aggregate terminal velocity/temperature relations. *Journal of Applied Meteorology and Climatology*, *47*(10), 2729–2736. https://doi.org/10.1175/2008JAMC1869.1

Brdar, S., & Seifert, A. (2018). McSnow: A Monte-Carlo particle model for riming and aggregation of ice particles in a multidimensional microphysical phase space. *Journal of Advances in Modeling Earth Systems*, *10*, 187–206. https://doi.org/10.1002/2017MS001167

Brown, S. R. (1970). Terminal velocities of ice crystals (*Tech. Rep.*) Fort Collins, Colorado: Department of Atmospheric Science Colorado State University.

Bürgesser, R. E., Giovacchini, J. P., & Castellano, N. E. (2019). Sedimentation analysis of columnar ice crystals in viscous flow regimes. *Quarterly Journal of the Royal Meteorological Society*, *146*, 426–437. https://doi.org/10.1002/qj.3684

Connolly, P. J., Emersic, C., & Field, P. R. (2012). A laboratory investigation into the aggregation efficiency of small ice crystals. *Atmospheric Chemistry and Physics*, *12*(4), 2055–2076. https://doi.org/10.5194/acp-12-2055-2012

Cornford, S. G. (1965). Fall speeds of precipitation elements. *Quarterly Journal of the Royal Meteorological Society*, *91*(387), 91–94. https://doi.org/10.1002/qj.49709138713

Dunnavan, E. L., Jiang, Z., Harrington, J. Y., Verlinde, J., Fitch, K., & Garrett, T. J. (2019). The shape and density evolution of snow aggregates. *Journal of the Atmospheric Sciences*, *76*(12), 3919–3940. https://doi.org/10.1175/JAS-D-19-0066.1

Frick, C., Seifert, A., & Wernli, H. (2013). A bulk parametrization of melting snowflakes with explicit liquid water fraction for the COSMO model. *Geoscientific Model Development*, *6*(6), 1925–1939. https://doi.org/10.5194/gmd-6-1925-2013

Garrett, T. J., Fallgatter, C., Shkurko, K., & Howlett, D. (2012). Fall speed measurement and high-resolution multi-angle photography of hydrometeors in free fall. *Atmospheric Measurement Techniques*, *5*(11), 2625–2633. https://doi.org/10.5194/amt-5-2625-2012

Garrett, T. J., & Yuter, S. E. (2014). Observed influence of riming, temperature, and turbulence on the fallspeed of solid precipitation. *Geophysical Research Letters*, *41*, 6515–6522. https://doi.org/10.1002/2014GL061016

Hashino, T., Cheng, K. Y., Chueh, C. C., & Wang, P. K. (2016). Numerical study of motion and stability of falling columnar crystals. *Journal of the Atmospheric Sciences*, *73*(5), 1923–1942. https://doi.org/10.1175/JAS-D-15-0219.1

Hashino, T., & Tripoli, G. J. (2011). The Spectral Ice Habit Prediction System (SHIPS). Part IV: Box model simulations of the habit-dependent aggregation process. *Journal of the Atmospheric Sciences*, *68*(6), 1142–1161. https://doi.org/10.1175/2011JAS3667.1

Heinze, R., Dipankar, A., Henken, C. C., Moseley, C., Sourdeval, O., Trömel, S., et al. (2017). Large-eddy simulations over Germany using ICON: A comprehensive evaluation. *Quarterly Journal of the Royal Meteorological Society*, *143*(702), 69–100. https://doi.org/10.1002/qj.2947

Heymsfield, A. J. (1972). Ice crystal terminal velocities. *Journal of the Atmospheric Sciences*, *29*(7), 1348–1357. https://doi.org/10.1175/1520-0469(1972)029<1348:ictv>2.0.co;2

Heymsfield, A. J., & Westbrook, C. D. (2010). Advances in the estimation of ice particle fall speeds using laboratory and field measurements. *Journal of the Atmospheric Sciences*, *67*(8), 2469–2482. https://doi.org/10.1175/2010JAS3379.1

Jakob, C. (2002). Ice clouds in numerical weather prediction models—Progress, problems and prospects (pp. 327–345). Cambridge; New York: Oxford University Press.

Jensen, A. A., Harrington, J. Y., Morrison, H., & Milbrandt, J. A. (2017). Predicting ice shape evolution in a bulk microphysics model. *Journal of the Atmospheric Sciences*, *74*(6), 2081–2104. https://doi.org/10.1175/JAS-D-16-0350.1

Jiang, Z., Verlinde, J., Clothiaux, E. E., Aydin, K., & Schmitt, C. (2019). Shapes and fall orientations of ice particle aggregates. *Journal of the Atmospheric Sciences*, *76*(7), 1903–1916. https://doi.org/10.1175/JAS-D-18-0251.1

Kajikawa, M. (1972). Measurement of falling velocity of individual snow crystals. *Journal of the Meteorological Society of Japan. Ser. II*, *50*(6), 577–584. https://doi.org/10.2151/jmsj1965.50.6_577

Khain, A. P., Beheng, K. D., Heymsfield, A. J., Korolev, A., Krichak, S. O., Levin, Z., et al. (2015). Representation of microphysical processes in cloud-resolving models: Spectral (bin) microphysics versus bulk parameterization. *Reviews of Geophysics*, *53*, 247–322. https://doi.org/10.1002/2014RG000468

Khvorostyanov, V. I., & Curry, J. A. (2005). Fall velocities of hydrometeors in the atmosphere: Refinements to a continuous analytical power law. *Journal of the Atmospheric Sciences*, *62*(12), 4343–4357. https://doi.org/10.1175/JAS3622.1

Kruger, A., & Krajewski, W. F. (2002). Two-dimensional video disdrometer: A description. *Journal of Atmospheric and Oceanic Technology*, *19*(5), 602–617. https://doi.org/10.1175/1520-0426(2002)019<0602:TDVDAD>2.0.CO;2

Langleben, M. P. (1954). The terminal velocity of snowflakes. *Quarterly Journal of the Royal Meteorological Society*, *80*(344), 174–181. https://doi.org/10.1002/qj.49708034404

Lawson, R. P., Stewart, R. E., & Angus, L. J. (1998). Observations and numerical simulations of the origin and development of very large snowflakes. *Journal of the Atmospheric Sciences*, *55*(21), 3209–3229. https://doi.org/10.1175/1520-0469(1998)055 <3209:OANSOT>2.0.CO;2

Leinonen, J., Kneifel, S., & Hogan, R. J. (2018). Evaluation of the RayleighGans approximation for microwave scattering by rimed snowflakes. *Quarterly Journal of the Royal Meteorological Society*, *144*, 77–88. https://doi.org/10.1002/qj.3093

Leinonen, J., & Moisseev, D. (2015). What do triple-frequency radar signatures reveal about aggregate snowflakes? *Journal of Geophysical Research: Atmospheres*, *120*, 229–239. https://doi.org/10.1002/2014JD022072

Leinonen, J., & Szyrmer, W. (2015). Radar signatures of snowflake riming: A modeling study. *Earth and Space Science*, *2*, 346–358. https://doi.org/10.1002/2015EA000102

Locatelli, J. D., & Hobbs, P. V. (1974). Fall speeds and masses of solid precipitation particles. *Journal of Geophysical Research*, *79*(15), 2185–2197. https://doi.org/10.1029/jc079i015p02185

Mitchell, D. L. (1996). Use of mass- and area-dimensional power laws for determining precipitation particle terminal velocities. *Journal of the Atmospheric Sciences*, *53*(12), 1710–1723. https://doi.org/10.1175/1520-0469(1996)053<1710:UOMAAD>2.0.CO;2

Mitchell, D. L., & Heymsfield, A. J. (2005). Refinements in the treatment of ice particle terminal velocities, highlighting aggregates. *Journal of the Atmospheric Sciences*, *62*(5), 1637–1644. https://doi.org/10.1175/JAS3413.1

Morales, A., Posselt, D. J., Morrison, H., & He, F. (2019). Assessing the influence of microphysical and environmental parameter perturbations on orographic precipitation. *Journal of the Atmospheric Sciences*, *76*(5), 1373–1395. https://doi.org/10.1175/JAS-D-18-0301.1

Morrison, H., Curry, J. A., & Khvorostyanov, V. I. (2005). A new double-moment microphysics parameterization for application in cloud and climate models. Part I: Description. *Journal of the Atmospheric Sciences*, *62*(6), 1665–1677. https://doi.org/10.1175/JAS3446.1

Morrison, H., & Milbrandt, J. A. (2015). Parameterization of cloud microphysics based on the prediction of bulk ice particle properties. Part I: Scheme description and idealized tests. *Journal of the Atmospheric Sciences*, *72*(1), 287–311. https://doi.org/10.1175/JAS-D-14-0065.1

Nakaya, U., & Terada, T. J. (1935). Simultaneous observations of the mass, falling velocity and form of individual snow crystals. *Journal of the Faculty of Science*, *1*(7), 191–200.

Nettesheim, J. J., & Wang, P. K. (2018). A numerical study on the aerodynamics of freely falling planar ice crystals. *Journal of the Atmospheric Sciences*, *75*(9), 2849–2865. https://doi.org/10.1175/JAS-D-18-0041.1

Newman, A. J., Kucera, P. A., & Bliven, L. F. (2009). Presenting the snowflake video imager (SVI). *Journal of Atmospheric and Oceanic Technology*, *26*(2), 167–179. https://doi.org/10.1175/2008JTECHA1148.1

Ori, D., Maestri, T., Rizzi, R., Cimini, D., Montopoli, M., & Marzano, F. S. (2014). Scattering properties of modeled complex snowflakes and mixed-phase particles at microwave and millimeter frequencies. *Journal of Geophysical Research: Atmospheres*, *119*, 9931–9947. https://doi.org/10.1002/2014JD021616

Pruppacher, H. R., & Klett, J. D. (1998). Microphysics of clouds and precipitation. *Aerosol Science and Technology*, *28*(4), 381–382. https://doi.org/10.1080/02786829808965531

Przybylo, V. M., Sulia, K. J., Schmitt, C. G., Lebo, Z. J., & May, W. C. (2019). The ice particle and aggregate simulator (IPAS). Part I: Extracting dimensional properties of ice-ice aggregates for microphysical parameterization. *Journal of the Atmospheric Sciences*, *76*(6), 1661–1676. https://doi.org/10.1175/JAS-D-18-0187.1

Sanderson, B. M., Piani, C., Ingram, W. J., Stone, D. A., & Allen, M. R. (2008). Towards constraining climate sensitivity by linear analysis of feedback patterns in thousands of perturbed-physics GCM simulations. *Climate Dynamics*, *30*(2-3), 175–190. https://doi.org/10.1007/s00382-007-0280-7

Schmidt, G. A., Bader, D., Donner, L. J., Elsaesser, G. S., Golaz, J. C., Hannay, C., et al. (2017). Practice and philosophy of climate model tuning across six US modeling centers. *Geoscientific Model Development*, *10*(9), 3207–3223. https://doi.org/10.5194/gmd-10-3207-2017

Schmitt, C. G., & Heymsfield, A. J. (2010). The dimensional characteristics of ice crystal aggregates from fractal geometry. *Journal of the Atmospheric Sciences*, *67*(5), 1605–1616. https://doi.org/10.1175/2009JAS3187.1

Schmitt, C. G., Sulia, K. J., Lebo, Z. J., Heymsfield, A. J., Przybyo, V., & Connolly, P. (2019). The fall speed variability of similarly sized ice particle Aggregates. *Journal of Applied Meteorology and Climatology*, *58*(8), 1751–1761. https://doi.org/10.1175/JAMC-D-18-0291.1

Seifert, A., & Beheng, K. D. (2006). A two-moment cloud microphysics parameterization for mixed-phase clouds. Part 1: Model description. *Meteorology and Atmospheric Physics*, *92*(1-2), 45–66. https://doi.org/10.1007/s00703-005-0112-4

Seifert, A., Blahak, U., & Buhr, R. (2014). On the analytic approximation of bulk collision rates of non-spherical hydrometeors. *Geoscientific Model Development*, *7*(2), 463–478. https://doi.org/10.5194/gmd-7-463-2014

Seifert, A., Leinonen, J., Siewert, C., & Kneifel, S. (2019). The geometry of rimed aggregate snowflakes: A modeling study. *Journal of Advances in Modeling Earth Systems*, *11*, 712–731. https://doi.org/10.1029/2018MS001519

Shima, S., Kusano, K., Kawano, A., Sugiyama, T., & Kawahara, S. (2009). The super-droplet method for the numerical simulation of clouds and precipitation: A particle-based and probabilistic microphysics model coupled with a non-hydrostatic model. *Quarterly Journal of the Royal Meteorological Society*, *135*(642), 1307–1320. https://doi.org/10.1002/qj.441

Shima, S., Sato, Y., Hashimoto, A., & Misumi, R. (2019). Predicting the morphology of ice particles in deep convection using the super-droplet method: Development and evaluation of SCALE-SDM 0.2.5-2.2.0/2.2.1. *Geoscientific Model Development*. https://doi.org/10.5194/gmd-2019-294

Szyrmer, W., & Zawadzki, I. (2010). Snow studies. Part II: Average relationship between mass of snowflakes and their terminal fall velocity. *Journal of the Atmospheric Sciences*, *67*(10), 3319–3335. https://doi.org/10.1175/2010JAS3390.1

Tiira, J., Moisseev, D. N., Von Lerber, A., Ori, D., Tokay, A., Bliven, L. F., & Petersen, W. A. (2016). Ensemble mean density and its connection to other microphysical properties of falling snow as observed in Southern Finland. *Atmospheric Measurement Techniques*, *9*(9), 4825–4841. https://doi.org/10.5194/amt-9-4825-2016

Tsai, T.-C., & Chen, J.-P. (2020). Multi-moment ice bulk microphysics scheme with consideration for particle shape and apparent density. Part I: Methodology and idealized simulation. *Journal of the Atmospheric Sciences*, *77*(5), 1821–1850. https://doi.org/10.1175/jas-d-19-0125.1

von Lerber, A., Moisseev, D., Bliven, L. F., Petersen, W. A., Harri, A. M., & Chandrasekar, V. (2017). Microphysical properties of snow and their link to Ze-S relations during BAECC 2014. *Journal of Applied Meteorology and Climatology*, *56*(6), 1561–1582. https://doi.org/10.1175/JAMC-D-16-0379.1

Westbrook, C. D., Ball, R. C., Field, P. R., & Heymsfield, A. J. (2004a). Theory of growth by differential sedimentation, with application to snowflake formation. *Physical Review E - Statistical Physics, Plasmas, Fluids, and Related Interdisciplinary Topics*, *70*(2), 7. https://doi.org/10.1103/PhysRevE.70.021403

Westbrook, C. D., Ball, R. C., Field, P. R., & Heymsfield, A. J. (2004b). Universality in snowflake aggregation. *Geophysical Research Letters*, *31*, L15104. https://doi.org/10.1029/2004GL020363

Westbrook, C. D., & Sephton, E. K. (2017). Using 3-D-printed analogues to investigate the fall speeds and orientations of complex ice particles. *Geophysical Research Letters*, *44*, 7994–8001. https://doi.org/10.1002/2017GL074130

Woods, C. P., Stoelinga, M. T., & Locatelli, J. D. (2007). The IMPROVE-1 storm of 1-2 February 2001. Part III: Sensitivity of a mesoscale model simulation to the representation of snow particle types and testing of a bulk microphysical scheme with snow habit prediction. *Journal of the Atmospheric Sciences*, *64*(11), 3927–3948. https://doi.org/10.1175/2007JAS2239.1

Zawadzki, I., Jung, E., & Lee, G. (2010). Snow studies. Part I: A study of natural variability of snow terminal velocity. *Journal of the Atmospheric Sciences*, *67*(5), 1591–1604. https://doi.org/10.1175/2010JAS3342.1

Zikmunda, J., & Vali, G. (1972). Fall patterns and fall velocities of rimed ice crystals. *Journal of the Atmospheric Sciences*, *29*(7), 1334–1347. https://doi.org/10.1175/1520-0469(1972)029<1334:fpafvo>2.0.co;2

4 CONSTRAIN BULK SCHEME PARAMETERIZATIONS

Karrer, M., Seifert, A., Ori, D., & Kneifel, S. (2021a). **Improving the Representation of Aggregation in a Two-moment Microphysical Scheme with Statistics of Multi-frequency Doppler Radar Observations**. *Atmospheric Chemistry and Physics*, https://doi.org/10.5194/acp-21-17133-2021

Atmos. Chem. Phys., 21, 17133–17166, 2021
https://doi.org/10.5194/acp-21-17133-2021

Atmospheric Chemistry and Physics
Open Access
EGU

Improving the representation of aggregation in a two-moment microphysical scheme with statistics of multi-frequency Doppler radar observations

Markus Karrer[1], **Axel Seifert**[2], **Davide Ori**[1], **and Stefan Kneifel**[1]

[1]Institute for Geophysics and Meteorology, University of Cologne, Cologne, Germany
[2]Deutscher Wetterdienst, Offenbach, Germany

Correspondence: Markus Karrer (markus.karrer@uni-koeln.de)

Received: 6 May 2021 – Discussion started: 1 July 2021
Revised: 14 September 2021 – Accepted: 20 October 2021 – Published: 25 November 2021

Abstract. Aggregation is a key microphysical process for the formation of precipitable ice particles. Its theoretical description involves many parameters and dependencies among different variables that are either insufficiently understood or difficult to accurately represent in bulk microphysics schemes. Previous studies have demonstrated the valuable information content of multi-frequency Doppler radar observations to characterize aggregation with respect to environmental parameters such as temperature. Comparisons with model simulations can reveal discrepancies, but the main challenge is to identify the most critical parameters in the aggregation parameterization, which can then be improved by using the observations as constraints. In this study, we systematically investigate the sensitivity of physical variables, such as number and mass density, as well as the forward-simulated multi-frequency and Doppler radar observables, to different parameters in a two-moment microphysics scheme. Our approach includes modifying key aggregation parameters such as the sticking efficiency or the shape of the size distribution. We also revise and test the impact of changing functional relationships (e.g., the terminal velocity–size relation) and underlying assumptions (e.g., the definition of the aggregation kernel). We test the sensitivity of the various components first in a single-column "snowshaft" model, which allows fast and efficient identification of the parameter combination optimally matching the observations. We find that particle properties, definition of the aggregation kernel, and size distribution width prove to be most important, while the sticking efficiency and the cloud ice habit have less influence. The setting which optimally matches the observations is then implemented in a 3D model using the identical scheme setup. Rerunning the 3D model with the new scheme setup for a multi-week period revealed that the large overestimation of aggregate size and terminal velocity in the model could be substantially reduced. The method presented is expected to be applicable to constrain other ice microphysical processes or to evaluate and improve other schemes.

1 Introduction

Ice growth processes which lead to precipitable particles are essential to understand because more than 60 % of the global precipitation reaching the surface is formed in the ice phase (Heymsfield et al., 2020). Besides depositional growth and riming, aggregation is one of the key growth mechanisms in ice clouds. Aggregation is found to be active in a large temperature range (Hobbs et al., 1974; Kajikawa and Heymsfield, 1989; Field, 2000). As revealed, for example, by radar observations (e.g., Barrett et al., 2019), aggregation can cause a rapid increase in the particle size in favorable conditions, such as the dendritic growth zone close to $-15\,^{\circ}$C or close to the melting layer (Lamb and Verlinde, 2011). Unlike depositional growth, sublimation, or riming, aggregation does not directly modify the ice and snow water content. However, its strong influence on particle shape, particle size distribution, and terminal velocity v_t links aggregation to other processes, such as depositional growth, sublimation, and riming, that alter the mass flux considerably. Therefore, it is important to accurately represent aggregation in microphysical schemes.

A central component of the theoretical description of aggregation (see also Sect. 3.1) is the aggregation kernel. Therefore, many challenges in accurately simulating aggregation can be discussed by considering the various components of this kernel. The aggregation kernel is defined analogously to collision–coalescence of droplets in liquid clouds.

$$K(D_i, D_j) = \frac{\pi}{4}(D_i + D_j)^2 |v_t(D_i) - v_t(D_j)| \\ E_{coll}(D_i, D_j) E_{stick}(T) E_{i,j}(D_i D_j) \quad (1)$$

The aggregation kernel is proportional to the probability K of two particles i and j colliding (Gillespie, 1975) and sticking together after collision. This probability increases with increasing size D and relative v_t of the particles, as well as the collision E_{coll} and sticking efficiency E_{stick}. Obviously, the size D is well-defined for spherical particles by their diameter, but this is already much more complex for ice and snow particles which have a nonspherical shape. How large v_t of ice and snow particles is also strongly depends on their size, shape, and orientation (Böhm, 1992; Mitchell and Heymsfield, 2005; Heymsfield and Westbrook, 2010). For smaller particles, v_t increases strongly, but the increase in v_t flattens with size and finally v_t approaches a constant value of $1\,m\,s^{-1}$ for centimeter-sized aggregates (Lohmann et al., 2016). The size ranges in which v_t increases most rapidly (i.e., has the largest slope) are highly shape-dependent (Barthazy and Schefold, 2006; Hashino and Tripoli, 2011; Karrer et al., 2020). Consequently, the slope of the v_t–size relation is uncertain but at the same time crucial for aggregation. Two remaining parameters, E_{coll} and E_{stick}, are also multiplicative in the kernel. E_{coll} describes the ratio between the actual collision cross section and the geometric cross section. E_{coll} is smaller than 1 for most particle pairs because typically the smaller and slower particle is deflected due to hydrodynamics as the larger particle approaches. For ice collisions, E_{coll} is generally poorly constrained (Wang, 2010). This can be easily understood given the enormous variety of particle shapes and orientation, leading to very complex flow fields. In the temperature region most relevant for aggregation ($T > -20\,°C$), the number of activated ice-nucleating particles (INPs) and hence also the concentration of small ice particles rapidly decrease with increasing temperature (Kanji et al., 2017). Except for small ice particles generated by secondary ice production, the effect of small ice particles being deflected around larger particles might therefore be less important for aggregation. In fact, many bulk microphysical schemes (e.g., Seifert and Beheng, 2006) assume the bulk E_{coll} to be 1.

E_{stick} is the probability of two ice particles sticking after the collision. Although laboratory (Hosler and Hallgren, 1960; Connolly et al., 2012; Phillips et al., 2015) and in situ (Mitchell, 1988; Kajikawa and Heymsfield, 1989) estimates, as well as multi-frequency radar retrievals (Barrett et al., 2019) of E_{stick} exist, the exact value of E_{stick} and its dependency on parameters such as temperature or supersaturation are very uncertain. However, there is widespread agreement in the literature on two main temperature ranges in which E_{stick} is enhanced: around $-15\,°C$, the mechanical interlock of dendrites increases E_{stick} compared to the surrounding temperature regions (Pruppacher et al., 1998). In addition, sintering of ice particles due to an increasingly thick quasi-liquid layer (Slater and Michaelides, 2019) on the ice surface causes a general increase in E_{stick} when temperature rises up to $0\,°C$. In addition to the aggregation kernel, the aggregation rate is also influenced by the particle size distribution. Simply put, the particles that have a high probability of aggregation, given by the aggregation kernel, must be present in the cloud to have efficient aggregation.

Bulk microphysics schemes cannot simulate aggregation on an individual particle level but require the calculation of bulk aggregation rates. Analytic solutions for the bulk aggregation rates are in principle possible (Verlinde et al., 1990). However, these solutions are computationally expensive and require the usage of power-law relationship for v_t and size, which cannot represent the asymptotic behavior known from observations for large sizes. Approximations of the bulk aggregation rates consider characteristic velocity differences (Wisner et al., 1972; Seifert and Beheng, 2006) and allow the use of more complex v_t–size relations, which consider the asymptotic behavior of v_t at large sizes and nonspherical particle shapes (Seifert et al., 2014).

In general, we need to distinguish between three different aspects of uncertainty in aggregation simulations: (1) a general lack of understanding or quantification of parameters, such as the absolute values of E_{stick}; (2) formulation of functional relationships, which cannot adequately represent the whole relevant range (e.g., v_t–size relationship); and (3) simplifications that must be made to keep the computational cost affordable, e.g., considering only bulk properties of the particle population. Because of these uncertainties, it is important to constrain the model by observations of aggregation in clouds.

In situ and remote sensing observations have provided valuable information on the general characteristics of aggregation and have allowed estimation of the relative importance of aggregation with respect to other processes. Decades ago, observations had already reported that the largest aggregates are found around $-15\,°C$, which is considered to be a consequence of mechanical interlocking of dendrites, and at temperatures a few degrees below $0\,°C$, which is related to the quasi-liquid layer (Lamb and Verlinde, 2011).

Radar observations contain valuable information about the aggregation process, which also is the reason we rely on them in this study. The strong temperature dependence of aggregation observed in early studies could be confirmed by radar observations, especially in profiles of absolute and differential reflectivity (Kennedy and Rutledge, 2011; Andrić et al., 2013; Schrom and Kumjian, 2016; Moisseev et al., 2015). By additionally considering the mean Doppler velocity, the relative importance of aggregation and riming can be estimated (Mosimann, 1995; Mason et al., 2018; Kneifel et al., 2020). Furthermore, using radars of different frequencies allows for the estimation of mean particle size (Matrosov, 1998; Hogan et al., 2000; Liao et al., 2005; Szyrmer and Zawadzki, 2014; Kneifel et al., 2015) and therefore better characterization of temperatures at which aggregation is dominant.

Ori et al. (2020, O20) evaluated ice particle growth in simulations of the Icosahedral Nonhydrostatic Model (Zängl et al., 2015, ICON) using the Seifert–Beheng two-moment microphysics scheme (Seifert and Beheng, 2006, SB06) by comparing it with measurements in observational space. To this end, O20 used the multi-month cloud radar dataset from Dias Neto et al. (2019, D18). This quality-controlled dataset is particularly suitable because it contains multi-frequency and Doppler-measured data and thus fingerprints of aggregation and sedimentation. While model–observation comparisons based on a single or few cases can be difficult to interpret due to the specific conditions (specific water vapor field, synoptic situation, etc.) of the case, the statistical comparison of O20 could reveal model-inherent mean biases. The comparison of models and observations in the radar space using a radar forward operator simplifies the assessment of uncertainties because the deviations between models and observations can be directly compared to the variability of the observations. The alternative approach of applying a retrieval to the observations might seem more intuitive because microphysical variables, such as number density, can be compared directly. However, ensuring consistency between a model and retrieval as well as tracing the propagation of uncertainties, for example in the observables or the forward model, is often more complicated (e.g., Reitter et al., 2011).

O20 found an overall correct temperature dependency of aggregation but also revealed an overestimation of the snow size and v_t at temperatures above $-7\,°C$. O20 suggested that inaccurate E_{stick} and v_t–size parameterization might cause this overestimation. However, direct attribution of the observed biases (e.g., snow that is too large) to a specific component of the aggregation process (e.g., E_{stick}) requires simultaneous investigation of the influence of all parameters relevant for the aggregation process in a suitable modeling setup.

Microphysics schemes are usually tuned to improve the prediction of key variables, such as precipitation, the energy balance at the top of the atmosphere, or the near-surface temperature (Schmidt et al., 2017; Morrison et al., 2020). Only a small subset of variables (e.g., v_t of cloud ice) are varied during the tuning process, and tuning might be ad hoc rather than evidence-based. As the models simulate complex interacting processes, several parameter combinations can improve the predicting skill of modeled variables such as precipitation. Therefore, it is likely that tuning introduces compensating errors. For example, if two parameters are not accurately implemented, adjusting one of them might improve the model performance even when the adjustment leads away from the true value of the parameter. Detailed remote sensing observations can be used to adjust parameters and make improvements on the process level rather than improving the performance of the entire modeling system. However, because remote sensing observations are sensitive to a limited number of parameters and within a limited range of variability, there is a risk that model parameters may be adjusted to match observations well but still be inaccurate in regimes wherein these observations have low sensitivity. To reduce this risk, new methods for model improvement and development have been proposed whose parameter selection is still based on physical constraints, namely theory and laboratory measurements, but can be optimized by Bayesian inference of observations (Morrison et al., 2020). The advantage of this approach is that uncertainty of both laboratory measurements and remote sensing observations can be considered, and new knowledge about parameters can be continuously incorporated. The combination of several radar observables, such as multiple frequencies, Doppler spectra, and polarimetry, allows the observed signatures to be assigned to a specific microphysical process under some conditions (Kneifel et al., 2015; Kalesse et al., 2016; Pfitzenmaier et al., 2018; Barrett et al., 2019). For example, Barrett et al. (2019) focused their multi-frequency study on the dendritic growth zone, where aggregation is known to be particularly efficient. Hence, the rapidly changing size-dependent, multi-frequency variables could be clearly related to aggregation and a retrieval of E_{stick} could be obtained.

In addition, novel cloud radar techniques, e.g., multi-frequency Doppler observations, enable the identification of key growth mechanisms (Kneifel et al., 2015; Kalesse et al., 2016; Pfitzenmaier et al., 2018; Barrett et al., 2019). Barrett et al. (2019) identified a temperature range in which aggregation rapidly increases particle size and estimated E_{stick} from a retrieval using multi-frequency Doppler spectra. Identifying a dominant growth mechanism allows focusing on a single process, which simplifies the inverse problem by reducing the number of parameters and observables to be considered simultaneously.

In this study, we constrain the parameters that influence aggregation by confronting idealized and realistic simulations with the multi-frequency Doppler radar observations from D18. The methods used are described in Sect. 2. We revise all main parameters and functional relationships regarding the aggregation formulation in SB06 by incorporating recently published parameters and revising the bulk aggregation equations. We describe these parameters and formulations in Sect. 3.1 and compare them with the choices in the default SB06 scheme. In Sect. 3.1.5 the selection of the snow particle properties, which is a critical component of both aggregation and radar simulations, is described. The sensitivity of the aggregation and associated radar variables to individual parameters of the revised formulation is evaluated with an ensemble of 1D model simulations (Sect. 3.2). The optimal combination of these simulations is chosen and tested in sensitivity studies in ICON-LEM simulations (Sect. 3.3). Finally, we perform ICON-LEM simulations of several weeks, which we evaluate against the default simulations from O20 and the observations from D18 (Sect. 3.4). This approach allows testing many different parameters against observed statistics of several weeks in a numerically efficient way. Section 4 summarizes the approach and draws conclusions regarding the following questions: how can we investigate the sensitivity of aggregation to the components of its parameterization? How can we improve the representation of aggregation in a two-moment microphysical scheme? Which microphysical parameters influence the simulation of aggregation the most?

2 Methods

The Icosahedral Nonhydrostatic Model (ICON; Zängl et al., 2015) has numerous applications due to its different configurations. ICON-NWP (ICON numerical weather prediction) is used by the Deutscher Wetterdienst (DWD) for operational weather forecast in a global and recently also in all regional setups. ICON's large-eddy mode is called ICON-LEM (Dipankar et al., 2015; Heinze et al., 2017). We use the SB06 two-moment microphysics scheme instead of the single-moment scheme currently used in operational weather forecasting, as do most studies that perform simulations with ICON-LEM. Since simulations with ICON-LEM are relatively computationally expensive, we also use a simple 1D model to efficiently test different parameterizations and their influence on the simulation.

Since we want to further investigate the causes and reduce the discrepancies between modeled and simulated observables, we use the same simulation setup of ICON-LEM as in O20. We only briefly describe the setup here, since an extensive description can be found in O20. The modifications we make to the SB06 microphysics scheme are described in detail in Sect. 3.1.

2.1 "Snowshaft" model

Simple 1D models have been used to assess the influence of several parameters or processes on microphysical or observed quantities (e.g., precipitation rates, polarimetric variables) and to test new parameterizations (Seifert, 2008; Kumjian and Ryzhkov, 2010; Milbrandt and Morrison, 2016; Paukert et al., 2019). These models are much simpler than full 3D models (like ICON-LEM) and are therefore also referred to as rain-shaft models. Because we apply such a simple model to ice microphysics we use the term "snowshaft" model. In these simple models, the atmospheric variables (e.g., temperature gradient, relative humidity) are predefined and feedback mechanisms from microphysics to thermodynamic and thus dynamic variables are neglected. These simplifications allow the analysis of selected processes and their sensitivity to a range of parameters without having to consider the full range of complexity. Another advantage of the snowshaft model is the low computational effort, which allows testing a large number of parameter combinations and process formulations.

The snowshaft model has 250 layers and the temperature spans the range from 0 to $-40\,^{\circ}$C, which covers the most relevant range for precipitating ice clouds. The temperature profile is linear with a gradient of $0.0062\,\mathrm{K\,m^{-1}}$. Consequently, the top of the model is at 6450 m. The relative humidity with reference to ice (RH_i) is constant for $h > 3000\,\mathrm{m}$ and increases linearly until it reaches $\mathrm{RH} = 100\,\%$ (RH is the relative humidity with reference to water; Fig. B5). The thermodynamic variables are constant in time and there is no air motion. These simplifications can be justified by the nearly stationary nature of many clouds and the low vertical velocity seen in the dataset of D18.

At the top of the model, a gamma distribution (following the size distribution parameter as described in Table 3) is initialized for cloud ice and snow. Together with the size distribution parameter, the mass density Q and the number density N completely define the size distribution at the model top. Below the model top, the size distribution evolves through the following microphysical processes: sedimentation, depositional growth, and aggregation. These processes are considered dominant below the cloud top (where nucleation is especially important) and above temperatures near the melt layer, where riming rates increase sharply (Kneifel and Moisseev, 2020). The values of RH_i, Q, and N are chosen in Sect. 3.2.1 to match profiles of observables with substantial precipitation.

2.2 ICON-LEM setup

In our simulations, we use a small domain setup of ICON-LEM. This setup has been shown to be both computationally efficient and to represent clouds well in various conditions (Marke et al., 2018; Schemann and Ebell, 2020; Schemann et al., 2020). The domain is circular with a radius of 110 km, and the observational site Jülich Observatory for Cloud Evolution Core Facility (JOYCE-CF; Löhnert et al., 2015) is in the center. At JOYCE the TRIple-frequency and Polarimetric radar Experiment for improving process observation of winter precipitation (Tripex, D18) took place, which we use in the model–observation comparison. The horizontal grid spacing of the simulations is ca. 400 m, and the vertical grid spacing ranges from 20 m at the surface to 380 m at the model top. With a total of 150 vertical layers, the atmosphere is simulated up to a height of 21 km. Initial and lateral boundary conditions are taken from the ECMWF Integrated Forecasting System (IFS). Initialization is carried out each day at 00:00 UTC. IFS data are incorporated as forcing on the lateral boundary every hour.

2.3 SB06 scheme

The SB06 scheme is used in the snowshaft simulations (Sect. 3.2) and as the microphysics scheme in the ICON-LEM simulations (Sect. 3.3 and 3.4). The SB06 scheme is a two-moment scheme that simulates the evolution of the number ($N = M^{(0)}$) and mass density ($L = M^{(1)}$) from which the mixing ratio ($Q = L \cdot \rho_{\mathrm{air}}^{-1}$) can be easily derived. ρ_{air} is the air density and M^n (Eq. 2) represents the moments of the mass distribution (Eq. 5).

$$M^{(n)} = \int_0^\infty m^n f(m) dm \tag{2}$$

The scheme simulates six different hydrometeor classes (cloud water, cloud ice, rain, snow, graupel, and hail). The conversion from one class to another is in general associated with a specific microphysical process. For example, if cloud ice forms aggregates, Q and N of cloud ice are converted to snow (Sect. 3.1). Therefore, it is consistent to assume properties of monomers for cloud ice and properties of aggregates for snow. The predefined particle properties of the default setting of the scheme are listed in Table 2 for each hydrometeor, along with the properties of the cloud ice and snow class alternatives proposed in Sect. 3.1.

In the SB06 scheme, aggregation rates are the product of collision rates and E_{stick} because E_{coll} is assumed to be 1. In the scheme, the variance approximation (SB06), based on the work of Wisner et al. (1972), provides a computationally feasible analytical solution of bulk collision rates. The variance approximation of Seifert and Beheng (2006) avoids the usage of pre-calculated lookup tables (Seifert et al., 2014) and, unlike Wisner et al. (1972), is able to estimate collision rates of self-collection, i.e., aggregation within a particle class. The latter is made possible by considering the square root of the second moment of the velocity differences, which also has the advantage over the approximation by Wisner et al. (1972) that the collision rates between different particles are nonzero even if their bulk velocities are equal. The default SB06 scheme assumes power-law relations for the v_{t}–size relation in the calculation of the collision rates. The extension of the variance approximation of Seifert et al. (2014), which allows using Atlas-type v_{t}–size relations (Sect. 3.1.3), is applied in the SB06 scheme for the first time in this study.

Details of the components of the aggregation process considered in the SB06 scheme can be found in Sect. 3.1 and Appendix A.

2.4 Passive and Active Microwave radiative TRAnsfer tool (PAMTRA)

The Passive and Active Microwave radiative TRAnsfer tool (PAMTRA; Mech et al., 2020) is used to simulate synthetic radar observations. Microphysical properties are represented consistently in the SB06 scheme and PAMTRA (Table 2).

Throughout the study, we adopt the same scattering assumptions for each of the hydrometeor classes in the SB06 default scheme (“SB cloud ice”, “SB snow”, “cloud droplet”, “rain”, “graupel”, and “hail” in Table 2). As in O20, we apply the self-similar Rayleigh–Gans approximation (SSRGA; Hogan and Westbrook, 2014; Hogan et al., 2017) and coefficients derived from 3D models of aggregates of plates for cloud ice and aggregates of needles for snow. In O20, the coefficients used for the snow class were slightly adjusted to closely match the observed triple-frequency signature. The SSRGA parameters of aggregates of plates are also used for the new cloud ice categories (“column” and “needle” in Table 2). For Mix2, SSRGA parameters derived from the same 3D models used for the determination of particle properties (Karrer et al., 2020, K20) are available (Ori et al., 2021). Since we find little influence of SSRGA parameters in Sect. 3.1.5, we use the adjusted SSRGA properties of the aggregates of needles from O20 for the Mix2 aggregates throughout the study to be consistent with 020, although using the SSRGA parameters derived from the same 3D aggregate models would be most physically consistent.

2.5 Multi-frequency radar approach

Like O20, we use multi-frequency observations to derive information about the aggregation process. Multi-frequency observations are useful to distinguish the size of particles, since the ratio of wavelength and particle size along with the particle density are the main factors that determine their scattering properties. The scattering of particles much smaller than the wavelength can be approximated well by the Rayleigh approximation. For larger particles, however, the interference of waves scattered from different parts of the particles must be considered (Kneifel et al., 2020), which leads to differential scattering among the various frequencies.

The ratio between the reflectivities of two radars with operating wavelengths λ_1 and λ_2 ($\lambda_1 < \lambda_2$),

$$\mathrm{DWR}_{\lambda_1,\lambda_2} = \frac{\mathrm{Ze}(\lambda_1)}{\mathrm{Ze}(\lambda_2)} = \frac{\lambda_1^4 \int \sigma_b(m,\lambda_1) f(m) dm}{\lambda_2^4 \int \sigma_b(m,\lambda_2) f(m) dm}, \tag{3}$$

quantifies the amount of differential scattering. DWR is called the dual-wavelength ratio, Ze is the reflectivity, and σ_b is the backscattering cross section (all variables in linear units). Although differential attenuation can also contribute to DWR (Battaglia et al., 2020), we did not include this effect in Eq. (3) because the processing of D18 already corrects for the impact of differential attenuation on DWR.

D18 evaluated the absolute calibration of the observed Ze values from the Ka-band radar using disdrometer measurements during rainfall. After correcting differential attenuation due to gases at all three frequencies, the Ka-band radar was then used as a reference for estimating calibration biases and differential attenuation effects due to hydrometeors by comparing the three Ze values at cloud top. The DWRs caused by differential scattering are usually close to 0 dB for small ice particles present at the cloud top. Calibration biases can be identified as DWR biases which are relatively constant over time; differential attenuation effects due to supercooled liquid water, rainfall, or the melting layer vary more strongly on shorter timescales (minutes to hours). The path-integrated differential attenuation estimated at cloud top was then used to correct the DWRs in the entire profile. A more in-depth discussion of various correction methods for multi-frequency radar observations is provided in Tridon et al. (2020). If differential scattering effects are the only contributor to DWR, it correlates well with the mean mass of the distribution $f(m)$ (Sect. 3.1.1), as can be seen from Eq. (3). For small particles, the Rayleigh approximation is valid for all frequencies and σ_b scales with the mass squared. However, for larger particles and shorter wavelengths, σ_b is smaller than predicted by the Rayleigh approximation and $\sigma_b(m,\lambda_2)$ is smaller than $\sigma_b(m,\lambda_1)$. As a result, particle populations that contain larger particles, e.g., due to their large mean mass, have larger DWRs than particle populations with smaller mean masses. Mason et al. (2019) and others have shown that not only the mean mass, but also the shape of the distribution, the particle density, and the internal structure of the particles (through σ_b) can substantially affect the DWRs. Given the radars available in D18, we investigate the sensitivity of aggregation by analyzing $\mathrm{DWR}_{\mathrm{X,Ka}}$ and $\mathrm{DWR}_{\mathrm{Ka,W}}$. The subscripts W, Ka, and X denote the radar bands and, more specifically, the wavelengths of 3.3, 8.6, and 31 mm. Each combination of wavelengths is sensitive to a different range of particle sizes. For example, $\mathrm{DWR}_{\mathrm{Ka,W}}$ is most sensitive to mean particle sizes of unrimed cloud ice and snow between 0.5 and 3 mm, and $\mathrm{DWR}_{\mathrm{X,Ka}}$ is sensitive between 1.5 and 15 mm (O20). Outside this sensitivity range, DWRs are zero (small mean size) or asymptotically approach (saturate) a DWR value (large mean sizes) that depends on the scattering properties of the particles present. More detailed information on the approach and its sensitivities can be found in O20.

Moreover, D18 reported that strong riming is rare in their dataset, so aggregation is the main contributor to particle growth and thus the increasing DWRs from cloud top to cloud bottom.

3 Results and discussion

3.1 Ice microphysical parameters influencing aggregation

To interpret the following sensitivity experiments, we describe which parameters need to be considered in the simulation of aggregation in a bulk scheme, which parameters and process formulations are currently used in the SB06 scheme, and how the assumptions could be updated with recently published parameterizations.

The stochastic collection equation (SCE) describes how the particle distribution (PSD_m) changes with time under the action of aggregation (Khain et al., 2015).

$$\frac{\partial f(m_i)}{\partial t} = \int\limits_0^{m_i/2} f(m_j) f(m_i - m_j) K(m_i - m_j, m_j) dm_j - \int\limits_0^{\infty} f(m_i) f(m_j) K(m_i, m_j) dm_j \tag{4}$$

Here, $f(m)$ is the particle distribution as a function of mass and K is the aggregation kernel described in Sect. 3.1.2. The first term of Eq. (4) describes the gain of particles of mass m_i by aggregation of particles with masses m_j and $m_i - m_j$. The second term considers the loss of particles of mass m_i by aggregation with particles of mass m_j (illustrated in Fig. 1a and b). In general, PSDs cannot be perfectly described by simple functional relationships (e.g., gamma distribution) but can have complex shapes (Fig. 1a). Thus, explicit prediction of the evolution of PSDs must take into account the full SCE.

Bulk schemes, however, can only account for the evolution of the PSD in a simplified form. The tendencies of the moments in the SB06 scheme (mass density: $\partial Q/\partial t$, number density: $\partial N/\partial t$) can be calculated by considering only the loss term. The reason for this can be further explained by Fig. 1c–h, where the collision events are separated among the ice (monomers) and snow (aggregates) classes. In fact, because of the mass conservation, the total mass of particles gained (integral of the first term) has to match the total mass of particles lost (integral of the second term). Since it is assumed that within one time step a particle can participate only in one collision event, only one snow particle results from the collision of two ice particles (number of arrows in Fig. 1c and d). The same applies for the ice–snow and snow–snow collisions, but here there is no conversion of N from one category to another but only a loss of N_i or N_s. Thus, it is sufficient to calculate only one collision rate for each of the three considered collision scenarios (ice–ice, ice–snow, snow–snow) and moments (N and Q).

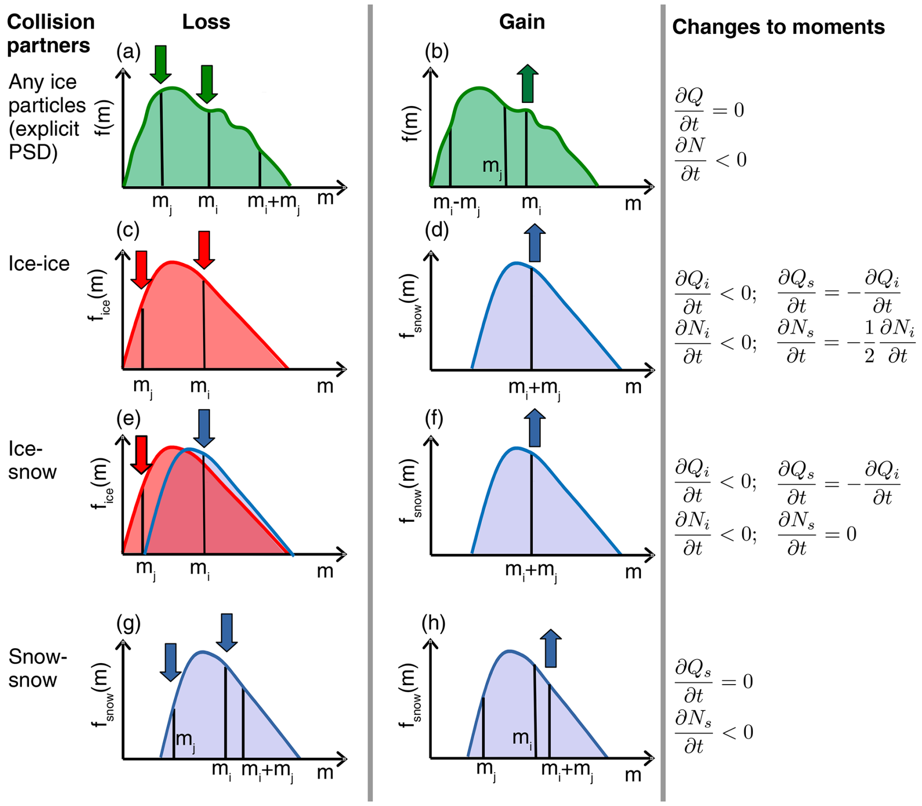

Figure 1. Illustration of the SCE (Eq. 4) for an explicitly resolved PSD$_m$ **(a, b)** and when applied to the cloud ice and snow classes of the SB06 scheme **(c, h)**. The left column depicts the loss term (second term in Eq. 4) and the middle column the gain term (first term in Eq. 4). The right column shows the sign and connection of the tendency of the bulk moments. Arrows indicate whether the number density is rising or falling at the specified mass. Red lines indicate the ice distribution and blue the snow distribution. The arrows are red if ice particles are collected and blue if snow particles are collected or are created as a result of the collision.

3.1.1 Size distribution

In most bulk schemes, the PSD is described by the generalized gamma distribution or simplifications thereof. With the mass m as a primary variable, the generalized gamma distribution can be written as

$$f_m(m) = N_{0,m}\, m^{\nu_m} \exp(-\lambda_m m^{\mu_m}). \tag{5}$$

For some applications, using the mass-equivalent diameter

$$D_{\mathrm{eq}} = \left(\frac{6m}{\pi \rho_{\mathrm{w}}}\right)^{1/3} \tag{6}$$

as a primary variable and the ordinary gamma distribution is more convenient:

$$f(D_{\mathrm{eq}}) = N_{0,\mathrm{eq}}\, D_{\mathrm{eq}}^{\mu_{\mathrm{eq}}} \exp(-\lambda_{\mathrm{eq}} D_{\mathrm{eq}}), \tag{7}$$

where D_{eq} is the mass-equivalent diameter. One such application is the use of the Atlas-type v_{t}–size relationship (Eq. 11) in the calculation of collision rates in Appendix A. Size distributions derived from in situ observations are usually presented as a function of the maximum dimension D_{max}, which is often derived by circumscribing a sphere or spheroid to the projected particle image.

$$f(D_{\mathrm{max}}) = N_{0,\mathrm{max}}\, D_{\mathrm{max}}^{\mu_{\mathrm{max}}} \exp(-\lambda_{\mathrm{max}} D_{\mathrm{max}}) \tag{8}$$

In general, a distribution described by Eq. (5) cannot be expressed by Eq. (7) or (8). Only when $\mu_m = 1/3$ can Eq. (5) be expressed by Eq. (7). To allow conversion of Eq. (5) to (8), μ_m must be set to b_m^{-1} (exponent in the m–D_{max} relation; Eq. 12). As we calculate the collision rates of particles following an Atlas-type v_{t}–size relation (Appendix A), we need to set $\mu_m = 1/3$. Since $b_m \neq 3$ for cloud ice and snow, μ_{max} in Eq. (8) can only be approximated.

The PSD shape can vary strongly, e.g., for nonstationary events (Seifert, 2008). Furthermore, ν_m, or equivalent parameters in distributions that use a different primary variable, is often described as a function of other parameters (e.g., the mean size; Heymsfield, 2003). Nevertheless, in the current version of the SB06 scheme, we must choose a single value of ν_m in each simulation. Therefore, we test two different values of ν_m in the simulations and later (Sect. 3.2) select the one with which the simulations can reproduce the observations the best. The SB06 standard configuration ($\nu_m = 0$) cor-

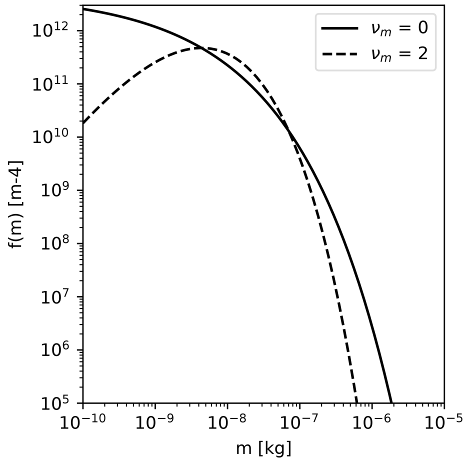

Figure 2. Particle distribution as a function of mass (PSD$_m$) with a mass density of $q = 2 \times 10^{-4}\,\mathrm{kg\,m^{-3}}$ and a number density of $qn = 10^4\,\mathrm{m^{-3}}$ illustrating PSDs with a different shape parameter μ_m.

responds to $\mu_{\mathrm{eq}} = 2.0$ and $\mu_{\max} = -0.11$. If we use $\nu_m = 2$ instead of $\nu_m = 0$, we obtain a narrower distribution with much fewer particles at small masses and a peak near the mean mass. Considering Heymsfield (2003), $\nu_m = 0$ is representative of a mean mass diameter D_{mean} of about 0.5 mm, and ν_m=2 is representative for D_{mean} of about 0.2 mm. Many studies have shown that the size distribution parameters are correlated (e.g., Field et al., 2005; Mcfarquhar et al., 2015), further complicating the selection of ν_m. Moreover, PSDs can exhibit bimodalities, e.g., due to secondary ice generation (Korolev and Leisner, 2020), which can be accounted for by the two classes of cloud ice and snow in the SB06 scheme.

The PSD width affects the aggregation rates and the radar variables. The narrower the distribution is, the lower the aggregation rates are. This is obvious from the bulk collision rates in Appendix A and can be explained by the small v_{t} difference of similarly sized particles (Sect. 3.1.2). The PSD width also affects the radar observables. The reflectivity in the Rayleigh regime is proportional to the second moment of the PSD. A narrower distribution reduces the number of large particles (above 10^{-7} kg in Fig. 2). Therefore, the reflectivity (Ze) and mean Doppler velocity (MDV) are slightly lower for a narrower distribution compared to a broader distribution with the same Q and N. This effect is even stronger for DWRs, as the large particles contribute the most to the differential scattering signal (Table 1).

3.1.2 Collision kernel

The D-kernel (Eq. 1), defined analogously to the collisional coalescence of droplets in liquid clouds, is often used not only for particles that can be approximated well by spheres (e.g., cloud droplets, hail), but for all particles. However, the collision cross section of nonspherical particles is smaller than the one of spheres with the same $D_{\max}$ because of the presence of voids in their circumscribing sphere. This deviation was previously considered, e.g., a part of E_{coll} (Keith and Saunders, 1989; Pruppacher and Klett, 2010) by using the equivalent circular radii $r_i = (A_i/\pi)^{0.5}$ as a characteristic length. Using the D-kernel with a constant E_{coll} that does not depend on particle size (as done, e.g., in SB06), the D-kernel approximation cannot account for the decrease in A_{r} with increasing size (Fig. 3d). Therefore, we test whether an alternative formulation of the collision kernel that takes the projected areas into account (A-kernel; Connolly et al., 2012) provides a better approximation.

$$K(D_i, D_j) = \left(A_i(D_i)^{0.5} + A_j(D_j)^{0.5}\right)^2$$
$$|v_i(D_i) - v_j(D_j)|E_{\mathrm{stick}}(T)E_{\mathrm{coll}}(D_i, D_j) \quad (9)$$

The A-kernel approximation has been used previously in the same or similar formulation (Kienast-Sjögren et al., 2013; Morrison and Milbrandt, 2015; Dunnavan, 2021). In these studies, the aggregation rates are calculated numerically and, in the case of the scheme proposed by Morrison and Milbrandt (2015), stored in lookup tables that are used at the model run time. Lookup tables can accurately store precomputed process rates and might be numerically more efficient than analytical solutions, depending on the computer architecture, size of the lookup table, and complexity of the analytical solution. However, Seifert et al. (2014) argue that the use of lookup tables also has disadvantages, like increasing complexity during preprocessing, additional memory access, and difficult reproducibility for follow-up studies. To avoid these disadvantages, the SB06 scheme uses analytical solutions of the variance approximation introduced by Seifert and Beheng (2006). To use the A-kernel we have to generalize the collision rates. For brevity, we moved the lengthy derivations to Appendix A. To our knowledge, this is the first application of an A-kernel in a bulk microphysics scheme that uses an analytical formulation of the aggregation rates. How large the difference is between the D- and the A-kernel depends on the particle properties (e.g., area–size and v_{t}–size relation).

3.1.3 Particle properties

Particle properties influence aggregation because they are an essential part of the aggregation kernel. According to Eqs. (1) and (9) collection is enhanced if the product of the difference in v_{t} and the joint cross section is large. Thus, a particle population will aggregate rapidly if the mean mass is relatively large and particles with largely different v_{t} are present. The coefficients of area–size and v_{t}–size relations of the SB06 default scheme and the particle from K20 are included in Table 2.

While the particle properties of the SB06 default scheme particle classes are taken from in situ observations, K20 used an aggregation model and hydrodynamic theory to simulate

Table 1. Size distribution parameter for $\mu_m = 1/3$, the mass–size relationship of the Mix2 particles (Table 2), $q = 2 \times 10^{-4}\,\mathrm{kg\,m^{-3}}$, and $N = 10^4\,\mathrm{m}^4$ (same as Fig. 2). $\mathrm{Ze_{Ka}}$, $\mathrm{MDV_{Ka}}$, and $\mathrm{DWR_{X,Ka}}$ are calculated using the self-similar Rayleigh–Gans approximation (SSRGA) and the SSRGA parameters of Mix2 as provided by Ori et al. (2021). $\mu_{\max}$ is estimated by the zeroth, third, and sixth moment of the distribution.

ν_m	μ_{eq}	$\mu_{\max}$	$\mathrm{Ze_{Ka}}$ [dBz]	$\mathrm{MDV_{Ka}}$ [m/s]	$\mathrm{DWR_{X,Ka}}$ [dB]	$\mathrm{DWR_{Ka,W}}$ [dB]
0.0	2.0	−0.11	12.11	0.91	1.21	3.89
2.0	8.0	2.19	9.83	0.83	0.02	1.12

the particle properties. The advantages of this approach are that particle properties can be studied over a large size range, are physically consistent, and can be studied in great detail. Particle property relations from in situ observations have a comparably small sample size. Thus, extrapolation to small and large sizes is unavoidable because microphysics schemes need information about particle properties in a large size range. This extrapolation might lead to inaccuracies, such as the overestimation of v_t at large sizes (K20). Since we take all snow particle properties (m–size, A–size, v_t–size; Table 2) from the same aggregate type within the dataset, all properties are physically consistent. By comparing with in situ observations, K20 found that their mixed aggregates consisting of small columns and large dendrites (Mix2) can approximate mean aggregate properties well. Besides aggregates (including aggregates of columns and aggregates of dendrites; Sect. 3.1.5), K20 also summarized different monomer particle properties, e.g., the columns and needles shown in Fig. 3.

v_t of the default cloud ice and snow class increases continuously with increasing size (Fig. 3) due to the power-law relation used.

$$v_t = a_{\mathrm{vel}} m^{b_{\mathrm{vel}}} \tag{10}$$

Due to this continuous increase, the self-collection rates of these hydrometeor classes stay relatively large at large sizes (Figs. B3 and B4). In contrast, the asymptotic approach to a limit of v_t in the new relations leads to rapidly decreasing collision rates at large sizes. The asymptotic approach is evident from in situ observations and can be accounted for by using an Atlas-type v_t–size relation.

$$v_t = \alpha_v - \beta_v \exp(-\gamma_v D_{\mathrm{eq}}) \tag{11}$$

The relative v_t of cloud ice and snow particles also plays a role in ice–snow collection rates. In the SB06 default scheme, v_t of cloud ice and v_t of snow differ greatly. However, K20 showed that v_t of cloud ice and snow should have similar values. The difference between cloud ice and snow v_t determines the location and magnitude of the minimum of the collection rates.

The projected area A is derived differently in the D- and the A-kernel. In the D-kernel, the m–$D_{\max}$ relation,

$$m = a_m D_{\max}^{b_m}, \tag{12}$$

determines the relation between A and size. Since m is the primary variable in the SB06 scheme, it is most useful to consider the differences between the kernels and the particle classes as a function of D_{eq} (which is directly related to the mass).

$$A_{\mathrm{sphere}} = \frac{\pi}{4} D_{\max}^2 = \frac{\pi}{4} \left(\frac{\pi \rho_{\mathrm{w}} D_{\mathrm{eq}}^3}{6 a_m} \right)^{\frac{2}{b_m}} \tag{13}$$

Thus, the particles which have the lowest effective density,

$$\rho_{\mathrm{eff}} = \frac{6m}{\pi \rho_{\mathrm{ice}} D_{\max}^3}, \tag{14}$$

have the largest A for a given D_{eq} (e.g., needles of K20 in Fig. 3b). The other particles have similar A. In the A-kernel, the actual projected area A_{act} derived from the particle shape is relevant.

$$A_{\mathrm{act}} = \gamma_A D_{\mathrm{eq}}^{\sigma_A} \tag{15}$$

The particle shapes and thus A_{act} are not defined for the SB06 default classes because this property is not required. The area ratio A_r is commonly defined as the ratio of A_{act} to the area of a sphere with diameter $D_{\max}$.

$$A_r = \frac{4 \gamma_A D_{\mathrm{eq}}^{\sigma_A}}{\pi D_{\max}^2} \tag{16}$$

At small sizes, A_r is close to 1, indicating compact particles and small differences between the D- and the A-kernel (Fig. 3d). With increasing size, A_r decreases down to 0.2 at $D_{\mathrm{eq}} = 5$ mm for the Mix2 class and lower for the cloud ice classes needle and column. A_{act} is similar to observations of Mitchell (1996) as shown in K20.

However, the low values of A_r of the cloud ice classes are less important because such large sizes of cloud ice are rarely reached in the model. The decrease in A_r leads to a decrease in collision rates, especially at large sizes, similar to the Atlas-type v_t–size relations. Thus, combining the new v_t–size relations with the A-kernel substantially decreases collision rates at large sizes.

While the properties of snow can be validated well against mean observed quantities (as done in K20 and in Sect. 3.1.5 of this study), selecting a single habit for cloud ice is a strong simplification that is necessary for a simplified microphysics scheme.

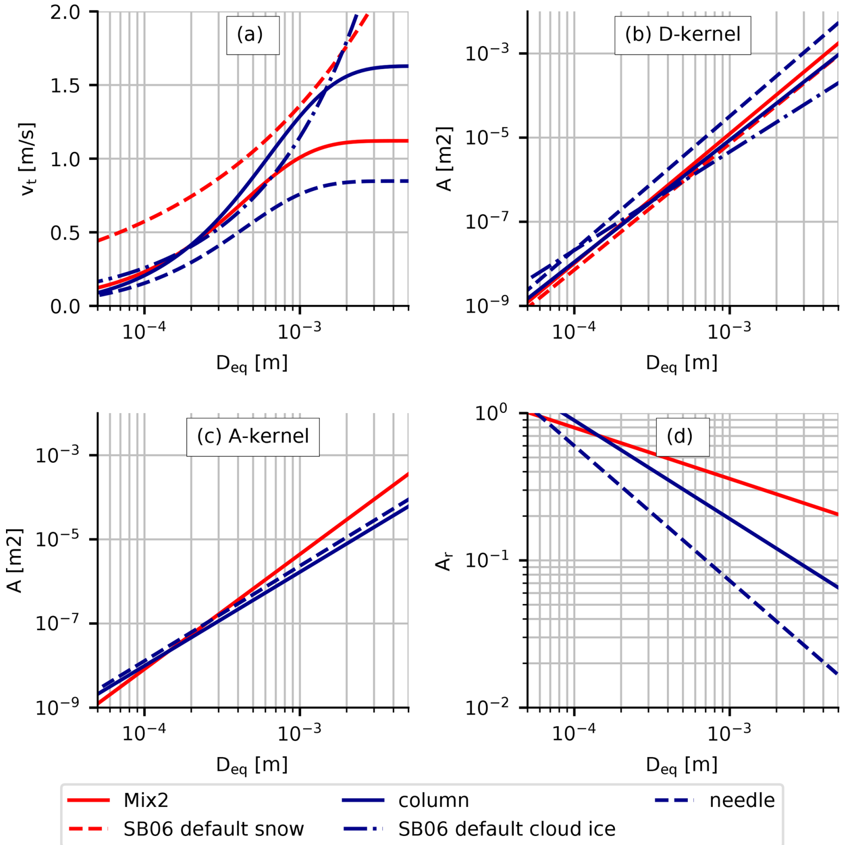

Figure 3. Particle properties from the default (SB06 default cloud ice, SB06 default snow) and modified version (column, needle, Mix2) of the scheme. **(a)** Terminal velocity v_t, **(b)** projected area A of a circumscribing sphere (as assumed in D-kernel), **(c)** "real" projected area A considering the voids in the circumscribing sphere (as assumed in A-kernel), and **(d)** area ratio (Eq. 16). The default scheme does not assume an A–D relation explicitly, and therefore the real projected area and the area ratio are not given.

3.1.4 Sticking efficiency

The parameters discussed so far determine how often collisions occur. The percentage of the colliding particles that stick together after a collision is defined by the sticking efficiency E_{stick}.

E_{stick} is mostly only described as a function of the temperature (Mitchell, 1988; Connolly et al., 2012, M88, C12). To stick to each other, ice particles must form ice bonds (Lamb and Verlinde, 2011), which is highly unlikely for colliding solid-ice particles when the temperature is well below the melting temperature and the particles only touch for a short time. There are two main mechanisms that increase the likelihood of adhesion after a collision and explain the temperature dependence. The first mechanism is explained by the quasi-liquid layer (QLL) on the ice particle surface. The phenomenon of QLL has been studied since the mid-19th century (Slater and Michaelides, 2019). QLL thickens with increasing temperature and consists of weakly bound molecules on the particle surface (Slater and Michaelides, 2019). When two particles touch, the molecules form a solid bond at the point of contact. The second mecha-

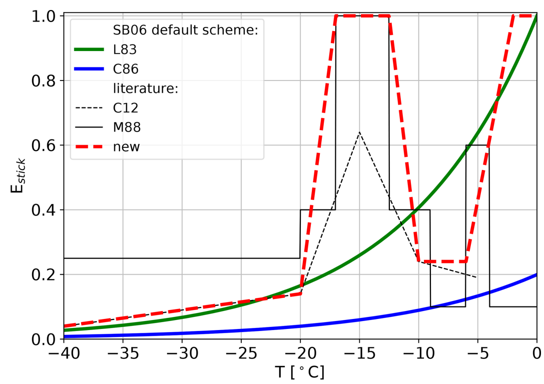

Figure 4. The sticking efficiency (E_{stick}) in the SB06 scheme for collisions among ice particles (ice self-collection) follows L83; for other collisions (ice–snow collection, snow self-collection) it applies the C86 parameterization. Our new relation (red) combines the relations from M88 and C12 with a characteristic maximum around $-15°$ C and values quickly approaching unity for temperature larger than $-5°$ C.

Table 2. Parameterizations used in ICON-LEM, the snowshaft model, and radar forward simulations of hydrometeor properties in PAMTRA. D represents the particle maximum dimension and $D_{\mathrm{eq}} = \left(\frac{6\,\mathrm{m}}{\pi\,\rho_{\mathrm{w}}}\right)^{1/3}$ the mass-equivalent diameter; m is the particle mass and ρ_{w} the density of water. The mass–size (m–D), terminal velocity v_{t}–size, and projected area–size (A–D) relations are reported in their full mathematical form. For the SSRGA scattering model, the four parameters (κ, β, γ, ζ_0) are given in parentheses. SB indicates that the properties are exclusively used in the default setup. Cloud droplets, rain, graupel, and hail (which are only relevant for the 3D simulations) follow the same properties in all simulations. The aspect ratio is 1.0 for all classes except for the snow classes (SB snow, Mix2, and Mix2; O20 scat), for which an aspect ratio of 0.6 is assumed. All variables are in SI units.

Hydrometeor classes	m–D	A–D	v–D	Scattering
SB cloud ice	$1.588D_{\mathrm{max}}^{1.56}$	–	$30.6D_{\mathrm{max}}^{0.55}$	SSRGA(0.18,0.89,2.06,0.08)
Column	$0.046D_{\mathrm{max}}^{2.07}$	$8.21D_{\mathrm{eq}}^{2.23}$	$1.63-1.67\mathrm{e}^{-1586D_{\mathrm{eq}}}$	SSRGA(0.18,0.89,2.06,0.08)
Needle	$0.0047D_{\mathrm{max}}^{1.89}$	$13.97D_{\mathrm{eq}}^{2.26}$	$1.41-1.43\mathrm{e}^{-1650D_{\mathrm{eq}}}$	SSRGA(0.18,0.89,2.06,0.08)
SB snow	$0.038D_{\mathrm{max}}^{2.0}$	–	$5.51D_{\mathrm{max}}^{0.25}$	SSRGA(0.25,1.00,1.66,0.04)
Mix2 (O20 scat)	$0.017D_{\mathrm{max}}^{1.95}$	$685.93D_{\mathrm{eq}}^{2.73}$	$1.12-1.19\mathrm{e}^{-2292D_{\mathrm{eq}}}$	SSRGA(0.25,1.00,1.66,0.04)
Mix2	$0.017D_{\mathrm{max}}^{1.95}$	$685.93D_{\mathrm{eq}}^{2.73}$	$1.12-1.19\mathrm{e}^{-2292D_{\mathrm{eq}}}$	SSRGA(0.22,0.60,1.81,0.11)
Aggregates of columns	$0.074D_{\mathrm{max}}^{2.15}$	$69.34D_{\mathrm{eq}}^{2.50}$	$1.583-1.6\mathrm{e}^{-1419D_{\mathrm{eq}}}$	SSRGA(0.23,1.45,2.05,0.02)
Aggregates of dendrites	$0.027D_{\mathrm{max}}^{2.22}$	$367.91D_{\mathrm{eq}}^{2.53}$	$0.88-0.895\mathrm{e}^{-1393D_{\mathrm{eq}}}$	SSRGA(0.23,0.75,1.88,0.10)
Cloud drop	$\frac{\pi}{6}\rho_{\mathrm{w}}D_{\mathrm{max}}^{3}$	–	$2.49\times10^{7}D_{\mathrm{max}}^{2}$	Mie
Rain	$\frac{\pi}{6}\rho_{\mathrm{w}}D_{\mathrm{max}}^{3}$	–	$9.3-9.6\mathrm{e}^{-622.2D_{\mathrm{eq}}}$	Mie
Graupel	$500.86D_{\mathrm{max}}^{3.18}$	–	$406.7D_{\mathrm{max}}^{0.85}$	soft-sphere Mie
Hail	$392.33D_{\mathrm{max}}^{3.0}$	–	$106.3D_{\mathrm{max}}^{0.5}$	soft-sphere Mie

nism is the mechanical interlocking of relatively large particles with dendritic features (Pruppacher et al., 1998). These dendritic features occur at temperatures between −17 and −12 °C.

The SB06 default scheme uses the E_{stick} parameterization of Cotton et al. (1982) for ice–ice collisions and Lin et al. (1983) for ice–snow and snow–snow collisions (Fig. 4). The exponential shape of both parameterizations can be justified by the approximately exponentially increasing QLL thickness. These relations, however, miss the maximum of E_{stick} suggested by studies (M88, C12) that consider the mechanical interlocking mechanism.

We combine M88 and C12 to propose a new parametrization. For $T < -20\,°\mathrm{C}$ we follow C12, then linearly approach the plateau proposed by M88 with $E_{\mathrm{stick}} = 1$ between −17 and −12 °C. As discussed in the Introduction, there is ample evidence from both in situ and remote sensing observations that E_{stick} is likely to be present at temperatures near −15 °C (at which particles with dendritic features are present) and near the melt boundary. At −10 °C the new parameterization again follows C12 but increases towards 1 at higher temperatures, at which C12 does not provide an estimate of E_{stick}. One might prefer to follow C12 rather than M88, since C12 derived E_{stick} directly from laboratory measurements and M88 provided only an ad hoc parameterization. However, C12 analyzed only the initial stage of aggregation, during which few monomers compose the aggregates. The interlocking mechanism might be more efficient for more complex aggregates compared to early aggregates as discussed in C12. Even considering only the initial stage of aggregation, the confidence interval of E_{stick} at −15 °C ranges from 0.35 to 0.85 (C12).

3.1.5 Selecting a particle type representative for a large aggregate ensemble

After discussing the various components of the aggregation process formulation, we need to decide which aggregate type to use to best represent the physical particle properties (e.g., v_{t}) and scattering properties. In O20, the particle properties were defined by the assumptions in the standard SB06 scheme. The best-fitting aggregate model and associated SSRGA parameters were selected based on the best fit in the triple-frequency DWR space. In this section, we ask whether there is an aggregate type in the database of K20 and Ori et al. (2021) that reproduces both the physical and scattering properties well compared to the observations.

O20 already noted that the representation of MDV as a function of DWR resembles to some extent the underlying v_{t}–size relation. In contrast to the triple-frequency DWR-DWR, the MDV-DWR space is rather insensitive to the PSD width. Different aggregate types composed of different monomer types generated and studied in K20 are used to simulate their corresponding MDV-DWR signatures (Fig. 5). The underlying distribution shows the observed values from D18, which naturally contain larger scatter and even negative DWR values, mainly due to imperfect radar volume matching (for a detailed discussion, see D18). Fortunately, as shown in D18, the dataset contains only very short and weak riming events. This scarcity of substantial riming is

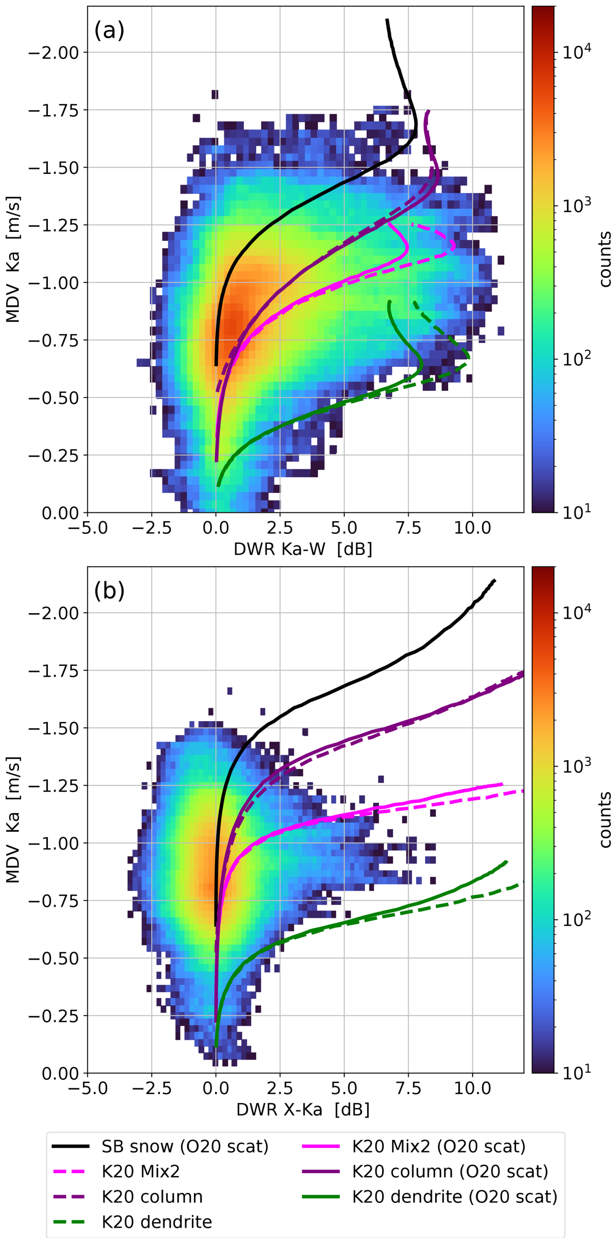

Figure 5. Comparison of the modeled and observed relationship between MDV and DWR: **(a)** $\mathrm{DWR_{Ka,W}}$, **(b)** $\mathrm{DWR_{X,Ka}}$. The histogram shows the observations from the Tripex campaign (D18). The lines show the theoretical MDV at a given DWR for the v_t size relations of snow particles as assumed in the SB default (black) and as modeled in K20. For the dashed lines, the SSRGA parameters have been directly derived from the corresponding aggregate ensemble properties (as found in Ori et al., 2021). The solid lines use SSRGA parameters as used in O20 in order to illustrate the uncertainty due to the scattering parameters. The lines are calculated using PAMTRA and the properties of the US standard winter atmosphere at 700 hPa.

important because the increased MDV due to riming would bias our comparison. Moderately or strongly rimed particles would exceed $1.5\,\mathrm{m\,s^{-1}}$ upon reaching a size that results in a nonzero $\mathrm{DWR_{Ka,W}}$ (Mason et al., 2018). The MDV-DWR space is also well-suited to evaluate our aggregate choice, as it combines the two radar variables that showed the largest discrepancies with the model simulations in O20.

O20 already recognized the overestimation of v_t at large sizes, which is also evident in Fig. 5. For example, at $\mathrm{DWR_{X,Ka}} = 5\,\mathrm{dB}$ the observed MDV scatters around $1\,\mathrm{m\,s^{-1}}$, while the snow falls at $1.7\,\mathrm{m\,s^{-1}}$ in the SB06 default scheme. From the aggregate dataset of K20 the aggregates of dendrites fall the slowest and the aggregates of columns fall the fastest. A mixture composed of small columns and large dendrites (Mix2), which fit in situ observations (K20) best, also matches the observations in the MDV-DWR space well. Therefore, we utilize the Mix2 aggregate properties as an improved description for the snow class in the following.

Interestingly, the use of the SSRGA coefficients of the aggregate type O20 does not lead to a strong change in the curves in the MDV-DWR space. Although it would be most consistent to use the SSRGA coefficients of Mix2 directly, we will use the scattering properties of O20 in the following analysis to allow a fair comparison of our new results with the discrepancies found in O20.

3.2 Exploring sensitivity to microphysical parameters in the snowshaft model

The snowshaft model (Sect. 2.1) allows us to test the influence of the particle properties, the formulation of the collision kernel, E_{stick}, and the size distribution on the aggregation rates with low computational effort and with reduced complexity. In Sect. 3.1 we showed how these parameters affect aggregation. We not only examine the influence of the parameters on the predicted model variables but also on the radar observables. After carefully setting up the model, the comparison in radar space enables us to directly contrast the statistics of the simulation and the observations, as given in O20 and D18. Since we compare the statistics of the model and observations over a relatively long time range this analysis already attempts to select a combination of parameters that can reproduce the observational statistics well. The optimal parameter combinations found in the snowshaft simulations will then be applied in the 3D model to simulate a case study (Sect. 3.3) before we use it to rerun simulations for the whole time period of the Tripex campaign (Sect. 3.4).

This comparison between the model and observation benefits from the simultaneous consideration of multiple model parameters and multiple observables. When looking at a single observable only, one might reduce a bias by an adjustment of a single process or parameter, even though this might just compensate for an inaccurate choice in another parameter, introducing compensating errors. As the number of independent observables increases, this problem is reduced as the inaccurate choice of a parameter might be detectable in one of the remaining observables. In other words, the larger degree of freedom in the observations helps to better constrain the parameters by comparison with the model when several observables are considered. We focus our comparison on the DWRs (as a measure of particle size) and the MDV (as a measure of v_t). These two quantities constrain the strength of aggregation and the assumed v_t–size relationship, and the statistical comparison in O20 also revealed the largest differences between observations and the model in these variables.

3.2.1 Optimizing the snowshaft model and selecting microphysical parameters for new setup

O20 pointed out that the inconsistencies between observed and synthetic MDV and DWRs are especially evident for raining periods. As we attempt to remove these inconsistencies, the atmospheric variables and the hydrometeor contents at the top of the simulation are chosen so that the hydrometeor profiles in the snowshaft simulation roughly follow the profiles of the ICON-LEM simulations from O20 wherein RR is larger than $1\,\mathrm{mm\,h^{-1}}$; compare "default" and the histogram in Fig. 6. To match the profiles the RH_i has to be set to 1 % above about $-18\,°\mathrm{C}$ with increasing values up to about 6 % at about $-7\,°\mathrm{C}$. These values of RH_i, which are relatively high compared to those from the ICON-LEM simulations (Fig. B5), might be necessary because of the absence of nucleation and advection in the snowshaft simulations. Also, the values of Q_i, N_i, Q_s, and N_s at the model top are chosen so that the hydrometeor profiles of the CTRL simulation (performed with the SB06 default setup) match those of the profiles of the ICON-LEM simulations of O20 with $\mathrm{RR} > 1\,\mathrm{mm}$ (Fig. 6). After this optimization of the snowshaft model, the simulated profiles from ICON-LEM (O20 and Figs. 11 and 12) and the snowshaft model (Figs. 6) reveal that a simple initialization (nucleation) of the profiles at cloud top is sufficient at least for testing the sensitivities of aggregation to our set of parameters and various formulations.

After iterating over many parameter combinations, we found one particular setup (which we refer to as colMix2_Akernel or simply as NEW) to match the observed profiles particularly well. In these iterations, we varied mostly the less-known components, e.g., the size distribution width, while parameters that we were already better able to constrain (Sect. 3.1.5), e.g., the v_t size relation, were not varied. Our approach can hence be seen as a combination of a purely physically based approach, incorporating current knowledge of parameters obtained, e.g., through laboratory studies, and an empirical correction based on observations.

3.2.2 Sensitivity of aggregation to individual ice microphysical parameters in the snowshaft model

The hydrometeor profiles (Fig. 6) and radar observables (Fig. 7) of the NEW setup exhibit many interesting differences from the profiles of the CTRL run. In the following, we discuss where the differences originate from by looking at the different sensitivity runs. In each sensitivity run only one set of parameters is different from the NEW run (Table 3).

The cloud ice mixing ratio Q_i and the cloud ice number density N_i are lower in the NEW run than in the CTRL run for $T < -10\,°\mathrm{C}$ (Fig. 6). At the same time, the snow mixing ratio Q_s and number density N_s are slightly larger in the NEW run at temperatures below $-17\,°\mathrm{C}$. These differences can be explained by the higher E_stick at lower temperatures in the NEW setup (Fig. 4), which leads to more collisions among cloud ice particles, and therefore more particles are converted from the cloud ice to the snow category. When using the E_stick parameterization of Cotton et al. (1982) and Lin et al. (1983) (colMix2_Akernel_LinCot;), Q_i and N_i are larger at lower temperatures (and Q_s and N_s are smaller).

The smaller values of E_stick in colMix2_Akernel_LinCot compared to NEW at lower temperatures (compare L83 and C86 with "new" in Fig. 4) lead to further differences; colMix2_Akernel_LinCot has a smaller mean mass $\overline{x}$, which is the mean mass of the sum of the cloud ice and snow class $((Q_i + Q_\mathrm{s})(N_i + N_\mathrm{s})^{-1})$, and correspondingly lower DWRs for $T < -7\,°\mathrm{C}$ (Fig. 7c and d). The smaller mean size also leads to slower-falling particles (visible in MDV; Fig. 7b). For $T > -7\,°\mathrm{C}$ the strong increase in E_stick in colMix2_Akernel_LinCot triggers a strong increase in $\overline{x}$ and $\mathrm{DWR}_\mathrm{X,Ka}$. A similar increase in the mean and median of the investigated statistics of $\mathrm{DWR}_\mathrm{X,Ka}$ was already discussed in O20. As in O20 the strong increase is not visible in $\mathrm{DWR}_\mathrm{Ka,W}$, since this observable already reaches saturation for mass median diameters of about 3 mm (Sect. 2.5). The local maximum of the new E_stick parameterization at temperatures from -17 to $-12.5\,°\mathrm{C}$ leads in the NEW run to a rapid increase in the $\overline{x}$, DWRs, and MDVs in the same temperature range and therefore matches the observed profile of $\mathrm{DWR}_\mathrm{Ka,W}$ better than the CTRL run.

O20 speculated that the overestimation of the particle sizes at high temperatures and the mismatch in the profiles of the DWRs might be mainly due to the E_stick parameterization and the v_t–size relation. However, Figs. 6 and 7 as well as the aggregation rates (Appendix A) reveal that the v_t relation at smaller sizes and the aggregation kernel formulation also strongly affect the aggregation rates. Both $\overline{x}$ (Fig. 6i) and $\mathrm{DWR}_\mathrm{X,Ka}$ are lower in colMix2_Akernel_LinCot than in the CTRL run. If E_stick were the dominating driver, these two simulations would be very similar. The differences in the $\overline{x}$ profiles of these two simulations can only be explained by relevant influences of other parameters on the aggregation rates.

The simulations with the D-kernel (colMix2_Dkernel) exhibit a strong influence on aggregation. This is evident in the rapid decrease in Q_i and N_i and a rapid increase in $\overline{x}_i$, $\overline{x}_\mathrm{s}$, and $\overline{x}$ caused by high aggregation rates (supported by Appendix A). From this simulation, it is evident that the use of the new particle properties (including the Atlas-type v_t–size relation) together with the D-kernel results in even larger particles than in the default run, and thus DWRs are strongly overestimated (Fig. 7d). This overestimation can only be reduced by using the A-kernel.

The vertical gradients of Q result from mass uptake by depositional growth and divergence of v_t (Fig. 6h). First, Q increases from the cloud top to the cloud bottom due to depositional growth. Second, deposition growth and aggregation increase particle size and thus v_t increases. If there were no mass uptake (no deposit growth) but only aggregation, Q could only decrease because the product of v_t and Q would be conserved. The v_t–size relation plays an important role in these processes: on the one hand, smaller v_t for a given particle size, e.g., as in NEW vs. CTRL, means more time for mass uptake, leading to a faster increase in Q per height. On the other hand, smaller v_t could also lead to less ventilation and thus less mass uptake due to depositional growth. The v_t–size relationship, which defines the slope of v_t with increasing size, influences the divergence of v_t with height and the aggregation rates (Sect. 3.1.3). These multiple effects also interact, which further complicates the interpretation of the profiles of Q. Nevertheless, we attempt to interpret the most obvious features of the profiles of Q.

At about $-17\,°\mathrm{C}$, MDV increases sharply in the NEW run (Fig. 7b), causing a decrease in Q at these temperatures (Fig. 6f), while Q increases continuously in the CTRL run. The differences in the profiles of Q between the sensitivity runs are relatively large. These large differences are likely due to the different conversion rates of cloud ice to snow and differently strong increasing $\overline{x}$ near the model top. For example, in colMix2_Dkernel the cloud ice converts rapidly to larger snow particles. As a result, particles near the model top fall faster and therefore have less time to grow by depositional growth (the increase in Q is weaker compared to the NEW run); colMix2_Akernel_LinCot shows a weaker increase in $\overline{x}$ for $T > -15\,°\mathrm{C}$ compared to the NEW run (Fig. 6i). This weaker increase in $\overline{x}$ leads to a weaker increase in MDV (Fig. 7b) and thus to a stronger increase in Q (Fig. 6h). The reflectivity Ze_Ka is closely related to Q so that colMix2_Dkernel (colMix2_Akernel_LinCot) has the lowest (highest) reflectivity. However, the CTRL run has the highest Ze_Ka, although Q is lower than in some sensitivity runs. The large Ze_Ka here could be caused by the relatively dense snow particles assumed in CTRL (Fig. 3). Overall, Q and Ze_Ka show relatively large sensitivity to the varied parameters in these snowshaft simulations. However, this observation must be interpreted with caution. The simulations assume a relatively large humidity in order to match the hydrometeor profiles and compensate for processes not considered (Sect. 3.2.1). This high humidity could lead to an overestimation of mass uptake due to depositional growth. Additionally, considering that supersaturation is not consumed by depositional growth but is held constant in our snowshaft simulations, one could hypothesize that Q and Ze might be more similar among the sensitivity runs in the ICON-LEM simulations.

The new particle properties reduce the bias of the scheme regarding MDV to a large extent (Fig. 7b). While all simulations with the new particle properties are within the deciles of the observations, the standard run is already outside the deciles at $-35\,°\mathrm{C}$ and is more than $0.5\,\mathrm{m\,s^{-1}}$ larger than the median at some temperatures (e.g., at $T = 5\,°\mathrm{C}$). The other parameters change the profile of the MDV to a much lesser extent. At temperatures from -18 to $-12\,°\mathrm{C}$, all simulations show an increase in MDV, while all quantiles of the observed MDV decrease. This discrepancy could be due to the lack of habit prediction, underestimated or missing upwinds, or the lack of collisional fragmentation (Korolev and Leisner, 2020) in the model. At these temperatures dendritic growth occurs, which could lead to decreasing particle density and thus decreasing v_t and/or updrafts as a result of strong latent heat release. Collisional fragmentation could furthermore lead to the formation of new small particles with low v_t, which also reduces the MDV.

In addition to the particle properties, the width of the size distribution changes the MDV the most. The simulation with the wider size distribution (colMix2broad_Akernel) has a larger MDV (Fig. 7b) than the NEW run, which is due to the increasing number of large particles at the larger end of the distribution (Sect. 3.1.1). These large particles contribute more to the MDV than the smaller particles; to calculate MDV, each particle must be weighted by reflectivity, which for Rayleigh scatterers scales approximately with mass to the power of 2. The higher weight of the large participants also explains why the DWRs in colMix2broad_Akernel are significantly higher compared to the NEW run, even though the mean size of the hydrometeors is relatively similar. This sensitivity illustrates that the DWRs can only to some extent be used to infer $\overline{x}$ and the size distribution width has to be additionally considered.

Despite the various simplifications in the snowshaft model (no nucleation, no advection, constant humidity) the mean profile of the radar profiles from the ICON-LEM simulations of O20 could be well-matched. This allowed us to investigate the sensitivity of aggregation to the individual model components and to select a model setup that best matches the observed radar profiles. The particle properties of the snow, the aggregation kernel formulation, and E_stick have a strong influence on the hydrometeor contents and the simulated radar observables. Interestingly, the choice of particle size distribution has little effect on the hydrometeor profiles but a large effect on the DWR values. The choice of cloud ice properties (needle or column) is less important than the choice of the other parameters in this cloud regime. However, the choice of cloud ice properties might be more important for clouds with smaller aggregation rates, e.g., cirrus. If we combine the A-kernel, the particle properties of Mix2 from K20, the newly proposed E_{stick} parameterization, and a relatively narrow size distribution the observed profiles of MDV and DWRs could be better matched. To test whether these sensitivities and improvements in NEW are also found persistently in more realistic simulations, in the next section we test whether these observations occur similarly in the ICON-LEM simulations.

3.3 ICON-LEM case study simulation using the new parameterizations

In the snowshaft simulations (Sect. 3.2) we had to use several idealized assumptions. ICON-LEM (Sect. 2.2) contains additional processes (e.g., advection, nucleation, varying humidity field) and therefore simulates a more realistic representation of the atmosphere. In this section, we investigate the impact of the various parameters studied in the sensitivity analysis in a more complex case study with an ICON-LEM simulation. Furthermore, the ICON-LEM simulations provide an opportunity to extend the analysis to various conditions (e.g., nonstationary regime during the frontal passage, sublimation layers).

The case study of interest was 3 January 2016, when a low-pressure area over the British Isles and an accompanying frontal system over western and central Europe determined the synoptic situation over the modeled domain. Shallow mixed-phase clouds are present in the morning and dissipate around noon (Fig. 8a). The passage of a warm front manifests itself at 10:00 UTC, first in high clouds and then in sinking cloud bases. These frontal clouds start to precipitate at 18:00 UTC. The selected case is particularly interesting because it contains clouds in different regimes and precipitation of weak to moderate intensity.

The observed and simulated Ze_{Ka} fields match relatively well for all simulations in terms of cloud structure and precipitation (Fig. 8). Both the shallow mixed-phase clouds and the frontal cloud are very well-captured in terms of temporal and spatial structure.

Ze_{Ka} exhibits strong differences between the observations and the simulation only in the rain and ice slightly above the melting temperature in the period from 19:00 to 23:00 UTC. The sharp decrease in the observed Ze_{Ka} indicates strong sublimation. The presence of sublimation is also revealed by the model showing subsaturated air in this time range (Fig. B6). There are three main reasons that explain why the model does not accurately represent the sharp decrease in Ze_{Ka} in this sublimation scenario. First, the humidity could be overestimated in the model, e.g., due to inaccurate forcing data. Second, particle sizes could be overestimated due to processes in microphysics that weaken the effect of sublimation. We cannot completely rule out the humidity mismatch, but we found good agreement between the model and radiosonde data when available. Unfortunately, there was no radiosonde launched on the considered day. Thus, we are confident in the general ability of the model to accurately simulate the humidity field, but we cannot rule out the possibility that inaccuracies in the simulated humidity field contribute to the bias in Ze_{Ka}. Lastly, the parameterization of sublimation could also be an error source. For example, the evolution of the PSD during sublimation is challenging to represent in a two-moment scheme (Seifert, 2008). Since all of these reasons might be able to explain the mismatch in Ze_{Ka}, we should be cautious in assessing the validity of the assumptions of the individual model settings based on this sublimation feature. However, regardless of the accuracy of the model in predicting the humidity or simulating sublimation, the following differences in Ze_{Ka} of the model simulations underscore the importance of accurate prediction.

While the NEW (Fig. 8c) and most sensitivity runs show a slight decrease in Ze_{Ka} due to sublimation in the time period when the air is subsaturated, the sublimation is barely seen in Ze_{Ka} of some other simulations (e.g., CTRL, colMix2_Dkernel; Fig. 8b and g). The differences between the simulations are caused by the differences in the particle size indicated by $DWR_{\mathrm{X,Ka}}$ (Fig. 9). Similar to the snowshaft simulations, $DWR_{\mathrm{X,Ka}}$ is strongly overestimated in colMix2_Dkernel and the CTRL run. In contrast, $DWR_{\mathrm{X,Ka}}$ is well-matched closely above the melting temperature in the NEW simulation. The hydrometeor populations with realistic particle sizes are more strongly affected by the subsaturated air and sublimate quickly, whereas particles that are too large sublimate less and therefore retain more mass. Thus, the overestimated particle size leads to overestimated precipitation. Between 18:00 and 24:00 UTC, 1.40 mm of accumulated rain was observed, 8.91 mm simulated by the default simulation and 2.29 mm by colMix2_Akernel. While this represents an overestimates of 536 % by the CTRL run during this time period, we emphasize the overall good agreement between modeled and observed precipitation reported by O20 for the entire campaign. While E_{stick} appeared to be important for the simulated $DWR_{\mathrm{Ka,W}}$ in the snowshaft simulations (Fig. 7), the differences between the simulation with the old (colMix2_Akernel_LinCot; Fig. 9d) and the new E_{stick} parameterization (colMix2_Akernel; Fig. 9c) are relatively small. In the ICON-LEM simulation, the weaker growth of the particles in colMix2_Akernel_LinCot at lower temperatures might be partly compensated for by advection or nucleation.

Besides the DWRs, MDV provides valuable information about the microphysical properties. As also reported by O20, MDV is overestimated in the SB06 default simulation, especially in regions where the particle sizes are overestimated (Fig. 10). MDV is often used to distinguish rimed from unrimed particles (e.g., Mosimann, 1995). Using this method, we detect some smaller episodes in which rimed particles dominate at about 04:00, 18:00, and 22:00 UTC. At other times, the observations indicate unrimed or only slightly rimed particles. In the SB06 default simulation, high MDVs

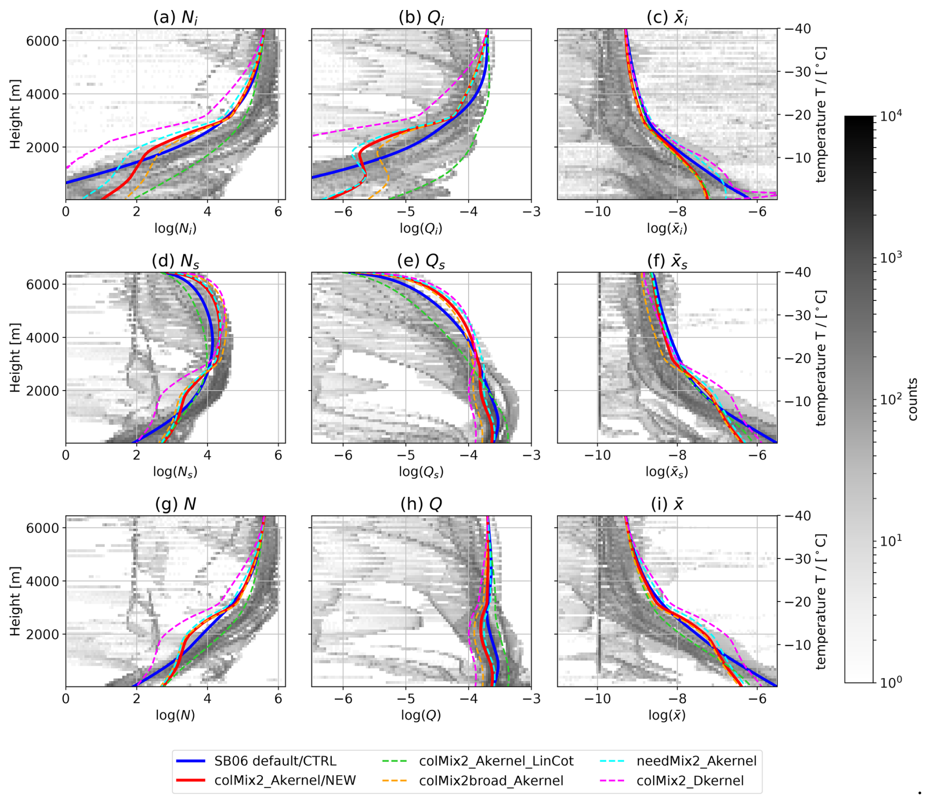

Figure 6. Profiles of model variables in the snowshaft simulations. Number density N **(a, d, g)**, mass mixing ratio Q **(b, e, h)**, and mean mass $\overline{x}$ **(c, f, i)** of the cloud ice **(a, b, c)**, snow **(d, e, f)**, and the sum of cloud ice and snow **(g, h, i)**. Lines: simulations using different model settings as described in Table 3. Greyscale: histogram of the hydrometeor contents vs. temperature from the ICON-LEM simulations of the Tripex campaign (O20) filtered to include only profiles for which the precipitation rate exceeds $1\,\mathrm{mm\,h^{-1}}$. The simulations in O20 used the default model settings.

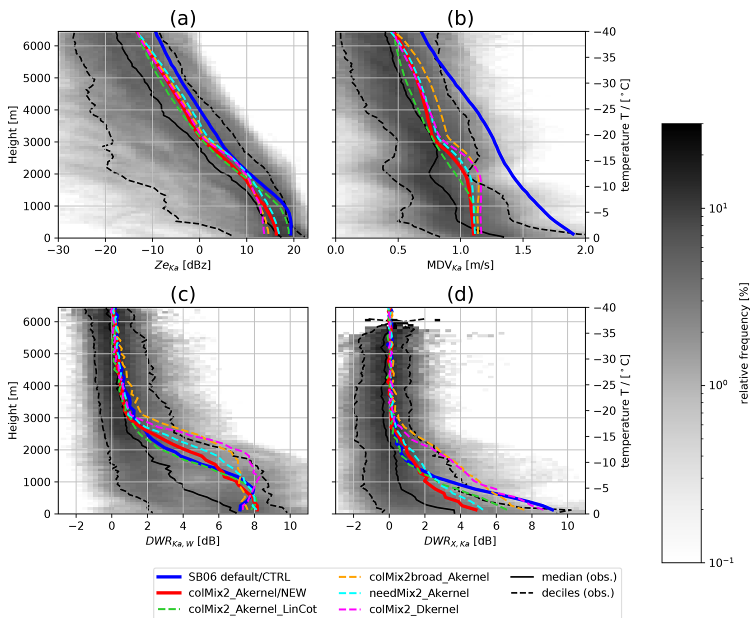

Figure 7. **(a)** Reflectivity $\mathrm{Ze_{Ka}}$, **(b)** mean Doppler velocity $\mathrm{MDV_{Ka}}$, **(c)** $\mathrm{DWR_{Ka,W}}$, and **(d)** $\mathrm{DWR_{X,Ka}}$. Lines: simulated profiles based on snowshaft simulations (Fig. 6) as well as the median and quartiles of the observations. Greyscale: histogram of observations from the Tripex campaign (O20).

Table 3. Overview of parameters and settings varied in the microphysical sensitivity experiments. The sensitivity runs have the same settings as colMix2_Akernel unless otherwise noted. K is the collision kernel, D the maximum dimension, and A the particle's projected area; μ and ν are parameters in the generalized gamma function describing the mass distribution in the microphysics scheme (Eq. 5).

	Main runs		Sensitivity runs (difference to colMix2Akernel)			
	SB06 default/ CTRL	colMix2_ Akernel/ NEW	needMix2_ A-kernel	colMix2_ D-kernel	colMix2_ Akernel_LinCot	colMix2 broad_Akernel
Particle properties (Fig. 3)	SB06 default cloud ice, SB06 default snow	Column Mix2	Needle			
Collision kernel	D-kernel: $K \propto (D_i + D_j)^2$	A-kernel: $K \propto (A_i^{0.5} + A_j^{0.5})^2$	D-kernel			
Sticking efficiency (Fig. 4)	L83/C86	Modification of M88			L83/C86	
Size distribution $N(m) = A\, \mathrm{m}^{\nu} e^{-\lambda m^{\mu}}$	$\nu = 0$ (cloud ice & snow)	$\nu = 2$ (cloud ice & snow)				$\nu = 2$ (cloud ice) $\nu = 0$ (snow)

are obtained in the whole time range after 18:00. Since the profiles of the hydrometeors show only very little mass of rimed particles during this period, the larger predicted MDV can be attributed to the overestimation of the unrimed snow particle v_t.

The new simulations, all using the new particle properties, have significantly lower values of MDV at all temperatures. This reduction of MDV compared to the SB06 default setup constitutes a significant reduction of the bias in MDV at temperatures below $-10\,°\mathrm{C}$. For $T > -10\,°\mathrm{C}$, MDV is even slightly underestimated. Considering that Fig. 5 shows good agreement of MDV between the observations and the v_t–size relation of Mix2, we assume that the underestimation of MDV is not caused by the underestimation of the v_t–size relation of aggregates. Since $\mathrm{DWR}_{\mathrm{X,Ka}}$ also matches well at these temperatures, processes other than aggregation and sedimentation of unrimed aggregates most probably cause this underestimation of MDV. One could speculate that riming rates are underestimated or that the vertical air motion is not well-simulated.

Most of the findings from the snowshaft simulations (e.g., the strong reduction of MDV and DWR at temperatures close to the melting temperature) are confirmed by the ICON-LEM simulation of this case study. However, the ICON-LEM simulations reveal that the influence of E_{stick} seems to be overestimated in the snowshaft simulations. Moreover, accurate modeling of particle sizes and v_t in the presence of a sublimating layer is critical. The simulations with the new particle properties showed a slight underestimation of the MDV. This underestimation most likely does not arise from an inaccurate representation of the particle properties or the aggregation rates but is caused by another process (e.g., riming, vertical air motion). In previous analyses of the SB06 default setup, this underestimation could not have been detected because it was masked by the overestimation of the aggregate's v_t. Because errors can be specific to the chosen day, such as a particular mismatch of the relative humidity, relying on only one case to detect a discrepancy in the microphysical properties is prone to error. Therefore, we analyze the statistics of a multi-month simulation in the next section.

3.4 Statistical comparison

After evaluating the choices of the new scheme in the snowshaft model and in a case study with ICON-LEM, we perform ICON-LEM simulations for the entire Tripex time period. By comparing observed and modeled histograms of DWR and MDV as a function of temperature, we can evaluate the new scheme. Since we additionally contrast the histograms of the NEW and CTRL simulations, we can test whether the reduction in the bias of DWRs and MDV found in Sect. 3.3 is specific to the selected case or rather a consistent feature of the model changes. As DWRs are related to the mean particle size, we can assess whether the chosen parameter combination can accurately simulate aggregation in various weather situations present in the simulated days. The same applies to MDV profiles, which are especially valuable in evaluating the suitability of the assumed v_t–size relationship.

The observed and synthetic radar profiles are filtered in the same way for comparability. For example, the first 6 h of simulation and observation are not considered because the model output could contain artifacts during this spin-up time. Moreover, we include only profiles in which the rain rate RR exceeds $1\,\mathrm{mm\,h^{-1}}$. The latter filter enables us to focus on the most relevant cases for precipitation. Interestingly, O20 found the discrepancy between the model and observations

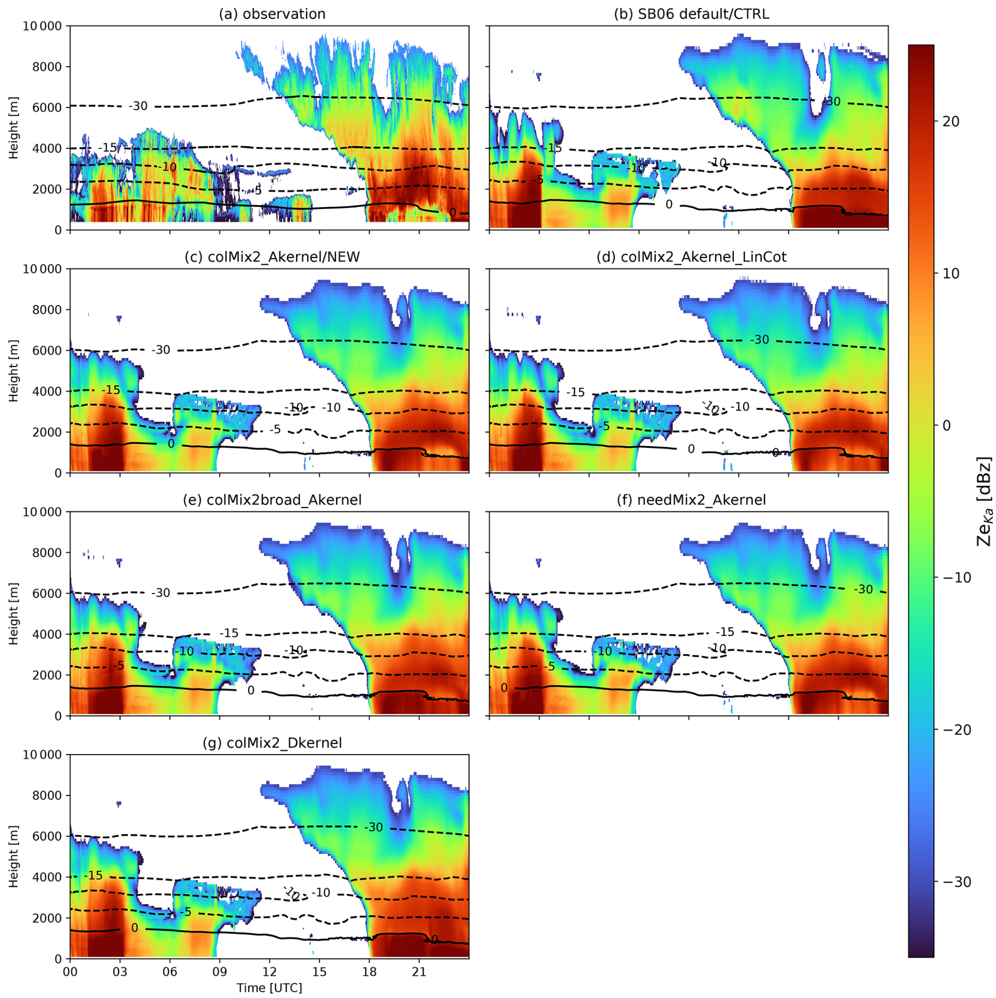

Figure 8. Time–height profile of Ze_{Ka} from 3 January 2016 as observed **(a)** and simulated **(b–g)** with various model settings (Table 3). Selected temperature isolines from CloudNet (Illingworth et al., 2007) for the observations **(a)** and the corresponding ICON-LEM output **(b–g)** are also shown.

to be especially obvious for these profiles. For a detailed description of the processing, we refer to O20.

To quantify the agreement between the histograms of the simulations and the observation, the Hellinger distance H is used. H can be defined for two distributions $P = (p_1, \ldots, p_k)$ and $Q = (q_1, \ldots, q_k)$ as

$$H(P,Q) = \frac{1}{\sqrt{2}} \sqrt{\sum_{i=1}^{k} \left(\sqrt{p_i} - \sqrt{q_i}\right)^2}. \quad (17)$$

H is zero for two identical distributions and 1 if the distributions do not overlap at all.

The medians and larger quantiles of the observed distributions of DWRs indicate a strong increase in particle size around $-15\,°C$ (most evident in $DWR_{Ka,W}$; Fig. 11a) and just above the melting temperature (most evident in $DWR_{X,Ka}$; Fig. 11e). Both of these characteristic increases in the particle sizes are found to some extent in CTRL (panels b and f in Fig. 11) and NEW (panels c and g in Fig. 11). The increase in particle sizes between -15 and $-10\,°C$ happens in the new simulations at slightly lower temperatures, and the different profiles reveal a greater variability (visible, e.g., in the difference of $DWR_{Ka,W}$ between the lower and upper decile). H indicates a slightly better match by CTRL in this temperature range. For $T > -10\,°C$ the mean and higher quantiles of $DWR_{X,Ka}$ increase very rapidly in CTRL and more slowly in NEW and the observation. The increase in particle sizes as simulated by NEW is in much better agreement with the observed profiles. The upper quartile of $DWR_{X,Ka}$ only slightly exceeds 5 dB in the observations and NEW but is higher than 10 dB in CTRL for $T > -1\,°C$. This better match is also indicated by H (Fig. 11h), which is about 5 times larger for CTRL compared to NEW.

Besides the overestimation of $DWR_{X,Ka}$ closely above the melting temperature, O20 also highlighted the overestimation of MDV by CTRL. This overestimation is present at all

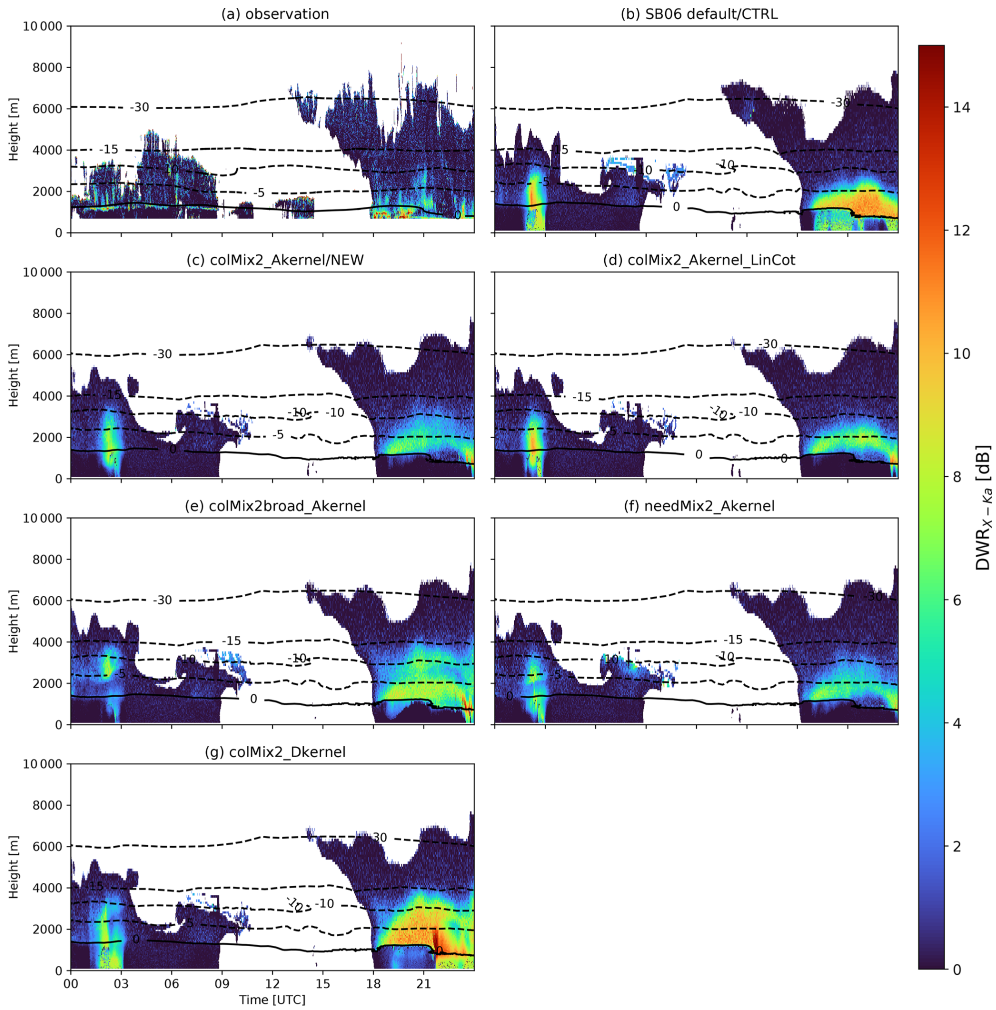

Figure 9. Same as Fig. 8 but displaying $DWR_{X,Ka}$, which is sensitive to mean mass diameters of 1 to 20 mm.

temperatures (compare panels a and b in Fig. 12) and can be attributed to the overestimation of the v_t–size relationship of the snow class as reported in Karrer et al. (2020) and the overestimated particle sizes for the higher temperatures. The overestimation of MDV by CTRL is most pronounced for $T > -15\,°C$. In this temperature range, CTRL cannot reproduce the asymptotic approach because of the power-law v_t–size relationship (Sect. 3.1.3). For example, the median of MDV_{Ka} at $-5\,°C$ is $1\,m\,s^{-1}$ in the observations and $1.3\,m\,s^{-1}$ in CTRL. In contrast, the new simulations agree better with the observations and H is about half as large as for CTRL. The new scheme setup is more accurate in this temperature range because the Atlas-type v_t–size relationship of the Mix2 particles (Fig. 3) correctly considers the asymptotic approach to $1\,m\,s^{-1}$ at large sizes. However, MDV is slightly underestimated by NEW for $T > -10\,°C$. Values substantially above $1\,m\,s^{-1}$ occur in the observations and the new simulations only closely above the melting temperature, where rain is present. At temperatures below $-15\,°C$, both simulations perform similarly, with H ranging from 0.2 to 0.5. While CTRL exhibits a continuous overestimation of MDV, the new simulations lack the observed increase in MDV for $T < -20\,°C$. At these temperatures, the selected PSD width (Sect.3.1.1) and cloud ice particle properties (Sect. 3.1.3) may not be ideal.

The statistical comparison shows that the changes we made to the model could eliminate the most striking biases, namely the overestimation of $DWR_{X,Ka}$ and MDV closely above the melting temperatures. The match of these quantities is important for accurate simulation of precipitation, as exemplified in the case study in Sect. 3.3. Some discrepancies remain, namely the overly strong increase in the DWRs at temperatures between -15 and $-10\,°C$ and the overestimation (underestimation) of MDV temperatures below $-25\,°C$ (above $-10\,°C$). These discrepancies can be caused by several model errors (inaccurate simulation of, e.g., PSD shape, E_{stick}, degree of riming, variability in cloud ice properties) that cannot be fully deciphered by this observational

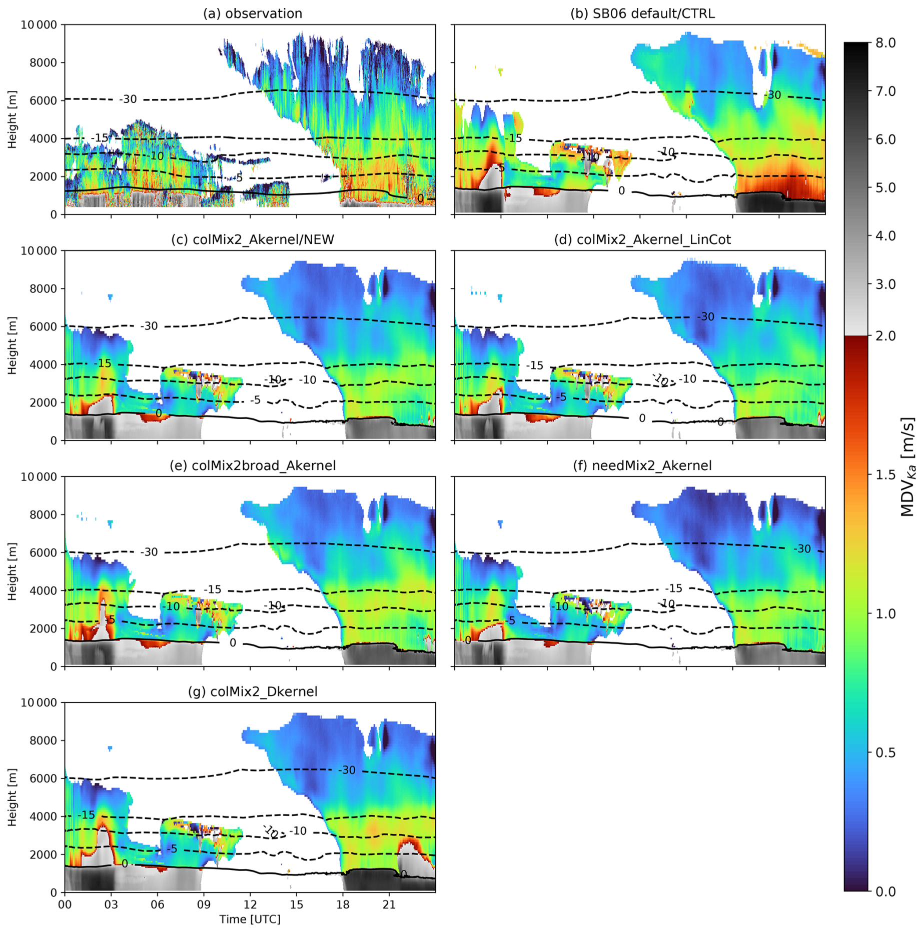

Figure 10. Same as Fig. 8 but displaying MDV_{Ka}, which is strongly linked to v_t.

setup and could benefit from advances in laboratory measurements, observational setup, and representation of cloud ice habits and riming degree in the model.

4 Conclusions

Aggregation is a key ice microphysical growth process for the formation of precipitating ice particles, which are the precursor of raindrops in cold rain formation. Recent studies using statistics from multi-frequency Doppler radar observations provided observational constraints on how critical radar quantities, such as DWRs or MDV, change with temperature. In this study, we aimed at a deeper analysis of the underlying causes for the observed discrepancies between radar statistics and a state-of-the-art two-moment microphysical scheme, and we improved its simulation of aggregation.

To this end, as a first step, we revisited all relevant components of aggregation as considered in the two-moment scheme to see how well they represent current knowledge of physics. These components are the size distribution width, the temperature dependence of E_{stick}, the particle properties (with a focus on the v_t–size relation of aggregates), and the representation of nonspherical particles in the aggregation kernel formulation.

To systematically test the sensitivities of various parameter combinations, we performed 1D simulations with the snowshaft model, which uses simple profiles of thermodynamic variables and a simple initialization of particles at the model top. Moreover, the model only accounts for a subset of all the microphysical processes that occur in real clouds. Nevertheless, by adjusting the model setup we could match the average profiles of radar observables obtained by the 3D simulations of O20, which used the SB06 default scheme setup.

The snowshaft simulations revealed high sensitivity of aggregation to particle properties, the aggregation kernel formulation, and E_{stick}. Surprisingly, the size distribution width had a relatively small effect on the modeled mean mass but a considerable influence on the simulated DWRs. The influence of the cloud ice properties was small in both the model and radar variables.

By comparing the profiles from the snowshaft simulation with the average observed profiles, we were able to select a set of parameters that provided the best agreement with the observations. In this selection process, we mainly varied

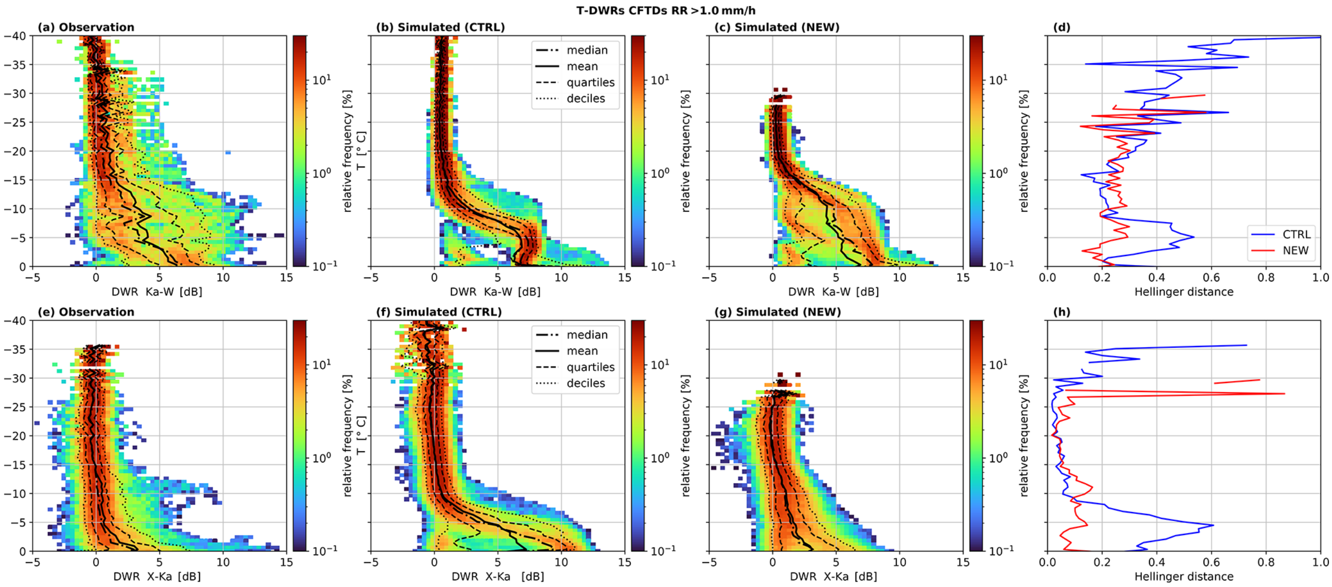

Figure 11. Contour frequency by temperature diagrams (CFTDs) for all profiles with RR > 1 mm h^{-1} of the dual-wavelength ratios between the X and Ka band ($DWR_{X,Ka}$, top) and between the Ka and W band ($DWR_{X,Ka}$, bottom) from the default simulation **(a, e)**, the new simulation (colMix2_Akernel; **b** and **f**), and measured **(c, g)**. The black lines represent the statistical measures (median, mean, quartiles, and deciles) at different temperatures. Panels **(d)** and **(h)** show the Hellinger distance between the simulated and observed distributions for all temperatures.

the less-known components, e.g., the size distribution width, and held other parameters constant that we could better constrain, e.g., the v_t–size relationship. The size distribution width proved to be a critical component in linking modeled $\overline{x}$ to observed DWRs and at the same time is difficult to constrain with the given observational setup. Therefore, using a microphysical scheme that explicitly simulates the width of the size distribution (e.g., a three-moment scheme) would provide a more consistent link between the model and observation. However, additional observational constraints from radar (e.g., Doppler spectrum width) and in situ observations should be considered in this case. In particular, we find that the v_t–size relationship, which accounts for the asymptotic behavior of v_t at large sizes, leads to better agreement with the observations. Moreover, the A-kernel appears to be a better approximation of the aggregation kernel when combined with a constant E_{coll}.

We implemented this improved scheme setup in the ICON-LEM and also tested the individual model modifications in a case study. These more realistic ICON-LEM simulations allowed us to derive potential differences in the analysis of sensitivities compared to the snowshaft simulations, possibly caused by effects such as dynamics and advection. Overall, the ICON-LEM simulations yielded similar sensitivities as the snowshaft simulations, but slight differences were apparent with respect to sensitivity to E_{stick}. The differences between simulations with different E_{stick} parameterization were less pronounced in the ICON-LEM simulations. This discrepancy between the simulation frameworks could result from accounting for feedback from microphysics to model humidity in the ICON-LEM simulation.

On the day considered in the case study, relatively dry low-level air resulted in strong sublimation of ice particles. This sublimation feature demonstrated the relevancy of accurately simulating $\overline{x}$. The SB06 default scheme with its largely overestimated aggregate sizes strongly overestimated the rainfall rate on the ground because the large snowflakes could not sublimate fast enough. In contrast, the more realistic aggregate sizes obtained with the new scheme were able to fit the observations much better.

Finally, the entire period of the campaign dataset (46 d) was simulated again with ICON-LEM using the best-matching parameter combination from the previous tests. This allowed us to directly compare the new statistics with the previous analysis of the default scheme provided in O20. The new aggregation formulation is clearly able to reduce the observed overestimation of MDV. This improvement can be attributed to the new Atlas-type v_t–size relationship. The overestimation of the mean particle size at high temperatures revealed in the DWRs was also substantially reduced by the new aggregation parameterization.

Remaining discrepancies are found for DWRs at temperatures of about −12 °C and for MDV at low and high temperatures. The overestimated DWRs by the new simulations could result in an overestimated $\overline{x}$ or overly broad size distribution in the model. Inclusion of a higher-frequency radar (Battaglia et al., 2014) may help to infer the particle growth above −12 °C. The analysis of Doppler spectra (e.g., simi-

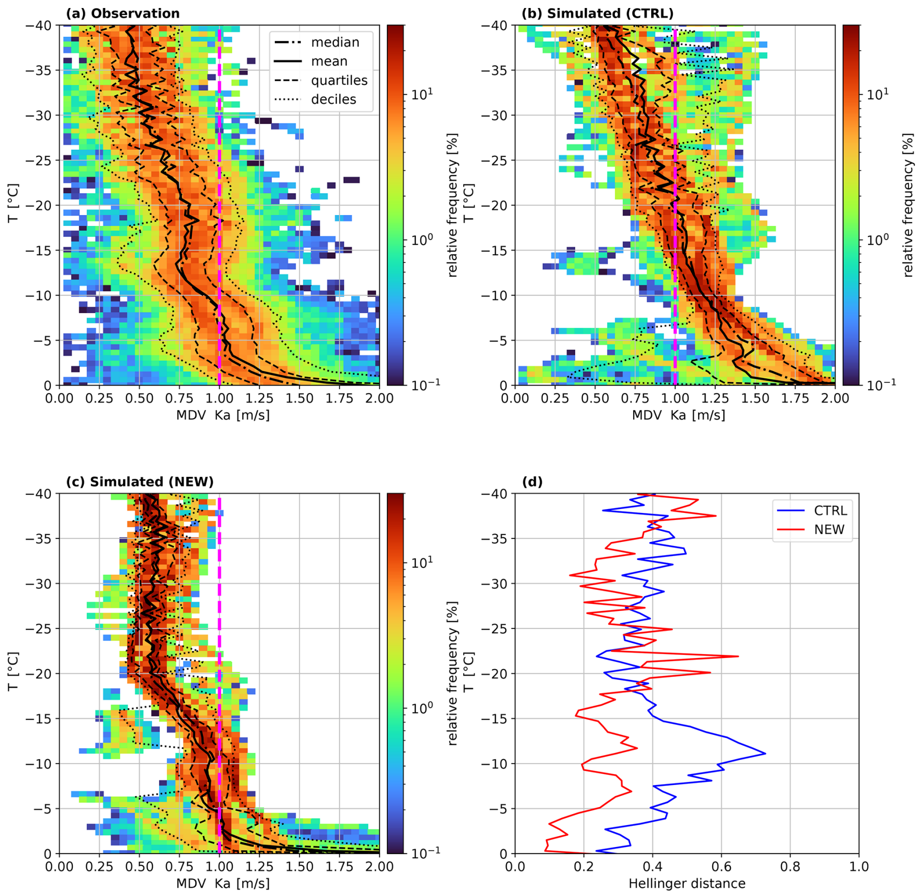

Figure 12. Contour frequency by temperature diagrams (CFTDs) of the mean Doppler velocity of the Ka band (MDV_{Ka}) from the default simulation **(a, e)**, the new simulation (colMix2_Akernel, **b** and **f**), and measured **(c, g)**. The black lines represent the statistical measures (median, mean, quartiles, and deciles) at different temperatures. The histograms on top are calculated including all data and on the bottom only data from profiles for which the precipitation rate RR exceeds 1 $mm\,h^{-1}$. A vertical line at 1 $m\,s^{-1}$ eases the comparison of the different distributions. Panels **(d)** and **(h)** show the Hellinger distance between the simulated and observed distributions for all temperatures.

lar to Barrett et al., 2019) or observational techniques, e.g., in situ probing of the particle size distribution, would provide additional constraints on the size distribution and ease the interpretation of the MDV and DWR. The mismatch of the MDV at lower temperatures could be caused by an inaccurate size distribution width, as well as E_{stick} or cloud ice properties. Future studies could focus on this temperature region, which is highly relevant for cloud radiative effects. The slight underestimation of MDV at high temperatures could be due to underestimated riming rates, the representation of partially rimed particles, or other effects such as vertical air motion. Further insight could be gained, e.g., from the analysis of the Doppler spectra or comparison with other microphysical schemes with a different representation of the riming process (Morrison and Milbrandt, 2015; Tsai and Chen, 2020).

In addition to the results obtained in this study for aggregation in the SB06 scheme, we think that our approach for how to utilize state-of-the-art radar datasets to improve parameterizations may also serve as a blueprint for future studies focusing on other processes or microphysical schemes. Therefore, we shortly summarize the approach in general terms with the following points.

1. Revisit components of the physical parameterization.

2. Set up single-column simulations which match the average profiles of simulated observables obtained from long-term 3D simulations with the default scheme setup.

3. Systematically test the sensitivities of various parameter combinations in 1D simulations.

4. Select the model configuration that best matches the observations.

5. Implement model modifications in the 3D model and infer possible differences in sensitivities between a 3D simulation and 1D simulations in a case study.

6. Rerun the long-term 3D simulation using the best-matching parameter combination and investigate the improvements by comparing observations with simulations using the default and the new scheme setup.

Appendix A: Bulk aggregation rates

We summarize the bulk aggregation formulas for all aggregation processes: ice–snow collection, ice self-collection, and snow self-collection. While the formulations using the D-kernel were already given by Seifert et al. (2014), the formulas using the A-kernel were newly derived in this study.

Combining the definition of the moments,

$$M_n = \int_0^\infty m^n f(m) dm, \tag{A1}$$

the SCE (Eq. 4) and its simplifications in the SB06 scheme (Sect. 3.1), an equation can be derived that allows for the calculation of all relevant aggregation rates between particles of the classes i and j:

$$\left.\frac{\partial M_{i,n}}{\partial t}\right|_{\mathrm{coll,ij}} = \Phi \int_0^\infty \int_0^\infty f_i (D_i) f_j(D_j) K_{i,j}(D_i, D_j) m_i^n dD_j dD_i, \tag{A2}$$

where $M_{j,n}$ is the nth moment of the hydrometeor class j, f is the particle size distribution for a selected size variable (D_{max}, D_{eq}, or m), K is the aggregation kernel, and m is the particle mass.

Seifert et al. (2014) use the variance approach proposed in Seifert and Beheng (2006), which parameterizes the bulk velocity difference by the square root of the second moment of the velocity differences. In this way, the integral is separated into a term containing the geometrical properties ($\mathcal{C}_{n,ij}$) and a part which contains the velocity difference ($\overline{\Delta v}_{n,ij}$) to enable the analytical integration.

$$\left.\frac{\partial M_{i,n}}{\partial t}\right|_{\mathrm{coll},ij} = \overline{E}_{i,j} \overline{\Delta v}_{n,ij} \mathcal{C}_{n,ij} \tag{A3}$$

The expressions of $\mathcal{C}_{n,ij}$ and $\overline{\Delta v}_{n,ij}$ depend on the expression of the PSD$_m$ (Sect. 3.1.1), the formulation of the aggregation kernel (Sect. 3.1.2), and the particle properties (Sect. 3.1.3). The SB06 scheme assumes a modified gamma distribution as a function of mass (Eq. 5), which can be easily converted to a gamma distribution as a function of D_{eq} if $\mu_m = 1/3$ (Eq. 7). The particle properties are characterized by power-law relations of m (Eq. 12) and A_{act} (Eq. 15) vs. D_{max} and D_{eq}. In the new scheme, v_{t} of cloud ice and snow is parameterized by an Atlas-type relation as a function of D_{eq} (Eq. 11). Coefficients of the relations can be found in Table 2.

A1 D-kernel

Inserting the D-kernel (Eq. 1) into Eq. (A2), the $\mathcal{C}_{n,ij}$ and $\overline{\Delta v}_{n,ij}$ can be written as

$$\mathcal{C}_{n,ij} = \frac{\pi}{4} \int_0^\infty \int_0^\infty \left(D_{\mathrm{max},i} + D_{\mathrm{max},j}\right)^2 f_i(m_i) f_j(m_j) m_j^n dm_i dm_j, \tag{A4}$$

$$\overline{\Delta v}_{n,ij} = \left\{ \frac{1}{\mathcal{N}_{n,ij}} \int_0^\infty \int_0^\infty \left[v_i(D_{\mathrm{eq},i}) - v_j(D_{\mathrm{eq},j})\right]^2 \times D_{\mathrm{eq},i}^2 D_{\mathrm{eq},j}^2 f_{\mathrm{eq},i}(D_{\mathrm{eq},i}) f_{\mathrm{eq},j}(D_{\mathrm{eq},j}) m_i^n dD_{\mathrm{eq},i} dD_{\mathrm{eq},j} \right\}^{\frac{1}{2}}, \tag{A5}$$

where $\mathcal{N}$ is the normalization factor given by

$$\mathcal{N}_{n,ij} = \int_0^\infty \int_0^\infty D_{\mathrm{eq},i}^2 D_{\mathrm{eq},j}^2 f_{\mathrm{eq},i}(D_{\mathrm{eq},i}) f_{\mathrm{eq},j}(D_{\mathrm{eq},j}) m_i^n dD_i dD_j. \tag{A6}$$

Inserting the $D_{\mathrm{max}} - m$ relation,

$$D_{\mathrm{max},i} = a_i m_i^{b_i} = \frac{\pi \rho_{\mathrm{w}} a_i}{6} D_{\mathrm{eq},i}^{3b_i}, \tag{A7}$$

and the PSD$_m$ (Eq. 5) into $\mathcal{C}_{n,ij}$ (Eq. A4) and solving the integral, we obtain

$$\mathcal{C}_{n,ij} = \left(\frac{\pi \rho_{\mathrm{w}}}{6}\right)^n \frac{\pi}{4} N_i N_j \left[\delta_{D,i}^0 \overline{D}_i^2 + \delta_{D,ij}^n \overline{D}_i \overline{D}_j + \delta_j^n \overline{D}_j^2\right], \tag{A8}$$

where δ_i^n and δ_j^n are equal to δ_p^0 of Eq. (90) of SB2006 and δ_{ij}^n is equal to δ_g^0 of Eq. (91) of SB2006.

$$\delta_{D,i}^n = \frac{\Gamma((2b_i + \nu_{m,i} + 1 + n)/\mu_{m,i})}{\Gamma((\nu_{m,i}+1)/\mu_{m,i})} \left[\frac{\Gamma((\nu_{m,i}+1)/\mu_{m,i})}{\Gamma((\nu_{m,i}+2)/\mu_{m,i})}\right]^{2b_i+n} \tag{A9}$$

$$\delta_{D,ij}^n = 2 \frac{\Gamma((b_i + \nu_{m,i} + 1 + n)/\mu_{m,i})}{\Gamma((\nu_{m,i}+1)/\mu_{m,i})} \frac{\Gamma((b_j + \nu_{m,j} + 1)/\mu_{m,j})}{\Gamma((\nu_{m,j}+1)/\mu_{m,j})} \times \left[\frac{\Gamma((\nu_{m,i}+1)/\mu_{m,i})}{\Gamma((\nu_{m,i}+2)/\mu_{m,i})}\right]^{b_i+n} \left[\frac{\Gamma((\nu_{m,j}+1)/\mu_{m,j})}{\Gamma((\nu_{m,j}+2)/\mu_{m,j})}\right]^{b_j} \tag{A10}$$

Inserting the velocity relation (Eq. 11) and the size distribution using D_{eq} (Eq. 7) into the velocity variance (Eq. A4) and solving the integral, we obtain

$$\overline{\Delta v}_{n,ij} = \Bigg[(\alpha_{v,j}-\alpha_{v,i})^2 - 2\beta_{v,j}(\alpha_{v,j}-\alpha_{v,i})\left(1+\frac{\gamma_{v,j}}{\lambda_{\mathrm{eq},j}}\right)^{-\xi^n_{D,i}}$$
$$-2\beta_{v,i}(\alpha_{v,i}-\alpha_{v,j})\left(1+\frac{\gamma_{v,i}}{\lambda_{\mathrm{eq},i}}\right)^{-\xi^n_{D,i}} + \beta^2_{v,j}\left(1+\frac{2\gamma_{v,j}}{\lambda_{\mathrm{eq},j}}\right)^{-\xi_{D,j}}$$
$$+\beta^2_{v,i}\left(1+\frac{2\gamma_{v,i}}{\lambda_{\mathrm{eq},i}}\right)^{-\xi^n_{D,i}} - 2\beta_{v,j}\beta_{v,i}\left(1+\frac{\gamma_{v,j}}{\lambda_{\mathrm{eq},j}}\right)^{-\xi_{D,j}}$$
$$\times\left(1+\frac{\gamma_{v,i}}{\lambda_{\mathrm{eq},i}}\right)^{-\xi^n_{D,i}}\Bigg]^{\frac{1}{2}}, \tag{A11}$$

with

$$\xi^n_{D,i} = \mu_{\mathrm{eq},i}+3+3n, \xi_{D,j} = \mu_{\mathrm{eq},j}+3. \tag{A12}$$

A2 A-kernel

Inserting the A-kernel (Eq. 9) into Eq. (A2), the velocity variance and the geometric part of the bulk collision rates can be written as

$$\mathcal{C}_{n,ij} = \int_0^\infty\int_0^\infty \left(A_i^{0.5}+A_j^{0.5}\right)^2 f_i(D_i) f_j(D_j) m_j^n dD_i dD_j \tag{A13}$$

$$\overline{\Delta v}_{n,ij} = \Bigg\{\frac{1}{\mathcal{N}_{n,ij}}\int_0^\infty\int_0^\infty \left[v_i(D_{\mathrm{eq},i})-v_j(D_{\mathrm{eq},j})\right]^2$$
$$\times D_{\mathrm{eq},i}^{\sigma_{A,i}} D_{\mathrm{eq},j}^{\sigma_{A,j}},$$
$$f_{\mathrm{eq},i}(D_{\mathrm{eq},i}) f_{\mathrm{eq},j}(D_{\mathrm{eq},j}) m_i^n dD_{\mathrm{eq},i} dD_{\mathrm{eq},j}\Bigg\}^{\frac{1}{2}} \tag{A14}$$

$$\mathcal{N}_{n,ij} = \int_0^\infty\int_0^\infty D_{\mathrm{eq},i}^{\sigma_{A,i}} D_{\mathrm{eq},j}^{\sigma_{A,j}} f_{\mathrm{eq},i}(D_{\mathrm{eq},i}) f_{\mathrm{eq},j}(D_{\mathrm{eq},j})$$
$$m_i^n dD_{\mathrm{eq},i} dD_{\mathrm{eq},j}. \tag{A15}$$

Inserting the A–D_{eq} relation (Eq. 15) and the size distribution as a function of D_{eq} (Eq. 7) into the geometric part (Eq. A13) and solving the integral leads to

$$\mathcal{C}_{n,ij} = \left(\frac{\pi\rho_{\mathrm{w}}}{6}\right)^n N_i N_j$$
$$\left[\delta^n_{A,i}\overline{D}^{\sigma^*_{A,i}}_{\max,i} + \delta^n_{A,ij}\overline{D}^{\sigma^*_{A,i}/2}_{\max,i}\overline{D}^{\sigma^*_{A,j}/2}_{\max,j} + \delta^n_{A,j}\overline{D}^{\sigma^*_{A,j}}_{\max,j}\right], \tag{A16}$$

with the following.

$$\delta^n_{A,i} = \gamma_{A,i}\frac{\Gamma(\mu_{\mathrm{eq},i}+\sigma_{A,i}+1+3n)}{\Gamma(\mu_{\mathrm{eq},i}+1)} c_{\lambda,i}^{\sigma_{A,i}+3n} \tag{A17}$$

$$\delta^n_{A,ij} = 2(\gamma_{A,i}\gamma_{A,j})^{0.5}\frac{\Gamma(\mu_{\mathrm{eq},i}+\sigma_{A,i}/2+1+3n)}{\Gamma(\mu_{\mathrm{eq},i}+1)} c_{\lambda,i}^{\sigma_{A,i}/2+3n}$$
$$\times\frac{\Gamma(\mu_{\mathrm{eq},j}+\sigma_{A,j}/2+1)}{\Gamma(\mu_{\mathrm{eq},j}+1)} c_{\lambda,j}^{\sigma_{A,j}/2} \tag{A18}$$

$$\delta^n_{A,j} = \gamma_{A,j}\frac{\Gamma(\mu_{\mathrm{eq},j}+\sigma_{A,j}+1)}{\Gamma(\mu_{\mathrm{eq},j}+1)} c_{\lambda,j}^{\sigma_{A,j}}$$
$$\times\left[\frac{\Gamma(\mu_{\mathrm{eq},i}+4)}{\Gamma(\mu_{\mathrm{eq},i}+1)}\right]^n c_{\lambda,i}^{3n} \tag{A19}$$

$$\sigma^*_{A,i} = \frac{b_{m,i}\sigma_{A,i}}{3} \tag{A20}$$

$$c_{\lambda,i} = \left[\frac{6a_{m,i}}{\pi\rho_{\mathrm{w}}}\frac{\Gamma(\mu_{\mathrm{eq},i}+1)}{\Gamma(\mu_{\mathrm{eq},i}+4)}\right]^{1/3} \tag{A21}$$

Inserting the velocity relation (Eq. 11) and the size distribution as a function of D_{eq} (Eq. 7) into the velocity variance (Eq. A14) and solving the integral, we obtain

$$\overline{\Delta v}_{n,ij} = \Bigg[(\alpha_{v,j}-\alpha_{v,i})^2 - 2\beta_{v,j}(\alpha_{v,j}-\alpha_{v,i})\left(1+\frac{\gamma_{v,j}}{\lambda_{\mathrm{eq},j}}\right)^{-\xi_{A,j}}$$
$$-2\beta_{v,i}(\alpha_{v,i}-\alpha_{v,j})\left(1+\frac{\gamma_{v,i}}{\lambda_{\mathrm{eq},i}}\right)^{-\xi^n_{A,i}} + \beta^2_{v,j}\left(1+\frac{2\gamma_{v,j}}{\lambda_{\mathrm{eq},j}}\right)^{-\xi_{A,j}}$$
$$+\beta^2_{v,i}\left(1+\frac{2\gamma_{v,i}}{\lambda_{\mathrm{eq},i}}\right)^{-\xi^n_{A,i}} - 2\beta_{v,j}\beta_{v,i}\left(1+\frac{\gamma_{v,j}}{\lambda_{\mathrm{eq},j}}\right)^{-\xi_{A,j}}$$
$$\times\left(1+\frac{\gamma_{v,i}}{\lambda_{\mathrm{eq},i}}\right)^{-\xi^n_{A,i}}\Bigg]^{\frac{1}{2}}, \tag{A22}$$

with

$$\xi^n_{i,A} = \mu_{\mathrm{eq},i}+\sigma_{A,i}+1+3n, \tag{A23}$$
$$\xi_{j,A} = \mu_{\mathrm{eq},j}+\sigma_{A,j}+1. \tag{A24}$$

A3 Ice self-collection

A3.1 D-kernel

For ice self-collection the geometry part (Eq. A13) simplifies to

$$\mathcal{C}_{n,ii} = \left(\frac{\pi\rho_{\mathrm{w}}}{6}\right)^n\frac{\pi}{4}N_i^2\left[2\delta^0_{D,i}+\delta^n_{D,ii}\right]\overline{D}_i^2, \tag{A25}$$

where δ_i^n is equal to δ_p^0 of Eq. (90) of SB2006 and δ_{ii}^n is equal to δ_g^0 of Eq. (91) of SB2006.

$$\delta_{D,i}^n = \frac{\Gamma((2b_i+\nu_{m,i}+1+n)/\mu_{m,i})}{\Gamma((\nu_{m,i}+1)/\mu_{m,i})} \left[\frac{\Gamma((\nu_{m,i}+1)/\mu_{m,i})}{\Gamma((\nu_{m,i}+2)/\mu_{m,i})}\right]^{2b_i+n} \tag{A26}$$

$$\delta_{D,ii}^n = 2\frac{\Gamma((b_i+\nu_{m,i}+1+n)/\mu_{m,i})}{\Gamma((\nu_{m,i}+1)/\mu_{m,i})^2} \Gamma((b_i+\nu_{m,i}+1)/\mu_{m,i}) \times \left[\frac{\Gamma((\nu_{m,i}+1)/\mu_{m,i})}{\Gamma((\nu_{m,i}+2)/\mu_{m,i})}\right]^{2b_i+n} \tag{A27}$$

The velocity variance simplifies to

$$\overline{\Delta v}_{n,ii} = \beta_{v,i}\sqrt{2}\left[\left(1+\frac{2\gamma_{v,i}}{\lambda_{\mathrm{eq},i}}\right)^{-\xi_{D,i}^n} - \left(1+\frac{\gamma_{v,i}}{\lambda_{\mathrm{eq},i}}\right)^{-2\xi_{D,i}^n}\right]^{\frac{1}{2}}, \tag{A28}$$

with

$$\xi_{D,i}^n = \mu_{\mathrm{eq},i} + 3 + 3n. \tag{A29}$$

A3.2 A-kernel

For ice self-collection $\mathcal{C}$ (Eq. A13) simplifies to

$$\mathcal{C}_{n,ii} = \left(\frac{\pi\rho_\mathrm{w}}{6}\right)^n N_i^2 \left[\delta_{A,i}^n + \delta_{A,ii}^n + \delta_{A,i2}^n\right] \left(\frac{6a_{m,i}}{\pi\rho_\mathrm{w}}\right)^{\frac{\sigma_{A,i}}{3}} \min\left(\gamma_{A,i}\left(\frac{\pi\rho_\mathrm{w}}{6a_{m,i}}\right)^{\frac{\sigma_{A,i}}{3}} \overline{D}_{\max,i}^{\sigma_{A,i}^*}, \frac{\pi}{4}\overline{D}_{\max,i}^2\right), \tag{A30}$$

with the following.

$$\delta_{A,i}^n = \frac{\Gamma(\mu_{\mathrm{eq},i}+\sigma_{A,i}+1+3n)}{\Gamma(\mu_{\mathrm{eq},i}+1)} c_{\lambda,i}^{\sigma_{A,i}+3n} \tag{A31}$$

$$\delta_{A,ii}^n = 2\frac{\Gamma(\mu_{\mathrm{eq},i}+\sigma_{A,i}/2+1+3n)}{\Gamma(\mu_{\mathrm{eq},i}+1)^2}\Gamma (\mu_{\mathrm{eq},i}+\sigma_{A,i}/2+1) c_{\lambda,i}^{\sigma_{A,i}+3n} \tag{A32}$$

$$\delta_{A,i2}^n = \frac{\Gamma(\mu_{\mathrm{eq},i}+\sigma_{A,i}+1)}{\Gamma(\mu_{\mathrm{eq},i}+1)} c_{\lambda,i}^{\sigma_{A,i}+3n} \left[\frac{\Gamma(\mu_{\mathrm{eq},i}+4)}{\Gamma(\mu_{\mathrm{eq},i}+1)}\right]^n \tag{A33}$$

$$\sigma_{A,i}^* = \frac{b_{m,i}\sigma_{A,i}}{3} \tag{A34}$$

$$c_{\lambda,i} = \left[\frac{6a_{m,i}}{\pi\rho_\mathrm{w}}\frac{\Gamma(\mu_{\mathrm{eq},i}+1)}{\Gamma(\mu_{\mathrm{eq},i}+4)}\right]^{1/3} \tag{A35}$$

For small sizes, the parametrization of A_act yields values of A_r larger than 1 (e.g., columns smaller than 8×10^{-5}; Fig. 3d). For small mean sizes, these particles with unphysical A_r can substantially contribute to $\mathcal{C}_{n,ii}$. Therefore, we limit A_act to A_sphere in Eq. (A30). The effect of this limiter can be seen in the kink of the bulk collision rates (Fig. B3c and d).

Inserting the velocity relation (Eq. 11) and the size distribution using D_eq (Eq. 7) into the velocity variance (Eq. A14) and solving the integral, we find

$$\overline{\Delta v}_{n,ii} = \sqrt{2}\beta_{v,i}\left[\left(1+\frac{2\gamma_{v,i}}{\lambda_{\mathrm{eq},i}}\right)^{-\xi_{A,i}^n} - \left(1+\frac{\gamma_{v,i}}{\lambda_{\mathrm{eq},i}}\right)^{-2\xi_{A,i}^n}\right]^{\frac{1}{2}}, \tag{A36}$$

with

$$\xi_{i,A}^n = \mu_{\mathrm{eq},i} + \sigma_{A,i} + 1 + 3n. \tag{A37}$$

A4 Snow self-collection

A4.1 D-kernel

For snow self-collection only the first moment is relevant and $\mathcal{C}$ (Eq. A13) simplifies to

$$\mathcal{C}_{0,\mathrm{ss}} = \frac{\pi}{4}N_\mathrm{s}^2\left[2\delta_{D,s}^0 + \delta_{D,ss}^0\right]\overline{D}_\mathrm{s}^2, \tag{A38}$$

where δ_s^n is equal to δ_p^0 of Eq. (90) of SB2006 and δ_ss^n is equal to δ_g^0 of Eq. (91) of SB2006.

$$\delta_{D,s}^0 = \frac{\Gamma((2b_\mathrm{s}+\nu_{m,\mathrm{s}}+1)/\mu_{m,\mathrm{s}})}{\Gamma((\nu_{m,\mathrm{s}}+1)/\mu_{m,\mathrm{s}})}\left[\frac{\Gamma((\nu_{m,\mathrm{s}}+1)/\mu_{m,\mathrm{s}})}{\Gamma((\nu_{m,\mathrm{s}}+2)/\mu_{m,\mathrm{s}})}\right]^{2b_\mathrm{s}} \tag{A39}$$

$$\delta_{D,ss}^0 = 2\left[\frac{\Gamma((b_\mathrm{s}+\nu_{m,\mathrm{s}}+1)/\mu_{m,\mathrm{s}})}{\Gamma((\nu_{m,\mathrm{s}}+1)/\mu_{m,\mathrm{s}})}\right]^2\left[\frac{\Gamma((\nu_{m,\mathrm{s}}+1)/\mu_{m,\mathrm{s}})}{\Gamma((\nu_{m,\mathrm{s}}+2)/\mu_{m,\mathrm{s}})}\right]^{2b_\mathrm{s}} \tag{A40}$$

The velocity variance simplifies to

$$\overline{\Delta v}_{0,\mathrm{ss}} = \sqrt{2}\beta_{v,\mathrm{s}}\left[\left(1+\frac{2\gamma_{v,\mathrm{s}}}{\lambda_{\mathrm{eq,\,s}}}\right)^{-\xi_{D,s}} - \left(1+\frac{\gamma_{v,\mathrm{s}}}{\lambda_{\mathrm{eq,\,s}}}\right)^{-2\xi_{D,s}}\right]^{\frac{1}{2}}, \tag{A41}$$

with

$$\xi_{D,s} = \mu_{\mathrm{eq,\,s}} + 3. \tag{A42}$$

A4.2 A-kernel

$\mathcal{C}$ of the A-kernel for snow self-collection simplifies to

$$\mathcal{C}_{0,\mathrm{ss}} = N_\mathrm{s}^2\left[2\delta_{A,\mathrm{s}}^0 + \delta_{\mathrm{A,ss}}^0\right]\left(\frac{6a_{m,\mathrm{s}}}{\pi\rho_\mathrm{w}}\right)^{\frac{\sigma_{A,\mathrm{s}}}{3}} \min\left(\gamma_{A,\mathrm{s}}\left(\frac{\pi\rho_\mathrm{w}}{6a_{m,\mathrm{s}}}\right)^{\frac{\sigma_{A,\mathrm{s}}}{3}}\overline{D}_{\max,\mathrm{s}}^{\sigma_{A,\mathrm{s}}^*}, \frac{\pi}{4}\overline{D}_{\max,\mathrm{s}}^2\right), \tag{A43}$$

with the following.

$$\delta_{A,\mathrm{s}}^0 = \frac{\Gamma(\mu_{\mathrm{eq,\,s}}+\sigma_{A,\mathrm{s}}+1)}{\Gamma(\mu_{\mathrm{eq,\,s}}+1)}c_{\lambda,\mathrm{s}}^{\sigma_{A,\mathrm{s}}} \tag{A44}$$

$$\delta_{\mathrm{A,ss}}^0 = 2\frac{\Gamma(\mu_{\mathrm{eq,s}}+\sigma_{A,\mathrm{s}}/2+1)^2}{\Gamma(\mu_{\mathrm{eq,s}}+1)^2}c_{\lambda,\mathrm{s}}^{\sigma_{A,\mathrm{s}}} \tag{A45}$$

$$\sigma_{A,\mathrm{s}}^* = \frac{b_{m,\mathrm{s}}\sigma_{A,\mathrm{s}}}{3} \tag{A46}$$

$$c_{\lambda,\mathrm{s}} = \left[\frac{6a_{m,\mathrm{s}}}{\pi\rho_\mathrm{w}}\frac{\Gamma(\mu_{\mathrm{eq,\,s}}+1)}{\Gamma(\mu_{\mathrm{eq,\,s}}+4)}\right]^{1/3} \tag{A47}$$

The area ratios are limited in the same way as for ice self-collection.

Table A1. Prefactor Φ of the aggregation rates (Eq. A2) for different aggregation processes and the predicted moments of the cloud ice and snow distribution.

Collision partners					
i	j	$\frac{\partial N_{\text{cloud ice}}}{\partial t}$	$\frac{\partial L_{\text{cloud ice}}}{\partial t}$	$\frac{\partial N_{\text{snow}}}{\partial t}$	$\frac{\partial L_{\text{snow}}}{\partial t}$
Cloud ice	cloud ice	−1	−1	+1/2	+1
Cloud ice	snow	−1	−1	0	+1
Snow	snow	0	0	−1	0

The velocity variance simplifies to

$$\overline{\Delta v}_{0,\text{s}} = \sqrt{2}\beta_{v,\text{s}}\left[\left(1+\frac{2\gamma_{v,\text{s}}}{\lambda_{\text{eq, s}}}\right)^{-\xi_{A,\text{s}}} - \left(1+\frac{\gamma_{v,\text{s}}}{\lambda_{\text{eq, s}}}\right)^{-2\xi_{A,\text{s}}}\right]^{0.5}, \quad \text{(A48)}$$

with

$$\xi_{A,\text{s}} = \mu_{\text{eq, s}} + \sigma_{A,\text{s}} + 1. \quad \text{(A49)}$$

Appendix B: Atmospheric setup for 1D simulation and atmospheric fields of the case study predicted by ICON-LEM

Figure B5 shows the atmospheric variables from O20 simulations and the setup for the snowshaft simulations. Figure B6 shows the atmospheric variables of the case study.

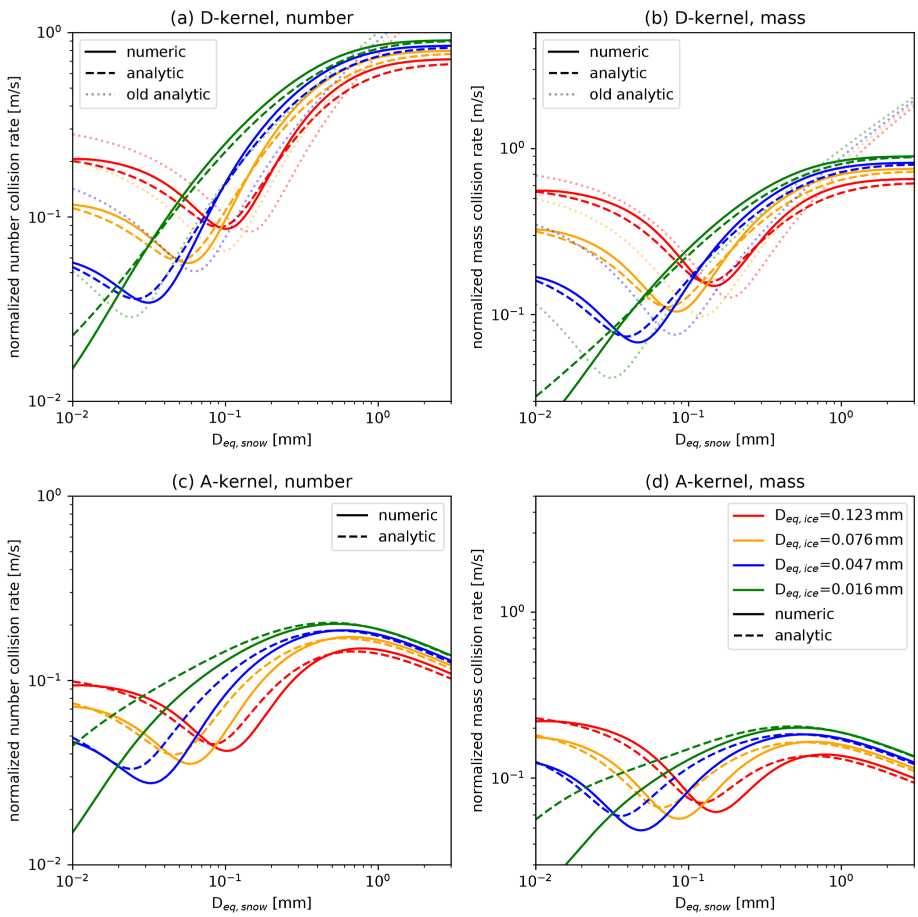

Figure B1. Numeric and analytic solution of the bulk collision rates for ice–snow (column and Mix2, respectively) collisions for Atlas-type and power-law velocity size relations. The shape parameter is $\mu_{eq} = 2$ (Eq. 7), which is equal to $\mu_m = 0$ (Eq. 5) for cloud ice and snow. Left: number density, right: mass density; top: D-kernel; bottom: A-kernel. **(a, c)** normalized number collision rate, **(b, d)** normalized mass collision rate, **(a, b)** D-kernel, **(c, d)** A-kernel.

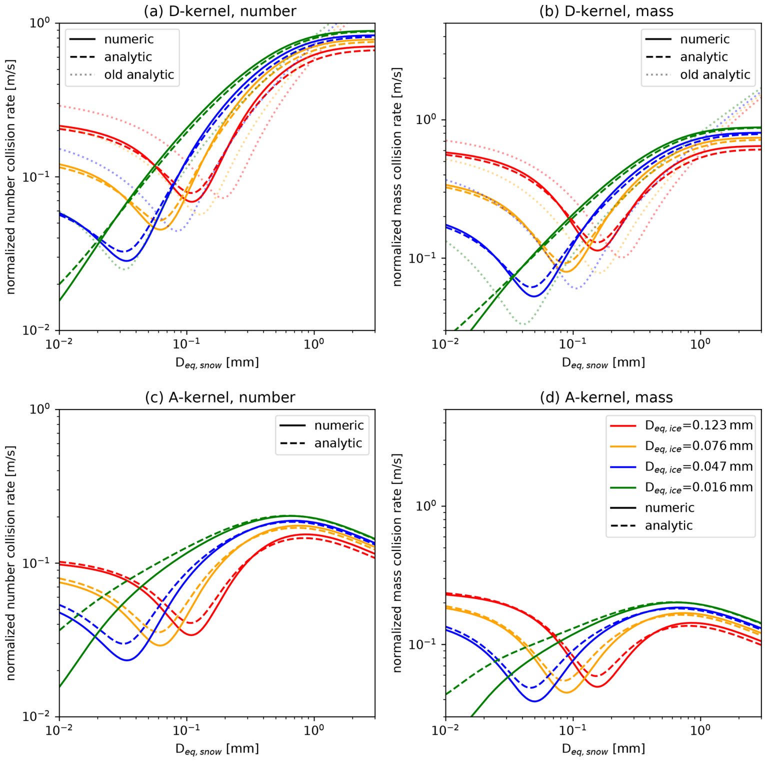

Figure B2. Same as Fig. B1 but with $\mu_{\mathrm{eq}} = 8$ (Eq. 7), which is equal to $\mu_m = 2$ (Eq. 5) for snow.

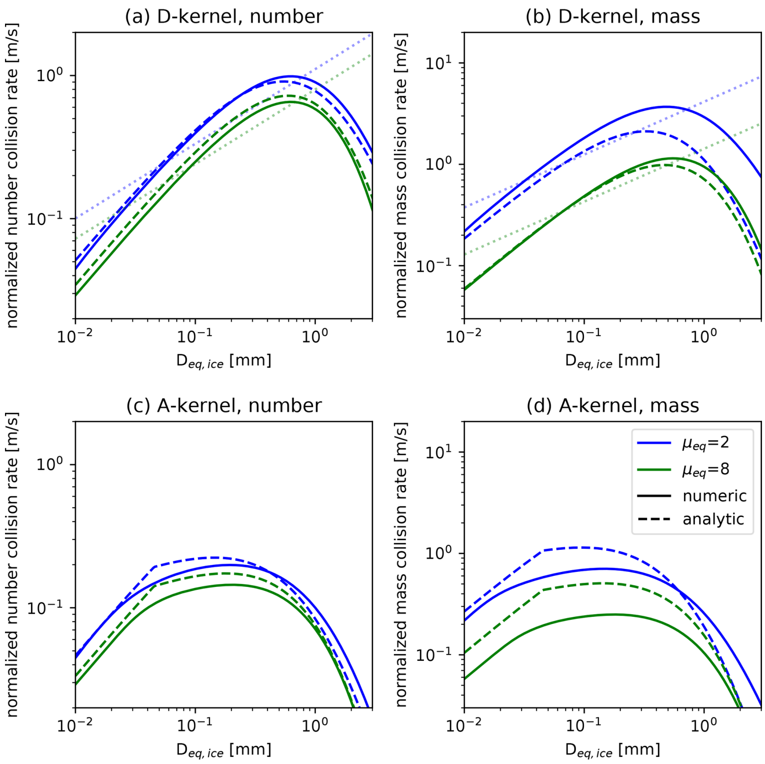

Figure B3. Numeric and analytic solution of the bulk collision rates for ice–ice (both column) collisions: **(a, c)** normalized number collision rate, **(b, d)** normalized mass collision rate, **(a, b)** D-kernel, **(c, d)** A-kernel.

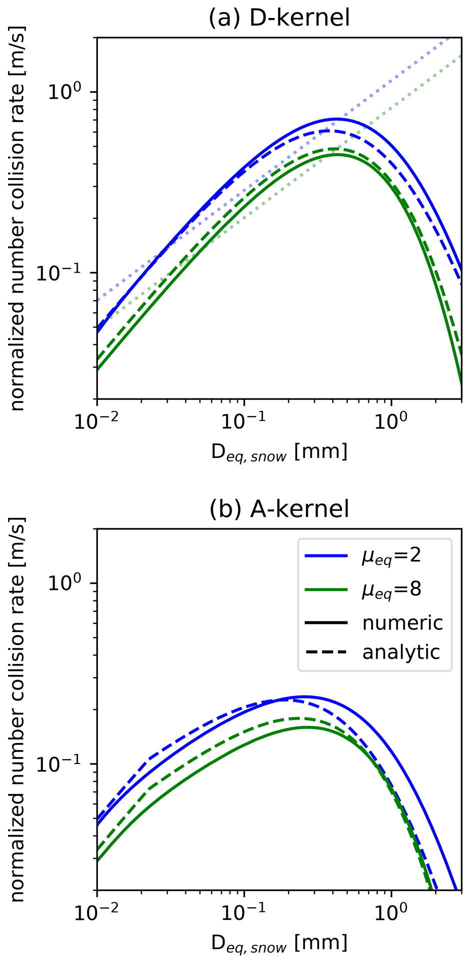

Figure B4. Numeric and analytic solution of the bulk collision rates for snow–snow (both Mix2) collisions: **(a)** D-kernel; **(b)** A-kernel.

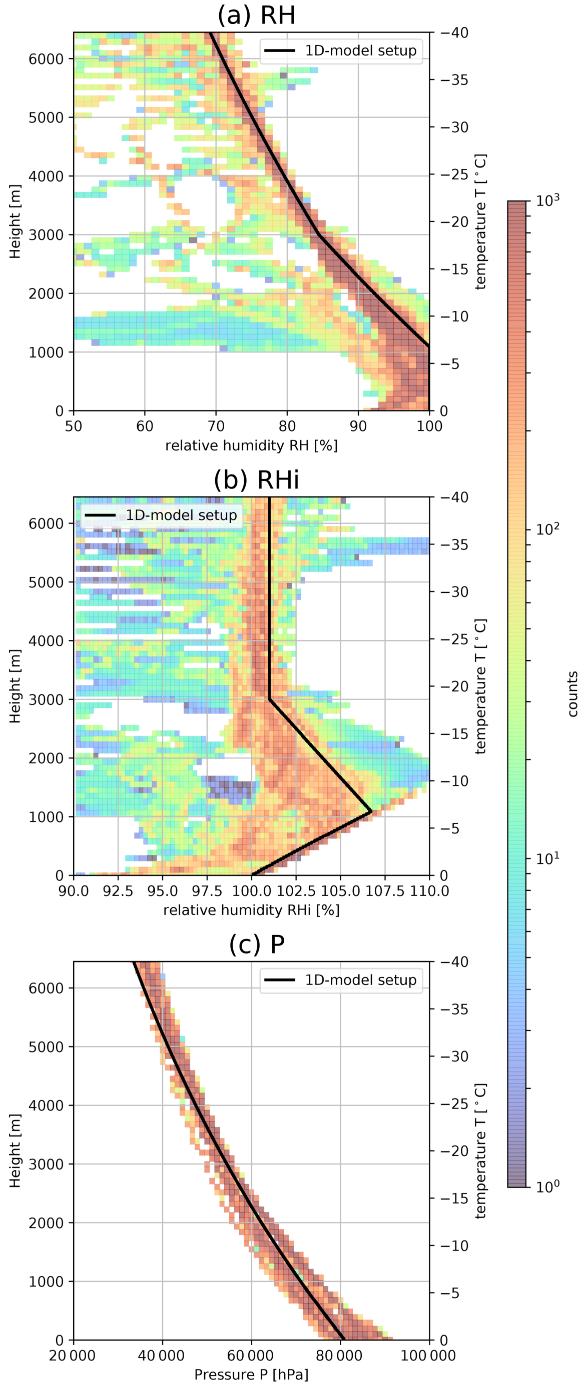

Figure B5. Setup of atmospheric variables in the 1D simulations (Sect. 3.2) (black line), which was chosen based on the histograms from the ICON-LEM simulation (the histogram is shown in the background, O20). The histogram is filtered to include only profiles for which the rain rate exceeds 1 mm h^{-1}. **(a)** Temperature, **(b)** relative humidity with respect to water, and **(c)** relative humidity with respect to ice. The height of the melting temperature 0°C is set to 0 m, and other heights are calculated assuming a temperature gradient of 0.0062 K m^{-1}. Counts in the ICON-LEM simulations from O20 are color-coded.

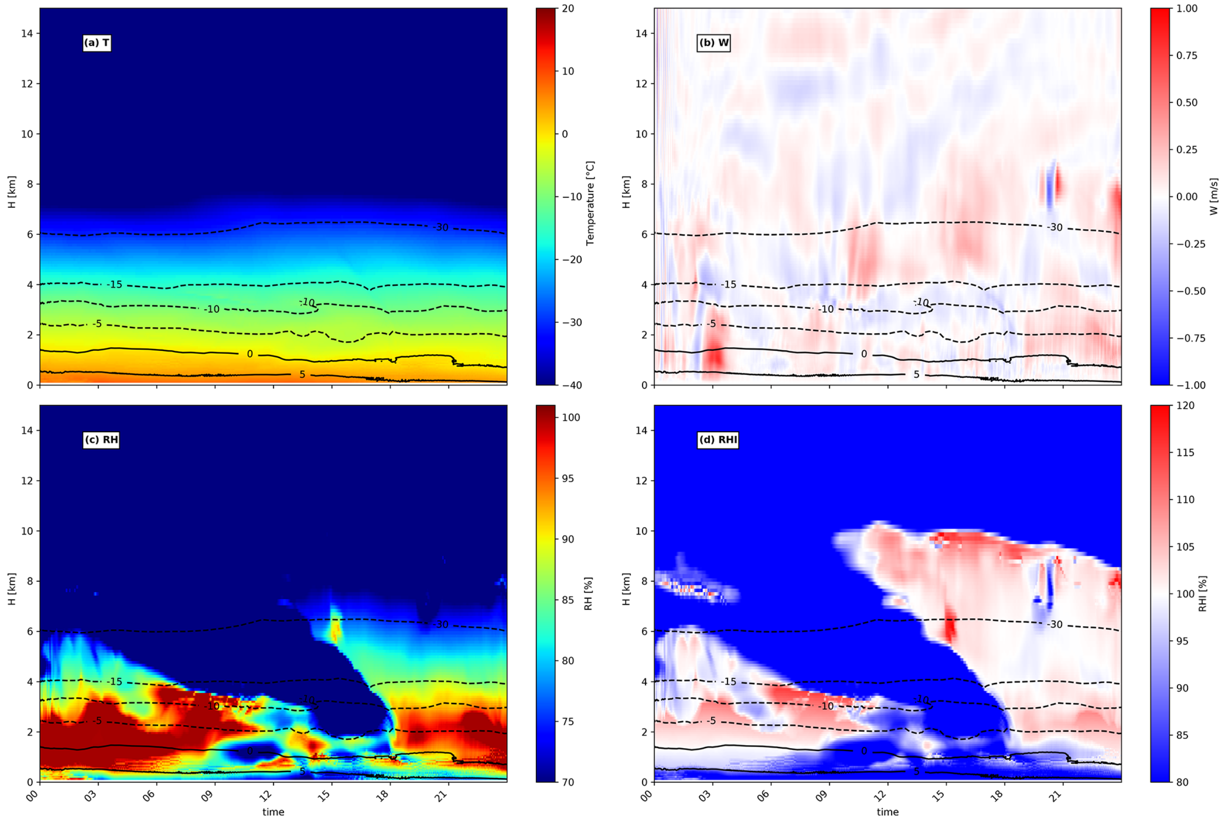

Figure B6. Temperature **(a)**, vertical velocity **(b)**, and relative humidity with respect to water **(c)** and ice **(d)** over Jülich in the SB06 default simulation on 3 January 2016. Temperature isolines are shown in each plot.

Code availability. The source code of the snowshaft model is part of the McSnow model. McSnow and the code to test and optimize the variance approximation of the bulk collision integrals (COLLINT) are hosted on GitLab. The DWD software used in this study (McSnow, COLLINT, etc.) is part of the ICON modeling framework, and access can be granted by AS based on an ICON license agreement. The version of ICON used in this study is available at: https://doi.org/10.5281/zenodo.4740092, Karrer et al., 2021).

Supplement. The supplement related to this article is available online at: https://doi.org/10.5194/acp-21-17133-2021-supplement.

Author contributions. MK performed and analyzed the snowshaft and ICON-LEM simulation. MK and AS derived the new bulk aggregation formulations. MK and DO performed the forward operation and analyzed the statistics of the multi-month ICON-LEM simulations. SK supervised the project. MK and SK prepared the paper with contributions from all co-authors.

Competing interests. The authors declare that they have no conflicts of interest.

Disclaimer. Publisher's note: Copernicus Publications remains neutral with regard to jurisdictional claims in published maps and institutional affiliations.

Acknowledgements. Contributions by Markus Karrer, Stefan Kneifel, and Davide Ori were funded by the German Research Foundation (DFG) under grant KN 1112/2-1 as part of the Emmy-Noether Group "Optimal combination of Polarimetric and Triple Frequency radar techniques for Improving Microphysical process understanding of cold clouds" (OPTIMIce). AS received funding from the German Science Foundation (DFG) under grant SE 1784/3-1, project ID 408011764 (IMPRINT), as part of the DFG priority program SPP 2115 (PROM) on radar polarimetry. Markus Karrer also acknowledges support by the Graduate School of Geosciences at the University of Cologne. We thank Vera Schemann for support with the ICON-LEM simulations. This work used resources of the Deutsches Klimarechenzentrum (DKRZ) granted by its Scientific Steering Committee (WLA) under project ID bb1086. We also acknowledge the constructive comments of two anonymous reviewers, which helped to improve the paper.

Financial support. This research has been supported by the Deutsche Forschungsgemeinschaft (grant no. KN 1112/2-1; grant no. SE 1784/3-1, project ID 408011764 (IMPRINT)) as part of the DFG priority program SPP 2115 (PROM).

Review statement. This paper was edited by Franziska Glassmeier and reviewed by two anonymous referees.

References

Andrić, J., Kumjian, M. R., Zrnić, D. S., Straka, J. M., and Melnikov, V. M.: Polarimetric signatures above the melting layer in winter storms: An observational and modeling study, J. Appl. Meteorol. Clim., 52, 682–700, https://doi.org/10.1175/JAMC-D-12-028.1, 2013.

Barrett, A. I., Westbrook, C. D., Nicol, J. C., and Stein, T. H. M.: Rapid ice aggregation process revealed through triple-wavelength Doppler spectrum radar analysis, Atmos. Chem. Phys., 19, 5753–5769, https://doi.org/10.5194/acp-19-5753-2019, 2019.

Barthazy, E. and Schefold, R.: Fall velocity of snowflakes of different riming degree and crystal types, Atmos. Res., 82, 391–398, https://doi.org/10.1016/j.atmosres.2005.12.009, 2006.

Battaglia, A., Westbrook, C. D., Kneifel, S., Kollias, P., Humpage, N., Löhnert, U., Tyynelä, J., and Petty, G. W.: G band atmospheric radars: new frontiers in cloud physics, Atmos. Meas. Tech., 7, 1527–1546, https://doi.org/10.5194/amt-7-1527-2014, 2014.

Battaglia, A., Tanelli, S., Tridon, F., Kneifel, S., Leinonen, J., and Kollias, P.: Triple-Frequency Radar Retrievals, Adv. Glob. Change Res., 67, 211–229, https://doi.org/10.1007/978-3-030-24568-9_13, 2020.

Böhm, J. P.: A general hydrodynamic theory for mixed-phase microphysics. Part I: drag and fall speed of hydrometeors, Atmos. Res., 27, 253–274, https://doi.org/10.1016/0169-8095(92)90035-9, 1992.

Connolly, P. J., Emersic, C., and Field, P. R.: A laboratory investigation into the aggregation efficiency of small ice crystals, Atmos. Chem. Phys., 12, 2055–2076, https://doi.org/10.5194/acp-12-2055-2012, 2012.

Cotton, W. R., Stephens, M. A., Nehrkorn, T., and Tripoli, G. J.: The Colorado State University three-dimensional cloud/mesoscale model 1982 – Part II: an ice phase parameterization, Journal de Recherches Atmospheriques, 16, 295–320, 1982.

Dias Neto, J., Kneifel, S., Ori, D., Trömel, S., Handwerker, J., Bohn, B., Hermes, N., Mühlbauer, K., Lenefer, M., and Simmer, C.: The TRIple-frequency and Polarimetric radar Experiment for improving process observations of winter precipitation, Earth Syst. Sci. Data, 11, 845–863, https://doi.org/10.5194/essd-11-845-2019, 2019.

Dipankar, A., Stevens, B., Heinze, R., Moseley, C., Zängl, G., Giorgetta, M., and Brdar, S.: Large eddy simulation using the general circulation model ICON, J. Adv. Model. Earth Sys., 7, 963–986, https://doi.org/10.1002/2015MS000431, 2015.

Dunnavan, E. L.: How snow aggregate ellipsoid shape and orientation variability affects fall speed and self-aggregation rates, J. Atmos. Sci., 78, 51–73, https://doi.org/10.1175/JAS-D-20-0128.1, 2021.

Field, P. R.: Bimodal ice spectra in frontal clouds, Q. J. Roy. Meteor. Soc., 126, 379–392, https://doi.org/10.1002/qj.49712656302, 2000.

Field, P. R., Hogan, R. J., Brown, P. R., Illingworth, A. J., Choularton, T. W., and Cotton, R. J.: Parametrization of ice-particle size distributions for mid-latitude stratiform cloud, Q. J. Roy. Meteor. Soc., 131, 1997–2017, https://doi.org/10.1256/qj.04.134, 2005.

Gillespie, D. T.: Three Models for the Coalescence Growth of Cloud Drops., J. Atmos.

Sci., 32, 600–607, https://doi.org/10.1175/1520-0469(1975)032<0600:TMFTCG>2.0.CO;2, 1975.

Hashino, T. and Tripoli, G. J.: The Spectral Ice Habit Prediction System (SHIPS). Part IV: Box model simulations of the habit-dependent aggregation process, J. Atmos. Sci., 68, 1142–1161, https://doi.org/10.1175/2011JAS3667.1, 2011.

Heinze, R., Dipankar, A., Henken, C. C., Moseley, C., Sourdeval, O., Trömel, S., Xie, X., Adamidis, P., Ament, F., Baars, H., Barthlott, C., Behrendt, A., Blahak, U., Bley, S., Brdar, S., Brueck, M., Crewell, S., Deneke, H., Di Girolamo, P., Evaristo, R., Fischer, J., Frank, C., Friederichs, P., Göcke, T., Gorges, K., Hande, L., Hanke, M., Hansen, A., Hege, H. C., Hoose, C., Jahns, T., Kalthoff, N., Klocke, D., Kneifel, S., Knippertz, P., Kuhn, A., van Laar, T., Macke, A., Maurer, V., Mayer, B., Meyer, C. I., Muppa, S. K., Neggers, R. A., Orlandi, E., Pantillon, F., Pospichal, B., Röber, N., Scheck, L., Seifert, A., Seifert, P., Senf, F., Siligam, P., Simmer, C., Steinke, S., Stevens, B., Wapler, K., Weniger, M., Wulfmeyer, V., Zängl, G., Zhang, D., and Quaas, J.: Large-eddy simulations over Germany using ICON: a comprehensive evaluation, Q. J. Roy. Meteor. Soc., 143, 69–100, https://doi.org/10.1002/qj.2947, 2017.

Heymsfield, A. J.: Properties of Tropical and Midlatitude Ice Cloud Particle Ensembles, Part II: Applications for Mesoscale and Climate Models in: Journal of the Atmospheric Sciences Volume 60 Issue 21 (2003), J. Atmos. Sci., 60, 2592–2611, 2003.

Heymsfield, A. J. and Westbrook, C. D.: Advances in the estimation of ice particle fall speeds using laboratory and field measurements, J. Atmos. Sci., 67, 2469–2482, https://doi.org/10.1175/2010JAS3379.1, 2010.

Heymsfield, A. J., Schmitt, C., Chen, C. C. J., Bansemer, A., Gettelman, A., Field, P. R., and Liu, C.: Contributions of the Liquid and Ice Phases to Global Surface Precipitation: Observations and Global Climate Modeling, J. Atmos. Sci., 77, 2629–2648, https://doi.org/10.1175/JAS-D-19-0352.1, 2020.

Hobbs, P. V., Chang, S., and Locatelli, J. D.: The dimensions and aggregation of ice crystals in natural clouds, J. Geophys. Res., 79, 2199–2206, https://doi.org/10.1029/jc079i015p02199, 1974.

Hogan, R. J. and Westbrook, C. D.: Equation for the microwave backscatter cross section of aggregate snowflakes using the self-similar Rayleigh-Gans approximation, J. Atmos. Sci., 71, 3292–3301, https://doi.org/10.1175/JAS-D-13-0347.1, 2014.

Hogan, R. J., Illingworth, A. J., and Sauvageot, H.: Measuring crystal size in cirrus using 35- and 94-GHz radars, J. Atmos. Ocean. Tech., 17, 27–37, https://doi.org/10.1175/1520-0426(2000)017<0027:MCSICU>2.0.CO;2, 2000.

Hogan, R. J., Honeyager, R., Tyynelä, J., and Kneifel, S.: Calculating the millimetre-wave scattering phase function of snowflakes using the self-similar Rayleigh–Gans Approximation, Q. J. Roy. Meteor. Soc., 143, 834–844, https://doi.org/10.1002/qj.2968, 2017.

Hosler, C. L. and Hallgren, R. E.: The aggregation of small ice crystals, Discussions of the Faraday Society, 30, 200–207, https://doi.org/10.1039/DF9603000200, 1960.

Illingworth, A. J., Hogan, R. J., O'Connor, E. J., Bouniol, D., Brooks, M. E., Delanoë, J., Donovan, D. P., Eastment, J. D., Gaussiat, N., Goddard, J. W., Haeffelin, M., Klein Baltinik, H., Krasnov, O. A., Pelon, J., Piriou, J. M., Protat, A., Russchenberg, H. W., Seifert, A., Tompkins, A. M., van Zadelhoff, G. J., Vinit, F., Willen, U., Wilson, D. R., and Wrench, C. L.: Cloud-net: Continuous evaluation of cloud profiles in seven operational models using ground-based observations, B. Am. Meteorol. Soc., 88, 883–898, https://doi.org/10.1175/BAMS-88-6-883, 2007.

Kajikawa, M. and Heymsfield, A. J.: Aggregation of ice crystals in cirrus, https://doi.org/10.1175/1520-0469(1989)046<3108:AOICIC>2.0.CO;2, 1989.

Kalesse, H., Szyrmer, W., Kneifel, S., Kollias, P., and Luke, E.: Fingerprints of a riming event on cloud radar Doppler spectra: observations and modeling, Atmos. Chem. Phys., 16, 2997–3012, https://doi.org/10.5194/acp-16-2997-2016, 2016.

Kanji, Z. A., Ladino, L. A., Wex, H., Boose, Y., Burkert-Kohn, M., Cziczo, D. J., and Krämer, M.: Overview of Ice Nucleating Particles, Meteorol. Monogr., 58, 1–33, https://doi.org/10.1175/AMSMONOGRAPHS-D-16-0006.1, 2017.

Karrer, M., Seifert, A., Siewert, C., Ori, D., von Lerber, A., and Kneifel, S.: Ice Particle Properties Inferred From Aggregation Modelling, J. Adv. Model. Earth Sys., 12, e2020MS002066, https://doi.org/10.1029/2020MS002066, 2020.

Karrer, M.: ICON-LEM version used for the publication "Improving the Representation of Aggregation in a Two-moment Microphysical Scheme with Statistics of Multi-frequency Doppler Radar Observations", Zenodo [code], https://doi.org/10.5281/zenodo.4740092, 2021.

Keith, W. D. and Saunders, C. P.: The collection efficiency of a cylindrical target for ice crystals, Atmos. Res., 23, 83–95, https://doi.org/10.1016/0169-8095(89)90059-8, 1989.

Kennedy, P. C. and Rutledge, S. A.: S-band dual-polarization radar observations of winter storms, J. Appl. Meteorol. Clim., 50, 844–858, https://doi.org/10.1175/2010JAMC2558.1, 2011.

Khain, A. P., Beheng, K. D., Heymsfield, A., Korolev, A., Krichak, S. O., Levin, Z., Pinsky, M., Phillips, V., Prabhakaran, T., Teller, A., Van Den Heever, S. C., and Yano, J. I.: Representation of microphysical processes in cloud-resolving models: Spectral (bin) microphysics versus bulk parameterization, Rev. Geophys., 53, 247–322, https://doi.org/10.1002/2014RG000468, 2015.

Kienast-Sjögren, E., Spichtinger, P., and Gierens, K.: Formulation and test of an ice aggregation scheme for two-moment bulk microphysics schemes, Atmos. Chem. Phys., 13, 9021–9037, https://doi.org/10.5194/acp-13-9021-2013, 2013.

Kneifel, S. and Moisseev, D. N.: Long-term statistics of riming in nonconvective clouds derived from ground-based doppler cloud radar observations, J. Atmos. Sci., 77, 3495–3508, https://doi.org/10.1175/JAS-D-20-0007.1, 2020.

Kneifel, S., Von Lerber, A., Tiira, J., Moisseev, D. N., Kollias, P., and Leinonen, J.: Observed relations between snowfall microphysics and triple-frequency radar measurements, J. Geophys. Res., 120, 6034–6055, https://doi.org/10.1002/2015JD023156, 2015.

Kneifel, S., Leinonen, J., Tyynelä, J., Ori, D., and Battaglia, A.: Scattering of Hydrometeors, in: Advances in Global Change Research, Springer, 67, 249–276, https://doi.org/10.1007/978-3-030-24568-9_15, 2020.

Korolev, A. and Leisner, T.: Review of experimental studies of secondary ice production, Atmos. Chem. Phys., 20, 11767–11797, https://doi.org/10.5194/acp-20-11767-2020, 2020.

Kumjian, M. R. and Ryzhkov, A. V.: The impact of evaporation on polarimetric characteristics of rain: Theoretical model and practical implications, J. Appl. Meteorol. Clim., 49, 1247–1267, https://doi.org/10.1175/2010JAMC2243.1, 2010.

Lamb, D. and Verlinde, J.: Physics and chemistry of clouds, Cambridge University Press, https://doi.org/10.1017/CBO9780511976377, 2011.

Liao, L., Meneghini, R., Iguchi, T., and Detwiler, A.: Use of dual-wavelength radar for snow parameter estimates, J. Atmos. Ocean. Tech., 22, 1494–1506, https://doi.org/10.1175/JTECH1808.1, 2005.

Lin, Y. L., Farley, R. D., and Orville, H. D.: Bulk parameterization of the snow field in a cloud model., J. Clim. Appl. Meteorol., 22, 1065–1092, https://doi.org/10.1175/1520-0450(1983)022<1065:BPOTSF>2.0.CO;2, 1983.

Lohmann, U., Lüönd, F., and Mahrt, F.: An introduction to clouds: From the microscale to climate, Cambridge University Press, https://doi.org/10.1017/CBO9781139087513, 2016.

Löhnert, U., Schween, J. H., Acquistapace, C., Ebell, K., Maahn, M., Barrera-Verdejo, M., Hirsikko, A., Bohn, B., Knaps, A., O'Connor, E., Simmer, C., Wahner, A., and Crewell, S.: JOYCE: Jülich Observatory for Cloud Evolution, B. Am. Meteorol. Soc., 96, 1157–1174, https://doi.org/10.1175/BAMS-D-14-00105.1, 2015.

Marke, T., Crewell, S., Schemann, V., Schween, J. H., and Tuononen, M.: Long-term observations and high-resolution modeling of midlatitude nocturnal boundary layer processes connected to low-level jets, J. Appl. Meteorol. Clim., 57, 1155–1170, https://doi.org/10.1175/JAMC-D-17-0341.1, 2018.

Mason, S. L., Hogan, R. J., Westbrook, C. D., Kneifel, S., Moisseev, D., and von Terzi, L.: The importance of particle size distribution and internal structure for triple-frequency radar retrievals of the morphology of snow, Atmos. Meas. Tech., 12, 4993–5018, https://doi.org/10.5194/amt-12-4993-2019, 2019.

Mason, S. L., Chiu, C. J., Hogan, R. J., Moisseev, D. N., and Kneifel, S.: Retrievals of Riming and Snow Density From Vertically Pointing Doppler Radars, J. Geophys. Res.-Atmos., 123, 13807–13834, https://doi.org/10.1029/2018JD028603, 2018.

Matrosov, S. Y.: A dual-wavelength radar method to measure snowfall rate, J. Appl. Meteorol., 37, 1510–1521, https://doi.org/10.1175/1520-0450(1998)037<1510:ADWRMT>2.0.CO;2, 1998.

Mcfarquhar, G. M., Hsieh, T. L., Freer, M., Mascio, J., and Jewett, B. F.: The characterization of ice hydrometeor gamma size distributions as volumes in N0-λ-μ phase space: Implications for microphysical process modeling, J. Atmos. Sci., 72, 892–909, https://doi.org/10.1175/JAS-D-14-0011.1, 2015.

Mech, M., Maahn, M., Kneifel, S., Ori, D., Orlandi, E., Kollias, P., Schemann, V., and Crewell, S.: PAMTRA 1.0: the Passive and Active Microwave radiative TRAnsfer tool for simulating radiometer and radar measurements of the cloudy atmosphere, Geosci. Model Dev., 13, 4229–4251, https://doi.org/10.5194/gmd-13-4229-2020, 2020.

Milbrandt, J. A. and Morrison, H.: Parameterization of cloud microphysics based on the prediction of bulk ice particle properties, Part III: Introduction of multiple free categories, J. Atmos. Sci., 73, 975–995, https://doi.org/10.1175/JAS-D-15-0204.1, 2016.

Mitchell, D. L.: Evolution of snow-size spectra in cyclonic storms. Part I: snow growth by vapor deposition and aggregation, J. Atmos. Sci., 45, 3431–3451, https://doi.org/10.1175/1520-0469(1988)045<3431:EOSSSI>2.0.CO;2, 1988.

Mitchell, D. L.: Use of mass- and area-dimensional power laws for determining precipitation particle terminal velocities, J. Atmos. Sci., 53, 1710–1723, https://doi.org/10.1175/1520-0469(1996)053<1710:UOMAAD>2.0.CO;2, 1996.

Mitchell, D. L. and Heymsfield, A. J.: Refinements in the treatment of ice particle terminal velocities, highlighting aggregates, J. Atmos. Sci., 62, 1637–1644, https://doi.org/10.1175/JAS3413.1, 2005.

Moisseev, D. N., Lautaportti, S., Tyynela, J., and Lim, S.: Dual-polarization radar signatures in snowstorms: Role of snowflake aggregation, J. Geophys. Res., 120, 12644–12665, https://doi.org/10.1002/2015JD023884, 2015.

Morrison, H. and Milbrandt, J. A.: Parameterization of cloud microphysics based on the prediction of bulk ice particle properties. Part I: Scheme description and idealized tests, J. Atmos. Sci., 72, 287–311, https://doi.org/10.1175/JAS-D-14-0065.1, 2015.

Morrison, H., van Lier-Walqui, M., Fridlind, A. M., Grabowski, W. W., Harrington, J. Y., Hoose, C., Korolev, A., Kumjian, M. R., Milbrandt, J. A., Pawlowska, H., Posselt, D. J., Prat, O. P., Reimel, K. J., Shima, S. I., van Diedenhoven, B., and Xue, L.: Confronting the Challenge of Modeling Cloud and Precipitation Microphysics, J. Adv. Model. Earth Sys., 12, 2019MS001689, https://doi.org/10.1029/2019MS001689, 2020.

Mosimann, L.: An improved method for determining the degree of snow crystal riming by vertical Doppler radar, Atmos. Res., 37, 305–323, https://doi.org/10.1016/0169-8095(94)00050-N, 1995.

Ori, D., Schemann, V., Karrer, M., Dias Neto, J., von Terzi, L., Seifert, A., and Kneifel, S.: Evaluation of ice particle growth in ICON using statistics of multi-frequency Doppler cloud radar observations, Q. J. Roy. Meteor. Soc., 146, 3830–3849, https://doi.org/10.1002/qj.3875, 2020.

Ori, D., von Terzi, L., Karrer, M., and Kneifel, S.: snowScatt 1.0: consistent model of microphysical and scattering properties of rimed and unrimed snowflakes based on the self-similar Rayleigh–Gans approximation, Geosci. Model Dev., 14, 1511–1531, https://doi.org/10.5194/gmd-14-1511-2021, 2021.

Paukert, M., Fan, J., Rasch, P. J., Morrison, H., Milbrandt, J. A., Shpund, J., and Khain, A.: Three-Moment Representation of Rain in a Bulk Microphysics Model, J. Adv. Model. Earth Sys., 11, 257–277, https://doi.org/10.1029/2018MS001512, 2019.

Pfitzenmaier, L., Unal, C. M. H., Dufournet, Y., and Russchenberg, H. W. J.: Observing ice particle growth along fall streaks in mixed-phase clouds using spectral polarimetric radar data, Atmos. Chem. Phys., 18, 7843–7862, https://doi.org/10.5194/acp-18-7843-2018, 2018.

Phillips, V. T., Formenton, M., Bansemer, A., Kudzotsa, I., and Lienert, B.: A parameterization of sticking efficiency for collisions of snow and graupel with ice crystals: Theory and comparison with observations, J. Atmos. Sci., 72, 4885–4902, https://doi.org/10.1175/JAS-D-14-0096.1, 2015.

Pruppacher, H. and Klett, J.: Hydrodynamics of Single Cloud and Precipitation Particles, PhD. thesis, https://doi.org/10.1007/978-0-306-48100-0_10, 2010.

Pruppacher, H. R., Klett, J. D., and Wang, P. K.: Microphysics of Clouds and Precipitation, Aerosol Sci. Technol., 28, 381–382, https://doi.org/10.1080/02786829808965531, 1998.

Reitter, S., Fröhlich, K., Seifert, A., Crewell, S., and Mech, M.: Evaluation of ice and snow content in the global numerical weather prediction model GME with CloudSat, Geosci.

Model Dev., 4, 579–589, https://doi.org/10.5194/gmd-4-579-2011, 2011.

Schemann, V. and Ebell, K.: Simulation of mixed-phase clouds with the ICON large-eddy model in the complex Arctic environment around Ny-Ålesund, Atmos. Chem. Phys., 20, 475–485, https://doi.org/10.5194/acp-20-475-2020, 2020.

Schemann, V., Ebell, K., Pospichal, B., Neggers, R., Moseley, C., and Stevens, B.: Linking Large-Eddy Simulations to Local Cloud Observations, J. Adv. Model. Earth Sys., 12, e2020MS002209, https://doi.org/10.1029/2020MS002209, 2020.

Schmidt, G. A., Bader, D., Donner, L. J., Elsaesser, G. S., Golaz, J.-C., Hannay, C., Molod, A., Neale, R. B., and Saha, S.: Practice and philosophy of climate model tuning across six US modeling centers, Geosci. Model Dev., 10, 3207–3223, https://doi.org/10.5194/gmd-10-3207-2017, 2017.

Schrom, R. S. and Kumjian, M. R.: Connecting microphysical processes in colorado winter storms with vertical profiles of radar observations, J. Appl. Meteorol. Clim., 55, 1771–1787, https://doi.org/10.1175/JAMC-D-15-0338.1, 2016.

Seifert, A.: On the parameterization of evaporation of raindrops as simulated by a one-dimensional rainshaft model, J. Atmos. Sci., 65, 3608–3619, https://doi.org/10.1175/2008JAS2586.1, 2008.

Seifert, A. and Beheng, K. D.: A two-moment cloud microphysics parameterization for mixed-phase clouds, Part 1: Model description, Meteorol. Atmos. Phys., 92, 45–66, https://doi.org/10.1007/s00703-005-0112-4, 2006.

Seifert, A., Blahak, U., and Buhr, R.: On the analytic approximation of bulk collision rates of non-spherical hydrometeors, Geosci. Model Dev., 7, 463–478, https://doi.org/10.5194/gmd-7-463-2014, 2014.

Slater, B. and Michaelides, A.: Surface premelting of water ice, Nature Reviews Chemistry, 3, 172–188, https://doi.org/10.1038/s41570-019-0080-8, 2019.

Szyrmer, W. and Zawadzki, I.: Snow Studies. Part IV: Ensemble Retrieval of Snow Microphysics from Dual-Wavelength Vertically Pointing Radars, J. Atmos. Sci., 71, 1158–1170, 2014.

Tridon, F., Battaglia, A., and Kneifel, S.: Estimating total attenuation using Rayleigh targets at cloud top: applications in multilayer and mixed-phase clouds observed by ground-based multifrequency radars, Atmos. Meas. Tech., 13, 5065–5085, https://doi.org/10.5194/amt-13-5065-2020, 2020.

Tsai, T. C. and Chen, J. P.: Multimoment ice bulk microphysics scheme with consideration for particle shape and apparent density. Part I: Methodology and idealized simulation, J. Atmos. Sci., 77, 1821–1850, https://doi.org/10.1175/JAS-D-19-0125.1, 2020.

Verlinde, J., Flatau, P. J., and Cotton, W. R.: Analytical solutions to the collection growth equation: comparison with approximate methods and application to cloud microphysics parameterization schemes, J. Atmos. Sci., 47, 2871–2880, https://doi.org/10.1175/1520-0469(1990)047<2871:ASTTCG>2.0.CO;2, 1990.

Wang, P. K.: Physics and dynamics of clouds and precipitation, Vol. 9781107005, Cambridge University Press, https://doi.org/10.1017/CBO9780511794285, 2010.

Wisner, C., Orville, H. D., and Myers, C.: A Numerical Model of a Hail-Bearing Cloud, J. Atmos. Sci., 29, 1160–1181, 1972.

Zängl, G., Reinert, D., Rípodas, P., and Baldauf, M.: The ICON (ICOsahedral Non-hydrostatic) modelling framework of DWD and MPI-M: Description of the non-hydrostatic dynamical core, Q. J. Roy. Meteor. Soc., 141, 563–579, https://doi.org/10.1002/qj.2378, 2015.

4.1 BENCHMARK SIMULATIONS: IMPROVED SB TWO-MOMENT SCHEME VS. LAGRANGIAN PARTICLE MODEL MCSNOW

Karrer et al., 2021a investigated the sensitivity of aggregation to various parameters in the process description implemented in the SB scheme. While many parameters, such as the v size relationship, could be well constrained, the selection of the particle size distribution (PSD) width parameter μ (Equation 2.9) was still not straightforward. μ affects the simulated mean mass relatively little, but it affects the DWRs strongly. Thus, knowledge about the PSD width is crucial to link modeled mean mass and observed DWRs accurately.

Although the sensitivity of the simulated mean mass $\overline{x}$ to the chosen μ was observed to be small in the SB scheme, there might be inaccuracies of the simulated $\overline{x}$ due to the simplified treatment of the PSD shape. These inaccuracies might be revealed by a comparison between simulations with the SB scheme and the Lagrangian particle model McSnow. In contrast to a two-moment scheme such as the SB scheme, where μ is fixed for each particle category, a Lagrangian particle model such as McSnow simulates the evolution of the PSD explicitly (Section 2.2).

Since this section builds on the analysis in Karrer et al., 2021a using McSnow additionally, the setup of the simulations (atmospheric variables, initialization of hydrometeors at the model top) and the microphysical settings in McSnow are chosen to be as close as possible to Karrer et al., 2021a. The profiles of the atmospheric variables are the same as shown in Figure A5 of Karrer et al., 2021a. In this study, the initialization values of the hydrometeor contents are chosen to match the mean profiles of the multi-month simulations performed with the three-dimensional large-eddy model (Figure 6 of Karrer et al., 2021a). In McSnow, the same formulation of the collision kernel (A-kernel) and sticking efficiency are used as in the new version of the SB scheme. Although McSnow allows a more detailed consideration of the particle properties (e.g., dependency of mass-size relation on monomer number; calculation of v directly from mass- and area size relations and hydrodynamic theory), the same simple functional relationships between particle size and particle properties are applied as in the SB scheme. In this way, differences between the simulations with the SB scheme and McSnow can be directly attributed to the representation of the particle PSD. McSnow allows the PSD to take any form without being restricted to functional relationships such as the gamma distribution (Equation 2.9). Minor differences between the SB scheme and McSnow might also arise because the processes act on the particles directly and some approximations made in bulk schemes are not required.

The profiles of the hydrometeors in Figure 4.1 indicate lower aggregation rates in McSnow compared to the SB scheme. Although

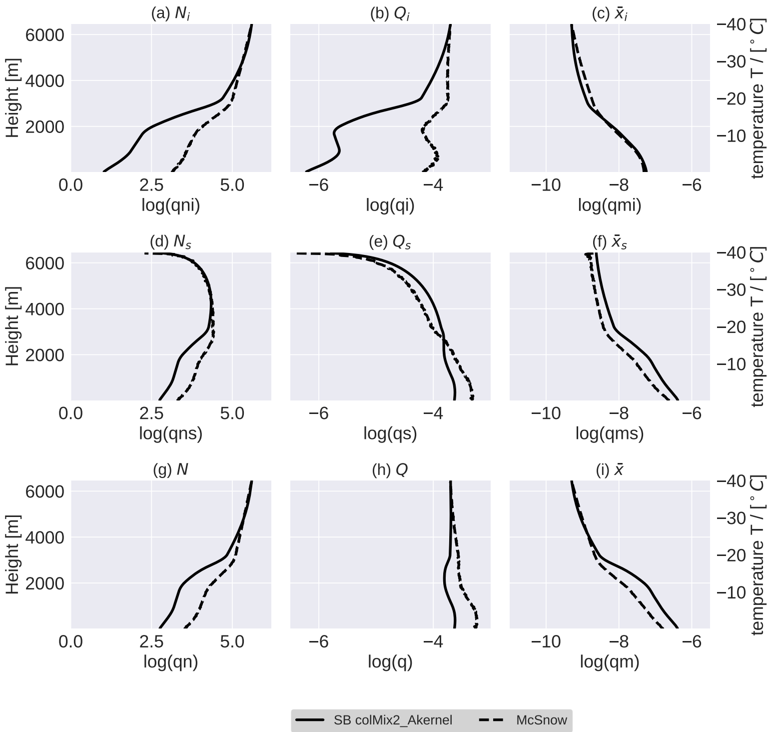

Figure 4.1: Profiles of model variables from the SB scheme (solid lines) and McSnow model (dashed line) in the "snowshaft" simulations using the same simulation setup as Karrer et al., 2021a. Shown are the vertical profiles of the number density N (left), mass mixing ratio Q (middle) and mean mass $\overline{x}$ (right) of the cloud ice (top), snow (middle) and the sum of both categories (bottom).

McSnow does not distinguish between particle categories such as cloud ice and snow, classifying the model output according to these classes helps its interpretation. Therefore, the rows in Figure 4.1 depict the profiles for cloud ice (a)-c)), snow (d)-f)) and the sum of both classes (g)-i)). The number (N; left column) and mass (Q, middle column) concentration of cloud ice (monomers; N_i and Q_i) decrease weaker in the McSnow simulation. The snow profiles (Figure 4.1, middle column) show a weaker increase of Q in the upper half. Both, the smaller decrease of cloud ice hydrometeor content and smaller increase of snow hydrometeor content (Figure 4.1; left and middle column) result from lower conversion rates from cloud ice to snow in the McSnow simulation. Also, the mean mass of all particles ($\overline{x}$; Figure 4.1 i)) increases more weakly in McSnow (especially below -20°C), indicating overall lower aggregation rates.

The lower aggregation rates in McSnow stem from the narrower PSD (Figure 4.2). Although both models are initialized with gamma distributions with the same width, substantial differences among the PSDs arise already at the highest height interval shown. Here, the snow PSD of the SB scheme is comparably broad, leading to a slight shift of the PSD tail towards larger sizes. At lower heights also the cloud ice distribution is considerably narrower in the McSnow model. The narrower PSD in McSnow leads to less spread of v and thus lower aggregation rates (Section 3.1.2 in Karrer et al., 2021a). The cloud ice distribution is particularly narrow since the cloud ice particles grow purely by depositional growth, and thus a narrowing is expected due to the diameter dependence of the depositional growth equation (Equation 2.1), which favors the growth of smaller particles.

Since other processes, e.g., nucleation and turbulence, could broaden the cloud ice PSD, the PSD width might be underestimated by McSnow. When nucleation is active in parallel with depositional growth, newly nucleated particles have significantly smaller sizes than particles already grown to larger sizes by depositional growth, thus broadening the distribution towards smaller sizes. Turbulence can widen the PSD in two ways. First, the mixing of different parts of the cloud can bring particles of different sizes together. Second, in turbulent air, supersaturation can vary spatially and lead to different particle growth rates depending on the supersaturation level. The latter effect is recognized as essential for liquid clouds (Cooper, 1989; Grabowski and Abade, 2017), but has not yet been studied for ice clouds.

Although the PSDs of the McSnow model are generally narrower, the right tail of the distribution is very similar to the one from the SB scheme, especially at lower heights (lowest two panels in Figure 4.2). Both models show a relatively steep decrease of number concentration at mass-equivalent sizes (D_{eq}) of several mm. Since the DWR is especially sensitive to large particle sizes, even slight differences in the number concentration at these sizes could induce substantial

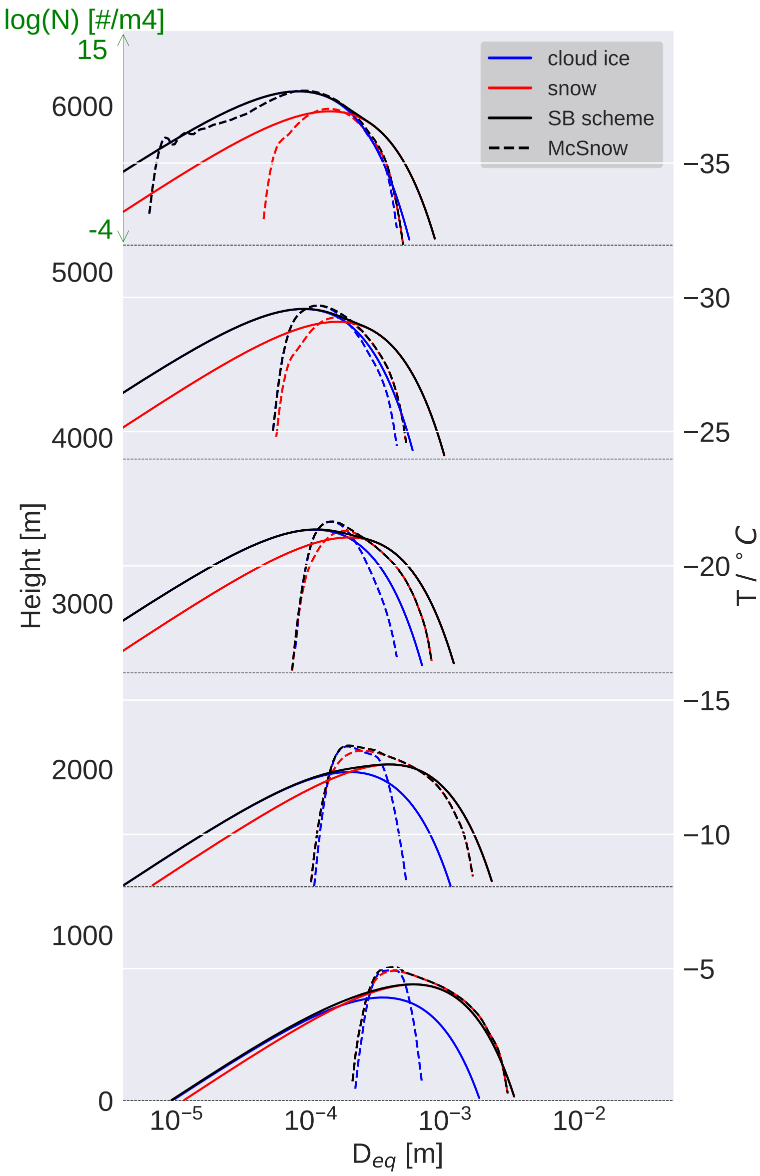

Figure 4.2: Size distributions (number concentration vs. mass-equivalent diameter D_{eq}) from the SB scheme (solid) and McSnow (dashed) averaged over different height intervals (indicated by black horizontal lines) of the same simulations as Figure 4.1. Black lines depict the size distribution, including all particles, while blue and red lines show the PSD of only cloud ice (monomers) and snow (aggregates) particles.

mismatches in DWR (Table 1 in Karrer et al., 2021a). Thus, the similar right tail indicates that a good agreement of observed and simulated DWRs with the new set of microphysical parameters can be expected even if the SB scheme would predict the PSD more explicitly. However, it can not be excluded that the possibly too narrow cloud ice PSD also affects the right tail of the snow PSD.

5 MELTING LAYER PROCESSES

Karrer, M., Dias Neto, J., von Terzi, L., & Kneifel, S. (2021b). **Differences of Microphysical Processes in the Melting Layer Found for Rimed and Unrimed Snowflakes Using Cloud Radar Statistics.** Submitted to *Journal of Geophysical Research: Atmospheres*

During the peer-review process, a programming error was found that changed the results. The revised manuscript is available at https://doi.org/10.1029/2021JD035907.

Differences of Microphysical Processes in the Melting Layer Found for Rimed and Unrimed Snowflakes Using Cloud Radar Statistics

Markus Karrer[1], José Dias Neto[1,2], Leonie von Terzi[1], Stefan Kneifel[1]

[1]University of Cologne, Institute of Meteorology and Geophysics
[2]Delft University of Technology, Department of Geosciences and Remote Sensing

Key Points:

- Investigate growth/shrinkage of snowflakes in the melting layer using multi-frequency Doppler radar and the reflectivity flux ratio method
- The mean sizes of the particle populations stay almost constant for unrimed and shrinks for rimed profiles in the melting layer
- Combined effect of aggregation and collisional breakup of melting particles might explain slight growth/shrinking of unrimed/rimed profiles

Corresponding author: Markus Karrer, `markus.karrer@uni-koeln.de`

Abstract

Understanding which microphysical processes are dominant while ice particles pass through the melting layer is essential for precipitation prediction by microphysics schemes and precipitation estimates by remote sensing. Comparing the reflectivity flux at the top and bottom of the melting layer reveals the overall effect of the microphysical processes occurring within the melting layer on the particle population. If the reflectivity flux increases more than expected due to the change in the dielectric factor, growth processes dominate. In contrast, a weaker increase in reflectivity flux indicates that shrinking processes dominate. However, inference of growth or shrinking dominance from the increase in reflectivity flux is only possible if other influences (e.g., vertical wind speed) are negligible or corrected for. By analyzing radar spectra and multi-frequency observations, we correct the reflectivity fluxes for vertical wind speed and categorize the height profiles by the riming degree at the melting layer top. Our statistical analysis shows the slight dominance of growth processes for unrimed and a clearer dominance of shrinking processes for rimed profiles. The reflectivity flux profiles within the melting layer indicate that the difference between unrimed and rimed profiles arises mainly in the upper half of the melting layer, where the melting fraction increases the strongest. We further narrow down which processes might be most important to explain the observed signature by analyzing additional radar variables. We suggest that whether the particle population is overall growing or shrinking depends on the relative importance of aggregation and collisional breakup of melting particles.

1 Introduction

More than 70% of rainfall reaching the earth's surface is generated in the ice phase (Heymsfield et al., 2020). After nucleation, ice particles can grow by a complex interplay of microphysical processes such as vapor deposition, aggregation, and riming. Once they sediment down to a temperature of $0°C$, they start to melt into raindrops. The transition layer, where partially melted ice particles and raindrops coexist, is commonly called the melting layer (ML).

Most prominently, the ML can be detected in radar observations. The big difference of the refractive index of ice and liquid water in the microwave and the higher particle velocity of liquid particles are mainly responsible for the well-known radar bright band, i.e., a region of strongly enhanced radar reflectivity (Fabry, 2015). In addition, also polarimetric observations and signal attenuation are affected by the ML (Ryzhkov & Zrnic, 2019). To avoid biases in surface precipitation estimates, one must carefully consider these ML effects. Specifically for space-borne retrievals based on observations from higher frequency radars (Ka- or W-Band), the attenuation effect of the ML is considered explicitly by a ML model (Kidd et al., 2020).

The characterization of the morphological changes during the melting of individual ice particles is only one important scientific problem that hampers a more accurate characterization of the particle's scattering properties and the development of improved microphysical parametrizations of melting. The melting of sedimenting ice particles does not happen instantaneously but depends on temperature and humidity of the surrounding air (Heymsfield et al., 2021). In addition, the temporal evolution of melting also depends on the properties of the ice particles themselves, such as size, density, and terminal fall velocity (Pruppacher et al., 1998). As a result, the ML can often have a vertical extension of a few hundred meters. This large vertical extent makes many microphysical processes likely to happen in the ML, which are currently only insufficiently understood.

Primarily in-situ observations have been used to infer the presence and relevance of different processes in the ML (Stewart et al., 1984; Willis & Heymsfield, 1989; Barthazy et al., 1998; Heymsfield et al., 2015). Depositional growth/condensation of ice and liquid particles is a relatively slow growth process compared to aggregation or riming at temperatures close to $0°C$ and therefore also within the ML (Heymsfield et al., 2015). Evidence for additional aggregation within the ML has been found in several studies (Stewart et al., 1984; Yokoyama et al., 1985; Willis & Heymsfield, 1989; Barthazy et al., 1998; McFarquhar, 2004; Heymsfield et al., 2015). In particular, the larger aggregates entering the ML can be expected to further aggregate due to increasing differential sedimentation velocities, enhanced sticking efficiency, and the longer time large aggregates need to melt (e.g., Willis & Heymsfield, 1989). In addition to aggregation, the mass of large snowflakes might also increase by riming, including capturing small drops originating from already melted small ice particles. Once completely melted, the resulting raindrop might not be aerodynamically stable, and drop breakup can occur for particles larger than about 5 mm (Pruppacher et al., 1998).

Besides processes affecting pure ice-phase (aggregation, riming, fragmentation) and pure liquid phase particles (e.g., collision-coalescence and hydrodynamic breakup), also partially melted particles might collide or fragment. Laboratory studies found that when large graupel or hail particles (larger than about 9 mm) melt, a water torus surrounds the particle, from which eventually drops are shed (Rasmussen & Heymsfield, 1987; Pruppacher et al., 1998). Breakup of smaller particles, which is usually referred to as melting fragmentation, were observed in laboratory (Knight, 1979; Oraltay & Hallett, 1989; Mitra et al., 1990; Oraltay & Hallett, 2005) and 3D particle models (Leinonen & von Lerber, 2018). However, Oraltay and Hallett (1989) observed melting fragmentation only for relative humidities below 70% with reference to water and certain ice particle habits such as dendrites. However, the description remains qualitative, and parameterization for the frequency of fragments produced by melting fragmentation does not exist. To our knowledge, collision processes of partially melted particles have not been studied, and thus the probability for coalescence or fragmentation is unknown.

Even more uncertain than the specific processes is their relative importance. Insitu studies such as Yokoyama et al. (1985) and Barthazy et al. (1998) suggested that aggregation in the upper part of the ML (close to the maximum of reflectivity) is in balance with breakup below. Studies comparing observed and simulated reflectivity (Ze) and mean Doppler velocity (MDV) profiles within the ML revealed that aggregation and breakup are not essential to explain the typical radar reflectivity profile within the ML but might still occur (Klaassen, 1988; Fabry & Zawadzki, 1995).

How much these processes might alter the particle population properties in the ML is particularly relevant because many microphysical schemes (Seifert & Beheng, 2006; Thompson et al., 2008; Morrison et al., 2009) and retrievals (Kidd et al., 2020) assume that the mass flux and mostly also the mean mass is conserved during melting. Although these microphysical schemes allow aggregation to continue in the ML, its effect might be underestimated because the depth of the ML is often underestimated (e.g., Frick et al., 2013). Microphysical schemes with an explicit treatment of the shapes of the melting particles (Szyrmer & Zawadzki, 1999; Phillips et al., 2007; Thériault & Stewart, 2010; Frick et al., 2013; Brdar & Seifert, 2018; Cholette et al., 2019) can more accurately simulate processes within the ML and even consider the shedding process (Rasmussen & Heymsfield, 1987). These schemes allow a more accurate simulation of ML depth, latent heat exchange, and phase (snow or rain) of the precipitation. However, many processes which could be relevant in the ML are not considered because they are poorly understood. Two of these are melting fragmentation and collisional fragmentation of melting particles. The further development of melting models within microphysics schemes benefits from observational evidence, e.g., about growth and shrinking processes within the ML. For example, the absence of melting fragmentation has been suspected to explain differences between modeled and observed rain size distributions (Bringi et al., 2020). Such findings can increase the understanding of processes in the ML and guide laboratory studies that allow considering new or improved process descriptions in the models.

Although the ML is a prominent feature in radar observations, its interpretation in terms of microphysical processes is very complicated. First, the scattering properties of the particles change drastically, as not only the shape and size of the ice particles change but also their refractive index. Second, the simultaneous occurrence of several microphysical processes in the ML makes identification or even quantification of specific processes extremely challenging. Drummond et al. (1996) presented an approach that avoids interpreting the radar signals inside the ML but instead intends to infer dominant processes by comparing the reflectivity flux between the top and the bottom of the ML. A specific ratio of the fluxes can be expected under the assumption of steady-state conditions and a scenario of every snowflake melting into a single drop (”melting-only” assumption). Any observed deviations from this ratio indicate additional growth or shrinking processes within the ML. Thus, these deviations imply a change in mean mass or even mass flux, which is not considered in many microphysical models, or precipitation retrievals. Two recent studies found that the reflectivity flux ratio is in general close to the melting only scenario but also observed dependencies of this ratio on the ML depth (Gatlin et al., 2018) and particle type (unrimed or rimed) on top of the ML (Mróz et al., 2021).

This study investigates the validity of the melting-only scenario based on a multi-month radar dataset obtained at a mid-latitude site. Previous studies revealed that ML characteristics and processes inside the ML might depend on the properties of the ice and snow particles entering the ML. For example, the observed sagging of the ML has been explained by either especially dense particles (due to riming) on top of the ML (Kumjian et al., 2016) or by intense precipitation (Li et al., 2020). Multi-frequency and Doppler radars are especially helpful to detect particle populations grown preferentially by aggregation or riming and have been used previously, e.g., by Li et al. (2020), to categorize the particle type on top of the ML. Using a revisited reflectivity flux ratio (ZFR) approach from Drummond et al. (1996) combined with multi-frequency and Doppler spectral methods, we investigate whether the mean mass and mass flux can be assumed to be constant in the ML for the different particle types (section 5). Analyzing radar profiles within the ML, we discuss which processes in the ML might be differently important for profiles dominated by unrimed and rimed particles (section 6).

The revisited ZFR approach from Drummond et al. (1996) is elaborated in detail in section 2 and applied to a multi-month dataset in section 3. Multi-frequency and Doppler spectral techniques are used to categorize the particles by their degree of riming at the ML top and estimate the impact of vertical wind on ZFRs (section 4). Finally, the results of ZFR statistics for unrimed, transitional, and rimed particle categories are presented in Section 5 followed by a discussion of the presumable relevance of different microphysical processes for explaining the observed ZFR signature (section 6). Section 7 provides conclusions and outlook.

2 Theoretical Background: Reflectivity Flux Ratio (ZFR) Approach

In contrast to regions above the ML, where the growth processes manifest themselves clearly in an increase in Ze, the gradient of Ze can not be used as an indicator of particle growth or shrinking within the ML (Figure 1a)) (Fabry, 2015). In the ML, the profile of Ze exhibits a local maximum, known as the radar bright band, which is a result of several superposing effects. Near the ML top, ice particles typically have a low density and thus have a much larger maximum dimension than a raindrop of the same mass. Once these ice particles start to melt and become wet, they backscatter more power than the dry ice particle. Simply put, radars see these ice particles roughly like raindrops with a large maximum dimension. The effect of the changing thermodynamic phase can be explained by considering the Clausius-Mossotti factor (also commonly called dielectric factor):

$$K = \frac{m^2 - 1}{m^2 + 1} \tag{1}$$

where m is the complex refractive index, which depends on the material (ice or liquid water), the frequency, and the temperature. $|K|^2$ is 0.93 for liquid water and about five times lower (0.18) for ice at a frequency of 9.6 GHz and $0°C$ (e.g., Ori & Kneifel, 2018). Lower down in the ML, the particles' shapes collapse, and their maximum dimension decrease leading to increasing velocity. As a result of this increase in velocity and the resulting divergence, the number concentration decreases. This decrease in the number concentration finally also reduces the reflectivity (Figure 1a) and b)).

Drummond et al. (1996) introduced the reflectivity flux (ZFR) approach, which makes it more accessible to identify the dominance of processes in the ML. ZFR is easier to interpret than the profile of Ze because fewer factors need to be considered. In the following, we present this approach and explain its limitations and difficulties step by step.

If each snowflake melts into a raindrop of the same mass (melting-only assumption), the product of number concentration N and velocity v for a given mass m is conserved through the ML (equation (2) in Drummond et al. (1996)):

$$N_{ice}(m)v_{snow}(m) = N_{rain}(m)v_{rain}(m) \tag{2}$$

A vertically pointing radar does usually not observe particle trajectories. Particles, e.g., observed while entering the melting layer at one particular time will be advected out of the radar beam before they reach the ML bottom. Hence, we implicitly assume homogeneous conditions for applying equation 2 using vertically pointing observations. Given the above considerations, the cloud must be so homogeneous that the properties of the particle population (size distribution, particle shapes) falling into the ML change only slightly within the time it typically takes a particle to pass through the ML. An implication of equation (2) is that the fluxes $F^{(n)}$ of any n-th moment

$$F^{(n)} = \int_0^\infty N_{snow}(m)v_{snow}(m)m^n dm = \int_0^\infty N_{rain}(m)v_{rain}(m)m^n dm \tag{3}$$

are conserved, including the number flux F_N=$F^{(0)}$, mass flux F_m=$F^{(1)}$ and equivalent reflectivity flux F_{Ze}=$F^{(2)}$. The conservation of F_{Ze} is particularly interesting because it is associated with the product of two observable quantities: Ze and MDV. To illustrate this connection, we decompose F_{Ze} into the product of the n-moment $M^{(n)}$ of the mass distribution:

$$M^{(n)} = \int_0^\infty N(m)m^n dm \tag{4}$$

and the m^n-weighted terminal velocity $v^{(n)}$:

$$v^{(n)} = \frac{1}{M^{(n)}}\int_0^\infty N(m)v(m)m^n dm \tag{5}$$

which gives:

$$F^{(n)} = M^{(n)}_{snow}v^{(n)}_{snow} = M^{(n)}_{rain}v^{(n)}_{rain} \tag{6}$$

If all particles can be considered as Rayleigh targets, the second moment of the mass distribution ($M^{(2)}$) is proportional to Ze and $v^{(2)}$ is the reflectivity weighted terminal velocity v_Z. The Rayleigh theory is a valid approximation if all particles are much smaller than the radar wavelength λ (Fabry, 2015).

Since the dielectric factor increases while melting, the ratio of the dielectric factors of rain and snow has to be added to the flux continuity equation (equation (6)):

$$F_{Ze} \propto \frac{|K_{rain}|^2}{|K_{snow,e}|^2} Ze_{snow}v_{Z,snow} = Ze_{rain}v_{Z,rain} \tag{7}$$

As snowflakes have air intrusions, not the bulk ice dielectric factor K_{ice}, but the effective dielectric factor $K_{snow,e}$ has to be considered. Following Bohren and Battan (1980),

$K_{snow,e}$ can be quantified as

$$|K_{snow,e}|^2 = |K_{ice}|^2 \frac{\rho_w^2}{\rho_{ice}^2} = 0.21 \tag{8}$$

using K_{ice} from above and the density of water ρ_w=$1{\cdot}10^3\,\mathrm{kg\,m^{-3}}$ and ice ρ_{ice}=$0.92{\cdot}10^3\,\mathrm{kg\,m^{-3}}$.

Now, we can insert K from snow and rain and use the fact that the MDV is a sum of v_Z and the vertical wind w and rewrite equation (7) to:

$$\frac{0.92}{0.21} Ze_{snow}(MDV_{snow} - w_{top}) = Ze_{rain}(MDV_{rain} - w_{bottom}) \tag{9}$$

where w_{top} and w_{bottom} (positive for wind towards the ground) are the vertical winds at the ML top and ML bottom.

Finally, we can introduce ZFR to quantify deviations from the melting-only assumption by adding it on the left-hand side of equation (9) and rearrange the terms:

$$ZFR = 0.23 \frac{Ze_{rain}(MDV_{rain} - w_{bottom})}{Ze_{snow}(MDV_{snow} - w_{top})}, \tag{10}$$

In this form, which deviates from previous studies (Drummond et al., 1996; Gatlin et al., 2018; Mróz et al., 2021), ZFR directly indicates the dominance of growth mechanisms for values above one and shrinking mechanisms for values below one. If additionally, F_m is unchanged within the ML (no deposition, sublimation, condensation, and evaporation), then ZFR indicates directly whether collisions (ZFR>1) or breakup processes (ZFR<1) are dominant.

Within the ML, the particle population can contain pure liquid phase, melting, and pure ice phase particles. Thus, many processes could be relevant and cause deviations from the melting-only assumption (ZFR=1). To simplify the discussion, we separated the ML into the upper part where ice-phase particles (or particles in the initial melting stage) are dominant and the lower part where liquid-phase particles (or almost melted particles) are dominant (Figure 1d)). Furthermore, we use the terminology of pure ice-phase and pure liquid-phase microphysical processes near the ML boundaries. Predominantly ice-phase particle populations can shrink due to ice breakup and sublimation and grow due to aggregation, riming, and depositional growth. Predominantly liquid-phase particle populations can shrink due to liquid breakup and evaporation and grow due to collision-coalescence, and condensation (Pruppacher et al., 1998). In the center of the ML, breakup due to melting fragmentation or as a result of collisions of melting particles might also be relevant to consider.

3 Dataset

For this study, we analyze vertically pointing multi-frequency and Doppler spectral information obtained during the "TRIple-frequency and Polarimetric radar Experiment for improving process observation of winter precipitation" (TRIPEx-pol) campaign. TRIPEx-pol took place at Jülich Observatory for Cloud Evolution Core Facility, Germany (Löhnert et al., 2015, JOYCE-CF) from 11 November 2018 to 21 February 2019. In total this dataset includes 132h of ML observations.

The data quality control and post-processing of the TRIPEx-pol dataset have been performed analogously to a previous multi-frequency campaign dataset described in detail in Dias Neto et al. (2019). The main difference in terms of instrumentation, is a new vertically pointing X-Band Doppler radar providing higher sensitivity and Doppler spectra. In order to limit radar volume mismatching, the three radars are installed on the same roof platform in less than 10m horizontal distance. Also, the temporal averaging and range gate resolution is very closely matched, as summarized in Table 1.

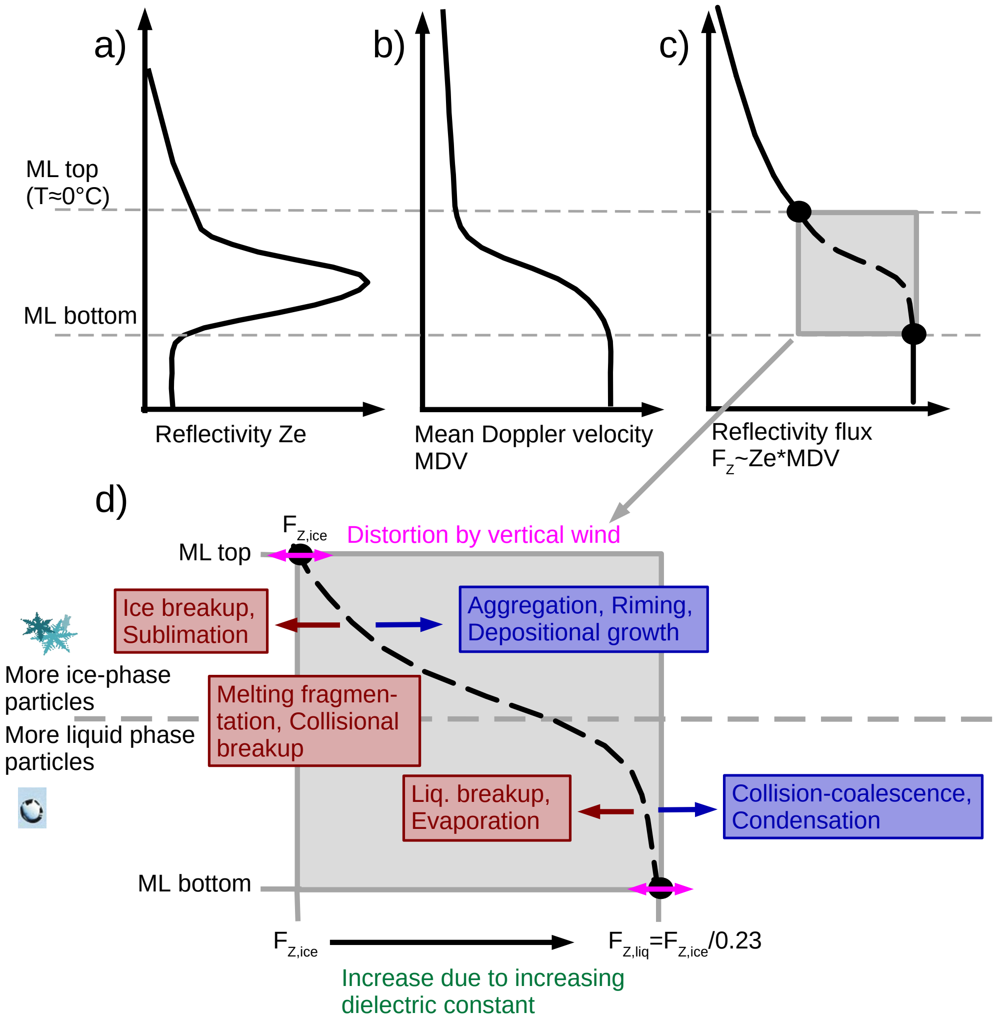

Figure 1. Schematic of radar profiles, which motivates the use of the reflectivity flux F_Z to diagnose the dominance of growth or shrinking processes within the ML.

The absolute calibration of Ze for all three radars has been evaluated using raindrop size distributions from several rain events measured by a Parsivel disdrometer (Löffler-Mang & Joss, 2000) installed directly next to the radars. As demonstrated with the TRIPEx-pol dataset in Myagkov et al. (2020), using rain as a calibration target provides similar accuracy (± 0.7dB) as compared to more comprehensive calibration methods. Differential attenuation has been mitigated in several steps. First, the temperature and humidity information from the European Centre for Medium-Range Weather Forecasts Integrated Forecast System (ECMWF-IFS) included in the Cloudnet products for JOYCE-CF (Illingworth et al., 2007) have been used to correct for gas attenuation (Dias Neto et al., 2019). The remaining path integrated differential attenuation due to rain, ML and snow was estimated at cloud top with a reflectivity threshold method as described, e.g., in Tridon et al. (2020). The estimated total differential attenuation is then applied to the entire Ze profile.

The corrected dataset has been used and described before by Mróz et al. (2021), who also studied ML processes on a single day from the campaign, and Vogel et al. (2021), who applied a neural network to identify riming events on several selected days.

Table 1. Technical specifications of the radars utilized during TRIPEx-pol at JOYCE-CF. The radars operate with frequencies in the X-, Ka- and W-Band and are all vertically pointing. Sensitivities are given at average heights of the ML top (1560 km) and bottom (1168 km).

Specifications	X Band	Ka Band	W Band
Frequency [GHz]	9.4	35.5	94.0
Pulse Repetition [kHz]	10	5.0	2.2-12.8
Number of Spectral Bins	4096	512	128-512
Number of Spectral Average	10	19	11-13
3dB Beam Width [°]	1.0	0.6	0.5
Nyquist Velocity [± ms^{-1}]	80	10.5	1.8-10.2
Sensitivity at 1560 km [dBZ], 2s integration	-40.7	-54.0	-51.1
Sensitivity at 1168 km [dBZ], 2s integration	-43.9	-56.6	-53.8
Range Resolution [m]	36	36	36
Temporal Sampling [s]	2	2	3
Lowest clutter-free range [m]	300	400	300
Polarimetry	No	LDR	No

4 Methods

Before we start applying the ZFR approach, we have in a first step to reliably identify the top and bottom of the ML for all profiles (section 4.1). In a second step, we categorize each profile whether the snow entering the ML is rimed using a new method presented in Li et al. (2020) based on DWR and MDV (section 4.3). A remaining problem, which was already discussed in Drummond et al. (1996) and section 2 is the influence of vertical wind on the ZFR. Using Doppler spectral signatures, we derive w for a subset of our profiles and test how much our statistical results of ZFR change when taking into account the influence of w

4.1 Detecting the ML boundaries

Numerous approaches have been used to define the ML top and bottom. Early studies used the absolute values, gradients, or curvature of Ze (Klaassen, 1988; Fabry & Zawadzki, 1995; Drummond et al., 1996) or MDV (Klaassen, 1988; Zrnic et al., 1994). Baldini and Gorgucci (2006) summarized previously established methods and added the ML detection based on the standard deviation of polarimetric variables (differential reflectivity, differential phase shift). Also absolute values (Devisetty et al., 2019) and gradients (Bandera et al., 1998) of the linear depolarization ratio:

$$\mathrm{LDR} = \frac{Ze_{hv}}{Ze_{hh}} \tag{11}$$

have been used. Here, Ze_{hv} (in mm^6/m^3) is the reflectivity detected in the cross-polarized (vertical) channel after emission in the horizontal polarisation. Ze_{hh} is the reflectivity received in the horizontal polarisation, in which the radiation was also emitted. LDR is large for particles in the early and intermediate melting stage, which are still large in size (compared to the fully melted particles), but already have increased Ze_{hv} due to the presence of liquid, which increases the dielectric factor.

We use the inflection points (points of maximum curvature) above and below the maximum LDR_{Ka} to infer the ML boundaries (Figure 2a). We think that these points characterize the boundaries of the ML well because they mark the region of a large change in LDR, expected when particles start to get wet (ML top) and when the shape of the particle collapses (ML bottom). The main advantage of this method is that the curvature of LDR_{Ka} is relatively independent of the growth/shrinking processes of interest and mainly dependent on the degree of melting. In contrast, if the ML detection is based on Ze curvature, strong aggregation above the ML might cause a false ML top detection.

Although the use of the inflection points of LDR_{Ka} has advantages over other methods for detecting the ML boundaries, the determination of the inflection points and their connection to the ML boundaries must still be done carefully to detect only the heights associated with the ML boundaries. As many inflection points might be present in noisy profiles, we apply a temporal moving average of 5 min on LDR_{Ka}. Second, local maxima, and thus local inflection points, can also be caused by prolate ice particles, such as needles growing at about -6$°C$ (Li et al., 2021, and references therein). Therefore, we disregard maxima, and corresponding inflection points, at temperatures below -1$°C$. Finally, we want to make sure that we exclude melting particles at the diagnosed ML top ($h_{melt,top}$) and ML bottom ($h_{melt,bottom}$). Since LDR_{Ka} increases already slightly above the height of the upper inflection point and decreases still slightly below the height of the lower inflection point, these points might be slightly within the ML. Therefore, $h_{melt,top}$ (and $h_{melt,bottom}$) are chosen as the heights of the inflection points plus (minus) 36 m (which is the height of one range gate).

Figure 2 shows qualitatively that our definition of the ML boundaries is similar to previous approaches. The ML top is close to the maximum gradient of Ze (Figure 2e)). Moreover, the ML bottom is close to the height, where the MDV reaches its maximum (Figure 2b)). Furthermore, the spectral LDR reveals just above the ML small and slow particles with slightly enhanced LDR (up to -15 dB) typical for columnar or needle ice crystals (Li et al., 2021). From 1600m towards the ground, the LDR increases rapidly across all velocity bins while the smaller and slower ice particles appear to melt fastest.

4.2 Estimating Vertical Wind at ML Top and Bottom

Radar Doppler spectral methods for deriving w rely on the identification of spectral features whose terminal velocity is well known. Any deviation of the measured Doppler velocity can then be assigned to vertical air motion. In mixed-phase clouds, the spectral peak of supercooled cloud droplets is commonly used as a tracer for w (Battan, 1964; Luke & Kollias, 2013; Zhu et al., 2021). Cloud droplets can be assumed to have negligible terminal velocity and hence their spectral peak should be close to 0 m/s Doppler velocity in the absence of w. Due to the rapid increase of terminal velocity of ice crystals even at small sizes, the cloud liquid peak is usually well separated from the ice and snow peak in the spectrum (e.g, in Figure 2b),c),d)). The technique is often limited by two factors: The sensitivity to small liquid drops increases with higher frequencies. However, as attenuation also increases with frequency, e.g., rain and the ML might severely attenuate the signal causing the liquid peak to be undetectable. In this study, we therefore decided to use the Ka-Band spectra to identify the liquid peak as it provides a good compromise between sensitivity and attenuation.

To identify the peaks, a fourth-degree polynomial is fitted to the spectrum. Each local maximum is recognized as a peak, and the mean Doppler velocity (DV) and Ze of the peak are calculated. The main peak (Peak-0), identified as the peak with the largest reflectivity, follows the MDV closely. The DVs of the other peaks are mostly smaller than 1m/s (Figure 2d)). These peaks with smaller DV could be caused by cloud droplets, drizzle (Kollias et al., 2007), ice phase particles created by nucleation at warmer temperatures or secondary ice production (Li et al., 2021), or noise in the spectrum. To identify the cloud droplet peaks, we apply a rather simple criterium based on the integrated reflectivity of the peaks and the DV of the peaks, in the case of more than two peaks. Only peaks with Ze between -50 dBz and -30 dBz are taken into account. The lower reflectivity limit is chosen to disregard spurious peaks in the noise floor, the upper limit to disregard drizzle and ice-phase peaks. The upper limit can be considered relatively carefully since other studies have set this value somewhat higher (e.g., Radenz et al. (2019) with -20 dBz). If there are several peaks other than Peak-0, the peak with the smallest DV is identified as the liquid peak. Besides more sophisticated techniques that also use higher radar moments (e.g. Zhu et al., 2021), this DV-based separation is commonly used (Kalesse et al., 2016; Radenz et al., 2019) and takes advantage of the fact that even relatively small ice particles have considerable velocity (e.g. about 0.4m/s at 200μ according to Locatelli and Hobbs (1974)). After identifying the cloud droplet peak, the deviation of its peak DV is taken as an estimate for w at the ML top. In the exemplarily shown profile (Figure 2), w_{top} is 0.1 m/s, which is according to our convention a slight downwind. Considering this downwind in the calculation of ZFR shifts it to a slightly larger value (from 1.14 to 1.18). In the absence of a cloud liquid peak, the lower spectral edge velocity SEV (Figure 2d)) could be used to estimate w, too. We defined the SEVs as the smallest and largest velocities, where Ze exceeds the noise level by 3 dB. However, using SEV as an estimate might underestimate w since the cloud droplet peak can be broadened by turbulence.

In rain, a separated cloud liquid peak is usually not detectable in the Doppler spectra. However, differential scattering signatures, which can be attributed to a certain drop size, can be used to derive w (Kollias et al., 2002). These signatures have e.g., been used in size distribution retrievals (Tridon & Battaglia, 2015). More precisely, the backscattering cross-section of raindrops that are larger than the radar wavelength exhibit local minima due to destructive interference (Kollias et al., 2002). At a frequency of 94.0 GHz (W-Band), the first local minimum occurs for particles with a size of 1.67mm, which corresponds to v_t=5.9m/s in standard conditions. When considering the effect of the density on the particle velocity (Heymsfield et al., 2007) by multiplying $(\frac{101325hPa}{p})^{0.54}$ the expected Mie-notch velocity for w=0 can be calculated for each height (Figure 2c)). With decreasing pressure, the Mie notch appears at higher velocities as the air density and hence also the air resistance drag decreases. Figure 2c) clearly shows local minima in the observed spectrogram that are associated with this Mie-notch. Deviations from the actually observed DVs of these minima and the theoretically expected DVs directly indicate w (e.g. -0.2 m/s at the ML bottom). Taking w_{bottom} into account when calculating the ZFR shifts it (like the correction at the ML top) to a slightly higher value (from 1.14 to 1.23). Since the Mie-Notch minima can be superimposed by noise or can lie at the edge of the spectra, averaging and filtering of the spectra must be carried out. Before identifying the local minima as the Mie-notch position, the spectra are averaged with a moving window over six DV bins (corresponds to 0.12m/s). If the spectral reflectivity at the DV bin of the actual Mie notch is smaller than -40 dBz, the profile is disregarded to avoid noisy signatures.

4.3 Categorizing Profiles by their Degree of Riming

Riming can be well detected by vertically pointing Doppler radars, as riming initially strongly increases the particle mass and, to a lesser extend, it's size and cross-sectional area. As a result, v of rimed particles quickly exceeds that of unrimed particles (Mosimann, 1995; Kneifel & Moisseev, 2020). However, when particles fall with velocities smaller than 1.5 m/s, large unrimed snowflakes might be indistinguishable from small rimed crystals. As demonstrated by Mason et al. (2018) or Li et al. (2020), the addition of multi-frequency information can be used to improve the detection of riming, especially in this lower Doppler velocity regime (v <1.5 m/s). We make use of the separation into three categories (unrimed, transitional, rimed) by Li et al. (2020). They used ground-based in-situ observations combined with collocated multi-frequency radar observations to derive the rime fraction for each profile and fitted a dual-wavelength ratio $\mathrm{DWR}_{X,Ka}$-MDV_X relation which separates the observed profiles well into unrimed, transitional and rimed ice particles. Li et al. (2020) provide these fits for several ranges of precipitation rates, which are overall relatively similar. We use the relations fitted to precipitation rates between 1mm/h and 4mm/h, which is the typical range of rain rates observed during the Tripex-pol campaign when a ML could be detected:

$$\mathrm{DWR}_{X,Ka} = 0.6 \cdot \mathrm{MDV}^{7.3}_{X,\rho-corr} \tag{12}$$

separates unrimed from transitional profiles, and

$$\mathrm{DWR}_{X,Ka} = 0.75 \cdot \mathrm{MDV}^{2.85}_{X,\rho-Corr} \tag{13}$$

separates transitional from rimed profiles. In both equations (equation (12) and (13)), $\mathrm{MDV}_{X,\rho-Corr}$ is the MDV of the X-Band, which was corrected to standard conditions applying the relation from Heymsfield et al. (2007).

4.4 Application of the ZFR Method Including Filtering, Averaging and Riming Degree Categorization on a Case Study

The ZFR diagnostic strictly holds only if multiple conditions are fulfilled (section 1). We discuss the condition of inhomogeneity and the categorization into different riming degrees exemplarily on the time range between 06:00 and 07:30 on 13 January 2019 (Figure 3). Inhomogeneities are evident in Ze (Figure 3b)) in the form of slanted fallstreaks (e.g., around 06:17 UTC, periods of high reflectivity) or periods of low Ze ("cloud holes", 06:55 UTC). Both, the region of enhanced Ze associated with the fallstreak and the low Ze from the "cloud hole" appear slightly earlier at the ML top than at the ML bottom. As a result, ZFR goes first through a minimum/maximum in case of the fallstreak/cloud hole, followed by a maximum/maximum. In these cases, the temporal average of two minutes already reduces the fluctuation due to the inhomogeneity to a great extent. These two minutes can be considered a typical time a particle with an average v of 2-3m/s requires passing a 300-400m thick ML. At the passage of slanted cloud boundaries and "cloud holes", a significant amount of hydrometeors and thus F_Z exist only at ML top or bottom. In this scenario, ZFR also reaches extreme values (e.g., at 06:52 UTC) that are not due to growth or shrinking processes within the ML. Therefore, we introduce a filter, that removes low fluxes ($F_{Z,top}$<20 dBzm/s or $F_{Z,bottom}$/0.23<20 dBzm/s). Figure 3f) illustrates well that the most extreme ZFRs are removed by applying this filter.

The filtering of small fluxes also helps to disregard profiles where the particle type can not be categorized confidently. Small fluxes are correlated with small mean particle sizes and thus low MDV_X and $\mathrm{DWR}_{X,Ka}$. $\mathrm{DWR}_{X,Ka}$ is very weakly sensitive to particles of size below 1 mm (Ori et al., 2020), and MDV_X can not be used to distinguish the degree of riming if the particle sizes are not known. For example, a particle population with low $\mathrm{DWR}_{X,Ka}$ and MDV_X of about 1.5 m/s (e.g., in the time range between 06:00 and 06:10 UTC) could be composed of small rimed particles or larger but unrimed

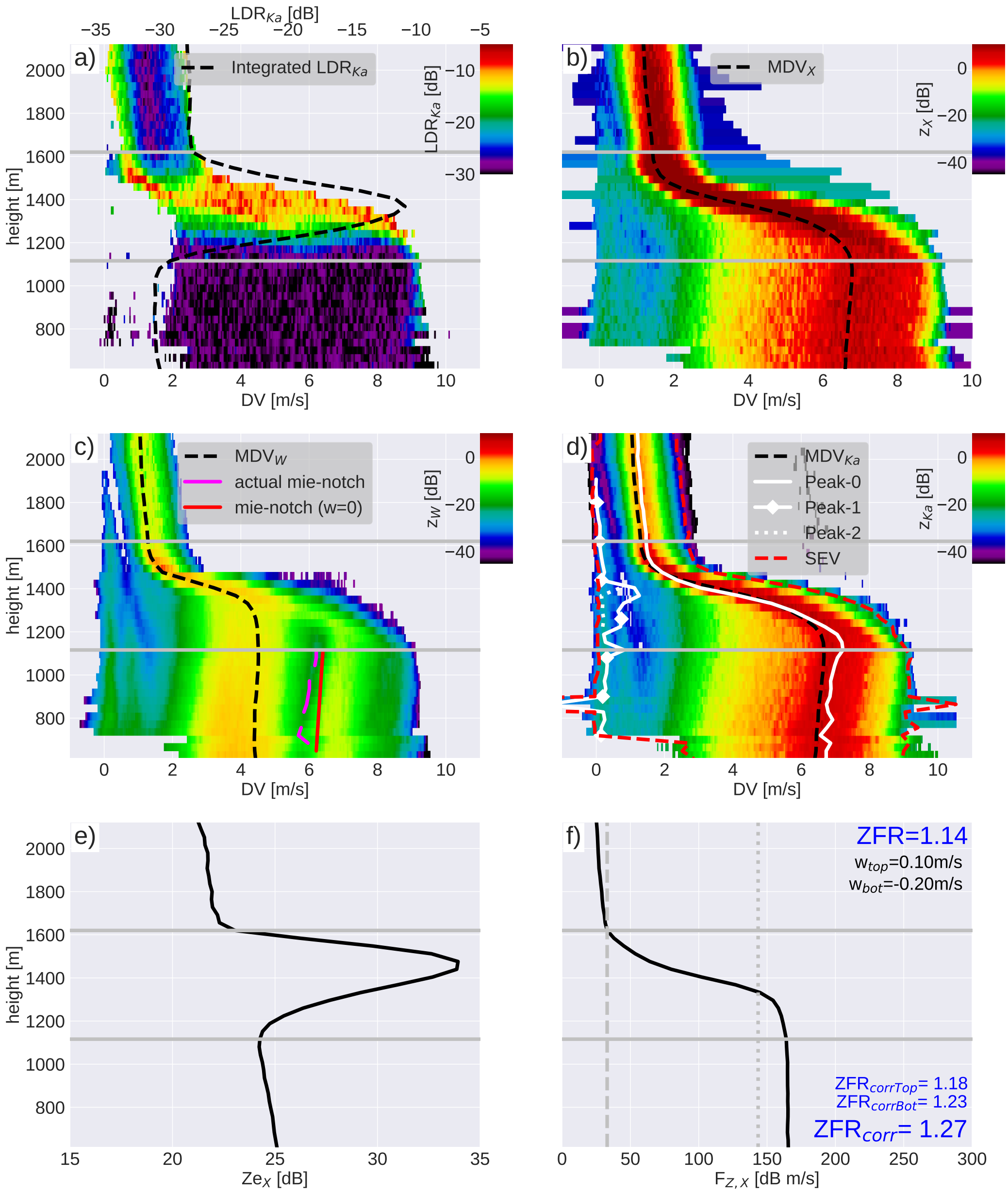

Figure 2. Spectra and profiles of integrated quantities from the 13 January 2019 07:25UTC illustrating our ML detection, calculation of ZFR and corrections based on vertical wind estimate. a) Spectral and integrated LDR$_{Ka}$; b)-d) Spectrogram and MDV of the X- (b)), W- (c)), and Ka-Band (d)); e)Ze_X; f) F_Z. c) also shows the actual mie-notch Doppler velocity (DV) and the one expected for w=0; d) also shows the DV of the main peak and the peaks with slower DV; f) also shows the estimate of w at ML top derived from the peaks in e) and at ML bottom derived from the mie-notch in d). Finally, also ZFR corrected by w$_{bot}$ (ZFR$_{corrTop}$), w$_{top}$ (ZFR$_{corrBot}$) and both w$_{top}$ and w$_{bot}$ (ZFR$_{corr}$) is shown in f). LDR$_{Ka}$ of melting particles are up to 20 dB larger than the minimum observable LDR$_{Ka}$ visible in the rain part.

particles. Considering only the time ranges, with sufficiently high F_Z the shown case is dominated by the transitional category in the first 70 minutes before unrimed particles dominate in the last 20 minutes (Figure 3e)), and ZFR is overall relatively close to one.

5 Results: Statistics of the ZFR

In this section, we derive the ZFR statistics for the different riming categories to determine whether the particle populations shrink (ZFR<1) or grow (ZFR>1) when viewed over the entire ML. Without applying any filter, the TRIPEx-pol dataset provides 131.8 hours of ML observations, which divide into 34.0% unrimed, 20.0% transitional, and 45.7% rimed profiles (Figure 4a)). Despite the large variability of ZFR for unrimed and rimed profiles, the median of ZFR decreases from unrimed over transitional to rimed profiles. A ZFR close to one for unrimed profiles means that the mean size of the particle population remains almost constant. A ZFR of 0.55 for rimed profiles indicates that the particle population is shrinking. In order to assure that the observed relation of ZFR to the degree of riming is a microphysical feature, we apply, in the following, several filters, averages, and corrections in order to minimize the effect of spurious signals caused by inhomogeneities, ambiguous riming degree characterization and vertical wind (section 4).

The scatter of ZFR narrows down strongly after we filter out low fluxes (flux filter F1; Figure 4b)). Although the flux filter removes about 70% of the profiles and changes the relative contribution of the riming categories, the dependency of ZFR on the particle type changes very little. Also, filtering out profiles of low relative humidity with respect to water (RH<95%) to exclude a potential impact of sublimation and evaporation on the ZFRs does not substantially affect the dependency of ZFR on the particle type. However, this filter removes about another half of the data (Figure 4b)). In the following analysis, we use the flux filter F1 as it is necessary to remove spurious signals. Since it changes little when low humidity profiles are filtered, we do not apply this filter in the following to maintain a balance between quality filtering and statistical robustness. Surprisingly, no matter which filter or associated profile reduction is applied (Figure 4a)-c)), the median ZFR is always about 1.0 for unrimed, 0.8 for transitional, and 0.6 for rimed profiles, with only minor deviations from the different applied filters.

Non-stationary regimes could cause a correlation between MDV and ZFR even in the absence of growth or shrinking processes, e.g., due to fallstreaks (section 4.4). For example, if riming sets on, F_Z increases first at the ML top. However, due to the time the particles take to pass the ML, F_Z does increase only later at the ML bottom, giving a temporary minimum in ZFR that might be associated with an increase in MDV. This correlation should decrease with increasingly long temporal average periods. In Figure 4d)-f) averaging periods of 2, 5, and 10 minutes are applied. These temporal averaging shifts the median only slightly to about 1.1 for unrimed and 0.7 for rimed profiles and stays almost constant for transitional profiles. The scatter of the data reduces further so that almost the full interquartile range of the unrimed profiles is below 1.0 after applying the 10 min average.

Also vertical wind could cause an “artificial” connection between the particle types and ZFR. Hypothetically, the profiles characterized as rimed could have a high MDV not only due to the higher v_t of the particles but also due to a systematic downwind at the ML top. In this scenario, the downwind at the ML top would cause an overestimation of $F_{Z,top}$, thus underestimating ZFR. However, only a slight difference exists between the uncorrected ZFR and the ZFR corrected for vertical wind at the ML top (Figure 4g)). Unfortunately, we can correct for w at ML top only in a slight number of cases (6.8h). Especially for unrimed profiles, the amount of data reduces strongly, so that these profiles contribute only about 10% to this subset of the data. The correction of w at the ML bottom is possible in slightly less than half of the cases (after the flux filter F1). The correction can be applied to many unrimed and transitional profiles since they have com-

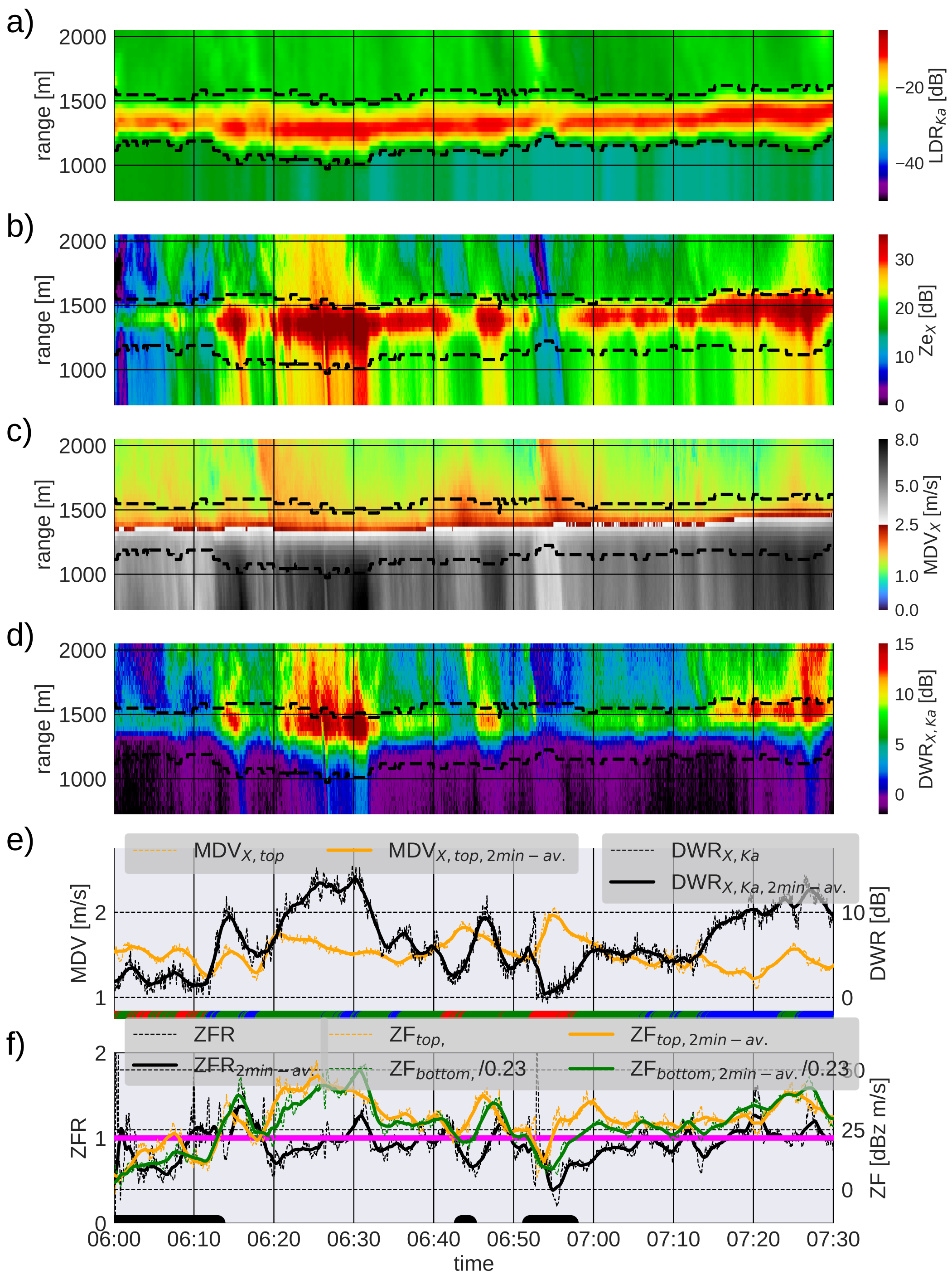

Figure 3. Radar variables and ML diagnostics from the morning hours of the 13 January 2019 illustrating the variability of the variables close to and within the ML, the categorization by the degree of riming, and challenges of the ZFR diagnostic. Time-height series: a) LDR$_{Ka}$ b) Ze_X c) MDV$_X$ d) DWR$_{X,Ka}$. In snow, positive DWR$_{X,Ka}$ indicate large particles; In rain, negative DWR$_{X,Ka}$ occur due to "super-Rayleigh scattering" (e.g. Mróz et al., 2020). Dashed lines mark the ML top and bottom. Timeseries of e) MDV$_X$ and DWR$_{X,Ka}$ at ML top and riming degree categorization (bottom of the plot: blue: unrimed; green: transitional; red: rimed) f) F_Z at ML top and bottom, and ZFR. At the bottom of f) all time ranges are marked by a black line where $F_{Z,top}$ is smaller than 20 dBzm/s or $F_{Z,bottom}$/0.23 is smaller than 20 dBzm/s (same as filter applied in section 5). The magenta line in f) marks ZFR=1, which is to be expected under the melting-only assumption. Dashed lines show values on the original time grid and solid after applying a 2 minute temporal average.

parably large raindrops below the ML and the Mie notch is often detectable. In contrast, the portion of rimed profiles decreases more strongly. Nevertheless, this reduction of profiles and scarcity of unrimed profiles which can be properly corrected for w does not substantially change the dependency of ZFR on the particle category. Finally, we apply a correction for w at ML top and bottom simultaneously. Again, the amount of data decreases and only 2.9h are left, but the median ZFR for each particle type, and thus the dependency between ZFR and particle type remains similar.

None of the filters and corrections applied to the dataset induced a considerable shift in ZFR. From this, we can conclude that the microphysical growth or shrinking processes for unrimed, transitional, and rimed profiles must act in different intensities (different process rates) to explain the difference in ZFR. In the case of unrimed profiles, shrinking and growth processes almost balance out (with a slight tendency to the dominance of growth processes), whereas shrinking processes dominate in the case of rimed profiles.

6 Discussion: What processes might affect the particle size of unrimed and rimed particles differently?

In section 5, we found that ZFR is close to one for unrimed profiles and around 0.6 for rimed profiles, suggesting that the melting-only assumption may be appropriate for unrimed profiles, while shrinkage processes dominate over growth processes for rimed profiles. In this section, we aim to find indications of which of the various processes that could potentially alter F_Z (Figure 1) are actually active in the ML for the different particle categories. To this end, we first characterize the melting stages for mean profiles of all particle categories (Figure 5). Then, we investigate whether processes in the predominantly liquid part (e.g., hydrodynamic breakup, collisional breakup), in the predominantly ice phase (e.g., aggregation) or during melting (e.g., melting fragmentation, collisional breakup of melting particles) can explain the differences in ZFR.

We normalize the height of each profile relative to the ML boundaries (h_{rel}) so that h_{rel}=0 corresponds to the ML bottom and h_{rel}=1 to the ML top. This normalization allows us to compare all profiles with each other even though the ML depth varies. On average, the ML is 391 m thick with a standard deviation of 90 m.

Melting progresses similarly with decreasing h_{rel} for all three particle types (Figure 5). The melting progress is indicated by the profiles of LDR$_{Ka}$ and the melting fraction f_{melt} (Figure 5a) and c)). The shapes of the LDR profiles are very similar and differ only slightly, e.g. in the height of the maximum which is at h_{rel}=0.51 for unrimed and h_{rel}=0.47 for transitional and rimed profiles (Figure 5a). Due to the higher density of rimed particles, we expect the melting of rimed particles to happen at a lower altitude. This is further confirmed when looking at the retrieved f_{melt} (dashed lines in Figure 5c)) defined as:

$$f_{melt} = \frac{m_{liq}}{m_{ice} + m_{liq}}, \tag{14}$$

To diagnose f_{melt}, we use the method of Mitra et al. (1990), which derived a relation between f_{melt} and the relative increase in v from laboratory experiments. In agreement with LDR, also f_{melt} increases somewhat slower for rimed profiles in the upper part of the ML (Figure 5c)). According to the diagnosed f_{melt}, 50% of the mass is liquid at h_{rel}=0.73 (h_{rel}=0.69) for unrimed (rimed), and 90% of the mass is melted at h_{rel}=0.49 (h_{rel}=0.43) for unrimed (rimed).

Since the shapes of the raindrops differ only slightly from each other, the mean size and the size of the largest particles can be inferred from the values of Ze_X, MDV$_X$ and the spectral edge velocity SEV (Figure 5b)-d)) at the lower edge of the ML. Owing to these similar shapes, raindrop v can be mapped relatively unambiguously to raindrop size (e.g, Tridon & Battaglia, 2015), and we can attribute the increasing MDV$_X$ (Fig-

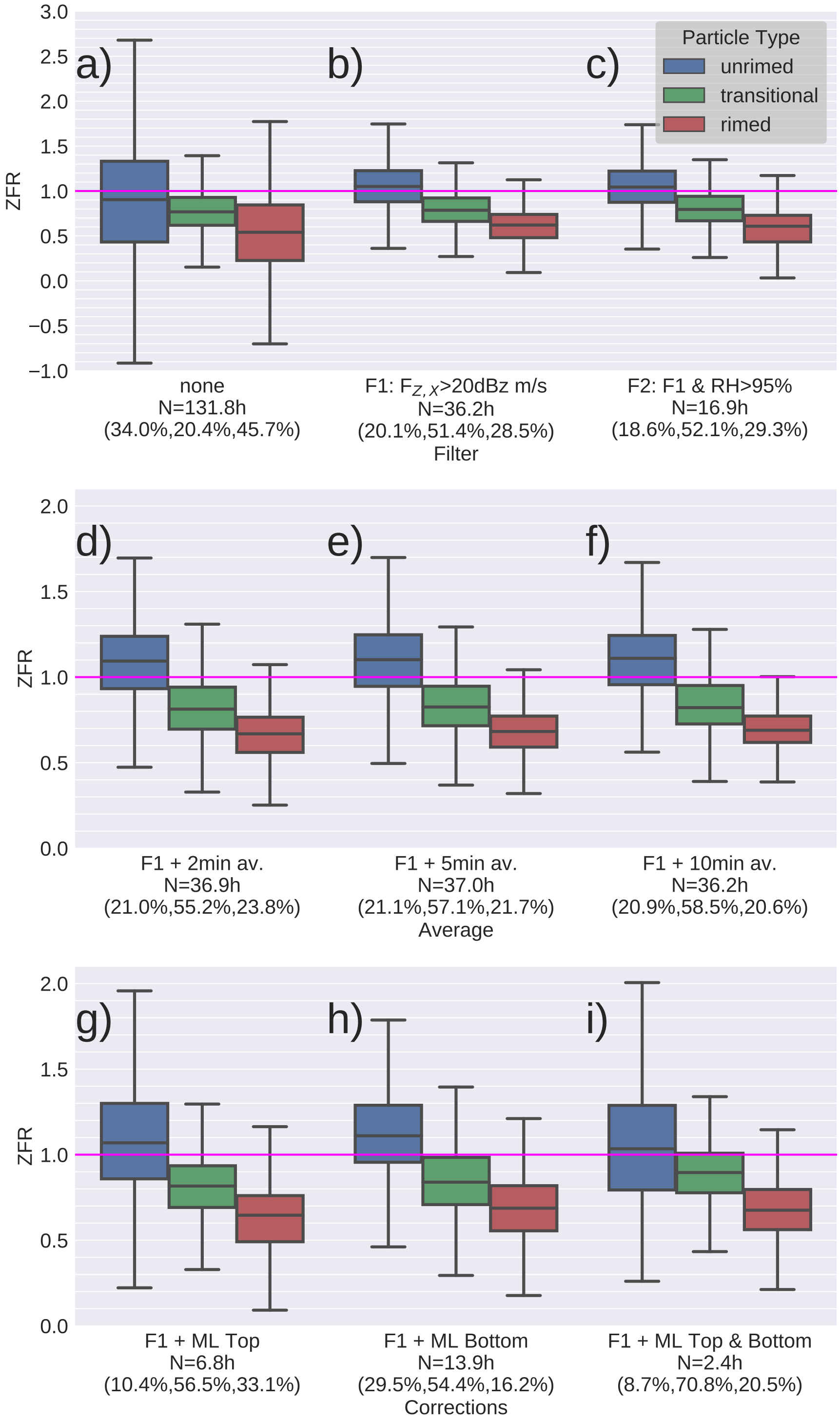

Figure 4. Boxplot of ZFR for different particle types (unrimed, transitional, rimed) and different filters (first row, a)-c)), average periods (middle row, d)-f)) and corrections (last row, g)-i)). Each box shows the interquartile range of the distribution. The horizontal line within each box depicts the median. The whiskers show the rest of the distribution excluding outliers. Filters applied: F1: Profiles with $F_{Z,top}$<20 dBzm/s or $F_{Z,bottom}/0.23$< 20 dBzm/s are removed. F2: In addition to Filter 1, profiles with relative humidity with respect to water RH below 95% are removed. In g)-i) ZFR is correct for w_{top} only (g)), w_{bottom} only (h)), and w_{top} and w_{bottom} (i)).

ure 5c)) from rimed (4.65m/s) to transitional (5.38m/s) to unrimed (5.67m/s) profiles to the increase in mean particle sizes. The upper spectral edge velocity SEV (right lines in Figure 5d)) confirms the surprising finding that the larger MDV$_X$ found for raindrops originating from rimed particles is indeed due to the presence of larger drops. This observation is exactly the opposite of what we might have expected from stronger drop breakup or shedding of melting rimed particles. Thus, these breakup mechanisms cannot explain the ZFR<1 for rimed profiles. Ze_X at the ML bottom also increases from rimed to unrimed profiles. This increase could again indicate an increase in mean mass, but might also be partly due to differences in number concentration. Due to the influence of the different ice and melting particle shapes, the profiles of Ze, MDV$_X$ and SEV can not be used to infer characteristic sizes and strength of the growth processes.

The smaller mean mass of the rimed compared to unrimed profiles indicates that breakup of pure liquid particles and shedding of graupel and hailstones can not explain the stronger decrease of F_Z for rimed profiles because both processes are especially efficient in the presence of large drops. Hydrodynamic breakup occurs only for particles larger than 5 mm, which corresponds to velocities of about 9 m/s at the average pressure at the ML bottom (9234 hPa) (Pruppacher et al., 1998). Velocities above 9 m/s are not reached by the upper quantiles of any particle type (right side of Figure 5d)). Also, collisional breakup of liquid particles most likely can not explain the difference between unrimed and rimed profiles. The process rates of collisional breakup increase with increasing sizes (Low & List, 1982; McFarquhar, 2004; Straub et al., 2010), which would suggest higher rates for unrimed particles if this process is important at all. Furthermore, the profiles of F_Z below the ML (h_{rel}<0) indicate that these pure liquid processes are not important or are greatly compensated by collision-coalescence because F_Z is almost constant here (Figure 5e)-g)). To ease the comparison of the profiles and allow closer inspection of the slope, F_Z is normalized by $F_{Z,top}$ ($F_{Z,X,norm}$) in Figure 5f) and the derivative of $F_{Z,X,norm}$ is shown in Figure 5g). Shedding occurs only for graupel and hailstones with a mass-equivalent size larger than about 8 mm, which corresponds to velocities of about 10 m/s once the particle is fully soaked and no air intrusions are left (Pruppacher et al., 1998).

Again, F_Z might be currently our best indicator for growth processes within the ML and can indicate the height regions at which processes differ the most for unrimed and rimed profiles (Figure 5e)-g)). However, the profiles of F_Z within the ML are hard to interpret because of the poorly known scattering properties of wet ice particles (Ori & Kneifel, 2018; Kneifel et al., 2020). Comparing the mean profiles of the different particle types, we can assume that the change of K, and thus its' contribution to the increase of F_Z, occurs similarly for all particle types. For all particle types, the increase of F_Z is strongest at h_{rel} of about 0.7 (Figure 5g)), where f_{melt} is about 0.8 (Figure 5c)). This region is also responsible for most of the difference between the ZFR of unrimed and rimed particles since F_Z increases much stronger for unrimed than for rimed profiles. Besides the melting process, aggregation, depositional growth, and riming could increase F_Z in this region. The strong increase of F_Z due to melting (increasing K) could also mask shrinking processes like sublimation and breakup of melting particles.

Condensation/deposition and presence of supercooled liquid water require sufficiently large supersaturation that can be generated by vertical wind (Lohmann et al., 2016). In contrast, evaporation/sublimation occurs in subsaturated air. In addition to the humidity information from Cloudnet, we can use w (Figure 5h)) as an indicator for potentially super- or subsaturated conditions favoring either condensation/deposition or sublimation/evaporation. The case of upwind is especially interesting since many models, including ECMWF-IFS, which is used in Cloudnet, apply saturation adjustment and thus do not predict RH above 100%. We excluded already strongly subsaturated air conditions to be important for the statistics of ZFR by excluding profiles with low humidities (RH<95%; section 5). However, the mass flux could be modified by large-scale lifting (Houze, 1993), or small-scale dynamics (Szyrmer & Zawadzki, 1999) even though the humidity is close to saturation. Changes in the mass flux could efficiently consume the locally generated sub-/supersaturation, especially in presence of supercooled liquid water and if the mean size is relatively small (Lamb & Verlinde, 2011, section 10.4). As a specific feature of the ML, melting particles can also grow by depositional growth below 100% relative humidity due to the temperature difference between surrounding air and the particle. We find that small upwinds (w<0.25 m/s; bottom of Figure 5h)) are present for all particle types near the ML bottom which indicates conditions for condensation. Interestingly, near the ML top, the unrimed profiles are associated with upwind and rimed profiles with downwind (top of Figure 5h)). Thus, depositional growth could occur for unrimed profiles. Rimed profiles might experience weaker depositional growth rates or even sublimation. It has to be noted that the w estimate near the ML top is only available if a cloud droplet peak is present, which applies only to a subset of the dataset and reduces especially the number of unrimed profiles drastically (Figure 4).

So far, our analysis revealed that the origin for the lower ZFR for unrimed profiles can not be explained by shrinking processes in the rain or predominantly melted part of the ML. As we will show in the following, there are indications that the relative strength of aggregation and breakup determines the ZFR for each particle type (Figure 6). As many studies before (Stewart et al., 1984; Fabry & Zawadzki, 1995; Barthazy et al., 1998; Heymsfield et al., 2015; Gatlin et al., 2018), we suspect that aggregation is continuing within the ML. Aggregation rates are high for particles with a large maximum dimension and high number concentration. Thus, the unrimed profiles could continue to grow efficiently in the upper part of the ML. In contrast, the rimed profiles have a smaller particle size, compact shape, and perhaps smaller number concentration, and, thus, we expect weaker aggregation (indicated by smaller arrows in Figure 6). Since ZFR is substantially below one for unrimed profiles, shrinking processes like melting fragmentation (Oraltay & Hallett, 1989, 2005; Leinonen & von Lerber, 2018), collisional breakup, or sublimation must be present as well. Most likely, these shrinking processes also occur in the unrimed profiles but appear to be strongly compensated by the growth processes. This reasoning is supported by in-situ observations of the size distribution and derived number flux by Yokoyama et al. (1985) and Barthazy et al. (1998). They saw indications of an almost exact balance of aggregation and breakup, similar to our observations of the unrimed category. Barthazy et al. (1998) characterized the particle type as unrimed to moderately rimed based on MDV_X observations, which might be similar to our unrimed category. Yokoyama et al. (1985) did not report the riming degree, but snowflakes presented by photographs appear relatively unrimed. Changes in the mass flux (e.g., sublimation) have been considered negligible by previous studies (Drummond et al., 1996; Szyrmer & Zawadzki, 1999; Heymsfield et al., 2007). However, differently strong depositional growth near the ML top could also contribute slightly to the different ZFR. Melting fragmentation only occurs in strongly subsaturated conditions (Oraltay & Hallett, 1989). Since we also see decreasing ZFR if we exclude profiles with RH<95% (Figure 4c)), it is also unlikely that melting fragmentation is the dominant process that can explain the observed signature. Consequently, among the mechanisms proposed above, only the collisional breakup of melting particles remains in our opinion as an explanation for the decreasing F_Z seen for rimed profiles (Figure 6).

7 Conclusions and Outlook

Knowledge about processes in the ML is crucial for precipitation modeling and estimation by remote sensors. Different radar remote sensing approaches and in-situ observations have been used to infer the importance of different processes within the ML. Of these approaches, the ZFR approach initially proposed by Drummond et al. (1996) is particularly promising to infer the evolution of properties such as mean mass in the ML. The main advantage of the method is that it provides a simple diagnostic of whether

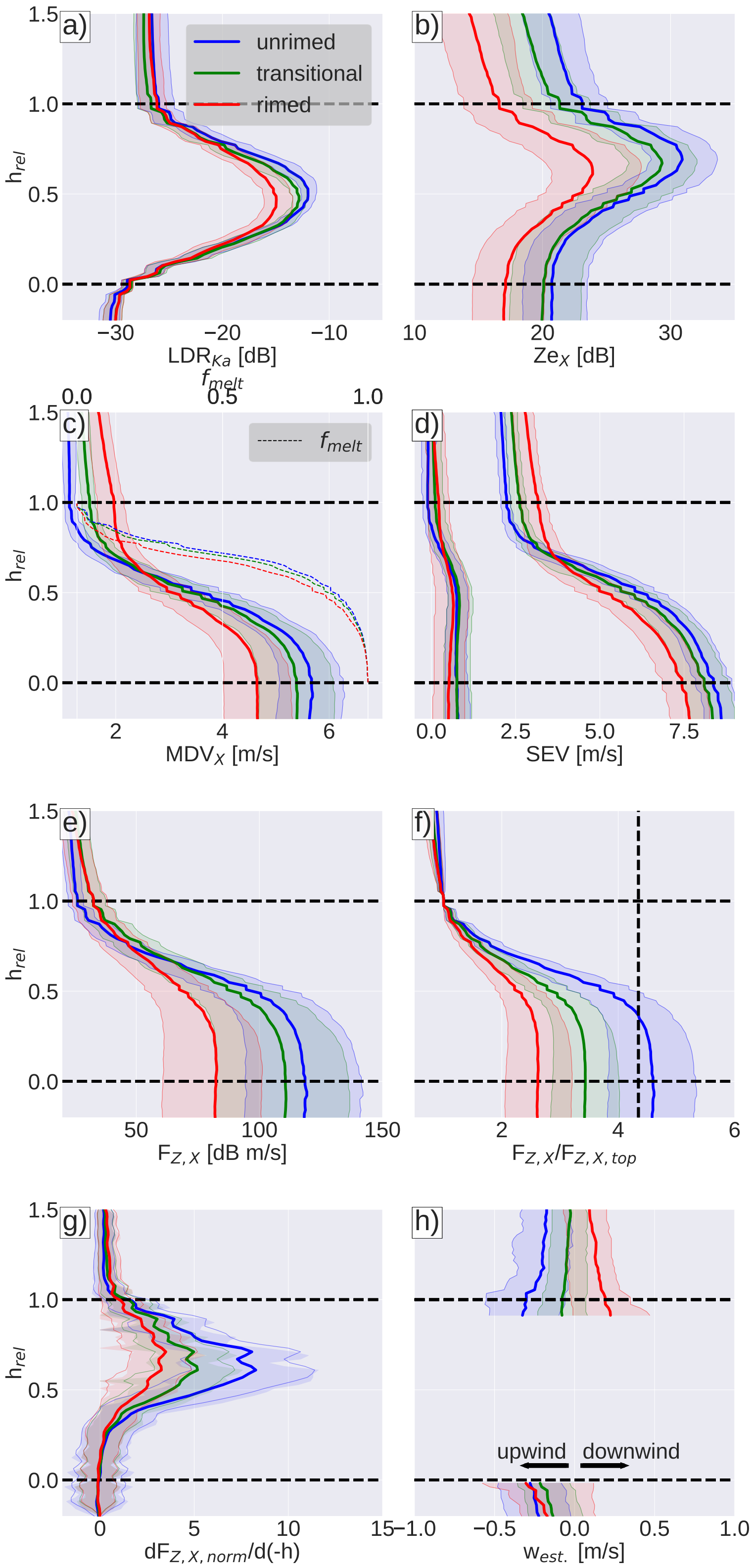

Figure 5. Profiles of the median (solid lines) and interquartile range (shading) of several variables in the ML indicating the melting degree, general properties of the particle population and processes ocurring within the ML. a) LDR_{Ka}, b) Ze_X, c) MDV_X and f_{melt}, d) spectral edge velocities SEV, e) F_Z, f) F_Z normalized by $F_{Z,top}$ ($F_{Z,X,norm}$), g) the derivative of $F_{Z,X,norm}(dF_{Z,X,norm}/d(-h))$ and h) vertical wind w estimated from the spectral peaks for h_{rel}>1 and from the Mie notches for h_{rel}<0.0. The height coordinate h_{rel} shows the relative position in the ML, where 0.0 corresponds to $h_{melt,bottom}$ and 1.0 to $h_{melt,top}$. f_{melt} in c) is derived using Figure 2 from Mitra et al. (1990) as fitted by Frick et al. (2013). The vertical dashed line in f) indicates ZFR=1. Only profiles with $F_{Z,top}$>20 dBzm/s and $F_{Z,bottom}$/0.23>20 dBzm/s are used to calculate medians and quantiles.

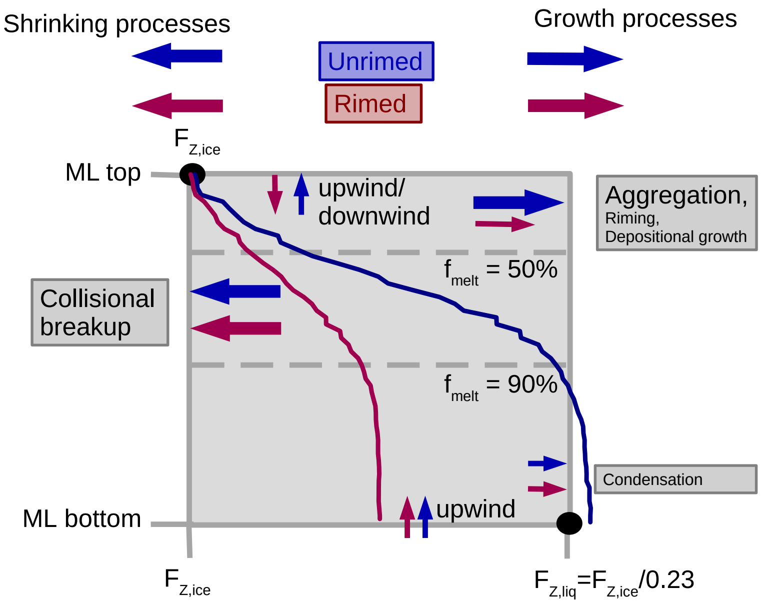

Figure 6. Schematic of the growth and shrinking processes that potentially modify the reflectivity flux in addition to the increasing dielectric factor. In blue for unrimed and red for rimed profiles. The thickness of horizontal arrows indicates the estimated magnitude of the processes at the different height regions. Vertical arrows indicate up- or downwind. The typical height, where the melting fraction f_{melt} is at 50 and 90% is indicated by gray dashed lines.

mean mass and mass flux are conserved within the ML or if rather growth/shrinking processes have to be considered. In this study, we assess the uncertainty of the ZFR approach and derive statistics of ZFR to systematically investigate how the mean mass changes within the ML. Furthermore, we investigated whether the differences between profiles with unrimed and rimed snowflakes above the ML found in previous studies can also be seen in our statistics. For this, we apply the ZFR approach proposed initially by Drummond et al. (1996) on 132 hours of observed ML and combine it with novel radar methods: 1. We infer w from characteristics of the Doppler spectra 2. We categorize between three different categories of the riming degree (unrimed, transitional, rimed), applying the methodology of Li et al. (2020), which uses dual-wavelength ratios and Doppler velocity observations.

The large dataset allows us to derive robust statistics about ZFR for different particle types. The most intriguing feature of these statistics is that ZFR indicates slight growth for unrimed profiles but substantial shrinking for rimed profiles. Furthermore, the ZFR statistics holds even when various quality filters (low F_Z), temporal averages, and corrections for w are applied.

Previous studies using the ZFR approach assumed that changes in the mass flux could be neglected in the atmosphere. Thus, the ZFR directly indicates whether aggregation or breakup dominates. Drummond et al. (1996) reported that aggregation dominates in most cases, but breakup dominates in the case of high precipitation rates. Mróz et al. (2021) analyzed a 6 hour period, in which breakup is more important than aggregation for unrimed but less important for rimed profiles. Drummond et al. (1996) and Mróz et al. (2021) considered a rather short time range, which did not allow them to apply as detailed filters and corrections as in this study. Thus, differences from our study might be rather coincidental. Gatlin et al. (2018) showed that breakup is dominant for thin MLs, which corresponds to small particles, and aggregation is dominant for thick ML (large particles). This dependency is consistent with our analysis since unrimed profiles, which show increasing fluxes, are associated with larger sizes, and rimed profiles, which show decreasing fluxes, are associated with smaller sizes.

We analyzed profiles of several variables within the ML to infer which processes might cause the slightly increasing F_Z for unrimed and the decreasing F_Z for rimed profiles. As many previous studies (Stewart et al., 1984; Fabry & Zawadzki, 1995; Barthazy et al., 1998; Heymsfield et al., 2015; Gatlin et al., 2018), we suspect that aggregation is continuing within the ML. Aggregation might be more efficient for unrimed than for rimed profiles, e.g., due to particle shape. Since ZFR is significantly below one for unrimed profiles, shrinking processes must be present, too. Since the SEV suggests that even the largest particles are not large enough to be affected by hydrodynamic breakup or shedding, we concluded that these processes are not active in the clouds of our dataset. Surprisingly, the rain population at the ML bottom of the unrimed profiles revealed larger MDV_X, SEV and Ze_X than the rimed profiles indicating larger mean sizes and potentially higher number concentrations. Since collisional breakup of pure liquid particles is more effective for larger mean sizes, it is also unlikely that this breakup mechanism can explain the lower ZFR for rimed profiles. Also, sublimation and melting fragmentation are probably not considerably changing F_Z, because both processes would be efficient only at low relative humidities. Consequently, in our opinion, only the collisional breakup of melting particles remains as an explanation for the lower ZFR seen for rimed profiles. Collisional breakup of melting particles might occur in similar magnitude for both unrimed and rimed profiles. However, the aggregation rates could compensate for the breakup processes to a greater extent for unrimed than for rimed particles. Competing effects of aggregation and breakup were also suspected to explain number flux estimate from in-situ observations (Yokoyama et al., 1985; Barthazy et al., 1998).

Obtaining a more complete picture of the ML processes is hampered by the limited knowledge of the relevant processes on the particle level, their significance, and the difficulty in interpreting radar observations of the ML. In our opinion, a closure between detailed modeling, e.g., with novel Lagrangian particle models like Brdar and Seifert (2018) and all observational fields (laboratory, in-situ and remote sensing) is the most promising way forward. More detailed and extensive laboratory studies, including collisional breakup of melting particles, and advances in melting particle scattering properties are crucial for the successful application of such an approach. These laboratory studies could help to improve the detailed models. Better knowledge of scattering properties (e.g., the dielectric factor for melting particles of complex shape) could ease the interpretation of the radar observation and enable comparison with the models.

Acknowledgments

Contributions by MK, SK, and JD were funded by the German Research Foundation (DFG) under grant KN 1112/2-1 as part of the Emmy-Noether Group "Optimal combination of Polarimetric and Triple Frequency radar techniques for Improving Microphysical process understanding of cold clouds" (OPTIMIce). The TRIPEx-pol campaign and work provided by LvT have been supported by the DFG Priority Program SPP2115 "Fusion of Radar Polarimetry and Numerical Atmospheric Modelling Towards an Improved Understanding of Cloud and Precipitation Processes" (PROM) under grant PROM-IMPRINT (project number 408011764). We thank Davide Ori and Axel Seifert for the detailed discussion on the theory of the ZFR approach, flux conservation, and breakup processes implemented in state-of-the-art models. MK also acknowledges support from the Graduate School of Geosciences of the University of Cologne. Code used for the data analysis and already processed data is freely available on GitHub: `https://github.com/markuskarrer/ZFR_riming`. All data obtained at JOYCE-CF are freely available on request from `http://`

cpex-lab.de/cpex-lab/EN/Home/JOYCE-CF/JOYCE-CF_node.html. The Tripex-pol dataset is available at 10.5281/zenodo.5025636.

References

Baldini, L., & Gorgucci, E. (2006, jun). Identification of the melting layer through dual-polarization radar measurements at vertical incidence. *Journal of Atmospheric and Oceanic Technology*, *23*(6), 829–839. Retrieved from https://journals.ametsoc.org/view/journals/atot/23/6/jtech1884_1.xml doi: 10.1175/JTECH1884.1

Bandera, J., Papatsoris, A. D., Watson, P. A., Tan, J., & Goddard, J. W. (1998, oct). Method for detecting the extent of the melting layer. *Electronics Letters*, *34*(22), 2104–2105. doi: 10.1049/el:19981462

Barthazy, E., Henrich, W., & Waldvogel, A. (1998, jun). Size distribution of hydrometeors through the melting layer. *Atmospheric Research*, *47-48*, 193–208. doi: 10.1016/S0169-8095(98)00065-9

Battan, L. J. (1964). Some Observations of Vertical Velocities and Precipitation Sizes in a Thunderstorm. *Journal of Applied Meteorology*, *3*(4), 415–420. Retrieved from https://journals.ametsoc.org/view/journals/apme/3/4/1520-0450_1964_003_0415_soovva_2_0_co_2.xml doi: 10.1175/1520-0450(1964)003⟨0415:soovva⟩2.0.co;2

Bohren, C. F., & Battan, L. J. (1980). Radar backscattering by inhomogeneous precipitation particles. *Journal of the Atmospheric Sciences*, *37*(8), 1821–1827. Retrieved from https://journals.ametsoc.org/view/journals/atsc/37/8/1520-0469_1980_037_1821_rbbipp_2_0_co_2.xml doi: 10.1175/1520-0469(1980)037⟨1821:RBBIPP⟩2.0.CO;2

Brdar, S., & Seifert, A. (2018). McSnow: A Monte-Carlo Particle Model for Riming and Aggregation of Ice Particles in a Multidimensional Microphysical Phase Space. *Journal of Advances in Modeling Earth Systems*, *10*(1), 187–206. doi: 10.1002/2017MS001167

Bringi, V., Seifert, A., Wu, W., Thurai, M., Huang, G. J., & Siewert, C. (2020, aug). Hurricane dorian outer rain band observations and 1d particle model simulations: A case study. *Atmosphere*, *11*(8), 879. Retrieved from www.mdpi.com/journal/atmosphere doi: 10.3390/ATMOS11080879

Cholette, M., Morrison, H., Milbrandt, J. A., & Thériault, J. M. (2019, feb). Parameterization of the bulk liquid fraction on mixed-phase particles in the predicted particle properties (P3) Scheme: Description and idealized simulations. *Journal of the Atmospheric Sciences*, *76*(2), 561–582. Retrieved from www.ametsoc.org/PUBSReuseLicenses doi: 10.1175/JAS-D-18-0278.1

Devisetty, H. K., Jha, A. K., Das, S. K., Deshpande, S. M., Krishna, U. V., Kalekar, P. M., & Pandithurai, G. (2019, jul). A case study on bright band transition from very light to heavy rain using simultaneous observations of collocated X- and Ka-band radars. *Journal of Earth System Science*, *128*(5), 136. Retrieved from https://doi.org/10.1007/s12040-019-1171-0 doi: 10.1007/s12040-019-1171-0

Dias Neto, J., Kneifel, S., Ori, D., Trömel, S., Handwerker, J., Bohn, B., … Simmer, C. (2019). The TRIple-frequency and Polarimetric radar Experiment for improving process observations of winter precipitation. *Earth System Science Data*, *11*(2), 845–863. Retrieved from https://www.earth-syst-sci-data-discuss.net/essd-2018-142/ doi: 10.5194/essd-11-845-2019

Drummond, F. J., Rogers, R. R., Cohn, S. A., Ecklund, W. L., Carter, D. A., & Wilson, J. S. (1996, mar). A new look at the melting layer. *Journal of the Atmospheric Sciences*, *53*(5), 759–769. Retrieved from http://journals.ametsoc.org/jas/article-pdf/53/5/759/3428250/1520-0469 doi: 10.1175/1520-0469(1996)053⟨0759:ANLATM⟩2.0.CO;2

Fabry, F. (2015). *Radar meteorology: Principles and practice.* Retrieved from https://www.cambridge.org/de/academic/subjects/earth-and-environmental-science/atmospheric-science-and-meteorology/radar-meteorology-principles-and-practice?format=PB doi: 10.1017/CBO9781107707405

Fabry, F., & Zawadzki, I. (1995, apr). Long-term radar observations of the melting layer of precipitation and their interpretation. *Journal of the Atmospheric Sciences*, *52*(7), 838–851. Retrieved from https://journals.ametsoc.org/view/journals/atsc/52/7/1520-0469_1995_052_0838_ltroot_2_0_co_2.xml doi: 10.1175/1520-0469(1995)052⟨0838:LTROOT⟩2.0.CO;2

Frick, C., Seifert, A., & Wernli, H. (2013). A bulk parametrization of melting snowflakes with explicit liquid water fraction for the COSMO model. *Geoscientific Model Development*, *6*(6), 1925–1939. Retrieved from www.geosci-model-dev.net/6/1925/2013/ doi: 10.5194/gmd-6-1925-2013

Gatlin, P. N., Petersen, W. A., Knupp, K. R., & Carey, L. D. (2018, aug). Observed response of the raindrop size distribution to changes in the melting layer. *Atmosphere*, *9*(8), 319. Retrieved from http://www.mdpi.com/2073-4433/9/8/319 doi: 10.3390/atmos9080319

Heymsfield, A. J., Bansemer, A., Poellot, M. R., & Wood, N. (2015, aug). Observations of ice microphysics through the melting layer. *Journal of the Atmospheric Sciences*, *72*(8), 2902–2928. Retrieved from https://journals.ametsoc.org/view/journals/atsc/72/8/jas-d-14-0363.1.xml doi: 10.1175/JAS-D-14-0363.1

Heymsfield, A. J., Bansemer, A., Theis, A., & Schmitt, C. (2021, jun). Survival of Snow in the Melting Layer: Relative Humidity Influence. *Journal of the Atmospheric Sciences*, *78*(6), 1823–1845. Retrieved from https://journals.ametsoc.org/view/journals/atsc/aop/JAS-D-20-0353.1/JAS-D-20-0353.1.xml doi: 10.1175/JAS-D-20-0353.1

Heymsfield, A. J., Bansemer, A., & Twohy, C. H. (2007, apr). Refinements to ice particle mass dimensional and terminal velocity relationships for ice clouds. Part I: Temperature dependence. *Journal of the Atmospheric Sciences*, *64*(4), 1047–1067. Retrieved from https://journals.ametsoc.org/view/journals/atsc/64/4/jas3890.1.xml doi: 10.1175/JAS3890.1

Heymsfield, A. J., Schmitt, C., Chen, C. C. J., Bansemer, A., Gettelman, A., Field, P. R., & Liu, C. (2020, aug). Contributions of the Liquid and Ice Phases to Global Surface Precipitation: Observations and Global Climate Modeling. *Journal of the Atmospheric Sciences*, *77*(8), 2629–2648. Retrieved from https://journals.ametsoc.org/view/journals/atsc/77/8/jasD190352.xml doi: 10.1175/JAS-D-19-0352.1

Houze, R. A. (1993). Cloud dynamics. *Cloud dynamics*. Retrieved from https://books.google.com/books?hl=en&lr=&id=GXEpAgAAQBAJ&oi=fnd&pg=PP1&dq=houze+cloud+dynamics&ots=jBbMT2qA-W&sig=mYyz2ZZQxpGGqQ64-mIzOEsAMqo doi: 10.1016/0377-0265(87)90017-0

Illingworth, A. J., Hogan, R. J., O'Connor, E. J., Bouniol, D., Brooks, M. E., Delanoë, J., . . . Wrench, C. L. (2007). Cloudnet: Continuous evaluation of cloud profiles in seven operational models using ground-based observations. *Bulletin of the American Meteorological Society*, *88*(6), 883–898. Retrieved from https://journals.ametsoc.org/view/journals/bams/88/6/bams-88-6-883.xml doi: 10.1175/BAMS-88-6-883

Kalesse, H., Szyrmer, W., Kneifel, S., Kollias, P., & Luke, E. (2016, mar). Fingerprints of a riming event on cloud radar Doppler spectra: Observations and modeling. *Atmospheric Chemistry and Physics*, *16*(5), 2997–3012. doi: 10.5194/acp-16-2997-2016

Kidd, C., Takayabu, Y. N., Skofronick-Jackson, G. M., Huffman, G. J., Braun, S. A., Kubota, T., & Turk, F. J. (2020). The Global Precipitation Measurement

(GPM) Mission. *Advances in Global Change Research*, *67*, 3–23. Retrieved from `https://link.springer.com/chapter/10.1007/978-3-030-24568-9_1` doi: 10.1007/978-3-030-24568-9_1

Klaassen, W. (1988). Radar observations and simulation of the melting layer of precipitation. *Journal of the Atmospheric Sciences*, *45*(24), 3741–3753. Retrieved from `https://journals.ametsoc.org/view/journals/atsc/45/24/1520-0469_1988_045_3741_roasot_2_0_co_2.xml` doi: 10.1175/1520-0469(1988)045⟨3741:ROASOT⟩2.0.CO;2

Kneifel, S., Leinonen, J., Tyynelä, J., Ori, D., & Battaglia, A. (2020). Scattering of Hydrometeors. In *Advances in global change research* (Vol. 67, pp. 249–276). Springer. Retrieved from `https://link.springer.com/chapter/10.1007/978-3-030-24568-9_15` doi: 10.1007/978-3-030-24568-9_15

Kneifel, S., & Moisseev, D. N. (2020, aug). Long-term statistics of riming in non-convective clouds derived from ground-based doppler cloud radar observations. *Journal of the Atmospheric Sciences*, *77*(10), 3495–3508. Retrieved from `www.ametsoc.org/PUBSReuseLicenses` doi: 10.1175/JAS-D-20-0007.1

Knight, C. A. (1979). Observations of the morphology of melting snow. *Journal of the Atmospheric Sciences*, *36*(6), 1123–1130. Retrieved from `https://journals.ametsoc.org/view/journals/atsc/36/6/1520-0469_1979_036_1123_ootmom_2_0_co_2.xml` doi: 10.1175/1520-0469(1979)036⟨1123:OOTMOM⟩2.0.CO;2

Kollias, P., Albrecht, B. A., & Marks, F. (2002, oct). Why mie? Accurate observations of vertical air velocities and raindrops using a cloud radar. *Bulletin of the American Meteorological Society*, *83*(10), 1471–1484. Retrieved from `https://journals.ametsoc.org/view/journals/bams/83/10/bams-83-10-1471.xml` doi: 10.1175/bams-83-10-1471

Kollias, P., Clothiaux, E. E., Miller, M. A., Albrecht, B. A., Stephens, G. L., & Ackerman, T. P. (2007, oct). Millimeter-wavelength radars: New frontier in atmospheric cloud and precipitation research. *Bulletin of the American Meteorological Society*, *88*(10), 1608–1624. Retrieved from `https://journals.ametsoc.org/view/journals/bams/88/10/bams-88-10-1608.xml` doi: 10.1175/BAMS-88-10-1608

Kumjian, M. R., Mishra, S., Giangrande, S. E., Toto, T., Ryzhkov, A. V., & Bansemer, A. (2016, apr). Polarimetric radar and aircraft observations of saggy bright bands during MC3E. *Journal of Geophysical Research*, *121*(7), 3584–3607. Retrieved from `https://agupubs.onlinelibrary.wiley.com/doi/full/10.1002/2015JD024446https://agupubs.onlinelibrary.wiley.com/doi/abs/10.1002/2015JD024446https://agupubs.onlinelibrary.wiley.com/doi/10.1002/2015JD024446` doi: 10.1002/2015JD024446

Lamb, D., & Verlinde, J. (2011). *Physics and chemistry of clouds.* Cambridge University Press. Retrieved from `https://www.cambridge.org/core/books/physics-and-chemistry-of-clouds/8047669DCB91440F5A07AF5BC65A72C6` doi: 10.1017/CBO9780511976377

Leinonen, J., & von Lerber, A. (2018, feb). Snowflake Melting Simulation Using Smoothed Particle Hydrodynamics. *Journal of Geophysical Research: Atmospheres*, *123*(3), 1811–1825. Retrieved from `https://doi.org/10.1002/2017JD027909` doi: 10.1002/2017JD027909

Li, H., Möhler, O., Petäjä, T., & Moisseev, D. N. (2021). Multiyear statistics of columnar ice production in stratiform clouds over Hyytiälä , Finland. *ACPD*(May), 1–26. Retrieved from `https://acp.copernicus.org/preprints/acp-2021-332/`

Li, H., Tiira, J., von Lerber, A., & Moisseev, D. N. (2020). Towards the connection between snow microphysics and melting layer: Insights from multi-frequency and dual-polarization radar observations during BAECC. *Atmospheric Chemistry and Physics*, 1–23. doi: 10.5194/acp-2020-16

Locatelli, J. D., & Hobbs, P. V. (1974). Fall speeds and masses of solid precipitation particles. *Journal of Geophysical Research*, *79*(15), 2185–2197. Retrieved from http://doi.wiley.com/10.1029/JC079i015p02185 doi: 10.1029/jc079i015p02185

Löffler-Mang, M., & Joss, J. (2000). An optical disdrometer for measuring size and velocity of hydrometeors. *Journal of Atmospheric and Oceanic Technology*, *17*(2), 130–139. Retrieved from https://journals.ametsoc.org/view/journals/atot/17/2/1520-0426_2000_017_0130_aodfms_2_0_co_2.xml doi: 10.1175/1520-0426(2000)017⟨0130:AODFMS⟩2.0.CO;2

Lohmann, U., Lüönd, F., & Mahrt, F. (2016). *An introduction to clouds: From the microscale to climate*. Cambridge University Press. Retrieved from https://www.cambridge.org/core/books/an-introduction-to-clouds/F5A8096E7A3BD5C8FFD9208248DD1839 doi: 10.1017/CBO9781139087513

Löhnert, U., Schween, J. H., Acquistapace, C., Ebell, K., Maahn, M., Barrera-Verdejo, M., … Crewell, S. (2015). JOYCE: Jülich Observatory for Cloud Evolution. *Bulletin of the American Meteorological Society*, *96*(7), 1157–1174. Retrieved from https://journals.ametsoc.org/view/journals/bams/96/7/bams-d-14-00105.1.xml doi: 10.1175/BAMS-D-14-00105.1

Low, T. B., & List, R. (1982). Collision, coalescence and breakup of raindrops. Part II: parameterization and fragment size distributions. *Journal of the Atmospheric Sciences*, *39*(7), 1607–1618. Retrieved from https://journals.ametsoc.org/view/journals/atsc/39/7/1520-0469_1982_039_1607_ccabor_2_0_co_2.xml doi: 10.1175/1520-0469(1982)039⟨1607:ccabor⟩2.0.co;2

Luke, E. P., & Kollias, P. (2013, aug). Separating cloud and drizzle radar moments during precipitation onset using doppler spectra. *Journal of Atmospheric and Oceanic Technology*, *30*(8), 1656–1671. Retrieved from https://journals.ametsoc.org/view/journals/atot/30/8/jtech-d-11-00195_1.xml doi: 10.1175/JTECH-D-11-00195.1

Mason, S. L., Chiu, C. J., Hogan, R. J., Moisseev, D. N., & Kneifel, S. (2018, dec). Retrievals of Riming and Snow Density From Vertically Pointing Doppler Radars. *Journal of Geophysical Research: Atmospheres*, *123*(24), 13,807–13,834. Retrieved from https://onlinelibrary.wiley.com/doi/abs/10.1029/2018JD028603 doi: 10.1029/2018JD028603

McFarquhar, G. M. (2004). A new representation of collision-induced breakup of raindrops and its implications for the shapes of raindrop size distributions. *Journal of the Atmospheric Sciences*, *61*(7), 777–794. Retrieved from https://journals.ametsoc.org/view/journals/atsc/61/7/1520-0469_2004_061_0777_anrocb_2.0.co_2.xml?tab_body=fulltext-display doi: 10.1175/1520-0469(2004)061⟨0777:ANROCB⟩2.0.CO;2

Mitra, S. K., Vohl, O., Ahr, M., & Pruppacher, H. R. (1990, mar). A wind tunnel and theoretical study of the melting behaviour of atmospheric ice particles. IV: experiment and theory for snow flakes. *Journal of the Atmospheric Sciences*, *47*(5), 584–591. Retrieved from https://journals.ametsoc.org/view/journals/atsc/47/5/1520-0469_1990_047_0584_awtats_2_0_co_2.xml doi: 10.1175/1520-0469(1990)047⟨0584:AWTATS⟩2.0.CO;2

Morrison, H., Thompson, G., & Tatarskii, V. (2009). Impact of cloud microphysics on the development of trailing stratiform precipitation in a simulated squall line: Comparison of one- and two-moment schemes. *Monthly Weather Review*, *137*(3), 991–1007. doi: 10.1175/2008MWR2556.1

Mosimann, L. (1995, aug). An improved method for determining the degree of snow crystal riming by vertical Doppler radar. *Atmospheric Research*, *37*(4), 305–323. doi: 10.1016/0169-8095(94)00050-N

Mróz, K., Battaglia, A., Kneifel, S., D'Adderio, L. P., & Dias Neto, J. (2020, mar). Triple-Frequency Doppler Retrieval of Characteristic Raindrop Size. *Earth and Space Science*, *7*(3). Retrieved from https://onlinelibrary.wiley.com/

doi/abs/10.1029/2019EA000789 doi: 10.1029/2019EA000789

Mróz, K., Battaglia, A., Kneifel, S., Von Terzi, L., Karrer, M., & Ori, D. (2021, jan). Linking rain into ice microphysics across the melting layer in stratiform rain: A closure study. *Atmospheric Measurement Techniques*, *14*(1), 511–529. doi: 10.5194/AMT-14-511-2021

Myagkov, A., Kneifel, S., & Rose, T. (2020, nov). Evaluation of the reflectivity calibration of W-band radars based on observations in rain. *Atmospheric Measurement Techniques*, *13*(11), 5799–5825. doi: 10.5194/AMT-13-5799-2020

Oraltay, R. G., & Hallett, J. (1989, dec). Evaporation and melting of ice crystals: A laboratory study. *Atmospheric Research*, *24*(1-4), 169–189. doi: 10.1016/0169-8095(89)90044-6

Oraltay, R. G., & Hallett, J. (2005, feb). The melting layer: A laboratory investigation of ice particle melt and evaporation near 0°C. *Journal of Applied Meteorology*, *44*(2), 206–220. Retrieved from https://journals.ametsoc.org/view/journals/apme/44/2/jam2194.1.xml doi: 10.1175/JAM2194.1

Ori, D., & Kneifel, S. (2018, sep). Assessing the uncertainties of the discrete dipole approximation in case of melting ice particles. *Journal of Quantitative Spectroscopy and Radiative Transfer*, *217*, 396–406. doi: 10.1016/j.jqsrt.2018.06.017

Ori, D., Schemann, V., Karrer, M., Dias Neto, J., von Terzi, L., Seifert, A., & Kneifel, S. (2020, jul). Evaluation of ice particle growth in ICON using statistics of multi-frequency Doppler cloud radar observations. *Quarterly Journal of the Royal Meteorological Society*, *146*(733), 3830–3849. Retrieved from https://rmets.onlinelibrary.wiley.com/doi/full/10.1002/qj.3875https://rmets.onlinelibrary.wiley.com/doi/abs/10.1002/qj.3875https://rmets.onlinelibrary.wiley.com/doi/10.1002/qj.3875 doi: 10.1002/qj.3875

Phillips, V. T., Pokrovsky, A., & Khain, A. (2007, feb). The influence of time-dependent melting on the dynamics and precipitation production in maritime and continental storm clouds. *Journal of the Atmospheric Sciences*, *64*(2), 338–359. Retrieved from https://journals.ametsoc.org/view/journals/atsc/64/2/jas3832.1.xml doi: 10.1175/JAS3832.1

Pruppacher, H. R., Klett, J. D., & Wang, P. K. (1998). Microphysics of Clouds and Precipitation. *Aerosol Science and Technology*, *28*(4), 381–382. doi: 10.1080/02786829808965531

Radenz, M., Bühl, J., Seifert, P., Griesche, H., & Engelmann, R. (2019, sep). Peak-Tree: A framework for structure-preserving radar Doppler spectra analysis. *Atmospheric Measurement Techniques*, *12*(9), 4813–4828. doi: 10.5194/AMT-12-4813-2019

Rasmussen, R. M., & Heymsfield, A. J. (1987, oct). Melting and Shedding of Graupel and Hail. Part I: Model Physics. *Journal of the Atmospheric Sciences*, *44*(19), 2754–2763. Retrieved from https://journals.ametsoc.org/view/journals/atsc/44/19/1520-0469_1987_044_2754_masoga_2_0_co_2.xml doi: 10.1175/1520-0469(1987)044⟨2754:masoga⟩2.0.co;2

Ryzhkov, A. V., & Zrnic, D. S. (2019). Polarimetric Microphysical Retrievals. In *Radar polarimetry for weather observations* (pp. 435–464). doi: 10.1007/978-3-030-05093-1_11

Seifert, A., & Beheng, K. D. (2006). A two-moment cloud microphysics parameterization for mixed-phase clouds. Part 1: Model description. *Meteorology and Atmospheric Physics*, *92*(1-2), 45–66. doi: 10.1007/s00703-005-0112-4

Stewart, R. E., Marwitz, J. D., Pace, J. C., & Carbone, R. E. (1984). Characteristics through the melting layer of stratiform clouds. *Journal of the Atmospheric Sciences*, *41*(22), 3227–3237. Retrieved from https://journals.ametsoc.org/view/journals/atsc/41/22/1520-0469_1984_041_3227_cttmlo_2_0_co_2.xml doi: 10.1175/1520-0469(1984)041⟨3227:CTTMLO⟩2.0.CO;2

Straub, W., Beheng, K. D., Seifert, A., Schlottke, J., & Weigand, B. (2010, mar). Numerical investigation of collision-induced breakup of raindrops. Part II: Parameterizations of coalescence efficiencies and fragment size distributions. *Journal of the Atmospheric Sciences*, *67*(3), 576–588. Retrieved from `https://journals.ametsoc.org/view/journals/atsc/67/3/2009jas3175.1.xml` doi: 10.1175/2009JAS3175.1

Szyrmer, W., & Zawadzki, I. (1999, oct). Modeling of the melting layer. Part I: Dynamics and microphysics. *Journal of the Atmospheric Sciences*, *56*(20), 3573–3592. Retrieved from `https://journals.ametsoc.org/view/journals/atsc/56/20/1520-0469_1999_056_3573_motmlp_2.0.co_2.xml` doi: 10.1175/1520-0469(1999)056⟨3573:MOTMLP⟩2.0.CO;2

Thériault, J. M., & Stewart, R. E. (2010, may). A parameterization of the microphysical processes forming many types of winter precipitation. *Journal of the Atmospheric Sciences*, *67*(5), 1492–1508. doi: 10.1175/2009JAS3224.1

Thompson, G., Field, P. R., Rasmussen, R. M., & Hall, W. D. (2008). Explicit forecasts of winter precipitation using an improved bulk microphysics scheme. Part II: Implementation of a new snow parameterization. *Monthly Weather Review*, *136*(12), 5095–5115. doi: 10.1175/2008MWR2387.1

Tridon, F., & Battaglia, A. (2015, jun). Dual-frequency radar doppler spectral retrieval of rain drop size distributions and entangled dynamics variables. *Journal of Geophysical Research*, *120*(11), 5585–5601. Retrieved from `https://agupubs.onlinelibrary.wiley.com/doi/full/10.1002/2014JD023023https://agupubs.onlinelibrary.wiley.com/doi/abs/10.1002/2014JD023023https://agupubs.onlinelibrary.wiley.com/doi/10.1002/2014JD023023` doi: 10.1002/2014JD023023

Tridon, F., Battaglia, A., & Kneifel, S. (2020, sep). Estimating total attenuation using Rayleigh targets at cloud top: Applications in multilayer and mixed-phase clouds observed by ground-based multifrequency radars. *Atmospheric Measurement Techniques*, *13*(9), 5065–5085. doi: 10.5194/AMT-13-5065-2020

Vogel, T., Maahn, M., Kneifel, S., Schimmel, W., Moisseev, D. N., & Kalesse, H. (2021). Using artificial neural networks to predict riming from Doppler cloud radar observations. *Atmospheric Measurement Techniques*. Retrieved from `https://amt.copernicus.org/preprints/amt-2021-137/`

Willis, P. T., & Heymsfield, A. J. (1989). Structure of the melting layer in mesoscale convective system stratiform precipitation. *Journal of the Atmospheric Sciences*, *46*(13), 2008–2025. Retrieved from `https://journals.ametsoc.org/view/journals/atsc/46/13/1520-0469_1989_046_2008_sotmli_2_0_co_2.xml` doi: 10.1175/1520-0469(1989)046⟨2008:SOTMLI⟩2.0.CO;2

Yokoyama, T., Tanaka, H., Akaeda, K., Ohtani, T., Yoshizawa, N., Yamanaka, M. D., ... Ono, A. (1985). Observation on Microphysical Processes in the Stratiform Precipitations Including Melting Layers at Mt. Fuji. *Journal of the Meteorological Society of Japan. Ser. II*, *63*(1), 100–111. doi: 10.2151/jmsj1965.63.1_100

Zhu, Z., Kollias, P., Yang, F., & Luke, E. (2021, jan). On the Estimation of In-Cloud Vertical Air Motion Using Radar Doppler Spectra. *Geophysical Research Letters*, *48*(1), e2020GL090682. Retrieved from `https://onlinelibrary.wiley.com/doi/10.1029/2020GL090682` doi: 10.1029/2020GL090682

Zrnic, D. S., Raghavan, R., & Chandrasekar, V. (1994). Observations of copolar correlation coefficient through a bright band at vertical incidence. *Journal of Applied Meteorology*, *33*(1), 45–52. Retrieved from `https://journals.ametsoc.org/view/journals/apme/33/1/1520-0450_1994_033_0045_occct_2_0_co_2.xml` doi: 10.1175/1520-0450(1994)033⟨0045:OOCCCT⟩2.0.CO;2

5.1 SIMULATION OF MELTING LAYER PROCESSES WITH THE LAGRANGIAN PARTICLE MODEL MCSNOW

Karrer et al., 2021b analyzed which processes are dominant in the melting layer (ML) by comparing the observed reflectivity flux at the top and the bottom of the ML and investigating mean profiles of several radar variables. It is found that the observed reflectivity flux, when corrected for the change of the dielectric factor, increases slightly for unrimed and decreases substantially for rimed profiles. This increase/decrease in the reflectivity flux can be directly related to a change in the mean mass, where an increase (decrease) indicates an increase (decrease) in the mean mass. This additional study investigates whether growth and breakup mechanisms currently implemented in the Lagrangian particle model McSnow can explain the observed reflectivity flux ratio for unrimed and rimed profiles.

Since the mass distribution is explicitly known in the model simulations, the equivalent reflectivity flux F_Z (Equation 3 in Karrer et al., 2021b) can be calculated simply as a product of the second moment of the mass distribution and the mean velocity weighted with mass squared. Thus, in contrast to the observations, the reflectivity flux ratio ZFR can be defined without considering the dielectric factor:

$$\mathrm{ZFR} = \frac{F_{Z,\mathrm{bottom}}}{F_{Z,\mathrm{top}}}, \tag{5.1}$$

Here, $F_{Z,\mathrm{bottom}}$ and $F_{Z,\mathrm{top}}$ are the F_Z at the ML bottom and top. Values of ZFR below one indicate shrinking (decreasing mean mass), values above one indicate growth (increasing mean mass).

Since McSnow contains a sophisticated and up-to-date representation of particle melting, including some breakup mechanisms, this study aims to answer the question of whether the known and parameterized breakup mechanisms (hydrodynamic and collision breakup of liquid particles and shedding of large graupel and hail particles) can explain the observations. If McSnow can not reproduce the observations of Karrer et al., 2021b, new parameterizations of already observed (melting fragmentation) and new processes (collision fragmentation of melting particles) must be considered.

5.1.1 *Modeling Setup and Implemented Microphysical Processes*

In the McSnow simulations, the particle population is initialized at the model top and is modified by several microphysical processes as it sediments through the simulation column. The particles are initialized as unrimed aggregates following a gamma-distribution of the number distribution as a function of mass with ν=2.0 and μ=1/3 (Equation 2.9). The unrimed aggregates follow the geometry of "Mix2" from Karrer et al., 2020 and riming modifies this particle geometry according to the similarity theory of Seifert et al., 2019. The simulations have 150 vertical levels, which gives a vertical resolution of 20 m considering the model height of 3000m. The multiplicity increases with increasing number concentration N (Table 5.1), so that all simulations are computationally feasible, but enough superparticles are simulated to sample the hydrometeor population realistically. For simulations with very low N, the multiplicity is set to one, and the model can simulate all particles explicitly (Table 5.1). The simulations are run for 20 hours from which the last 10 hours are averaged to ensure steady-state conditions and to reduce the noise in the profiles. Thermodynamic profiles are constant over time, and thus no feedbacks from microphysical processes such as depositional growth are considered.

The profiles of temperature and humidity and processes active at different heights are sketched in Figure 5.1. The temperature increases linearly with decreasing height from -8°C to 8°C, so that ice growth processes are simulated in the upper half and processes in and below the melting layer are simulated in the lower half of the simulation column. The particles are initialized at the model top as a population of aggregates with various combinations of hydrometeor contents (Table 5.1), similar to those simulated in the 3D LES simulations of Karrer et al., 2021a (Figure 5.2). In the upper 1000m of the simulation, the humidity is above the saturation level with respect to ice but below the saturation level with respect to water. Thus, depositional growth, but not riming, occurs. However, riming happens between 1500m and 2000m if supercooled drops are present (Table 5.1). Aggregation/collisions can occur at all temperatures below 0°C and additionally within the melting layer also when one or both colliding particles already started to melt. Only collisions between a purely liquid particle and an ice or mixed phase particle are not considered. Near the ML bottom, pure liquid processes could happen. This possibility of pure liquid processes within the ML is possible because smaller particles melt faster than larger particles. As a result, the smaller particles can already be purely liquid and coexist with still melting particles. These pure liquid processes include collision-coalescence and breakup due to the collision of liquid particles (Straub et al., 2010) and hydrodynamic instability of large liquid particles (Srivastava, 1971). Both processes occur only in the presence of rather large particle sizes of several mm.

The mass melted per timestep is calculated by considering the available heat for the melting process following Rasmussen and Heymsfield, 1987 and assuming a constant particle temperature of 0°C. As the melting particles fall into the increasingly warmer ambient air but remain at T=0°C, the air near the surface of the particle is supersaturated and thus grows by absorbing vapor from the ambient air. The vapor transfer is assumed to happen on the liquid surface of the particle and is thus referred to as condensation. During the melting of large graupel and hail particles, liquid particles are shed according

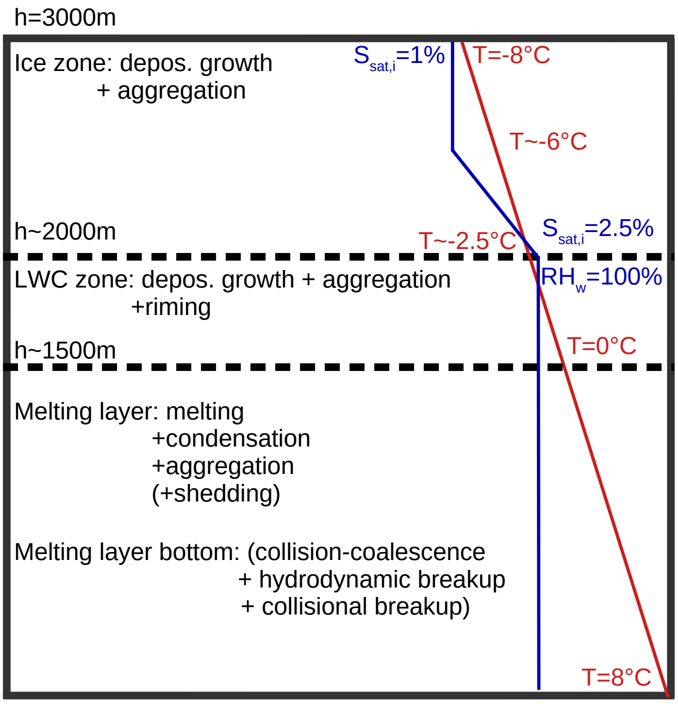

Figure 5.1: Schematic of atmospheric variables and active processes in the McSnow simulations. Initialization occurs at 3000m at a temperature of -8°C and 1% supersaturation with respect to ice ($S_{sat,i}$). The temperature increases linearly so that 0°C (8°C) is reached at 1500m (0m). At heights below 2500m, $S_{sat,i}$ increases linearly and reaches 2.5% at 2000m, which corresponds to the water saturation level. Below 2000m, the relative humidity stays at water saturation level. Processes, which could occur in the different height intervals, are listed on the left.

Parameter	values
Mass concentration Q [kg/m^3]	$1{\cdot}10^{-5}$,$5{\cdot}10^{-5}$,$1{\cdot}10^{-4}$,$5{\cdot}10^{-4}$
Mean mass $\bar{x}$ [kg]	$1{\cdot}10^{-9}$,$5{\cdot}10^{-8}$, $1{\cdot}10^{-7}$
Number concentration $N=Q\cdot\bar{x}^{-1}$ [1/m^3]	$1{\cdot}10^2$, $2{\cdot}10^2$, $5{\cdot}10^2$, $1{\cdot}10^3$, $2{\cdot}10^3$, $5{\cdot}10^3$, $1{\cdot}10^4$, $5{\cdot}10^4$, $1{\cdot}10^5$, $5{\cdot}10^5$
Multiplicity $\chi=\max(N{\cdot}2{\cdot}10^{-4},1)$	1,2,5,25
Liquid water content (LWC) [kg/m^3]	0, $2{\cdot}10^{-4}$, $5{\cdot}10^{-4}$, $1{\cdot}10^{-3}$

Table 5.1: Parameters used for the initialization at model top and generation of differently rimed particles. The number concentration N is calculated from the mass concentration Q and mean mass $\bar{x}$. The multiplicity depends on N, so that all simulations are computational feasible, but enough superparticles are simulated to sample the hydrometeor population realistically. Considering the number of different settings of Q, $\bar{x}$ and LWC, a total number of 60 simulations are performed.

to the parameterization of Rasmussen and Heymsfield, 1987. Similar to the hydrodynamic breakup of purely liquid droplets, shedding also happens due to the hydrodynamic instability and occurs only for mass-equivalent sizes larger than about 8mm (Pruppacher et al., 1998).

As a forward model to simulate LDR from the McSnow output is not available and thus the ML top and bottom can not be defined in the same way as in Karrer et al., 2021b, the ML boundaries are estimated from the ratio of Z_e from the purely liquid to the total Z_e. The ML top is defined as the height where the purely liquid particles contribute only with $1 \cdot 10^{-16}$ to the total reflectivity. At the ML top, the non-liquid particles (pure ice and melting particles) are responsible for only $1 \cdot 10^{-16}$ of the total reflectivity.

5.1.2 *Simulated Profiles and Reflectivity Flux Ratio*

The profiles of all McSnow simulations in Figure 5.2 allow discussing the effect of the microphysical processes at different heights, qualitatively. At temperatures below 0°C, depositional growth and aggregation increase the mean mass $\overline{x}$ and F_Z. Aggregation increases $\overline{x}$ especially effectively if N is large (e.g, purple profiles). In the LWC zone, riming quickly increases Q, $\overline{x}$ and F_Z. Riming and melting lead to a strong decrease of Q and N since these processes strongly increase the terminal velocities v. Due to these low values of N, the profiles appear noisy even though low multiplicities χ are chosen and 10 hours of temporal average is performed. Just below the ML top, F_Z still increases due to aggregation and depositional growth, but then quickly approaches a constant value. Since F_Z does neither increase nor decrease near the ML bottom in most of the simulations, collision-coalescence and breakup due to collision and hydrodynamic instability of liquid particles are either occuring at low rates or compensate for each other.

The observed and simulated Z_e and MDV are displayed together in Figure 5.3 to facilitate their comparison. Z_e is calculated from the simulations as the second moment of the mass distribution. MDV is calculated from the simulations as the v weighted with the second moment of the mass distribution. Effects like non-Rayleigh scattering are not considered because the simulated particles are relatively small and the wavelength of the radar (X-Band) is relatively large. If non-Rayleigh scattering would be important, then the simulated reflectivities would be overestimated. Comparing the observed ZFRs with ZFRs calculated from profiles with similar $Z_{e,\mathrm{top}}$ and $\mathrm{MDV}_{\mathrm{top}}$ allows assessing how well the simulations can reproduce the observations of the different particle categories. All simulated ZFRs are near or above one with a mean of 1.15 and do not show a clear dependency on $Z_{e,\mathrm{top}}$ and $\mathrm{MDV}_{\mathrm{top}}$. The simulations fit well to the statistics of

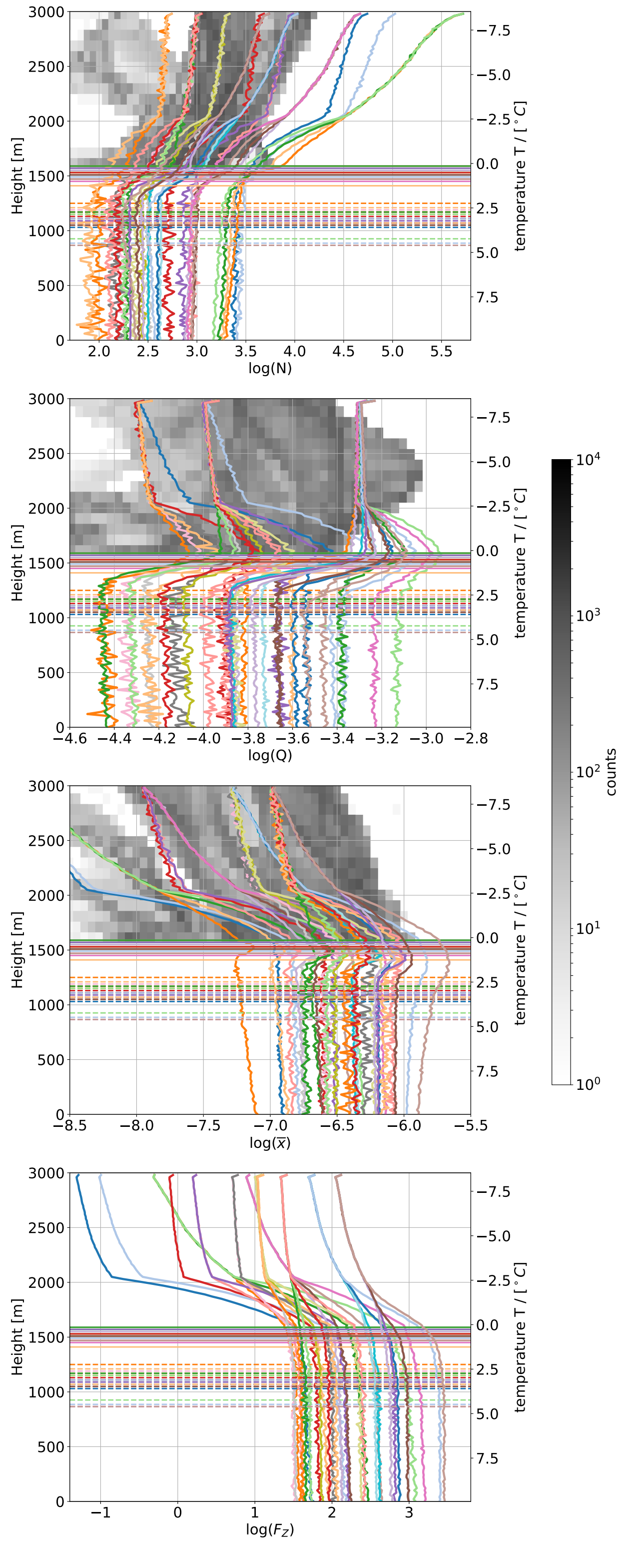

Figure 5.2: Profiles of all McSnow runs which are initialized with different hydrometeor content and where the liquid water content is varied. Number concentration N (top left), mass concentration Q (top right), mean mass $\overline{x}$ (lower left) and F_Z (lower right). For N, Q, and $\overline{x}$ the histogram of the hydrometeor contents vs. temperature from the ICON-LEM simulations of Karrer et al., 2021a are shown grayshaded in the background. Solid horizontal lines depict the ML top and dashed horizontal lines the ML bottom of each simulation. Runs with $F_Z < 30\,\mathrm{mm^6\,m^{-3}\,m\,s^{-1}}$ are not shown for the sake of clarity.

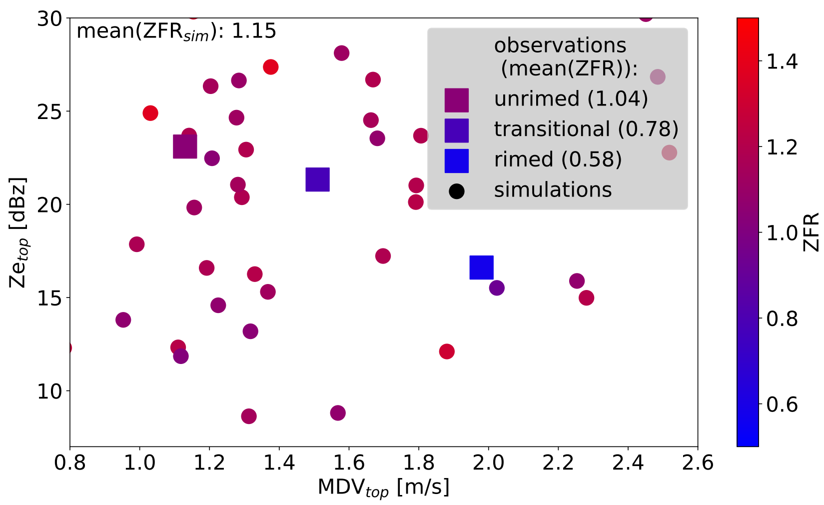

Figure 5.3: Observed and simulated ZFRs for different profiles, represented as points in Z_e-MDV space, in which similar profiles (similar riming degrees, similar hydrometeor contents) are close to each other. Squares display the observed median of Z_e, MDV and ZFR for the three riming categories found in Karrer et al., 2021b. Each circle depicts the values for one McSnow simulation.

the observed unrimed profiles, which have a mean ZFR of 1.04. In contrast, the profiles can not reproduce the transitional and rimed profiles, which have a mean ZFR of 0.78 and 0.58.

If all breakup mechanisms (shedding, collision and hydrodynamic breakup of liquid particles) are switched off in the simulations the mean ZFR increases only slightly from 1.15 to 1.19 and again no clear dependency of ZFR on $Z_{e,top}$ and MDV_{top} is found (Figure 5.4). Thus, these breakup mechanisms do not have a considerable effect on the ZFR.

Karrer et al., 2021b suggested that hydrodynamic and collision breakup of liquid particles and shedding of large graupel and hail particles can not explain the decrease of F_Z in the observed ML profiles, consisting of unrimed and moderately rimed regimes in winter stratiform clouds. This hypothesis could be confirmed by comparing the simulations with and without these breakup processes. As a result, the observed decrease of F_Z for transitional and rimed profiles within the ML can not be explained by these processes. Most likely, other breakup mechanisms such as melting fragmentation and collision breakup of melting particles must be taken into account within the ML to reproduce the observed dependency of ZFR on the particle category.

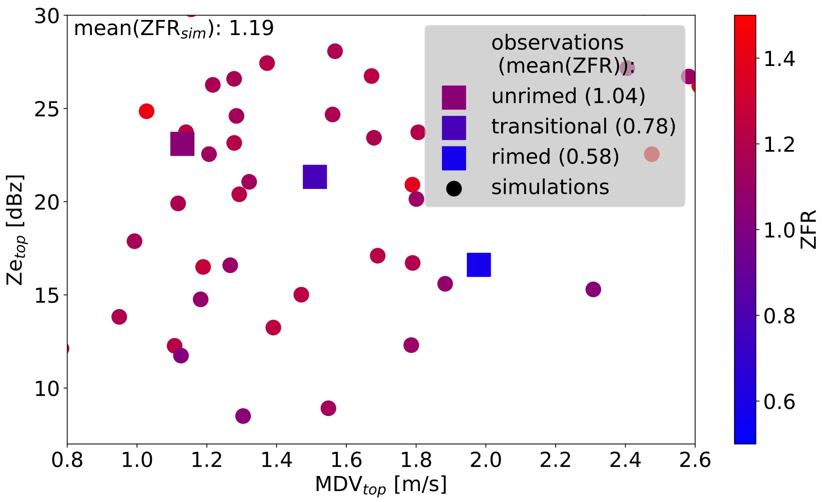

Figure 5.4: Same as Figure 5.3 but for simulations with all breakup processes (shedding, collision and hydrodynamic breakup of liquid particles) switched off.

6 CONCLUSIONS AND OUTLOOK

Precipitation prediction is crucial for many societally relevant areas, e.g., mitigation of disasters caused by heavy rain. In this dissertation, important precipitation forming processes have been investigated.

This investigation has been performed with a variety of microphysical models and observational methods. First, particle properties have been derived with a 3D snowflake model and hydrodynamic theory, revealing characteristics of the sedimentation and aggregation process. Second, parameters relevant to the simulation of these processes, including the previously derived particle properties, were constrained with a two-moment bulk microphysics scheme (SB scheme) by comparing synthetic and observed multi-frequency Doppler observations. Lastly, these observations have been used alongside Lagrangian particle model (McSnow) simulations to uncover processes that might be missing in the current understanding of the melting layer.

The different models used complement each other excellently. The more explicit models (the 3D snowflake and the Lagrangian particle model) can examine the processes in great detail and even provide new parameterizations. The less explicit bulk schemes, which are the "workhorses" for operational forecasting and climate prediction, can incorporate the results (including the newly derived parameterizations) from the explicit models. Due to the numerical efficiency of the bulk schemes, long-term simulations can be performed that allow a statistical comparison between model and observations. This statistical comparison represents a thorough evaluation of the microphysical parameters, which would not be possible with the explicit models alone.

In this chapter, the various approaches to constrain parameters and improve process knowledge that are applied throughout this dissertation are summarized (Figure 6.1). The improvements to the microphysical models achieved through these studies are also discussed. Furthermore, this chapter describes the remaining knowledge gaps of the processes and highlights the benefits and challenges of the different approaches. Finally, an outlook is given on how to address both the general challenge of microphysics model improvement as well as the individual challenges raised in the various studies.

6.1 STUDY I: ICE PARTICLE PROPERTIES INFERRED FROM AGGREGATION MODELLING

In Study I (Chapter 3), the most explicit model employed in this study, the 3D snowflake model of Leinonen, 2013 was used to derive parameterizations of ice particle properties, which are applied in Study I and Study II in the less explicit models, namely McSnow and the SB scheme. Whereas 3D snowflake models have primarily been used to derive scattering properties (e.g. Leinonen and Moisseev, 2015; Leinonen et al., 2018) and perform theoretical studies (e.g. Westbrook et al., 2004b), these models are applied here for the first time to develop parameterizations specifically tailored for microphysics schemes. The application of the 3D snowflake model allowed to address little-studied research questions, which are relevant for microphysical modeling. In combination with hydrodynamic theory, the dependency of aggregate properties on the monomer number and type and the asymptotic behavior of particle properties, such as the terminal velocity, at large and small sizes could be studied. These investigations could hardly be done by in situ observations because of the limited sample size, limited observed size range, and difficulty in analyzing the monomer composition within the aggregates.

"Natura non facit saltus." - "Nature does not make jumps." has been a principle of natural philosophy propagated, e.g., by Leibniz, 1873

Study I found that particle properties, such as mass-size and velocity-size relations, change smoothly during aggregation. "Jumps" in particle properties from monomers to early aggregates found in bulk microphysics which separate between monomers (cloud ice) and snow are found to be too abrupt simplifications and introduce artificial discontinuities that are not physically based. These "jumps" probably stem from limitations of the parameterization from in situ particle observations applied in the schemes and the difficulty of selecting suitable particle property relations for a wide range of applications. For example, even for a single particle property (e.g., terminal velocity) many different relations are given in Study I. This variety of relations is necessary because at different atmospheric conditions, many different monomer types appear. However, most microphysics schemes only allow the selection of one relation for monomers and one for aggregates. This restriction is extremely challenging because the relations must represent a broad range of sizes and be somehow realistic in many cloud regimes. Therefore, these relations must be carefully selected, and the selection might need to be revisited if the model is applied to another regime, such as Arctic mixed-phase clouds.

Not only the selection of the relations representing different monomer types, but also inaccurate parameters can introduce errors in the models that apply these simiplified representations. Therefore the 3D snowflake model and hydrodynamic models should be further improved. In the 3D snowflake model used in this study, the point of contact of the colliding particles is nearly random and only constrained by the preferentially horizontal alignment of the particles. However, the flow in the vicinity of the falling particles, which is determined by the particles boundary layer, may make collision particularly likely at certain points on the particle surface. Considering the flow around the particles explicitly using direct numerical simulations that resolve turbulence completely could improve the realism of the aggregate shape and the derived properties. The uncertainty of the modeled terminal velocity is further increased by uncertainties of the hydrodynamic models for complex-shaped particles. More precisely, this uncertainty stems from incomplete knowledge about the relationships between drag coefficients and particle properties for complex-shaped particles and is particularly large when secondary motions (e.g., tumbling of the particles) have to be considered. Laboratory experiments performed with 3D-printed complex particles sedimenting in a fluid tank, such as McCorquodale and Westbrook, 2021, represent a promising way to refine hydrodynamic models.

McSnow allows using very explicit particle property parameterizations that consider the monomer number dependency of the aggregate properties. Nevertheless, also simpler parameterizations can be used. By comparing these different simulations, one can assess how sensitive the model is to each simplification. This comparison allows quantification of the error caused by a given simplification that has to be made, e.g., in bulk schemes. The classification of unrimed frozen particles into two categories, namely monomers and aggregates, introduces a relatively small error compared to a more detailed parameterization that accounts for the number of monomers in each aggregate snowflake. This small error might be explained by the fact that the biggest change of monomer properties occurs at low monomer numbers, but aggregation often occurs rapidly. As a result, aggregates with low monomer numbers are present only in a short stage of the aggregation process. In contrast, it is crucial to consider the asymptotic behavior of the terminal velocity at large sizes, e.g., by using Atlas-type velocity-size relations. The relatively large deviation of the terminal velocity predicted by the commonly used power-law relations from recent in situ observations and our Atlas-type relations might stem, again, from the fact that these relations have been derived from a sample with a relatively narrow size range.

Another finding of the study that the aggregate properties depend relatively strongly on the composing monomers could not be used in the SB scheme because this scheme does currently not allow the use of several particle property relations for a single hydrometeor category. However, the dataset from Study I could be used to improve the dependence of aggregate properties on the monomers composing them in recently developed (Tsai and Chen, 2020; Shima et al., 2020) and developing (McSnow) habit-predicting schemes. In turn, these habit-predicting models could be used to make the selection of monomers

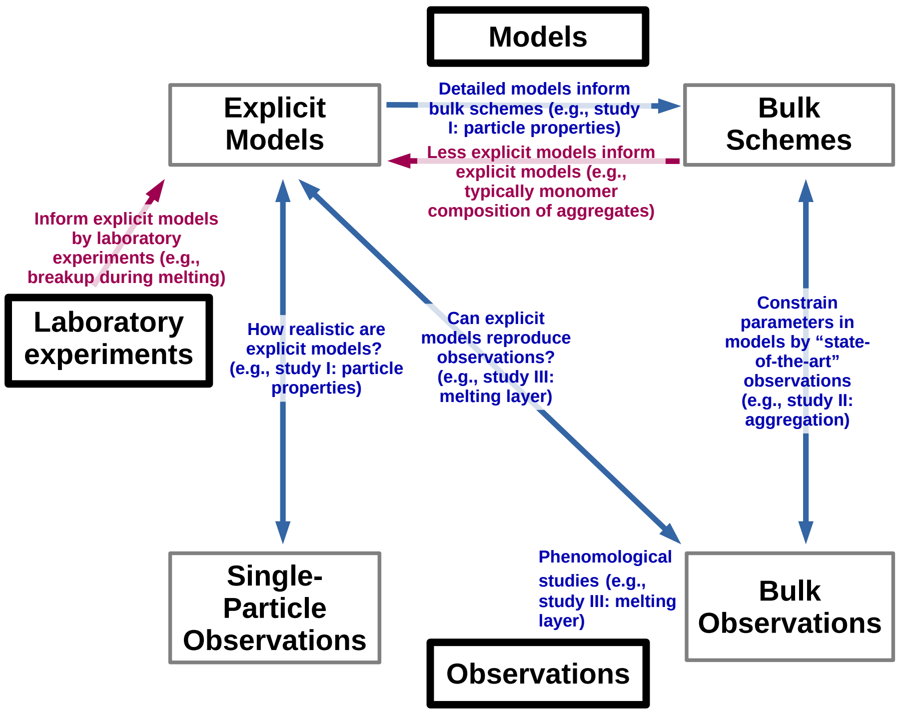

Figure 6.1: Schematic of the approaches applied (blue) and proposed (red) in this dissertation to improve the understanding and simulation of precipitation forming processes. The explicit models are valuable for in-depth process understanding and can be used to improve bulk schemes, which are essential for weather forecasting and climate modeling. While single-particle observations allow studying the evolution of individual particles in situ, bulk observations (remote sensing) allow investigating particle populations and processes considering bulk properties observed over larger volumes, e.g., by radars.

(type and size) composing an aggregate more physically consistent, which might make the 3D snowflake model more realistic.

From a broader perspective, Study I shows that the combination of models which represent microphysics in different degrees of detail allows investigating many aspects along various scales that are important for the microphysical processes (upper part of Figure 6.1). The 3D snowflake model allowed deriving a detailed parameterization of the particle properties but cannot simulate the evolution of the particle population. Therefore, McSnow is an ideal complement to it. In McSnow, the particle properties from the 3D snowflake model can be used to simulate the particle population's evolution and investigate which assumptions are a good approximation in bulk schemes, which are less explicit but more computationally efficient.

Study I also illustrates the importance of the comparison of explicit models with particle-based in situ observations (left side of Figure 6.1). While many aggregate types which consist of only one type of monomers (e.g., needle, plate) can not represent well the mean of the particle properties observed in situ, a specific type of aggregate composed of small needles and large dendrites agreed well with mean properties of these observations.

6.2 STUDY II: CONSTRAIN BULK SCHEME PARAMETERIZATIONS

In Study II (Chapter 4), the parameters affecting the aggregation rates in the SB scheme are constrained by comparison with multi-frequency Doppler radar observations. The goal of this approach is not only to improve the simulation of a single or few processes, but also to assist the interpretation of the observations. Using an idealized single-column simulation, new parameters could be tested in a computationally efficient way, and it could be evaluated how these parameters affect simulated variables in model and observational space. This evaluation benefits from the idealized model setup because it allows to exclude feedbacks from the cloud dynamics and to control which microphysical processes are considered. A combination of parameters could be found that best fit the statistics from the observation. Only after this parameter combination is found are the more computationally intensive and more difficult to interpret 3D LES simulations performed with modified microphysical parameters. The synthetic observational output of these LES simulations shows that some biases, already highlighted by Ori et al., 2020, could be reduced.

The single-column simulations allowed to address these biases by revealing that aggregation is most sensitive to the particle properties and the aggregation kernel formulation. Modifying these two parameterizations reduced the biases of particle velocity and size. After implementing the particle properties from Study I into the SB scheme and carefully considering the effects on the aggregation rates predicted by the scheme, the biases of too high velocities and large particle sizes were reduced. A new area-based formulation of the aggregation kernel also contributed to the reduction of simulated particle sizes. The area-based formulation can take the gaps in the projection of the snowflakes into account, which reduces the probability of collisions. The effect of the model improvements on the precipitation rate was tested on a day with a strong subsaturated air layer near the ground. The particles in the new model setup experienced stronger sublimation above the melting layer and evaporation below the melting layer, and, thus, the precipitation rate decreased. In this case, the precipitation rate predicted by the modified scheme agreed much better with the observed rain rate than the rate predicted by the default scheme because of the large reduction of the biases in particle size and velocity. In the 6-hour period of that day, in which most of the precipitation occurred, the modified scheme overestimated accumulated precipitation by 64%, while the default scheme overestimated it by 536%.

Although the size distribution width parameter showed a relatively small effect on the simulated moments and mean mass, it turned out to be an essential link between model and observation. Unfortunately, the size distribution width could not be well constrained by the observations, and further work is required. This work could focus on using the full Doppler spectrum, e.g. in a retrieval framework. In addition, an in-depth analysis of Lagrangian particle modeling promises further improvements in the understanding and simulation of particle distribution. As the first step in this direction, the size distributions simulated by McSnow and the SB scheme were compared in an idealized simulation in Section 4.1. The main difference between the distributions simulated by McSnow and the SB scheme is that the number concentrations predicted by McSnow at small diameters are lower. However, it is not clear whether McSnow can yet serve as a reference for this application since it has not been thoroughly evaluated against observations, and some processes that could broaden the spectra (e.g., inhomogeneous humidity field) have not been considered.

At temperatures below -20°C, the frequencies combinations employed do not allow to draw conclusions about the characteristic particle sizes. At these temperatures, the typical particle sizes are small and mostly well approximated by the Rayleigh theory even for the highest frequency (W-Band). Therefore, even the dual-wavelength ratios between the shortest wavelengths (Ka- and W-Band) is not sensitive to these particles. This lower sensitivity of the observation, together with the poorly constrained size distribution width, hampers the interpretation of the biases. At temperatures below -25°C, the mean Doppler velocity is slightly overestimated. The overestimation of the dual-wavelength ratio at about -12°C could be mainly propagated from model biases at lower temperatures rather than errors at the temperatures where the mismatches are detectable. Stratifying clouds by their cloud-top temperature could help narrow down the causes of the errors more precisely. Both biases, the overestimation of the mean Doppler velocity and the dual-wavelength ratio, could result from a too broad distribution, too large sticking efficiency, (especially at lower temperatures) or inaccurate monomer (cloud ice) properties. Inclusion of higher frequencies (Battaglia et al., 2014; Lamer et al., 2021) could illuminate the model performance regarding smaller particle size and thus lower temperatures. However, including higher frequencies, e.g., in the G-band, requires special effort to separate differential scattering from differential attenuation effects. Again, analysis of the full Doppler spectra, including retrieval of the size distribution and velocity-size relationship, e.g., similar to Barrett et al., 2019, could help to better constrain parameters, such as size distribution width, sticking efficiency, and monomer properties. Even though monomer properties were estimated to be secondary to precipitation formation in this study, they are particularly important for the radiative effects of clouds in previous studies (e.g., Jakob, 2002).

Other remaining discrepancies between model and observation are the too small mean Doppler velocities at temperatures above -5°C predicted by the revised model. This bias could result from inaccurate simulation of the vertical air motion, riming rates, or the representation of partially rimed particles. In addition to the general challenges of simulating vertical air motion, at these temperatures, the latent heat release during melting can cause mesoscale thermal circulations (Lin and Stewart, 1986). In case of horizontal variability of ice mass, the latent heat release can produce even convective cells with associated vertical winds of several 0.1m/s (Szyrmer and Zawadzki, 1999).

The remaining potential error sources - the inaccuracies in riming rates and the representation of partially rimed particles - are strongly linked, as one can see exemplary when considering the riming implementation in the SB scheme. The SB scheme separates snow from graupel with large differences in the particle properties between those categories. Once riming starts and riming rates exceed the depositional growth rates, snow is converted to graupel leading to a sudden increase in particle velocity and density. This representation of the riming process gives rise to two errors that could cause the underestimation of the mean Doppler velocity. First, at riming rates lower than depositional growth, riming adds mass to the snow category without increasing the particle velocity as one would expect in reality. Second, at riming rates higher than depositional growth rates, riming changes particle properties too rapidly, and the resulting underestimated cross-sectional area leads to too low riming rates and thus underestimated particle velocity. The problem of representing particles of different riming stages can be mitigated by introducing additional prognostic variables that allow a more continuous transition of particle properties (Morrison and Milbrandt, 2015; Tsai and Chen, 2020). However, this approach requires additional assumptions, e.g., about the distribution of the rime mass among the particles of different sizes, which necessitates additional constraints from observations and explicit models to constrain all parameters well. Here, again, polarimetric radars would be helpful due to their ability to infer particle densities. On top of these issues related to the representation of particle properties of partially rimed particles, the parameterization of the collision efficiency could be improved. The relatively simple dependency of the collision efficiency on the snow and cloud droplet mean mass in the SB scheme could be replaced by a new relation derived from the integration of a particle-based collision efficiency proposed, e.g., by Böhm, 1994 over the size distributions of cloud droplets and snow.

Overall, Study II provides an example of how state-of-the-art observations can be used to improve bulk microphysics schemes and reduce gaps in process knowledge (right side of Figure 6.1). More specifically, the multi-frequency setup and Doppler capabilities of the vertically oriented radars have proven to be an abundant source for gaining information on the size and velocity of ice particles and thus on the aggregation and sedimentation process. Polarimetric radars could help to even better constrain these and other processes by providing information, e.g., about the particles' shape, particles' density, and number concentration. For example, polarimetric radars could help to constrain particle properties at lower temperatures or better discriminate particle growth by aggregation from growth by riming.

6.3 STUDY III: PROCESSES IN THE MELTING LAYER

Understanding processes occurring in the melting layer and their relative importance is essential to link properties of the snow above and the rain below the melting layer, which is crucial for microphysical models and precipitation estimation by remote sensors. The case study in Study II showed exemplary that the size of snow particles is closely related to the size of raindrops, and, thus, the snow particle size also affects pure liquid processes such as evaporation which in turn influences the surface precipitation rates.

A connection between ice and rain properties has been investigated in several studies by deriving the ratio of reflectivity from the top and the bottom of the melting layer (Drummond et al., 1996; Gatlin et al., 2018; Mróz et al., 2021; Neto, 2021). These studies assumed that this reflectivity flux ratio (ZFR) reveals whether breakup or collisions dominate the change of mean mass within the melting layer if certain assumptions are met. These assumptions are the negligible influence of vertical wind, homogeneity of the particle population entering the ML, and mass flux conservation. If ZFR is corrected for the change of the dielectric factor during melting, values above/below one indicate an increasing/decreasing mean mass. Similar to Neto, 2021, Study III (Chapter 5) leverages on multi-month statistics from multi-frequency Doppler observations. Going beyond the previous studies, Study III includes the inference of the vertical wind at the melting layer top and bottom from Doppler spectra characteristics into this melting layer analysis. Furthermore, the multi-frequency Doppler observations allow categorizing each profile as unrimed, transitional, or rimed following Li et al., 2020.

These combinations of techniques are used to investigate the difference of microphysical processes when unrimed or rimed ice particles are dominating the particle population above the melting layer. This observational study is extended by a model-observation comparison using McSnow in Section 5.1, which assesses whether this model with a state-of-the-art implementation of microphysical processes can reproduce the observations.

The statistics of Study III show a ZFR slightly above one for unrimed and a ZFR substantially below one for rimed profiles. Since this statistic does not change systematically when corrected for vertical wind, and mass uptake is estimated to be secondary, the deviations of ZFR from one are explained by changes in mean mass. Therefore, a slight dominance of collision processes is present for unrimed profiles and a more pronounced dominance of breakup processes for rimed profiles. Based on the mean characteristics of the different categories and their vertical profiles, it is speculated that breakup of melting particles is occurring for unrimed and rimed profiles at similar rates. However, aggregation could compensate for the effect of breakup stronger in the unrimed than in the rimed profiles.

In all McSnow simulations, which simulate a similar range of mean Doppler velocity and reflectivity as the observations, the ZFR increases within the melting layer independently of the degree of riming. Furthermore, disabling all breakup processes implemented in McSnow does not impact the ZFR systematically. Thus, this study supports the statement from Karrer et al., 2021b that besides the breakup processes currently implemented in McSnow (shedding, collisional breakup of pure liquid particles, and hydrodynamic breakup of raindrops), also other breakup mechanisms should be considered.

Two breakup mechanisms for melting particles might explain the decreasing ZFR. For weakly or moderately rimed particles melting fragmentation was described by laboratory and modeling studies. These studies report that meltwater is observed at several parts of the particles in the early melting stage and the different parts of the particles are only held together by fragile ice bonds. Occasionally, these fragile bonds break, which results in the formation of several fragments (Knight, 1979; Oraltay and Hallett, 1989; Mitra et al., 1990; Oraltay and Hallett, 2005; Leinonen and Lerber, 2018). However, melting fragmentation was described to occur mainly in subsaturated conditions (relative humidity with respect to water RH<70%). Since the mean values of ZFR remained below one for rimed profiles, even if subsaturated conditions were excluded, it is doubtful whether melting fragmentation can explain the decreasing ZFR. Another potential breakup mechanism has not yet been described and therefore not parameterized: the breakup after the collision of melting particles. Similar to what has been described for the case of collision-induced breakup of pure ice particles (Vardiman, 1978; Takahashi et al., 1995; Phillips et al., 2017), breakup could occur at the fragile connections of the melting particles. Therefore, its efficiency could strongly depend on the shape of the particles, which is known to be strongly influenced by the riming degree and melting stag stagee. The efficiency of such a breakup process could be studied in a temperature-controlled vertical wind tunnel, where one particle is levitated, and another faster-falling particle is added and made to collide with the levitated particle. Based on such a laboratory experiment, this breakup process could be included in the McSnow model, and the effect on the simulated ZFR could be investigated, again.

Overall, one can conclude that studying the processes in the melting layer is challenging due to several factors. First, scattering properties of melting particles are poorly known (Kneifel et al., 2020), which limits the interpretability of observed radar signatures. Thus, further advances in scattering property parameterizations using 3D snowflake models and scattering theory such as in Ori and Kneifel, 2018 are crucial. Second, not all potential microphysical processes involving melting particles are well studied or quantified. This lack of laboratory studies hampers its simulation even with the most explicit microphysical models. Compared to aggregation and sedimentation of purely ice-phased particles, the study of melting layer processes is still in its infancy. At this stage, laboratory studies and phenomenological studies, e.g., using state-of-the-art radar techniques as in Study III (lower part of Figure 6.1), are beneficial and a prerequisite for further advances in process understanding and modeling. Furthermore, a comparison between basic quantities from the model and the observations can already give hints on missing processes (center of Figure 6.1).

6.4 GENERALIZATION AND PERSPECTIVES

The approaches used in this dissertation can be viewed as different components of a general concept to constrain model parameterization and reduce gaps in process knowledge (Figure 6.1), which matches well in several aspects to the comprehensive discussion of Morrison et al., 2020. They divide the challenge of simulating clouds and precipitation into two topics: the knowledge gaps about microphysical processes and the representation of these processes in bulk schemes, which are and will remain the "workhorses" for weather forecast and climate prediction in the foreseeable future. Morrison et al., 2020 surmise that Lagrangian particles, such as the McSnow model, will be indispensable for process understanding and bulk scheme improvement in the next decades. This dissertation provides an example that models even more explicit than Lagrangian particle models, such as 3D snowflake models, are also helpful in this regard when direct in situ observations or laboratory experiments are lacking or too difficult to execute. Again in line with Morrison et al., 2020, this dissertation emphasizes that detailed observations, such as the multi-frequency Doppler observations, should be used systematically to evaluate and improve the representation of microphysical processes in numerical models. An example of the systematic use of observations in this dissertation is the focus of the research on statistics of observations rather than case studies, which allowed to reduce the noise introduced by single-event weather dynamics highlighting the systematic signatures of cloud processes. The model evaluation is not only beneficial to improve the models' performance but also to improve process understanding.

Depending on how well the problem is already understood, different synergistic combinations of models and observations are the most promising (Figure 6.1). Phenomenological studies based on state-of-the-art observational techniques (e.g., Study III) can reveal fundamental gaps in process knowledge and can highlight the need for further laboratory experiments (lower part of Figure 6.1). If a metric can be established that allows direct comparison of observations with explicit microphysical models, the gap in process knowledge can be narrowed down further (center of Figure 6.1). Morrison et al., 2020 argue that surrogate models that emulate the explicit microphysical models with simplified functional approximations can facilitate model-observation comparison when a direct comparison is not feasible, e.g., because of computational costs. In contrast, if the underlying physics is better understood, the explicit models, can be used to improve the bulk models (e.g., Study I and Study II; upper part of Figure 6.1). Finally, the parameters of the bulk model can be constrained ("fine-tuned") by bulk observations such as radar observations (e.g., Study II, right part of Figure 6.1), not only for the sake of the model improvement but also to better understand the process. A systematic model-observation comparison using bulk models is more accessible than using explicit models because long-term simulations applying complex dynamical models can be run and compared to long-term observations.

In this dissertation the above-described concepts are applied to few ice-microphysical processes, namely sedimentation, aggregation, and melting. Furthermore, the application was mainly restricted to relatively simple dynamical systems (stratiform clouds). However, similar approaches could be applied to other processes, such as riming, ice habit evolution, or secondary ice processes, and not only stratiform but also convective clouds could be investigated. The application to convective clouds is of great concern, since these clouds have special significance for high impact weather situations. Therefore, knowing the effect of microphysical parameters on convective clouds, such as the aggregation parameters investigated in Study II, is highly relevant. Application of the methods to other processes would benefit from additional observational constraints given, e.g., by polarimetric radars, wind profilers or in situ observations, and different representations of particle properties (e.g., continuous description of riming, Morrison and Milbrandt, 2015) and size distributions (e.g., three-moment scheme, Milbrandt et al., 2021) in the microphysics schemes. However, the microphysics schemes should remain simple enough so that their parameters can be evaluated and constrained by observations. Detailed observational studies should accompany the introduction of more explicit representations of processes. Given the rapid advancement of models and observational techniques, it is essential to combine models and observations in different frameworks. As seen in this dissertation, such comparisons can improve the understanding and simulation of microphysical processes on the individual process level. These improvements can help to make weather forecasting more accurate and reduce the uncertainty of climate predictions.

BIBLIOGRAPHY

Abraham, F. F. (1970). "Functional dependence of drag coefficient of a sphere on reynolds number." In: *Physics of Fluids* 13.8 (1970), pp. 2194–2195. DOI: 10.1063/1.1693218.

Avramov, A., A. S. Ackerman, A. M. Fridlind, B. Van Diedenhoven, G. Botta, K. Aydin, J. Verlinde, A. V. Korolev, J. W. Strapp, G. M. McFarquhar, R. Jackson, S. D. Brooks, A. Glen, and M. Wolde (2011). "Toward ice formation closure in Arctic mixed-phase boundary layer clouds during ISDAC." In: *Journal of Geophysical Research Atmospheres* 116.19 (2011), D00T08. DOI: 10.1029/2011JD015910.

Bailey, M. P. and J. Hallett (2009). "A comprehensive habit diagram for atmospheric ice crystals: Confirmation from the laboratory, AIRS II, and other field studies." In: *Journal of the Atmospheric Sciences* 66.9 (2009), pp. 2888–2899. DOI: 10.1175/2009JAS2883.1.

Bailey, M. and J. Hallett (2004). "Growth rates and habits of ice crystals between - 20° and -70°C." In: *Journal of the Atmospheric Sciences* 61.5 (2004), pp. 514–544. DOI: 10.1175/1520-0469(2004)061<0514:GRAHOI>2.0.CO;2.

Baldini, L. and E. Gorgucci (2006). "Identification of the melting layer through dual-polarization radar measurements at vertical incidence." In: *Journal of Atmospheric and Oceanic Technology* 23.6 (2006), pp. 829–839. DOI: 10.1175/JTECH1884.1.

Barnett, T. P., J. C. Adam, and D. P. Lettenmaier (2005). *Potential impacts of a warming climate on water availability in snow-dominated regions*. 2005. DOI: 10.1038/nature04141.

Barrett, A. I., C. D. Westbrook, J. C. Nicol, and T. H. Stein (2019). "Rapid ice aggregation process revealed through triple-wavelength Doppler spectrum radar analysis." In: *Atmospheric Chemistry and Physics* 19.8 (2019), pp. 5753–5769. DOI: 10.5194/acp-19-5753-2019.

Barthazy, E. and R. Schefold (2006). "Fall velocity of snowflakes of different riming degree and crystal types." In: *Atmospheric Research* 82.1-2 (2006), pp. 391–398. DOI: 10.1016/j.atmosres.2005.12.009.

Barthazy, E., W. Henrich, and A. Waldvogel (1998). "Size distribution of hydrometeors through the melting layer." In: *Atmospheric Research* 47-48 (1998), pp. 193–208. DOI: 10.1016/S0169-8095(98)00065-9.

Battaglia, A., C. Kummerow, D. B. Shin, and C. Williams (2003). "Constaining microwave brightness temperatures by radar brightband observations." In: *Journal of Atmospheric and Oceanic Technology* 20.6 (2003), pp. 856–871. DOI: 10.1175/1520-0426(2003)020<0856:CMBTBR>2.0.CO;2.

Battaglia, A., C. D. Westbrook, S. Kneifel, P. Kollias, N. Humpage, U. Löhnert, J. Tyynelä, and G. W. Petty (2014). "G band atmospheric radars: New frontiers in cloud physics." In: *Atmospheric Measurement Techniques* 7.6 (2014), pp. 1527–1546. DOI: 10.5194/amt-7-1527-2014.

Battaglia, A., P. Kollias, R. Dhillon, R. Roy, S. Tanelli, K. Lamer, M. Grecu, M. Lebsock, D. Watters, K. Mroz, G. Heymsfield, L. Li, and K. Furukawa (2020a). "Spaceborne Cloud and Precipitation Radars: Status, Challenges, and Ways Forward." In: *Reviews of Geophysics* 58.3 (2020), pp. 1–59. DOI: 10.1029/2019RG000686.

Battaglia, A., S. Tanelli, F. Tridon, S. Kneifel, J. Leinonen, and P. Kollias (2020b). "Triple-Frequency Radar Retrievals." In: *Advances in Global Change Research* 67 (2020), pp. 211–229. DOI: 10.1007/978-3-030-24568-9_13.

Bauer, P., A. Thorpe, and G. Brunet (2015). *The quiet revolution of numerical weather prediction*. 2015. DOI: 10.1038/nature14956.

Bohm, H. P. (1989). *A general equation for the terminal fall speed of solid hydrometeors*. 1989. DOI: 10.1175/1520-0469(1989)046<2419:AGEFTT>2.0.CO;2.

Böhm, J. P. (1994). "Theoretical collision efficiencies for riming and aerosol impaction." In: *Atmospheric Research* 32.1-4 (1994), pp. 171–187. DOI: 10.1016/0169-8095(94)90058-2.

Böhm, J. P. (1992). "A general hydrodynamic theory for mixed-phase microphysics. Part I: drag and fall speed of hydrometeors." In: *Atmospheric Research* 27.4 (1992), pp. 253–274. DOI: 10.1016/0169-8095(92)90035-9.

Bohren, C. F. and L. J. Battan (1980). "Radar backscattering by inhomogeneous precipitation particles." In: *Journal of the Atmospheric Sciences* 37.8 (1980), pp. 1821–1827. DOI: 10.1175/1520-0469(1980)037<1821:RBBIPP>2.0.CO;2.

Boucher, O, D Randall, P Artaxo, C Bretherton, G Feingold, P Forster, V.-M. Kerminen, Y Kondo, H Liao, U Lohmann, P Rasch, S. K. Satheesh, S Sherwood, B. Stevens, and X. Y. Zhang (2013). "Clouds and aerosols." In: *Climate Change 2013 the Physical Science Basis: Working Group I Contribution to the Fifth Assessment Report of the Intergovernmental Panel on Climate Change*. Ed. by T. F. Stocker, D Qin, G.-K. Plattner, M Tignor, S. K. Allen, J Doschung, A Nauels, Y Xia, V Bex, and P. M. Midgley. Vol. 9781107057. Cambridge, UK: Cambridge University Press, 2013, pp. 571–658. DOI: 10.1017/CBO9781107415324.016.

Brdar, S. and A. Seifert (2018). "McSnow: A Monte-Carlo Particle Model for Riming and Aggregation of Ice Particles in a Multidimensional Microphysical Phase Space." In: *Journal of Advances in Modeling Earth Systems* 10.1 (2018), pp. 187–206. DOI: 10.1002/2017MS001167.

Bringi, V. N. and V. Chandrasekar (2001). *Polarimetric Doppler Weather Radar*. Cambridge University Press, 2001. DOI: 10.1017/cbo9780511541094.

Cholette, M., H. Morrison, J. A. Milbrandt, and J. M. Thériault (2019). "Parameterization of the bulk liquid fraction on mixed-phase particles in the predicted particle properties (P3) Scheme: Description and idealized simulations." In: *Journal of the Atmospheric Sciences* 76.2 (2019), pp. 561–582. DOI: 10.1175/JAS-D-18-0278.1.

Connolly, P. J., C. Emersic, and P. R. Field (2012). "A laboratory investigation into the aggregation efficiency of small ice crystals." In: *Atmospheric Chemistry and Physics* 12.4 (2012), pp. 2055–2076. DOI: 10.5194/acp-12-2055-2012.

Connolly, P. J., C. P. R. Saunders, M. W. Gallagher, K. N. Bower, M. J. Flynn, T. W. Choularton, J. Whiteway, and R. P. Lawson (2005). "Aircraft observations of the influence of electric fields on the aggregation of ice crystals." In: *Quarterly Journal of the Royal Meteorological Society* 131.608 (2005), pp. 1695–1712. DOI: 10.1256/QJ.03.217.

Cooper, W. A. (1989). "Effects of variable droplet growth histories on droplet size distributions. Part I: theory." In: *Journal of the Atmospheric Sciences* 46.10 (1989), pp. 1301–1311. DOI: 10.1175/1520-0469(1989)046<1301:EOVDGH>2.0.CO;2.

Cotton, W. R., M. A. Stephens, T. Nehrkorn, and G. J. Tripoli (1982). "The Colorado State University three-dimensional cloud/mesoscale model 1982 - part II: an ice phase parameterization." In: *Journal de Recherches Atmospheriques* 16.4 (1982), pp. 295–320.

Cotton, W. R., G. Bryan, and S. C. van den Heever (2011). "Fundamental Equations Governing Cloud Processes." In: *International Geophysics* 99.C (2011), pp. 15–52. DOI: 10.1016/S0074-6142(10)09908-0.

Deng, M. and G. G. Mace (2006). "Cirrus Microphysical Properties and Air Motion Statistics Using Cloud Radar Doppler Moments. Part I: Algorithm Description." In: *Journal of Applied Meteorology and Climatology* 45.12 (2006), pp. 1690–1709. DOI: 10.1175/JAM2433.1.

Ding, H. and L. Liu (2020). "Establishment and Preliminary Application of the Forward Modeling Method for Doppler Spectral Density of Ice Particles." In: *Remote Sensing 2020, Vol. 12, Page 3378* 12.20 (2020), p. 3378. DOI: 10.3390/RS12203378.

Drummond, F. J., R. R. Rogers, S. A. Cohn, W. L. Ecklund, D. A. Carter, and J. S. Wilson (1996). "A new look at the melting layer." In: *Journal of the Atmospheric Sciences* 53.5 (1996), pp. 759–769. DOI: 10.1175/1520-0469(1996)053<0759:ANLATM>2.0.CO;2.

Dunnavan, E. L. (2021). "How snow aggregate ellipsoid shape and orientation variability affects fall speed and self-aggregation rates." In: *Journal of the Atmospheric Sciences* 78.1 (2021), pp. 51–73. DOI: 10.1175/JAS-D-20-0128.1.

Fabry, F. and I. Zawadzki (1995). "Long-term radar observations of the melting layer of precipitation and their interpretation." In: *Journal of the Atmospheric Sciences* 52.7 (1995), pp. 838–851. DOI: 10.1175/1520-0469(1995)052<0838:LTROOT>2.0.CO;2.

Fabry, F. (2015). *Radar meteorology: Principles and practice*. 2015, pp. 1–256. DOI: 10.1017/CBO9781107707405.

Frick, C., A. Seifert, and H. Wernli (2013). “A bulk parametrization of melting snowflakes with explicit liquid water fraction for the COSMO model.” In: *Geoscientific Model Development* 6.6 (2013), pp. 1925–1939. DOI: 10.5194/gmd-6-1925-2013.

Gallagher, M. W., P. J. Connolly, I. Crawford, A. Heymsfield, K. N. Bower, T. W. Choularton, G. Allen, M. J. Flynn, G. Vaughan, and J. Hacker (2012). “Observations and modelling of microphysical variability, aggregation and sedimentation in tropical anvil cirrus outflow regions.” In: *Atmospheric Chemistry and Physics* 12.14 (2012), pp. 6609–6628. DOI: 10.5194/ACP-12-6609-2012.

Gatlin, P. N., W. A. Petersen, K. R. Knupp, and L. D. Carey (2018). “Observed response of the raindrop size distribution to changes in the melting layer.” In: *Atmosphere* 9.8 (2018), p. 319. DOI: 10.3390/atmos9080319.

Gillespie, D. T. (1975). “Three Models for the Coalescence Growth of Cloud Drops.” In: *Journal of the Atmospheric Sciences* 32.3 (1975), pp. 600–607. DOI: 10.1175/1520-0469(1975)032<0600:TMFTCG>2.0.CO;2.

Grabowski, W. W. and G. C. Abade (2017). “Broadening of Cloud Droplet Spectra through Eddy Hopping: Turbulent Adiabatic Parcel Simulations.” In: *Journal of the Atmospheric Sciences* 74.5 (2017), pp. 1485–1493. DOI: 10.1175/JAS-D-17-0043.1.

Grabowski, W. W., H. Morrison, S. I. Shima, G. C. Abade, P. Dziekan, and H. Pawlowska (2019). “Modeling of cloud microphysics: Can we do better?” In: *Bulletin of the American Meteorological Society* 100.4 (2019), pp. 655–672. DOI: 10.1175/BAMS-D-18-0005.1.

Heinze, R. et al. (2017). “Large-eddy simulations over Germany using ICON: a comprehensive evaluation.” In: *Quarterly Journal of the Royal Meteorological Society* 143.702 (2017), pp. 69–100. DOI: 10.1002/qj.2947.

Heymsfield, A. J. (2003). “Properties of Tropical and Midlatitude Ice Cloud Particle Ensembles. Part II: Applications for Mesoscale and Climate Models in: Journal of the Atmospheric Sciences Volume 60 Issue 21 (2003).” In: *Journal of the Atmospheric Sciences* 60.21 (2003), pp. 2592–2611.

Heymsfield, A. J., A. Bansemer, M. R. Poellot, and N. Wood (2015). “Observations of ice microphysics through the melting layer.” In: *Journal of the Atmospheric Sciences* 72.8 (2015), pp. 2902–2928. DOI: 10.1175/JAS-D-14-0363.1.

Heymsfield, A. J., A. Bansemer, A. Theis, and C. Schmitt (2021). “Survival of Snow in the Melting Layer: Relative Humidity Influence.” In: *Journal of the Atmospheric Sciences* 78.6 (2021), pp. 1823–1845. DOI: 10.1175/JAS-D-20-0353.1.

Heymsfield, A. J. and M. Kajikawa (1987). “Improved Approach To Calculating Terminal Velocities of Plate-Like Crystals and Graupel.”

In: *Journal of the Atmospheric Sciences* 44.7 (1987), pp. 1088–1099. DOI: 10.1175/1520-0469(1987)044<1088:AIATCT>2.0.CO;2.

Heymsfield, A. J., C. Schmitt, C. C. J. Chen, A. Bansemer, A. Gettelman, P. R. Field, and C. Liu (2020). "Contributions of the Liquid and Ice Phases to Global Surface Precipitation: Observations and Global Climate Modeling." In: *Journal of the Atmospheric Sciences* 77.8 (2020), pp. 2629–2648. DOI: 10.1175/JAS-D-19-0352.1.

Heymsfield, A. J. and C. D. Westbrook (2010). "Advances in the estimation of ice particle fall speeds using laboratory and field measurements." In: *Journal of the Atmospheric Sciences* 67.8 (2010), pp. 2469–2482. DOI: 10.1175/2010JAS3379.1.

Hobbs, P. V., S. Chang, and J. D. Locatelli (1974). "The dimensions and aggregation of ice crystals in natural clouds." In: *Journal of Geophysical Research* 79.15 (1974), pp. 2199–2206. DOI: 10.1029/jc079i015p02199.

Hoffmann, F. (2017). "On the limits of Köhler activation theory: How do collision and coalescence affect the activation of aerosols?" In: *Atmospheric Chemistry and Physics* 17.13 (2017), pp. 8343–8356. DOI: 10.5194/acp-17-8343-2017.

Hogan, R. J. and C. D. Westbrook (2014). "Equation for the microwave backscatter cross section of aggregate snowflakes using the self-similar Rayleigh-Gans approximation." In: *Journal of the Atmospheric Sciences* 71.9 (2014), pp. 3292–3301. DOI: 10.1175/JAS-D-13-0347.1.

Hoose, C. and O. Möhler (2012). *Heterogeneous ice nucleation on atmospheric aerosols: A review of results from laboratory experiments*. 2012. DOI: 10.5194/acp-12-9817-2012.

Huffman, G. J., R. F. Adler, D. T. Bolvin, and E. J. Nelkin (2010). "The TRMM Multi-Satellite Precipitation Analysis (TMPA)." In: *Satellite Rainfall Applications for Surface Hydrology*. Ed. by M. Gebremichael and F. Hossain. Dordrecht: Springer Netherlands, 2010, pp. 3–22. DOI: 10.1007/978-90-481-2915-7_1.

Illingworth, A. J., R. J. Hogan, E. J. O'Connor, D. Bouniol, M. E. Brooks, J. Delanoë, D. P. Donovan, J. D. Eastment, N. Gaussiat, J. W. Goddard, M. Haeffelin, H. Klein Baltinik, O. A. Krasnov, J. Pelon, J. M. Piriou, A. Protat, H. W. Russchenberg, A. Seifert, A. M. Tompkins, G. J. van Zadelhoff, F. Vinit, U. Willen, D. R. Wilson, and C. L. Wrench (2007). "Cloudnet: Continuous evaluation of cloud profiles in seven operational models using ground-based observations." In: *Bulletin of the American Meteorological Society* 88.6 (2007), pp. 883–898. DOI: 10.1175/BAMS-88-6-883.

Jacobson, M. Z. (2005). *Fundamentals of atmospheric modeling second edition*. Vol. 9780521839. Cambridge University Press, 2005, pp. 1–813. DOI: 10.1017/CBO9781139165389.

Jakob, C. (2002). "Ice Clouds in Numerical Weather Prediction Models: Progress, Problems, and Prospects." In: *Cirrus* (2002), pp. 327–345. DOI: 10.1093/oso/9780195130720.003.0020.

Jensen, A. A., J. Y. Harrington, H. Morrison, and J. A. Milbrandt (2017). "Predicting ice shape evolution in a bulk microphysics model." In: *Journal of the Atmospheric Sciences* 74.6 (2017), pp. 2081–2104. DOI: 10.1175/JAS-D-16-0350.1.

Kajikawa, M. (1972). "Measurement of Falling Velocity of Individual Snow Crystals." In: *Journal of the Meteorological Society of Japan. Ser. II* 50.6 (1972), pp. 577–584. DOI: 10.2151/jmsj1965.50.6_577.

Kanji, Z. A., L. A. Ladino, H. Wex, Y. Boose, M. Burkert-Kohn, D. J. Cziczo, and M. Krämer (2017). "Overview of Ice Nucleating Particles." In: *Meteorological Monographs* 58.1 (2017), pp. 1.1–1.33. DOI: 10.1175/AMSMONOGRAPHS-D-16-0006.1.

Karrer, M., A. Seifert, D. Ori, and S. Kneifel (2021a). "Improving the Representation of Aggregation in a Two-moment Microphysical Scheme with Statistics of Multi-frequency Doppler Radar Observations." In: *Atmospheric Chemistry and Physics Discussion* 2021 (2021), pp. 1–53.

Karrer, M., J. Dias Neto, L. von Terzi, and S. Kneifel (2021b). "Differences of Microphysical Processes in the Melting Layer Found for Rimed and Unrimed Snowflakes Using Cloud Radar Statistics." In: *Journal of Geophysical Research: Atmospheres* (2021).

Karrer, M., A. Seifert, C. Siewert, D. Ori, A. von Lerber, and S. Kneifel (2020). "Ice Particle Properties Inferred From Aggregation Modelling." In: *Journal of Advances in Modeling Earth Systems* 12.8 (2020). DOI: 10.1029/2020MS002066.

Kessler, E. (1969). "On the Distribution and Continuity of Water Substance in Atmospheric Circulations." In: *On the Distribution and Continuity of Water Substance in Atmospheric Circulations* (1969), pp. 1–84. DOI: 10.1007/978-1-935704-36-2_1.

Khain, A. P., K. D. Beheng, A. Heymsfield, A. Korolev, S. O. Krichak, Z. Levin, M. Pinsky, V. Phillips, T. Prabhakaran, A. Teller, S. C. Van Den Heever, and J. I. Yano (2015). "Representation of microphysical processes in cloud-resolving models: Spectral (bin) microphysics versus bulk parameterization." In: *Reviews of Geophysics* 53.2 (2015), pp. 247–322. DOI: 10.1002/2014RG000468.

Khain, A. P. and M. Pinsky (2018). *Physical Processes in Clouds and Cloud Modeling*. 2018. DOI: 10.1017/9781139049481.

Khvorostyanov, V. I. and J. A. Curry (2002). "Terminal velocities of droplets and crystals: Power laws with continuous parameters over the size spectrum." In: *Journal of the Atmospheric Sciences* 59.11 (2002), pp. 1872–1884. DOI: 10.1175/1520-0469(2002)059<1872:TVODAC>2.0.CO;2.

– (2005). "Fall velocities of hydrometeors in the atmosphere: Refinements to a continuous analytical power law." In: *Journal of the Atmospheric Sciences* 62.12 (2005), pp. 4343–4357. DOI: 10.1175/JAS3622.1.

Kienast-Sjögren, E., P. Spichtinger, and K. Gierens (2013). "Formulation and test of an ice aggregation scheme for two-moment bulk microphysics schemes." In: *Atmospheric Chemistry and Physics* 13.17 (2013), pp. 9021–9037. DOI: 10.5194/acp-13-9021-2013.

King, M. D., S. Platnick, W. P. Menzel, S. A. Ackerman, and P. A. Hubanks (2013). "Spatial and temporal distribution of clouds observed by MODIS onboard the terra and aqua satellites." In: *IEEE Transactions on Geoscience and Remote Sensing* 51.7 (2013), pp. 3826–3852. DOI: 10.1109/TGRS.2012.2227333.

Klaassen, W. (1988). "Radar observations and simulation of the melting layer of precipitation." In: *Journal of the Atmospheric Sciences* 45.24 (1988), pp. 3741–3753. DOI: 10.1175/1520-0469(1988)045<3741:ROASOT>2.0.CO;2.

Kneifel, S., M. S. Kulie, and R. Bennartz (2011). "A triple-frequency approach to retrieve microphysical snowfall parameters." In: *Journal of Geophysical Research: Atmospheres* 116.D11 (2011), p. 11203. DOI: 10.1029/2010JD015430.

Kneifel, S., J. Leinonen, J. Tyynelä, D. Ori, and A. Battaglia (2020). "Scattering of Hydrometeors." In: *Advances in Global Change Research*. Vol. 67. Springer, 2020, pp. 249–276. DOI: 10.1007/978-3-030-24568-9_15.

Kneifel, S. and D. N. Moisseev (2020). "Long-term statistics of riming in nonconvective clouds derived from ground-based doppler cloud radar observations." In: *Journal of the Atmospheric Sciences* 77.10 (2020), pp. 3495–3508. DOI: 10.1175/JAS-D-20-0007.1.

Kneifel, S., J. D. Neto, D. Ori, D. N. Moisseev, J. Tyynelä, I. S. Adams, K.-S. Kuo, R. Bennartz, A. Berne, E. E. Clothiaux, P. Eriksson, A. J. Geer, R. Honeyager, J. Leinonen, and C. D. Westbrook (2018). "Summer Snowfall Workshop: Scattering Properties of Realistic Frozen Hydrometeors from Simulations and Observations, as well as Defining a New Standard for Scattering Databases." In: *Bulletin of the American Meteorological Society* 99.3 (2018), ES55–ES58. DOI: 10.1175/BAMS-D-17-0208.1.

Kneifel, S., A. Von Lerber, J. Tiira, D. N. Moisseev, P. Kollias, and J. Leinonen (2015). "Observed relations between snowfall microphysics and triple-frequency radar measurements." In: *Journal of Geophysical Research* 120.12 (2015), pp. 6034–6055. DOI: 10.1002/2015JD023156.

Knight, C. A. (1979). "Observations of the morphology of melting snow." In: *Journal of the Atmospheric Sciences* 36.6 (1979), pp. 1123–1130. DOI: 10.1175/1520-0469(1979)036<1123:OOTMOM>2.0.CO;2.

Kollias, P., N. Bharadwaj, E. E. Clothiaux, K. Lamer, M. Oue, J. Hardin, B. Isom, I. Lindenmaier, A. Matthews, E. P. Luke, S. E. Giangrande, K. Johnson, S. Collis, J. Comstock, and J. H. Mather (2020). "The ARM Radar Network: At the Leading Edge of Cloud and Precipitation Observations." In: *Bulletin of the American Meteorological Society* 101.5 (2020), E588–E607. DOI: 10.1175/BAMS-D-18-0288.1.

Korolev, A. V., G. A. Isaac, S. G. Cober, J. W. Strapp, and J. Hallett (2003). “Microphysical characterization of mixed-phase clouds.” In: *Quarterly Journal of the Royal Meteorological Society* 129.587 PART A (2003), pp. 39–65. DOI: 10.1256/qj.01.204.

Korolev, A. (2007). “Limitations of the Wegener-Bergeron-Findeisen mechanism in the evolution of mixed-phase clouds.” In: *Journal of the Atmospheric Sciences* 64.9 (2007), pp. 3372–3375. DOI: 10.1175/JAS4035.1.

Korolev, A. and T. Leisner (2020). “Review of experimental studies of secondary ice production.” In: *Atmospheric Chemistry and Physics* 20.20 (2020), pp. 11767–11797. DOI: 10.5194/acp-20-11767-2020.

Kumjian, M. (2013). “Principles and applications of dual-polarization weather radar. Part I: Description of the polarimetric radar variables.” In: *Journal of Operational Meteorology* 1.19 (2013), pp. 226–242. DOI: 10.15191/NWAJOM.2013.0119.

Kummerow, C., W. Barnes, T. Kozu, J. Shiue, and J. Simpson (1998). “The Tropical Rainfall Measuring Mission (TRMM) Sensor Package.” In: *Journal of Atmospheric and Oceanic Technology* 15.3 (1998), pp. 809–817. DOI: 10.1175/1520-0426(1998)015<0809:TTRMMT>2.0.CO;2.

Lamb, D. and J. Verlinde (2011). *Physics and chemistry of clouds*. Cambridge University Press, 2011, pp. 1–584. DOI: 10.1017/CBO9780511976377.

Lamer, K., M. Oue, A. Battaglia, R. J. Roy, K. B. Cooper, R. Dhillon, and P. Kollias (2021). “Multifrequency radar observations of clouds and precipitation including the G-band.” In: *Atmospheric Measurement Techniques* 14.5 (2021), pp. 3615–3629. DOI: 10.5194/AMT-14-3615-2021.

Langleben, M. P. (1954). “The terminal velocity of snowflakes.” In: *Quarterly Journal of the Royal Meteorological Society* 80.344 (1954), pp. 174–181. DOI: 10.1002/qj.49708034404.

Lawson, R. P., R. E. Stewart, and L. J. Angus (1998). “Observations and numerical simulations of the origin and development of very large snowflakes.” In: *Journal of the Atmospheric Sciences* 55.21 (1998), pp. 3209–3229. DOI: 10.1175/1520-0469(1998)055<3209:OANSOT>2.0.CO;2.

Lazo, J. K., R. E. Morss, and J. L. Demuth (2009). “300 billion served.” In: *Bulletin of the American Meteorological Society* 90.6 (2009), pp. 785–798. DOI: 10.1175/2008BAMS2604.1.

Leibniz, G. W. (1873). *Neue Abhandlungen über den menschlichen Verstand*. 1873.

Leinonen, J. and D. N. Moisseev (2015). “What do triple-frequency radar signatures reveal about aggregate snowflakes?” In: *Journal of Geophysical Research* 120.1 (2015), pp. 229–239. DOI: 10.1002/2014JD022072.

Leinonen, J. (2013). *Impact of the microstructure of precipitation and hydrometeors on multi-frequency radar observations*. May. Aalto University, 2013, p. 140.

Leinonen, J., S. Kneifel, and R. J. Hogan (2018). “Evaluation of the Rayleigh–Gans approximation for microwave scattering by rimed snowflakes.” In: *Quarterly Journal of the Royal Meteorological Society* 144 (2018), pp. 77–88. DOI: 10.1002/qj.3093.

Leinonen, J. and A. von Lerber (2018). “Snowflake Melting Simulation Using Smoothed Particle Hydrodynamics.” In: *Journal of Geophysical Research: Atmospheres* 123.3 (2018), pp. 1811–1825. DOI: 10.1002/2017JD027909.

Leinonen, J. and W. Szyrmer (2015). “Radar signatures of snowflake riming: A modeling study.” In: *Earth and Space Science* 2.8 (2015), pp. 346–358. DOI: 10.1002/2015EA000102.

Li, H., J. Tiira, A. von Lerber, and D. N. Moisseev (2020). “Towards the connection between snow microphysics and melting layer: Insights from multi-frequency and dual-polarization radar observations during BAECC.” In: *Atmospheric Chemistry and Physics* (2020), pp. 1–23. DOI: 10.5194/acp-2020-16.

Libbrecht, K. G. (2017). “Physical Dynamics of Ice Crystal Growth.” In: *Annual Review of Materials Research* 47 (2017), pp. 271–295. DOI: 10.1146/annurev-matsci-070616-124135.

– (2019). “Snow Crystals.” In: *Contemporary Physics* 50.1 (2019), pp. 153–172.

Lin, C. A. and R. E. Stewart (1986). “Mesoscale circulations initiated by melting snow.” In: *Journal of Geophysical Research: Atmospheres* 91.D12 (1986), pp. 13299–13302. DOI: 10.1029/JD091ID12P13299.

Lin, Y. L., R. D. Farley, and H. D. Orville (1983). “Bulk parameterization of the snow field in a cloud model.” In: *Journal of Climate and Applied Meteorology* 22.6 (1983), pp. 1065–1092. DOI: 10.1175/1520-0450(1983)022<1065:BPOTSF>2.0.CO;2.

Liou, K. (2002). “Chapter 1 Fundamentals of radiation for atmospheric applications.” In: *International Geophysics*. Vol. 84. C. Academic Press, 2002, pp. 1–36. DOI: 10.1016/S0074-6142(02)80016-X.

Locatelli, J. D. and P. V. Hobbs (1974). “Fall speeds and masses of solid precipitation particles.” In: *Journal of Geophysical Research* 79.15 (1974), pp. 2185–2197. DOI: 10.1029/jc079i015p02185.

Loeb, N. G., D. R. Doelling, H. Wang, W. Su, C. Nguyen, J. G. Corbett, L. Liang, C. Mitrescu, F. G. Rose, and S. Kato (2018). “Clouds and the Earth’S Radiant Energy System (CERES) Energy Balanced and Filled (EBAF) top-of-atmosphere (TOA) edition-4.0 data product.” In: *Journal of Climate* 31.2 (2018), pp. 895–918. DOI: 10.1175/JCLI-D-17-0208.1.

Lohmann, U., F. Lüönd, and F. Mahrt (2016). *An introduction to clouds: From the microscale to climate*. Cambridge University Press, 2016, pp. 1–391. DOI: 10.1017/CBO9781139087513.

Mace, G. G., A. J. Heymsfield, and M. R. Poellot (2002). “On retrieving the microphysical properties of cirrus clouds using the moments of the millimeter-wavelength Doppler spectrum.” In: *Journal* *of Geophysical Research: Atmospheres* 107.D24 (2002), AAC 22–1. DOI: 10.1029/2001JD001308.

Maruyama, K. I. and Y. Fujiyoshi (2005). "Monte Carlo simulation of the formation of snowflakes." In: *Journal of the Atmospheric Sciences* 62.5 (2005), pp. 1529–1544. DOI: 10.1175/JAS3416.1.

Mason, S. L., C. J. Chiu, R. J. Hogan, D. N. Moisseev, and S. Kneifel (2018). "Retrievals of Riming and Snow Density From Vertically Pointing Doppler Radars." In: *Journal of Geophysical Research: Atmospheres* 123.24 (2018), pp. 13,807–13,834. DOI: 10.1029/2018JD028603.

Mason, S. L., J. C. Chiu, R. J. Hogan, and L. Tian (2017). "Improved rain rate and drop size retrievals from airborne Doppler radar." In: *Atmospheric Chemistry and Physics* 17.18 (2017), pp. 11567–11589. DOI: 10.5194/acp-17-11567-2017.

Mason, S., R. Hogan, C. D. Westbrook, S. Kneifel, D. N. Moisseev, and L. Von Terzi (2019). "The importance of particle size distribution and internal structure for triple-frequency radar retrievals of the morphology of snow." In: *Atmospheric Measurement Techniques* 12.9 (2019), pp. 4993–5018. DOI: 10.5194/amt-12-4993-2019.

Matrosov, S. Y., A. V. Korolev, and A. J. Heymsfield (2002). "Profiling cloud ice mass and particle characteristic size from doppler radar measurements." In: *Journal of Atmospheric and Oceanic Technology* 19.7 (2002), pp. 1003–1018. DOI: 10.1175/1520-0426(2002)019<1003:PCIMAP>2.0.CO;2.

McCorquodale, M. W. and C. D. Westbrook (2021). "TRAIL part 2: A comprehensive assessment of ice particle fall speed parametrisations." In: *Quarterly Journal of the Royal Meteorological Society* 147.734 (2021), pp. 605–626. DOI: 10.1002/qj.3936.

Mech, M., M. Maahn, S. Kneifel, D. Ori, E. Orlandi, P. Kollias, V. Schemann, and S. Crewell (2020). "PAMTRA 1.0: The Passive and Active Microwave radiative TRAnsfer tool for simulating radiometer and radar measurements of the cloudy atmosphere." In: *Geoscientific Model Development* 13.9 (2020), pp. 4229–4251. DOI: 10.5194/gmd-13-4229-2020.

Meneghini, R. and L. Liao (2007). "On the Equivalence of Dual-Wavelength and Dual-Polarization Equations for Estimation of the Raindrop Size Distribution." In: *Journal of Atmospheric and Oceanic Technology* 24.5 (2007), pp. 806–820. DOI: 10.1175/JTECH2005.1.

Meyers, M. P., R. L. Walko, J. Y. Harrington, and W. R. Cotton (1997). "New RAMS cloud microphysics parameterization. Part II: The two-moment scheme." In: *Atmospheric Research* 45.1 (1997), pp. 3–39. DOI: 10.1016/S0169-8095(97)00018-5.

Milbrandt, J. A., H. Morrison, D. T. Dawson, and M. Paukert (2021). "A triple-moment representation of ice in the predicted particle properties (P3) microphysics scheme." In: *Journal of the Atmospheric Sciences* 78.2 (2021), pp. 439–458. DOI: 10.1175/JAS-D-20-0084.1.

Milbrandt, J. A. and M. K. Yau (2005). "A multimoment bulk microphysics parameterization. Part I: Analysis of the role of the spectral shape parameter." In: *Journal of the Atmospheric Sciences* 62.9 (2005), pp. 3051–3064. DOI: 10.1175/JAS3534.1.

Mitchell, D. L., R. Zhang, and R. L. Pitter (1990a). "Mass-dimensional relationships for ice particles and the influence of riming on snowfall rates." In: *Journal of Applied Meteorology* 29.2 (1990), pp. 153–163. DOI: 10.1175/1520-0450(1990)029<0153:MDRFIP>2.0.CO;2.

Mitchell, D. L. (1988). "Evolution of snow-size spectra in cyclonic storms. Part I: snow growth by vapor deposition and aggregation." In: *Journal of the Atmospheric Sciences* 45.22 (1988), pp. 3431–3451. DOI: 10.1175/1520-0469(1988)045<3431:EOSSSI>2.0.CO;2.

Mitchell, D. L., R. Zhang, and R. L. Pitter (1990b). "Mass-dimensional relationships for ice particles and the influence of riming on snowfall rates." In: *Journal of Applied Meteorology* 29.2 (1990), pp. 153–163. DOI: 10.1175/1520-0450(1990)029<0153:MDRFIP>2.0.CO;2.

Mitra, S. K., O. Vohl, M. Ahr, and H. R. Pruppacher (1990). "A wind tunnel and theoretical study of the melting behaviour of atmospheric ice particles. IV: experiment and theory for snow flakes." In: *Journal of the Atmospheric Sciences* 47.5 (1990), pp. 584–591. DOI: 10.1175/1520-0469(1990)047<0584:AWTATS>2.0.CO;2.

Moisseev, D. N. and V. Chandrasekar (2007). "Nonparametric Estimation of Raindrop Size Distributions from Dual-Polarization Radar Spectral Observations." In: *Journal of Atmospheric and Oceanic Technology* 24.6 (2007), pp. 1008–1018. DOI: 10.1175/JTECH2024.1.

Moisseev, D. N., S. Lautaportti, J. Tyynela, and S. Lim (2015). "Dual-polarization radar signatures in snowstorms: Role of snowflake aggregation." In: *Journal of Geophysical Research* 120.24 (2015), pp. 12,644–12,665. DOI: 10.1002/2015JD023884.

Morrison, H., J. A. Curry, and V. I. Khvorostyanov (2005). "A new double-moment microphysics parameterization for application in cloud and climate models. Part I: Description." In: *Journal of the Atmospheric Sciences* 62.6 (2005), pp. 1665–1677. DOI: 10.1175/JAS3446.1.

Morrison, H., M. van Lier-Walqui, A. M. Fridlind, W. W. Grabowski, J. Y. Harrington, C. Hoose, A. Korolev, M. R. Kumjian, J. A. Milbrandt, H. Pawlowska, D. J. Posselt, O. P. Prat, K. J. Reimel, S. I. Shima, B. van Diedenhoven, and L. Xue (2020). "Confronting the Challenge of Modeling Cloud and Precipitation Microphysics." In: *Journal of Advances in Modeling Earth Systems* 12.8 (2020). DOI: 10.1029/2019MS001689.

Morrison, H. and J. A. Milbrandt (2015). "Parameterization of cloud microphysics based on the prediction of bulk ice particle properties. Part I: Scheme description and idealized tests." In: *Journal of the Atmospheric Sciences* 72.1 (2015), pp. 287–311. DOI: 10.1175/JAS-D-14-0065.1.

Mróz, K., A. Battaglia, S. Kneifel, L. P. D'Adderio, and J. Dias Neto (2020). "Triple-Frequency Doppler Retrieval of Characteristic Raindrop Size." In: *Earth and Space Science* 7.3 (2020). DOI: 10.1029/2019EA000789.

Mróz, K., A. Battaglia, S. Kneifel, L. Von Terzi, M. Karrer, and D. Ori (2021). "Linking rain into ice microphysics across the melting layer in stratiform rain: A closure study." In: *Atmospheric Measurement Techniques* 14.1 (2021), pp. 511–529. DOI: 10.5194/AMT-14-511-2021.

Mülmenstädt, J., O. Sourdeval, J. Delanoë, and J. Quaas (2015). "Frequency of occurrence of rain from liquid-, mixed-, and ice-phase clouds derived from A-Train satellite retrievals." In: *Geophysical Research Letters* 42.15 (2015), pp. 6502–6509. DOI: 10.1002/2015GL064604.

Naumann, A. K. and A. Seifert (2016). "Evolution of the Shape of the Raindrop Size Distribution in Simulated Shallow Cumulus." In: *Journal of the Atmospheric Sciences* 73.6 (2016), pp. 2279–2297. DOI: 10.1175/JAS-D-15-0263.1.

Neto, J. D. (2021). "Investigating aggregation in ice and snow clouds using novel combination of triple-frequency cloud radars and radar Doppler spectra." PhD thesis. 2021.

Neto, J. D., S. Kneifel, D. Ori, S. Trömel, J. Handwerker, B. Bohn, N. Hermes, K. Mühlbauer, M. Lenefer, and C. Simmer (2019). "The TRIple-frequency and Polarimetric radar Experiment for improving process observations of winter precipitation." In: *Earth System Science Data* 11.2 (2019), pp. 845–863. DOI: 10.5194/essd-11-845-2019.

Oraltay, R. G. and J. Hallett (1989). "Evaporation and melting of ice crystals: A laboratory study." In: *Atmospheric Research* 24.1-4 (1989), pp. 169–189. DOI: 10.1016/0169-8095(89)90044-6.

Oraltay, R. G. and J. Hallett (2005). "The melting layer: A laboratory investigation of ice particle melt and evaporation near 0°C." In: *Journal of Applied Meteorology* 44.2 (2005), pp. 206–220. DOI: 10.1175/JAM2194.1.

Ori, D. and S. Kneifel (2018). "Assessing the uncertainties of the discrete dipole approximation in case of melting ice particles." In: *Journal of Quantitative Spectroscopy and Radiative Transfer* 217 (2018), pp. 396–406. DOI: 10.1016/j.jqsrt.2018.06.017.

Ori, D., V. Schemann, M. Karrer, J. Dias Neto, L. von Terzi, A. Seifert, and S. Kneifel (2020). "Evaluation of ice particle growth in ICON using statistics of multi-frequency Doppler cloud radar observations." In: *Quarterly Journal of the Royal Meteorological Society* 146.733 (2020), pp. 3830–3849. DOI: 10.1002/qj.3875.

Ori, D., L. Von Terzi, M. Karrer, and S. Kneifel (2021). "SnowScatt 1.0: Consistent model of microphysical and scattering properties of rimed and unrimed snowflakes based on the self-similar Rayleigh-Gans approximation." In: *Geoscientific Model Development* 14.3 (2021), pp. 1511–1531. DOI: 10.5194/GMD-14-1511-2021.

Oue, M., M. R. Kumjian, Y. Lu, J. Verlinde, K. Aydin, and E. E. Clothiaux (2015). "Linear Depolarization Ratios of Columnar Ice Crystals in a Deep Precipitating System over the Arctic Observed by Zenith-Pointing Ka-Band Doppler Radar." In: *Journal of Applied Meteorology and Climatology* 54.5 (2015), pp. 1060–1068. DOI: 10.1175/JAMC-D-15-0012.1.

Parker, M. (2010). *Digital signal processing everything you need to know to get started*. 2010.

Pfitzenmaier, L., C. M. Unal, Y. Dufournet, and H. W. Russchenberg (2018). "Observing ice particle growth along fall streaks in mixed-phase clouds using spectral polarimetric radar data." In: *Atmospheric Chemistry and Physics* 18.11 (2018), pp. 7843–7862. DOI: 10.5194/acp-18-7843-2018.

Phillips, V. T. J., J.-I. Yano, and A. Khain (2017). "Ice Multiplication by Breakup in Ice–Ice Collisions. Part I: Theoretical Formulation." In: *Journal of the Atmospheric Sciences* 74.6 (2017), pp. 1705–1719. DOI: 10.1175/JAS-D-16-0224.1.

Phillips, V. T., M. Formenton, A. Bansemer, I. Kudzotsa, and B. Lienert (2015). "A parameterization of sticking efficiency for collisions of snow and graupel with ice crystals: Theory and comparison with observations." In: *Journal of the Atmospheric Sciences* 72.12 (2015), pp. 4885–4902. DOI: 10.1175/JAS-D-14-0096.1.

Phillips, V. T., A. Pokrovsky, and A. Khain (2007). "The influence of time-dependent melting on the dynamics and precipitation production in maritime and continental storm clouds." In: *Journal of the Atmospheric Sciences* 64.2 (2007), pp. 338–359. DOI: 10.1175/JAS3832.1.

Pinsky, M., A. Khain, and A. Korolev (2015). "Phase transformations in an ascending adiabatic mixed-phase cloud volume." In: *Journal of Geophysical Research* 120.8 (2015), pp. 3329–3353. DOI: 10.1002/2015JD023094.

Pruppacher, H. and J. Klett (2010). "Hydrodynamics of Single Cloud and Precipitation Particles." PhD thesis. 2010, pp. 361–446. DOI: 10.1007/978-0-306-48100-0_10.

Pruppacher, H. R., J. D. Klett, and P. K. Wang (1998). "Microphysics of Clouds and Precipitation." In: *Aerosol Science and Technology* 28.4 (1998), pp. 381–382. DOI: 10.1080/02786829808965531.

Raschke, E., S. Kinne, W. B. Rossow, P. W. Stackhouse, and M. Wild (2016). "Comparison of radiative energy flows in observational datasets and climate modeling." In: *Journal of Applied Meteorology and Climatology* 55.1 (2016), pp. 93–117. DOI: 10.1175/JAMC-D-14-0281.1.

Rasmussen, R. M. and A. J. Heymsfield (1987). "Melting and Shedding of Graupel and Hail. Part I: Model Physics." In: *Journal of the Atmospheric Sciences* 44.19 (1987), pp. 2754–2763. DOI: 10.1175/1520-0469(1987)044<2754:masoga>2.0.co;2.

Ryzhkov, A. V. and D. S. Zrnic (2019). “Polarimetric Microphysical Retrievals.” In: *Radar Polarimetry for Weather Observations*. 2019, pp. 435–464. DOI: 10.1007/978-3-030-05093-1_11.

Seifert, A. and K. D. Beheng (2006). “A two-moment cloud microphysics parameterization for mixed-phase clouds. Part 1: Model description.” In: *Meteorology and Atmospheric Physics* 92.1-2 (2006), pp. 45–66. DOI: 10.1007/s00703-005-0112-4.

Seifert, A., U. Blahak, and R. Buhr (2014). “On the analytic approximation of bulk collision rates of non-spherical hydrometeors.” In: *Geoscientific Model Development* 7.2 (2014), pp. 463–478. DOI: 10.5194/gmd-7-463-2014.

Seifert, A., J. Leinonen, C. Siewert, and S. Kneifel (2019). “The Geometry of Rimed Aggregate Snowflakes: A Modeling Study.” In: *Journal of Advances in Modeling Earth Systems* 11.3 (2019), pp. 712–731. DOI: 10.1029/2018MS001519.

Shima, S., K. Kusano, A. Kawano, T. Sugiyama, and S. Kawahara (2009). “The super-droplet method for the numerical simulation of clouds and precipitation: A particle-based and probabilistic microphysics model coupled with a non-hydrostatic model.” In: *Quarterly Journal of the Royal Meteorological Society* 135.642 (2009), pp. 1307–1320. DOI: 10.1002/qj.441.

Shima, S. I., Y. Sato, A. Hashimoto, and R. Misumi (2020). “Predicting the morphology of ice particles in deep convection using the super-droplet method: Development and evaluation of SCALE-SDM 0.2.5-2.2.0, -2.2.1, and -2.2.2.” In: *Geoscientific Model Development* 13.9 (2020), pp. 4107–4157. DOI: 10.5194/gmd-13-4107-2020.

Sills, D. M. and P. I. Joe (2019). “From Pioneers to Practitioners: A Short History of Severe Thunderstorm Research and Forecasting in Canada†.” In: *Atmosphere - Ocean* 57.4 (2019), pp. 249–261. DOI: 10.1080/07055900.2019.1673145.

Slater, B. and A. Michaelides (2019). *Surface premelting of water ice*. 2019. DOI: 10.1038/s41570-019-0080-8.

Smyth, T. J. and A. J. Illingworth (1998). “Radar estimates of rainfall rates at the ground in bright band and non-bright band events.” In: *Quarterly Journal of the Royal Meteorological Society* 124.551 (1998), pp. 2417–2434. DOI: 10.1256/smsqj.55111.

Srivastava, R. C. (1971). “Size distribution of raindrops generated by their breakup and coalescence.” In: *Journal of the Atmospheric Sciences* 28.3 (1971), pp. 410–415. DOI: 10.1175/1520-0469(1971)028<0410:sdorgb>2.0.co;2.

Stephens, G. L., D. G. Vane, S. Tanelli, E. Im, S. Durden, M. Rokey, D. Reinke, P. Partain, G. G. Mace, R. Austin, T. L’Ecuyer, J. Haynes, M. Lebsock, K. Suzuki, D. Waliser, D. Wu, J. Kay, A. Gettelman, Z. Wang, and R. Marchand (2008). “CloudSat mission: Performance and early science after the first year of operation.” In: *Journal of*

Geophysical Research: Atmospheres 113.D8 (2008). doi: https://doi.org/10.1029/2008JD009982.

Stewart, R. E., J. D. Marwitz, J. C. Pace, and R. E. Carbone (1984). "Characteristics through the melting layer of stratiform clouds." In: *Journal of the Atmospheric Sciences* 41.22 (1984), pp. 3227–3237. doi: 10.1175/1520-0469(1984)041<3227:CTTMLO>2.0.CO;2.

Stewart, R. E., J. M. Thériault, and W. Henson (2015). *On the characteristics of and processes producing winter precipitation types near 0°C.* 2015. doi: 10.1175/BAMS-D-14-00032.1.

Stith, J. L., J. E. Dye, A. Bansemer, A. J. Heymsfield, C. A. Grainger, W. A. Petersen, and R. Cifelli (2002). "Microphysical observations of tropical clouds." In: *Journal of Applied Meteorology* 41.2 (2002), pp. 97–117. doi: 10.1175/1520-0450(2002)041<0097:MOOTC>2.0.CO;2.

Stith, J. L., J. A. Haggerty, A. Heymsfield, and C. A. Grainger (2004). "Microphysical Characteristics of Tropical Updrafts in Clean Conditions." In: *Journal of Applied Meteorology and Climatology* 43.5 (2004), pp. 779–794. doi: 10.1175/2104.1.

Straub, W., K. D. Beheng, A. Seifert, J. Schlottke, and B. Weigand (2010). "Numerical investigation of collision-induced breakup of raindrops. Part II: Parameterizations of coalescence efficiencies and fragment size distributions." In: *Journal of the Atmospheric Sciences* 67.3 (2010), pp. 576–588. doi: 10.1175/2009JAS3175.1.

Stubenrauch, C. J., W. B. Rossow, S. Kinne, S. Ackerman, G. Cesana, H. Chepfer, L. Di Girolamo, B. Getzewich, A. Guignard, A. Heidinger, B. C. Maddux, W. P. Menzel, P. Minnis, C. Pearl, S. Platnick, C. Poulsen, J. Riedi, S. Sun-Mack, A. Walther, D. Winker, S. Zeng, and G. Zhao (2013). "Assessment of global cloud datasets from satellites: Project and database initiated by the GEWEX radiation panel." In: *Bulletin of the American Meteorological Society* 94.7 (2013), pp. 1031–1049. doi: 10.1175/BAMS-D-12-00117.1.

Szyrmer, W., S. Laroche, and I. Zawadzki (2005). "A Microphysical Bulk Formulation Based on Scaling Normalization of the Particle Size Distribution. Part I: Description." In: *Journal of the Atmospheric Sciences* 62.12 (2005), pp. 4206–4221. doi: 10.1175/JAS3620.1.

Szyrmer, W., A. Tatarevic, and P. Kollias (2012). "Ice clouds microphysical retrieval using 94-GHz Doppler radar observations: Basic relations within the retrieval framework." In: *Journal of Geophysical Research: Atmospheres* 117.D14 (2012), n/a–n/a. doi: 10.1029/2011JD016675.

Szyrmer, W. and I. Zawadzki (1999). "Modeling of the melting layer. Part I: Dynamics and microphysics." In: *Journal of the Atmospheric Sciences* 56.20 (1999), pp. 3573–3592. doi: 10.1175/1520-0469(1999)056<3573:MOTMLP>2.0.CO;2.

Takahashi, T., Y. Nagao, and Y. Kushiyama (1995). "Possible high ice particle production during graupel-graupel collisions." In: *Journal of* *the Atmospheric Sciences* 52.24 (1995), pp. 4523–4527. DOI: 10.1175/1520-0469(1995)052<4523:PHIPPD>2.0.CO;2.

Thériault, J. M. and R. E. Stewart (2010). "A parameterization of the microphysical processes forming many types of winter precipitation." In: *Journal of the Atmospheric Sciences* 67.5 (2010), pp. 1492–1508. DOI: 10.1175/2009JAS3224.1.

Thompson, G., P. R. Field, R. M. Rasmussen, and W. D. Hall (2008). "Explicit forecasts of winter precipitation using an improved bulk microphysics scheme. Part II: Implementation of a new snow parameterization." In: *Monthly Weather Review* 136.12 (2008), pp. 5095–5115. DOI: 10.1175/2008MWR2387.1.

Tridon, F. and A. Battaglia (2015). "Dual-frequency radar doppler spectral retrieval of rain drop size distributions and entangled dynamics variables." In: *Journal of Geophysical Research* 120.11 (2015), pp. 5585–5601. DOI: 10.1002/2014JD023023.

Tsai, T. C. and J. P. Chen (2020). "Multimoment ice bulk microphysics scheme with consideration for particle shape and apparent density. Part I: Methodology and idealized simulation." In: *Journal of the Atmospheric Sciences* 77.5 (2020), pp. 1821–1850. DOI: 10.1175/JAS-D-19-0125.1.

Tyynelä, J. and A. von Lerber (2019). "Validation of Microphysical Snow Models Using In Situ, Multifrequency, and Dual-Polarization Radar Measurements in Finland." In: *Journal of Geophysical Research: Atmospheres* 124.23 (2019), pp. 13273–13290. DOI: 10.1029/2019JD030721.

Ulaby, F. T., D. G. Long, W. J. Blackwell, C. Elachi, A. K. Fung, C. Ruf, K. Sarabandi, H. A. Zebker, and J. Van Zyl (2014). "Electromagnetic Wave Propagation and Reflection." In: *Microwave radar and radiometric remote sensing* 4.5 (2014), pp. 44–50.

Vardiman, L. (1978). "The Generation of Secondary Ice Particles in Clouds by Crystal–Crystal Collision." In: *Journal of the Atmospheric Sciences* 35.11 (1978), pp. 2168–2180. DOI: 10.1175/1520-0469(1978)035<2168:tgosip>2.0.co;2.

Vázquez-Martín, S., T. Kuhn, and S. Eliasson (2021). "Shape dependence of snow crystal fall speed." In: *Atmospheric Chemistry and Physics* 21.10 (2021), pp. 7545–7565. DOI: 10.5194/acp-21-7545-2021.

Verlinde, J., M. P. Rambukkange, E. E. Clothiaux, G. M. McFarquhar, and E. W. Eloranta (2013). "Arctic multilayered, mixed-phase cloud processes revealed in millimeter-wave cloud radar Doppler spectra." In: *Journal of Geophysical Research: Atmospheres* 118.23 (2013), pp. 13,199–13,213. DOI: 10.1002/2013JD020183.

Wacker, U. and A. Seifert (2000). "On shock-type solutions for the precipitation concentration in models with parameterized microphysics." In: *EPIC313 Int. Conf.on Clouds and Precipitation, Reno, Nevada (USA)August 2000., 14* (2000).

Ward, P. J., V. Blauhut, N. Bloemendaal, E. J. Daniell, C. M. De Ruiter, J. M. Duncan, R. Emberson, F. S. Jenkins, D. Kirschbaum, M. Kunz, S. Mohr, S. Muis, A. G. Riddell, A. Schäfer, T. Stanley, I. E. Veldkamp, and W. C. Hessel (2020). "Review article: Natural hazard risk assessments at the global scale." In: *Natural Hazards and Earth System Sciences* 20.4 (2020), pp. 1069–1096. DOI: 10.5194/nhess-20-1069-2020.

Weitzel, M., S. K. Mitra, M. Szakall, J. P. Fugal, and S. Borrmann (2020). "Application of holography and automated image processing for laboratory experiments on mass and fall speed of small cloud ice crystals." In: *Atmospheric Chemistry and Physics* 20.23 (2020), pp. 14889–14901. DOI: 10.5194/ACP-20-14889-2020.

Westbrook, C. D. (2004). "Universality in snowflake formation." PhD thesis. University of Warwick, 2004.

Westbrook, C. D., R. C. Ball, P. R. Field, and A. J. Heymsfield (2004a). "Theory of growth by differential sedimentation, with application to snowflake formation." In: *Physical Review E - Statistical Physics, Plasmas, Fluids, and Related Interdisciplinary Topics* 70.2 (2004), p. 7. DOI: 10.1103/PhysRevE.70.021403.

Westbrook, C. D., R. C. Ball, P. R. Field, and A. J. Heymsfield (2004b). "Universality in snowflake aggregation." In: *Geophysical Research Letters* 31.15 (2004). DOI: 10.1029/2004GL020363.

Yokoyama, T., H. Tanaka, K. Akaeda, T. Ohtani, N. Yoshizawa, M. D. Yamanaka, A. Mita, Y. Ishizaka, and A. Ono (1985). "Observation on Microphysical Processes in the Stratiform Precipitations Including Melting Layers at Mt. Fuji." In: *Journal of the Meteorological Society of Japan. Ser. II* 63.1 (1985), pp. 100–111. DOI: 10.2151/jmsj1965.63.1_100.

Zawadzki, I., F. Fabry, and W. Szyrmer (2001). "Observations of supercooled water and secondary ice generation by a vertically pointing X-band Doppler radar." In: *Atmospheric Research* 59-60 (2001), pp. 343–359. DOI: 10.1016/S0169-8095(01)00124-7.

Ziegler, C. L. (1985). "Retrieval of thermal and microphysical variables in observed convective storms. Part 1: model development and preliminary testing." In: *Journal of the Atmospheric Sciences* 42.14 (1985), pp. 1487–1509. DOI: 10.1175/1520-0469(1985)042<1487:ROTAMV>2.0.CO;2.

ACKNOWLEDGMENTS

I thank the German Research Foundation (DFG) for funding this project under the grant KN 1112/2-1 as part of the Emmy-Noether Group OPTIMIce.

I thank the Graduate School of Geosciences of the University of Cologne for providing so many opportunities, from organizing amazing workshops to funding conference trips. A big thank you to Dr. Karin Boessenkool for caring so much for us PhD students.

I thank my supervisors Dr. Axel Seifert, Prof. Roel Neggers, and Dr. Stefan Kneifel, for guiding me through this process! Axel for sharing his incredible knowledge of microphysics and modeling and always coming up with new ideas to tackle a problem. Roel for giving invaluable feedback from a broader view. Stefan for taking so much time for discussions and patience with reading, commenting, and revising drafts. I am grateful for having such a passionate mentor.

Thanks also to Martin Melles for taking the head chair of the defense committee!

A big thank you to Dr. Davide Ori! Not only for the thorough review of this dissertation but also for the countless and invaluable tips for tools, writing, and discussions about microphysics, scattering, etc. ... Not to forget the tasty bean dish.

I thank Dr. Christoph Siewert for introducing me to McSnow and all the discussions about microphysics, modeling, and fluid dynamics. Thanks to Axel and Christoph for hosting me several times at the DWD.

I thank the OPTIMIce group and the whole institute for keeping discussions active and provide welcome distractions even in the challenging times of a pandemic. I don't want to imagine how home office would have been without all those great slack-channels.

I thank everyone who spent enjoyable and recreating lunch breaks with me. You only realize how important such little meetups are when they are not possible.

I thank my family, especially my parents, for their support not only through the years of the PhD project but the whole way leading to it.

An especially hearty thanks to my love Corinna. I can't emphasize enough how important your support is that brought me through my studies back there in Karlsruhe and through the most challenging times of this PhD project.

ERKLÄRUNG

Hiermit versichere ich an Eides statt, dass ich die vorliegende Dissertation selbstständig und ohne die Benutzung anderer als der angegebenen Hilfsmittel und Literatur angefertigt habe. Alle Stellen, die wörtlich oder sinngemäß aus veröffentlichten und nicht veröffentlichten Werken dem Wortlaut oder dem Sinn nach entnommen wurden, sind als solche kenntlich gemacht. Ich versichere an Eides statt, dass diese Dissertation noch keiner anderen Fakultät oder Universität zur Prüfung vorgelegen hat; dass sie - abgesehen von unten angegebenen Teilpublikationen und eingebundenen Artikeln und Manuskripten - noch nicht veröffentlicht worden ist sowie, dass ich eine Veröffentlichung der Dissertation vor Abschluss der Promotion nicht ohne Genehmigung des Promotionsausschusses vornehmen werde. Die Bestimmungen dieser Ordnung sind mir bekannt. Darüber hinaus erkläre ich hiermit, dass ich die Ordnung zur Sicherung guter wissenschaftlicher Praxis und zum Umgang mit wissenschaftlichem Fehlverhalten der Universität zu Köln gelesen und sie bei der Durchführung der Dissertation zugrundeliegenden Arbeiten und der schriftlich verfassten Dissertation beachtet habe und verpflichte mich hiermit, die dort genannten Vorgaben bei allen wissenschaftlichen Tätigkeiten zu beachten uind umzusetzen. Ich versichere, dass die eingereichte elektronische Fassung der eingereichten Druckfassung vollständig entspricht.

Köln, Oktober 2021

M. Karrer

Markus Karrer

First author publications

Karrer, M., Seifert, A., Siewert, C., Ori, D., von Lerber, A., & Kneifel, S. (2020). **Ice particle properties inferred from aggregation modelling**. *Journal of Advances in Modeling Earth Systems*, 12(8), e2020MS002066, https://doi.org/10.1029/2020MS002066.

Karrer, M., Seifert, A., Ori, D., & Kneifel, S. (2021a) **Improving the Representation of Aggregation in a Two-moment Microphysical Scheme with Statistics of Multi-frequency Doppler Radar Observations**, *Atmos. Chem. Phys. Discuss. [preprint]*, https://doi.org/10.5194/acp-2021-382, in review

Karrer, M., Dias Neto, J., von Terzi, L., & Kneifel, S. (2021b). **Differences of Microphysical Processes in the Melting Layer Found for Rimed and Unrimed Snowflakes Using Cloud Radar Statistics** . Submitted to *Journal of Geophysical Research: Atmospheres*, 2021JD035907

Co-author publications

Ori, D., Schemann, V., **Karrer, M.**, Dias Neto, J., von Terzi, L., Seifert, A., & Kneifel, S. (2020). **Evaluation of ice particle growth in ICON using statistics of multi-frequency Doppler cloud radar observations**. *Quarterly Journal of the Royal Meteorological Society*, 146(733), 3830-3849.

Ori, D., von Terzi, L., **Karrer, M.**, & Kneifel, S. (2021). **snowScatt 1.0: consistent model of microphysical and scattering properties of rimed and unrimed snowflakes based on the self-similar Rayleigh–Gans approximation**. *Geoscientific Model Development*, 14(3), 1511-1531.

Mróz, K., Battaglia, A., Kneifel, S., von Terzi, L., **Karrer, M.**, & Ori, D. (2021). **Linking rain into ice microphysics across the melting layer in stratiform rain: a closure study**. *Atmospheric Measurement Techniques*, 14(1), 511-529.